

Determination of the neutron beta-decay asymmetry parameter  $A_0$  using polarized  
ultracold neutrons

---

DISSSERTATION

---

A dissertation submitted in partial  
fulfillment of the requirements for  
the degree of Doctor of Philosophy  
in Physics in the Department of  
Physics and Astronomy at the  
University of Kentucky

By  
Michael A-P Brown  
Lexington, Kentucky

Director: Dr. Bradley Plaster, Associate Professor of Physics  
Lexington, Kentucky 2018

Copyright<sup>©</sup> Michael A-P Brown 2018

## ABSTRACT OF DISSERTATION

### Determination of the neutron beta-decay asymmetry parameter $A_0$ using polarized ultracold neutrons

The UCNA Experiment at the Los Alamos Neutron Science Center (LANSCE) is the first measurement of the  $\beta$ -decay asymmetry parameter  $A_0$  using polarized ultracold neutrons (UCN).  $A_0$ , which represents the parity-violating angular correlation between the direction of the initial neutron spin and the emitted decay electron's momentum, determines  $\lambda = g_A/g_V$ , the ratio of the weak axial-vector and vector coupling constants. A high-precision determination of  $\lambda$  is important for weak interaction physics, and when combined with the neutron lifetime it permits an extraction of the CKM matrix element  $V_{ud}$  solely from neutron decay. At LANSCE, UCN are produced in a pulsed, spallation driven solid deuterium source and then polarized via transport through a 7 T magnetic field. Their spins can then be flipped via transport through an Adiabatic Fast Passage spin flipper located in a low-field-gradient 1 T field region prior to transport to a decay storage volume situated within a 1 T solenoidal spectrometer. Electron detector packages located at each end of the spectrometer provide for the measurement of decay electrons. Previous UCNA results (based on data collected in 2010 and earlier) were limited by systematic uncertainties, in particular those from the UCN polarization, calibration of the electron energy, electron backscattering, and angular acceptance of events. This dissertation will present a background of Neutron Decay, an overview of the UCNA Experiment, followed by a detailed report on the entire analysis process for data acquired during run periods in 2011-2012 and 2012-2013.

KEYWORDS: UCN,Neutrons

Author's signature: Michael A-P Brown

Date: January 10, 2018

Determination of the neutron beta-decay asymmetry parameter  $A_0$  using polarized  
ultracold neutrons

By  
Michael A-P Brown

Director of Dissertation: Dr. Bradley Plaster

Director of Graduate Studies: Dr. Chris Crawford

Date: January 10, 2018

## ACKNOWLEDGMENTS



## TABLE OF CONTENTS

Acknowledgments . . . . .	iii
Table of Contents . . . . .	iv
List of Figures . . . . .	viii
List of Tables . . . . .	xv
 Chapter 1 Introduction . . . . .	1
1.1 Properties of the neutron . . . . .	1
1.2 $\beta$ -decay and weak interactions: A brief history . . . . .	2
1.2.1 Fermi's theory of $\beta$ -decay . . . . .	3
1.2.1.1 Fermi and Gamow-Teller Transitions . . . . .	5
1.2.2 Parity Violation in Weak Decays . . . . .	5
1.2.2.1 Lee and Yang . . . . .	5
1.2.2.2 Discovery of Parity Violation . . . . .	6
1.2.3 Correlation Coefficients . . . . .	8
1.2.4 $V - A$ Structure . . . . .	9
1.2.5 Renormalizing the Hadronic Current . . . . .	12
1.2.5.1 Conserved Vector Current Hypothesis . . . . .	12
1.2.6 CKM Mixing Matrix . . . . .	13
1.3 What does this mean for the neutron? . . . . .	15
1.3.1 Matrix Element . . . . .	15
1.3.2 Neutron $\beta$ -decay Asymmetry Parameter $A$ . . . . .	16
1.3.2.1 Recoil order corrections . . . . .	18
1.3.2.2 Electromagnetic Corrections . . . . .	19
1.3.3 Neutron Lifetime . . . . .	19
1.4 Ultracold Neutrons . . . . .	20
1.4.0.1 Fermi Potential . . . . .	20
1.4.0.2 Gravity . . . . .	21
1.4.0.3 Magnetic Fields . . . . .	21
1.5 Motivation in a nutshell . . . . .	22
1.5.1 Why determine $\lambda$ ? . . . . .	22
1.5.2 Current status of $A_0$ measurements . . . . .	23
 Chapter 2 UCNA Experiment . . . . .	26
2.1 Overview . . . . .	26
2.2 Ultracold Neutron Source and Guide System . . . . .	27
2.3 Neutron Polarization . . . . .	29
2.4 Super-conducting Solenoidal Spectrometer . . . . .	30
2.4.1 Decay Trap . . . . .	31

2.4.2	Magnetic Field . . . . .	31
2.4.3	Detector Packages . . . . .	33
2.4.3.1	Multiwire Proportional Chamber . . . . .	33
2.4.3.2	Scintillator . . . . .	34
2.4.3.3	Scintillator Energy Calibration . . . . .	35
2.4.3.4	Muon Veto System . . . . .	36
2.5	Data Signals and Trigger Logic . . . . .	36
2.6	Data Taking Structure . . . . .	39
2.6.1	$\beta$ -decay run structure . . . . .	39
2.7	Backscattering . . . . .	39
Chapter 3	UCNA Analysis . . . . .	43
3.1	Outline of Analysis Steps . . . . .	43
3.2	Time-dependent Detector Corrections . . . . .	44
3.2.1	Pedestal Subtraction . . . . .	44
3.2.2	Gain Correction . . . . .	48
3.2.2.1	$^{207}\text{Bi}$ Pulser . . . . .	48
3.2.2.2	Endpoint Stabilization . . . . .	52
3.2.3	Time-dependent backgrounds . . . . .	54
3.3	Trigger Thresholds . . . . .	54
3.3.1	General Model for Trigger Determination . . . . .	54
3.3.2	Trigger Data Selection . . . . .	55
3.3.3	Determining the Trigger Probability . . . . .	55
3.3.3.1	Functional Fit of the Trigger Threshold . . . . .	56
3.4	Simulation . . . . .	57
3.4.1	Input . . . . .	57
3.4.1.1	Conversion Electron Sources . . . . .	57
3.4.1.2	Activated Xenon . . . . .	57
3.4.1.3	$\beta$ -decay Electrons . . . . .	57
3.4.2	Output . . . . .	57
3.4.2.1	Energy Deposition . . . . .	57
3.4.2.2	Quenched Energy . . . . .	58
3.4.2.3	Magnetic Field . . . . .	58
3.4.2.4	Position of Detector hits . . . . .	58
3.4.3	Simulating Detector Response . . . . .	58
3.4.4	Detector Response Model . . . . .	58
3.5	Energy Response from Detector Response . . . . .	59
3.5.1	Combining PMT Responses . . . . .	59
3.5.2	$E_{\text{vis}}$ to $E_{\text{recon}}$ . . . . .	61
3.6	Calibration Overview . . . . .	62
3.6.1	PMT Calibration . . . . .	62
3.6.2	Wirechamber Calibration . . . . .	63
3.7	Polarimetry . . . . .	63
Chapter 4	UCNA Calibrations . . . . .	66

4.1	Wirechamber Position Reconstruction . . . . .	66
4.1.1	Wirechamber signals . . . . .	66
4.1.1.1	Wirechamber trigger . . . . .	67
4.1.1.2	Cathode wire clipping . . . . .	67
4.1.2	Wirechamber position reconstruction . . . . .	67
4.1.2.1	Events with no cathode clipping . . . . .	68
4.1.2.2	Events with cathode clipping or missing wire signals . . . . .	69
4.1.3	Simulation of wirechamber positions . . . . .	71
4.1.3.1	Wire model . . . . .	71
4.1.3.2	Results of individual wire model . . . . .	73
4.2	Scintillator Energy Calibration . . . . .	73
4.2.1	Method . . . . .	73
4.2.2	Position Dependent Light Transport Maps . . . . .	75
4.2.2.1	Activated Xenon . . . . .	75
4.2.2.2	Position Maps . . . . .	76
4.2.3	Linearity Curves . . . . .	79
4.2.3.1	Fitting the source peaks . . . . .	79
4.2.3.2	Extracting the PMT response . . . . .	80
4.2.4	PMT Resolution Factors . . . . .	83
4.2.5	Applying the calibration . . . . .	84
4.2.6	Monte Carlo to Data Agreement . . . . .	85
4.3	Wirechamber Energy Calibration . . . . .	86
4.3.1	Method . . . . .	86
4.3.2	Position dependence of anode signal . . . . .	91
4.3.3	Relating Anode Signal to $E_{\text{MWPC}}$ . . . . .	92
4.3.4	Backscattering Separation for Type 2/3 Events . . . . .	95
4.3.4.1	Monte Carlo Study . . . . .	95
4.3.4.2	Determining a continuous separation cut . . . . .	97
4.3.4.3	Results . . . . .	98
Chapter 5	UCNA Results . . . . .	100
5.1	Constructing an Asymmetry . . . . .	100
5.1.1	Decay Rate Model . . . . .	100
5.1.2	Super-Ratio . . . . .	101
5.1.3	Extracting $A_0$ . . . . .	102
5.2	Systematic Corrections and Uncertainties . . . . .	103
5.2.1	Definition of $\Delta$ . . . . .	103
5.2.2	Energy Dependent Monte Carlo Corrections . . . . .	104
5.2.2.1	Backscattering Misidentification, $\Delta_2$ . . . . .	105
5.2.2.2	Angular Acceptance, $\Delta_3$ . . . . .	107
5.2.2.3	Uncertainty in $\Delta_{\text{MC}}$ . . . . .	110
5.2.2.4	Fidelity of Corrections . . . . .	114
5.2.3	Polarimetry Correction . . . . .	114
5.2.3.1	Extraction of $A_0$ using $\langle P \rangle_+$ and $\langle P \rangle_-$ . . . . .	117
5.2.4	Energy Reconstruction . . . . .	118

5.2.5	Background Contributions . . . . .	121
5.2.5.1	Background Subtraction . . . . .	122
5.2.5.2	Neutron Generated Backgrounds . . . . .	124
5.2.5.3	Veto Efficiency Uncertainty . . . . .	126
5.2.6	Miscellaneous Systematic Corrections and Uncertainties . . . . .	127
5.2.6.1	Wirechamber Efficiency . . . . .	127
5.2.6.2	Gain Uncertainty . . . . .	128
5.2.6.3	Magnetic Field Nonuniformity . . . . .	129
5.3	Theory Modifications . . . . .	131
5.3.1	Recoil Order Modification $\Delta_{\text{RO}}$ . . . . .	131
5.3.2	Radiative Modification $\Delta_{\text{rad}}$ . . . . .	132
5.4	Final Asymmetries . . . . .	132
5.4.1	Blinding . . . . .	133
5.4.2	Data Selection and Processing . . . . .	133
5.4.2.1	Cuts . . . . .	134
5.4.2.2	Data Taking Structure . . . . .	135
5.4.2.3	Analysis Choices . . . . .	135
5.4.3	Determining $A_0$ . . . . .	138
5.4.3.1	Combining Results . . . . .	138
5.4.3.2	Optimization of energy range . . . . .	138
5.4.3.3	Unblinded Result . . . . .	139
5.5	Future Outlook for UCNA and $A_0$ Measurements . . . . .	141
	Appendices . . . . .	148
	Chapter A Magnetic Field Non-Uniformity and the Super-Ratio . . . . .	148
	References . . . . .	150
	Vita . . . . .	157

## LIST OF FIGURES

<p>1.1 The electron kinetic energy spectrum in free neutron <math>\beta</math>-decay. The horizontal axis has units of energy in MeV in this case, but the shape of the spectrum is of general interest. Note that the decay probability does go to zero at zero MeV. . . . .</p> <p>1.2 The contact interaction of Fermi's theory of <math>\beta</math>-decay is shown in a.). The theory is capable of describing other processes which move one of the outgoing particle lines to the left side, like electron capture by the proton producing a neutron and an electron neutrino. b.) shows the decay at the quark level, where the initial state is the quark makeup of the neutron, and the subsequent decay of one of the down quarks into an up quark creates the W boson which decays into the electron and electron anti-neutrino. . . . .</p> <p>1.3 Data from C. S. Wu's experiment measuring the correlation between the emitted direction of the electron from the decay of polarized <math>^{60}\text{Co}</math>. The two curves represent the counting rates when the nuclei were oriented in opposite directions with respect to the electron detector. The existence of a splitting indicates a violation of parity as the electrons are preferentially emitted in the direction opposite the spin. . . . .</p> <p>1.4 Historical plot of <math>A_0</math> measurements prior to the analysis presented within this thesis [Bop+86; Ero+91; Yer+97; Lia+97; Abe+02; Mun+13; Men+13]. The shaded band indicates the Particle Data Group average value [PG+16] for the asymmetry parameter, where the solid data points are included in the average. Thank you to Dr. Plaster for inclusion of this plot. . . . .</p> <p>2.1 UCN source schematic. Inlay is a zoom in on the <math>\text{SD}_2</math> cell [Sau+13]. . . . .</p> <p>2.2 Schematic of guides and layout of the UCNA experiment [Pla+12]. . . . .</p> <p>2.3 Detailed rendering of the experimental area. . . . .</p> <p>2.4 Typical field profile from 2011-2012 run period. The smooth interpolation between discrete values utilizes a half-wave of a cosine as defined in 3.4.2.3. . . . .</p> <p>2.5 Schematic of the detector packages [Pla+12]. . . . .</p> <p>2.6 Schematic showing the mechanics of the scintillator calibration. The sources are located on a source paddle, which is inserted into the decay trap while under vacuum. The sources are then translated across the face of the detector, and a calibration run is completed at each stationary point. There are generally far more than four positions sampled, but for demonstrations sake only four points are included in the figure. . . . .</p> <p>2.7 Comparison of the raw ADC signal from a single PMT for any global trigger in panel a.) and upon requiring a two-fold PMT trigger on the side of the PMT of interest in panel b.). This type of cut is part of the electron trigger along with a coincidence with the wirechamber. . . . .</p>	<p>2</p> <p>4</p> <p>7</p> <p>23</p> <p>27</p> <p>28</p> <p>30</p> <p>32</p> <p>33</p> <p>35</p> <p>37</p>
--	--

2.8	Example TDC signal (converted to nanoseconds) from a $\beta$ -decay run for a single detector. Note that the horizontal axis is technically the time elapsed since a trigger occurred, so a longer time indicates an earlier trigger. The dashed line indicates the cut used to separate a self-trigger (right of the dashed line) from a backscattering trigger (left of the dashed line). The events at $t = 0$ are events which did not create a self-trigger. . . . .	37
2.9	Schematic of different event types and the trigger logic involved with identifying each type [Pla+12]. . . . .	40
3.1	Pedestal means as a function of run number for 2011-2012 East Detectors. Error bars are the RMS of the measured pedestal. The red lines indicate what ranges of runs belong to different calibration periods, and the red marker is the calibration reference run, which will be discussed in later sections. . . . .	46
3.2	Pedestal means as a function of run number for 2011-2012 West Detectors. Error bars are the RMS of the measured pedestal. The red lines indicate what ranges of runs belong to different calibration periods, and the red marker is the calibration reference run, which will be discussed in later sections. . . . .	47
3.3	Example $^{207}\text{Bi}$ spectrum and fit for a single PMT over the course of a run. The upper and lower bismuth conversion electron peaks are seen, along with a distribution from decay gammas. Note that the gamma rays are visible because the pulser is attached directly to PMT and there is no type of veto (like the MWPC) to remove them. . . . .	48
3.4	Gain factors, $g_i$ , as a function of run number for 2011-2012 East Detectors. The red lines indicate what ranges of runs belong to different calibration periods, and the red marker is the calibration reference run. . . . .	50
3.5	Gain factors, $g_i$ , as a function of run number for 2011-2012 West Detectors. The red lines indicate what ranges of runs belong to different calibration periods, and the red marker is the calibration reference run. . . . .	51
3.6	Example Kurie plot with linear fit to extract the y-intercept, which is the endpoint energy. The deviations from a straight line are due to the trigger efficiency at low energies and finite resolution at high energies. Care must be taken to fit in a region which more appropriately characterizes the true underlying electron energy spectrum. . . . .	52
3.7	Typical trigger thresholds as a function of pedestal subtracted ADC values from the West PMTs with fits shown in red. The y-axis is a probability of triggering given some ADC signal. . . . .	56
3.8	Parameterization between $E_{\text{vis}}$ and $E_{\text{recon}}$ for 2011-2012. The mapping for the other geometries are very similar and thus are not shown. . . . .	61

3.9	Figure courtesy of E. Dees and A. R. Young as published in [Bro+17]. “Switcher signal as a function of time, during “D”-type runs: (1) the shutter closes and the switcher state changes, permitting UCN in the guide outside the decay volume to drain to the switcher UCN detector, (2) the AFP spin-flipper changes state, allowing depolarized neutrons in the guides outside the decay volume to drain to the switcher, (3) the shutter opens, permitting depolarized neutrons within the decay volume to drain to the switcher detector, (4) the AFP spin-flipper returns to its initial state, allowing the initially loaded spin state to drain from the decay volume, (5) backgrounds are measured after the UCN population in the decay volume has drained away. The presented data were taken in 2011 and UCN loaded into the decay volume with the spin-flipper off.” . . . . .	64
4.1	Number of clipped wires in the $x$ -plane of the East detector. Most of the events ( $\tilde{92}\%$ ) exhibit no clipping. . . . .	68
4.2	Wirechamber reconstructed positions for all electron events in a single octet of $\beta$ -decay data. The black dashed line indicates the 50 mm fiducial cut applied to the data during asymmetry extraction. . . . .	69
4.3	Collection of extracted $\sigma$ values for the Gaussian determination of event position. The average of this distribution is an estimate of the characteristic width of the wirechamber charge cloud, $\sigma_c$ , used when only two wires are usable in the position reconstruction. . . . .	70
4.4	Comparisons between data (blue line) and simulation (red dashed line) after the application of the single wire trigger and clipping model. There is a discrepancy in the multiplicity, but the general features are captured. The number of clipped wires in data and simulation is in better agreement.	72
4.5	Position dependence of clipped events for data (blue line) and simulation (red dashed line) after the application of the single wire trigger and clipping model to the simulation. The model captures the position dependence of the clipping nicely. . . . .	73
4.6	Example energy spectrum of the neutron-activated xenon used for position map determination. . . . .	76
4.7	Typical set of position maps from a xenon position mapping period. The position maps remain fairly constant throughout the two run periods. . .	78
4.8	Ratio of $\eta_{\text{peak}}/\eta_{\text{endpoint}}$ for the East side PMTs. The differences are most pronounced in areas of high and low light collection. The West side shows more consistency when comparing maps calculated using the different features. . . . .	79
4.9	East linearity response curves for a single calibration run period in 2011-2012. The residuals reported are calculated as $100 \times (fit - data)/fit$ . The error bars on the points are the error on the extracted mean from the fits of the data and simulation peaks, but they are smaller than the markers.	81

4.10 West linearity response curves for a single calibration run period in 2011-2012. The residuals reported are calculated as $100 \times (fit - data)/fit$ . The error bars on the points are the error on the extracted mean from the fits of the data and simulation peaks, but they are smaller than the markers.	82
4.11 Plots of the data source widths vs. the simulated source widths for a single PMT on each side of the detector used for determination of the proper PMT resolution factors. When the slope $\approx 1$ , the resolution factors are recorded to be used in the final calibration. . . . .	84
4.12 Plots of the data source widths vs. the simulated source widths for the final $E_{recon}$ source spectra on each side of the detector. This is a measure of how well the individual PMT resolution factors combine to produce agreement between the final reconstructed energy spectra. The slopes of nearly unity indicate the final detector resolutions were very good for this calibration period. . . . .	85
4.13 Example spectra from each PMT for simulation (red dashed line) and data (blue line) for $^{137}\text{Ce}$ conversion electron source after application of the calibration. This is for a random run that included all three sources within the fiducial volume at the same time. . . . .	87
4.14 Example spectra from each PMT for simulation (red dashed line) and data (blue line) for $^{113}\text{Sn}$ conversion electron source after application of the calibration. This is for a random run that included all three sources within the fiducial volume at the same time. . . . .	88
4.15 Example spectra from each PMT for simulation (red dashed line) and data (blue line) for $^{207}\text{Bi}$ conversion electron source after application of the calibration. This is for a random run that included all three sources within the fiducial volume at the same time. . . . .	89
4.16 Example $E_{recon}$ spectra from combined PMT response for simulation (red dashed line) and data (blue line) for all conversion electron sources after application of the calibration. This plot is from the same run as the plots of the previous individual PMT spectra, showing how the spectra combine to produce a single final energy estimate. . . . .	90
4.17 Typical wirechamber anode signal for a xenon calibration run in a single pixel. The fit function is a TMath::Landau function from the ROOT Data Analysis Framework, and the extracted value is the MPV (most probable value) from the distribution. . . . .	91
4.18 Example position dependent anode response for each MWPC. These MWPC position maps were created using electrons with $300 \text{ keV} < E_{recon} < 350 \text{ keV}$ . . . . .	91
4.19 TMath::Landau fit of both simulation and data for electron events which deposited between 300-400 keV in the west scintillator. The fitted MPV (p1 in the statistics box) from each plot make up a single data point in the wirechamber energy calibration plot below (Figure 4.20). . . . .	93
4.20 Example MWPC calibration curve for a single run in 2011-2012. A calibration like this one is carried out for every $\beta$ -decay run. . . . .	93

4.21	Simulation vs. Data after application of the wirechamber calibration for a single run in 2011-2012. This plot includes only Type 0 events. . . . .	94
4.22	2011-2012 simulated wirechamber energy deposition of Type 2 and Type 3 events with $200 \text{ keV} < E_{\text{recon}} < 300 \text{ keV}$ . The vertical dashed line indicates the optimal cut on the wirechamber energy deposition to separate the two otherwise identical backscattering events. The position of this cut varies with $E_{\text{recon}}$ . The distributions for the other geometries are similar. . . . .	95
4.23	Fraction of properly identified events where $200 \text{ keV} < E_{\text{recon}} < 300 \text{ keV}$ as a function of the separation cut. The polynomial fit to the maximum is indicated by the solid red line, from which the location of the most effective separation cut is extacted. . . . .	96
4.24	Plot of optimal cuts for each detector from 2011-2012 and 2012-2013. The eight data points for each detector are a result of dividing the simulation data into 100 keV $E_{\text{recon}}$ groups from 0 – 800 keV. The average of the two detector sides are fit to determine a continuous function describing the optimal Type 2/3 separation cuts. . . . .	97
4.25	Fraction of properly identified events when the Type 2/3 separation is applied compared to when it is not applied. The results are shown for a single octet from all possible geometries. The shaded error band is purely statistical. . . . .	98
5.1	Backscattering corrections for analysis choice used in final asymmetry extraction (All event types included with 2/3 separated using the MWPC energy calibration). . . . .	106
5.2	Simulated detector efficiency as a function of electron energy for electrons which pass through the decay trap endcaps. . . . .	107
5.3	$\cos \theta$ corrections for analysis choice used in final asymmetry extraction (All event types included with 2/3 separated using the MWPC energy calibration). . . . .	108
5.4	Bin-by-bin $\Delta_2$ corrections with polynomial fit shown in red. . . . .	111
5.5	Bin-by-bin $\Delta_3$ corrections with polynomial fit shown in red. . . . .	112
5.6	Subfigures are broken into each event type. Left of each subfigure shows electron energy spectra for background subtracted data (blue open circles), Monte Carlo (black solid line), and the background (black closed circles). The right plot in each subfigure shows the fractional residual between background subtracted data and Monte Carlo, which is used when applying the conservative fractional uncertainty on the Monte Carlo corrections. . . . .	115
5.7	Extracted asymmetries from Monte Carlo data processed to mimic the experimental data. The dashed line indicates the 2017 PDG value $A_0 = -0.1184$ which was input into the simulation, thus the goal upon extraction of the final asymmetry parameter. The blue closed points indicate analysis choices that include type 0 events and utilize the scale on the left vertical axis values. The red open circles include only backscattering event types and use the right vertical axis values. . . . .	116

5.8	Distributions of the residuals for each conversion electron source line used in the 2011-2012 calibration. The mean and sigma reported in the fit box are not the same as those used in the energy uncertainty, as they are the results of the fit and not the calculated mean. . . . .	119
5.9	Distributions of the residuals for each conversion electron source line used in the 2012-2013 calibration. The mean and sigma reported in the fit box are not the same as those used in the energy uncertainty, as they are the results of the fit and not the calculated mean. . . . .	120
5.10	Plot of energy uncertainty vs. reconstructed energy. The points plotted are the mean and $\sigma$ of all reconstructed calibration peaks of $^{137}\text{Ce}$ , $^{113}\text{Sn}$ , and the lower and upper $^{207}\text{Bi}$ peaks in that order. The $x$ -axis offset in the 2011-2012 and 2012-2013 points is artificial and only meant for visualization. The bands represent the energy uncertainty at any given electron energy for the two data sets. . . . .	121
5.11	Plot of uncertainty on $A_0$ from the energy calibration vs. reconstructed energy for each of the 2011-2012 and 2012-2013 geometries. Weighting the energy dependent uncertainties shown here by the experimental statistics in each energy bin produces the final uncertainty on the extracted asymmetries. . . . .	122
5.12	Total background spectra summed over all background runs for each event type in 2011-2012. . . . .	123
5.13	Total background spectra summed over all background runs for each event type in 2011-2012. . . . .	124
5.14	Integrated event rates for 2011-2012 East and West sides. The splitting in the $\beta$ run rates is due to the difference between a spin-flipper “on” vs. spin-flipper “off” run, as the flipper “on” loading efficiency is approximately 2/3 that of a flipper “off” run. . . . .	125
5.15	Integrated event rates for 2012-2013 East and West sides. The splitting in the $\beta$ run rates is due to the difference between a spin-flipper “on” vs. spin-flipper “off” run, as the flipper “on” loading efficiency is approximately 2/3 that of a flipper “off” run. . . . .	126
5.16	Radiative and Recoil Order theory corrections to the measured asymmetry due to finite mass and non-zero charge of the final state proton. . . . .	131
5.17	All raw super-ratio asymmetries as a function of group number, whether octet, quartet, or pair. There are no systematic corrections applied, and the asymmetries are integrated over the analysis window 190-740 keV. The split in the data is a batch of data from 2012-2013 that had to be discarded due to bad timing information. . . . .	136
5.18	Asymmetries for different subsets of data. The * signifies unseparated Type 2 and Type 3 events. The inset shows the asymmetries that include Type 0 events, as the uncertainties are too small to see in the main figure. The only corrections applied to these asymmetries are the energy dependent Monte Carlo corrections and the polarization correction. The error bars are purely statistical, so the observed agreement between asymmetries is a lower limit. . . . .	137

5.19	Plots of the fractional uncertainty on the extracted asymmetry for given minimum and maximum limits on the analysis window. The minimum of the combined systematic and statistical uncertainty is used for the final analysis window, $190 \text{ keV} < T_e < 740 \text{ keV}$ . . . . .	140
5.20	Statistical and systematic errors used in minimization of the energy window. This is a projection of Figure 5.19 about the minimum window cut of 190 keV to show the dependence on energy cut more effectively. . . . .	141
5.21	Panel (a) shows the ratio of $(A - A_{\min})$ to $\delta A$ , where $\delta A$ is the $1\sigma$ total uncertainty taken from Figure 5.19 panel (c). The $z$ -axis is a measure of agreement between the asymmetry in a bin with the overall minimum uncertainty bin, $A_{\min}$ , in units of $\sigma$ of the bin being used. Values between $-1$ and $+1$ indicate that the asymmetry in the bin is in agreement with $A_{\min}$ at the $1\sigma$ level. Panel (b) shows the bins for which this $1\sigma$ agreement is met. The black circle in each figure indicates the location of $A_{\min}$ . . . . .	142
5.22	Final beta decay spectrum from data (open circles), Monte Carlo (solid line), and the subtracted background (closed circles). The bottom shows the difference between the Monte Carlo spectrum and the data. . . . .	143
5.23	Final unblinded 2011-2012 and 2012-2013 asymmetry with all systematic corrections applied. The dashed line in a.) and c.) uses PDG $A_0 = -0.1184$ for comparison. The fits in b.) and d.) are over the final analysis window, $190 \text{ keV} < T_e < 740 \text{ keV}$ . The uncertainties are statistical only. . . . .	144
5.24	Historical plot of $A_0$ measurements including the measurement resulting from this analysis [Bop+86; Ero+91; Yer+97; Lia+97; Abe+02; Mun+13; Men+13; Bro+17]. The shaded band indicates the Particle Data Group average value [PG+16] for the asymmetry parameter, where the solid data points are included in the average (not including the Brown <i>et al.</i> point, as this will be included in future averages). Thank you to Dr. Plaster for inclusion of this plot. . . . .	145
5.25	Status of $V_{ud}$ , the neutron lifetime, and $\lambda$ measurements. The $\lambda$ result bands (vertical) are divided into pre-2002 [Bop+86; Yer+97; Lia+97] and post-2002 [Mos+01; Sch+08; Mun+13; Men+13] results, where the distinction is made using the date of the most recent result from each experiment. The right axis shows publication year for the individual lambda measurements included in the calculation of the $\lambda$ bands (closed markers for post-2002, open markers for pre-2002). Note that the result of this work (Brown <i>et al.</i> ) is the combined UCNA result from [Men+13] and the current analysis, and the Mund <i>et al.</i> result is the combined PERKEOII result from [Abe+02; Mun+13]. The diagonal bands are derived from neutron lifetime measurements and are separated into neutron beam [Yue+13; Byr+96] and UCN bottle experiments, which consist of material bottle storage [Ser+05; Arz+15; Ste+12; Pic+10; Mam+93] and magnetic bottle storage [PJ+17]. The $V_{ud}$ band (horizontal) comes from superallowed $0^+ \rightarrow 0^+$ nuclear $\beta$ -decay measurements [PG+16]. The error bands include scale factors as prescribed by the Particle Data Group [PG+16]. . . . .	146

## LIST OF TABLES

1.1	Transformation behavior of all possible bilinear covariants. . . . .	3
1.2	The chirality projected operators. . . . .	11
1.3	Effective potentials for some UCN reflecting materials. . . . .	21
2.1	Octet structure, where $\pm$ indicates spin flipper on/off, B refers to background run, D refers to depolarization run, and $\beta$ refers to $\beta$ -decay runs.	39
5.1	Values for the effective statistical uncertainties from each event type. The value is reported as the uncertainty on $\frac{\Delta A}{A}$ . . . . .	113
5.2	Values for the fractional uncertainties from each event type. The value is reported as the uncertainty on $\frac{\Delta A}{A}$ . . . . .	113
5.3	Actual integrated event type fractions as percent of total events. Also reported is the % difference between Monte Carlo and data spectra for each event type. These are calculated over an energy window of 190-740 keV, chosen to minimize the total uncertainty as will be shown. . . .	114
5.4	Results for average polarization fractions for each dataset in spin-flipper off (-) and spin-flipper on (+) states. . . . .	117
5.5	Mean and $\sigma$ of each conversion electron residual distribution as used in the energy uncertainty, Figure 5.10. . . . .	120

# Chapter 1

## Introduction

The purpose of this dissertation is to describe in detail the methods used in extracting the  $\beta$ -decay asymmetry parameter for the UCNA Experiment. This chapter hopes to motivate the inception of the parameter of interest and its role in the theory of  $\beta$ -decay. Also introduced are characteristics of the neutron itself with an emphasis on ultracold neutrons (UCN), the namesake of the UCNA experiment. The chapter will conclude with a brief summary of the theory and the motivation for carrying out precision measurements of the  $\beta$ -decay asymmetry parameter in free neutron decay.

### 1.1 Properties of the neutron

Let us take a moment to give a very brief introduction to the neutron to motivate the upcoming sections. The majority of this dissertation can be read and mostly understood without much knowledge of the theoretical description behind neutron  $\beta$ -decay, so the properties of the neutron are a natural starting point.

The neutron is a net neutrally charged composite particle. The terms net and composite hint at the inner structure of the neutron, made up of fundamental particles called quarks, in this case two down ( $d$ ) quarks and one up ( $u$ ) quark. The quarks carry charge, with the  $u$  charge  $+2/3$  and the  $d$  charge  $-1/3$ , so that the net charge of the neutron is zero. This can be compared to the proton, another composite particle made up of three quarks (two  $u$  and one  $d$  quark), whose net charge is  $+1$ . Protons and neutrons are described by the common term nucleons, as they are the particles within the nucleus of all atoms. Four other quarks exist, the charm, strange, bottom, and top in order of increasing mass. The neutron is the second lightest three-quark composite particle (baryon) behind only the proton.

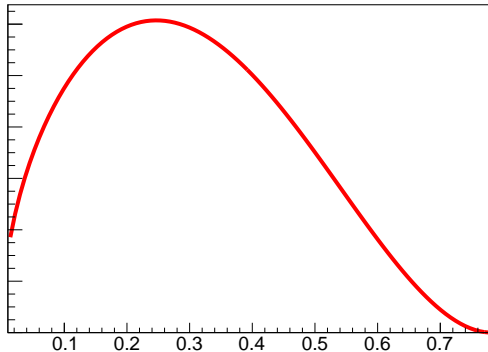


Figure 1.1: The electron kinetic energy spectrum in free neutron  $\beta$ -decay. The horizontal axis has units of energy in MeV in this case, but the shape of the spectrum is of general interest. Note that the decay probability does go to zero at zero MeV.

The free neutron undergoes  $\beta$ -decay, defined as a transition from the neutron to a proton, electron, and electron anti-neutrino,

$$n \rightarrow p + e^- + \bar{\nu}_e,$$

as is also seen pictorially in Figure 1.2 panel (a). The three-body decay gives rise to a continuous energy spectrum for the proton, electron, and anti-neutrino by conservation of energy and momentum. The electron kinetic energy ( $T_e$ ) spectrum, the measurement of which is a primary focus of this dissertation, is seen in Figure 1.1. The endpoint kinetic energy of the electron is  $\sim 782$  keV, as shown by the maximum energy in the spectrum. The lifetime of the free neutron is approximately fifteen minutes.

## 1.2 $\beta$ -decay and weak interactions: A brief history

Prior to 1930,  $\beta$ -decay of nuclei was a polarizing topic of debate. Originally only the decay electron was detected, and given such an observed a two-body decay (the recoil nucleus and the emitted electron being the two bodies) one would expect a discrete electron energy defined by the difference in mass between the mother and daughter nuclei. Instead, a continuous energy spectrum was observed for the electron, which initially led some to believe that energy conservation was moot. Others, like Wolfgang Pauli, were not ready to abandon energy conservation. He postulated that a neutral particle could also be emitted in the decay. This third particle would share

the energy available in the reaction, explain the continuous energy distribution of the electron, and go on undetected as it would not interact electromagnetically. The particle was termed the neutrino by Fermi, and it would be a crux of Fermi's theory of  $\beta$ -decay. A quarter century later, the existence of the neutrino would be confirmed experimentally [CJ+56].

### 1.2.1 Fermi's theory of $\beta$ -decay

After Pauli postulated the existence of the neutrino to explain the continuous energy distribution of the  $\beta$ -decay electron, Fermi attempted to theoretically describe the process in a similar manner to the theory of emission of gamma radiation from an excited nucleus [Fer34a; Wil68]. His theory relied on two postulates: the existence of the neutrino and that the nucleus consisted of heavy particles only, the neutron and the proton, both of which would turn out to be true.

Table 1.1: Transformation behavior of all possible bilinear covariants.

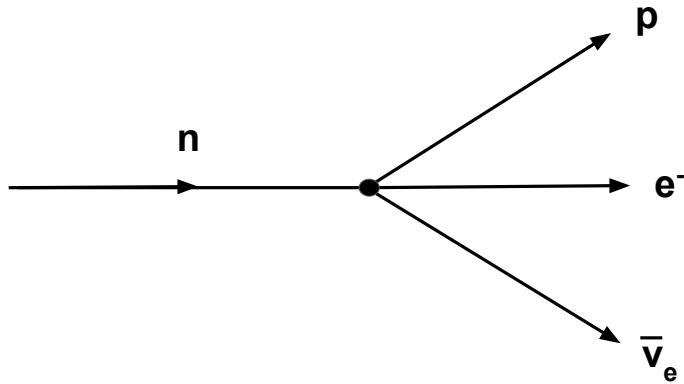
$\bar{\psi}\psi$	scalar
$\bar{\psi}\gamma^5\psi$	pseudoscalar
$\bar{\psi}\gamma^\mu\psi$	vector
$\bar{\psi}\gamma^\mu\gamma^5\psi$	axial vector
$\bar{\psi}\sigma^{\mu\nu}\psi$	antisymmetric tensor

Fermi's interaction Hamiltonian took the form (written in a different manner from Fermi's original paper on the subject for the sake of clarity)

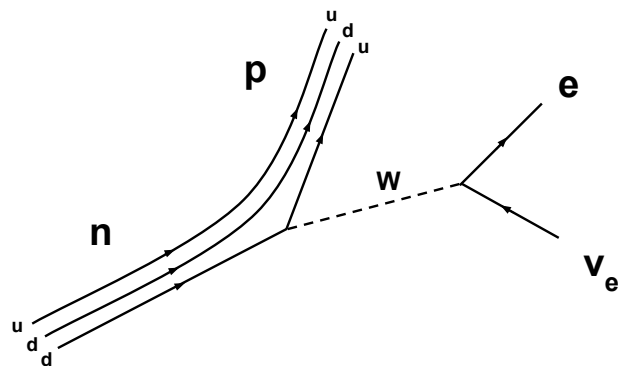
$$H = C_V (\bar{\psi}_p \gamma_\mu \psi_n) (\bar{\psi}_e \gamma^\mu \psi_\nu), \quad (1.1)$$

where  $\bar{\psi}\gamma_\mu\psi$  is a vector current (see Table 1.1). The assumption that the current-current interaction would be of the vector-vector variety was a natural choice as this is the case for electromagnetism.

Fermi's theory of  $\beta$ -decay treats the decay as a four-point contact interaction (see Figure 1.2 panel (a)), where the currents are evaluated at the same point in space and time [Ren90]. For those familiar with quantum field theory within the Standard Model, this differs from the typical interaction Hamiltonian as there is no propagator, or force carrier, to mediate the interaction between the two currents. At the most fundamental level, the decay proceeds as is shown in Figure 1.2 panel (b), where a  $d$  quark decays into a  $u$  quark via the emission of a massive  $W^-$  boson. The mass



(a) Contact Interaction at the particle level



(b) Quark level decay

Figure 1.2: The contact interaction of Fermi's theory of  $\beta$ -decay is shown in a.). The theory is capable of describing other processes which move one of the outgoing particle lines to the left side, like electron capture by the proton producing a neutron and an electron neutrino. b.) shows the decay at the quark level, where the initial state is the quark makeup of the neutron, and the subsequent decay of one of the down quarks into an up quark creates the W boson which decays into the electron and electron anti-neutrino.

of the  $W$  ( $\sim 80$  GeV) is much larger than the energy available in the decay, and thus the  $W$  almost instantaneously decays into the  $e^-$  and  $\bar{\nu}_e$ . The fact that the subsequent  $W$  decay is “almost” instantaneous makes Fermi’s contact interaction a good approximation. More formally, the small momentum transfer in nuclear  $\beta$ -decay compared to the mass of the  $W$  boson makes the propagator take a constant form, thus absorbing the propagator into the coupling constant.

The theory worked well at predicting the energy spectrum of the electron from which Fermi deduced that the neutrino must be nearly massless, but suffered one flaw. The vector nature of the theory did not permit the observed allowed nuclear  $\beta$ -decay transitions which can transform the spin of the decaying nucleus. This was pointed out by Gamow and Teller in 1936 [GT36], where they show that a current-current interaction that transforms like a pseudovector properly assigns the spins of the products in thorium decays. As such, one can generalize Fermi’s theory by including all possible bilinear covariant terms that satisfy Lorentz invariance:

$$H = C_S(\bar{\psi}_p \psi_n)(\bar{\psi}_e \psi_\nu) + C_V(\bar{\psi}_p \gamma_\mu \psi_n)(\bar{\psi}_e \gamma^\mu \psi_\nu) + C_T(\bar{\psi}_p \sigma^{\mu\nu} \psi_n)(\bar{\psi}_e \sigma^{\mu\nu} \psi_\nu) + C_A(\bar{\psi}_p \gamma_\mu \gamma^5 \psi_n)(\bar{\psi}_e \gamma^\mu \gamma^5 \psi_\nu) + C_P(\bar{\psi}_p \gamma^5 \psi_n)(\bar{\psi}_e \gamma^5 \psi_\nu), \quad (1.2)$$

where the coefficients quantify the coupling to each respective current.

### 1.2.1.1 Fermi and Gamow-Teller Transitions

This shortcoming of Fermi’s original vector-vector interaction lends itself to the definition of two types of allowed  $\beta$ -decay transitions. The Fermi transition proceeds through the scalar and vector currents with  $\Delta J = 0$  and no parity change. Gamow-Teller transitions correspond to the axial vector and tensor currents and have  $\Delta J = 0, \pm 1$  with no parity change, but excluding the  $0^+ \rightarrow 0^+$  nuclear transitions. The pseudoscalar terms does not contribute to the amplitude in the low energy limit [Ren90].

## 1.2.2 Parity Violation in Weak Decays

### 1.2.2.1 Lee and Yang

Prior to the 1950’s, all discrete symmetries (parity, charge conjugation, and time reversal) were thought to be conserved separately for all interactions in nature. A dilemma arose when two particles, called the  $\tau$  and  $\theta$  mesons at the time, posessed

the same mass and charge as the  $K^+$  meson, but decayed to different final states of parity. The  $\tau$  decayed into three pions and the  $\theta$  into two pions. The initial classification of the two observably identical particles into two different particles was logical given that parity conservation was then sacrosanct, but in 1956 Lee and Yang proposed a very different solution to the problem. They realized that there was no evidence that parity must be conserved in the weak interaction. In the full expression of Fermi's theory (Equation 1.2), while including all possible combinations of bilinear covariants, there was no mixing between the individual currents and each individual current-current term transforms like a scalar. For example, two individual axial vector currents would each transform as  $P(\bar{\psi}_p \gamma_\mu \gamma^5 \psi_n) \rightarrow -\bar{\psi}_p \gamma_\mu \gamma^5 \psi_n$  under parity, but the multiplication of two such terms transforms like a scalar. Thus, none of the terms in 1.2) are capable of violating parity, as the Hamiltonian would remain invariant under a parity transformation.

In their 1956 paper [LY56], Lee and Yang modified the weak interaction Hamiltonian by including the possibility of a pseudoscalar current-current interaction, namely

$$\begin{aligned} H = & \bar{\psi}_p \psi_n (C_S \bar{\psi}_e \psi_\nu + C'_S \bar{\psi}_e \gamma^5 \psi_\nu) \\ & + \bar{\psi}_p \gamma_\mu \psi_n (C_V \bar{\psi}_e \gamma^\mu \psi_\nu + C'_V \bar{\psi}_e \gamma^\mu \gamma^5 \psi_\nu) + \bar{\psi}_p \sigma^{\mu\nu} \psi_n (C_T \bar{\psi}_e \sigma^{\mu\nu} \psi_\nu + C'_T \bar{\psi}_e \sigma^{\mu\nu} \gamma^5 \psi_\nu) \\ & + \bar{\psi}_p \gamma_\mu \gamma^5 \psi_n (C_A \bar{\psi}_e \gamma^\mu \gamma^5 \psi_\nu + C'_A \bar{\psi}_e \gamma^\mu \psi_\nu) + \bar{\psi}_p \gamma^5 \psi_n (C_P \bar{\psi}_e \gamma^5 \psi_\nu + C'_P \bar{\psi}_e \psi_\nu). \end{aligned} \quad (1.3)$$

If any of the  $C'_i$  coefficients are nonzero, parity would not be conserved due to the scalar-pseudoscalar form of the current-current interactions that are labelled by the primed coefficients.

Along with the inclusion of potential parity violating terms in the Hamiltonian, Lee and Yang presented several potential tests of parity violation in the weak sector. One such proposition was the measurement of the correlation between the spin of a polarized nucleus and the momentum of the  $\beta$ -decay electron.

### 1.2.2.2 Discovery of Parity Violation

Following the publication of Lee and Yang's newly modified theory of  $\beta$ -decay, C. S. Wu and collaborators designed an experiment to test the potential violation of parity in the  $\beta$ -decay of  $^{60}\text{Co}$  ( $^{60}\text{Co} \rightarrow ^{60}\text{Ni} + e^- + \bar{\nu}_e$ ) [Wu+57]. The premise of the experiment was simple: place an electron detector along the  $+z$  axis, polarize the  $^{60}\text{Co}$  nuclei using a magnetic field in the  $\pm z$  direction, and measure the electron rate in each polarization configuration. If parity is violated, a clear asymmetry would be present between the two polarizations, which is precisely what was discovered and can be seen in Figure 1.3.

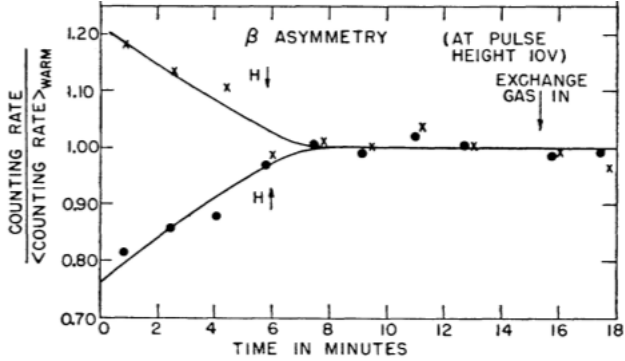


Figure 1.3: Data from C. S. Wu’s experiment measuring the correlation between the emitted direction of the electron from the decay of polarized  $^{60}\text{Co}$ . The two curves represent the counting rates when the nuclei were oriented in opposite directions with respect to the electron detector. The existence of a splitting indicates a violation of parity as the electrons are preferentially emitted in the direction opposite the spin.

The measurement showed that the electrons were preferentially emitted in the direction opposite the spin of the nuclei, which indicates parity violation due to the position inverted scenario not being observable. This is evident when considering that a correlation between the spin and the momentum takes the form  $\vec{\sigma} \cdot \vec{p}$ . The spin is a type of angular momentum and transforms as an axial vector under spatial inversion ( $P\vec{\sigma} = \vec{\sigma}$ ), while the momentum is a normal vector and simply changes sign under parity ( $P\vec{p} = -\vec{p}$ ). Thus the existence of such a term in the decay rate (as will be shown in Section 1.2.3) makes the decay rate noninvariant under a parity transformation, and the position inverted scenario is automatically impossible since the spin vector would not change but we would expect to see the electron direction flip. This would result in electrons emitted aligned with the direction of the spin, which is not the observed case. From the theory presented thus far, the interaction involved was either axial vector or tensor, because decay of  $^{60}\text{Co}(J^p = 5^+) \rightarrow ^{60}\text{Ni}(J^p = 4^+)$  proceeds strictly through the Gamow-Teller transition. Whether the tensor or axial vector current (or both) was responsible was yet to be determined.

It should be noted that, following the news of Wu’s result, Garwin, Lederman, and Weinrich [GLW57] from Columbia confirmed that parity is violated using the subsequent decays of  $\pi^+ \rightarrow \mu^+ + \nu_\mu$  followed by  $\mu^+ \rightarrow e^+ + \bar{\nu}_e + \nu_\mu$ . This was another process recommended by Lee and Yang. The premise is that the chiral odd neutrino in the first decay forces the muon to be polarized in the direction of its momentum to conserve angular momentum. The polarized muon then decays and can thus be analyzed much like one would analyze the  $\beta$ -decay of a polarized nucleus, looking

for correlations between the muon and electron polarizations. The results were again conclusive that parity is not conserved in the weak interaction.

### 1.2.3 Correlation Coefficients

Taking the interaction Hamiltonian from Lee and Yang with all generalized terms included, Jackson, Treiman, and Wyld [JTWJ57; JTW57] first derived an expression for the differential decay rate for polarized nuclei as a function of the emitted electron momentum and spin, the neutrino momentum, and the nuclear spin of the decaying nucleus. Ebel and Feldman [EF57] added terms to the expression of Jackson, Treiman, and Wyld, and, under the assumption that the spin of the mother nucleus and the spin of the outgoing electron are observable, this gives

$$\begin{aligned} \frac{d\Gamma}{dE_e dE_\nu d\Omega_e d\Omega_\nu} = & \frac{1}{2} \frac{F(\pm Z, E_e)}{(2\pi)^5} p_e E_e (E^0 - E_e)^2 \\ & \times \xi \left\{ 1 + a \frac{\vec{p}_e \cdot \vec{p}_\nu}{E_e E_\nu} + b \frac{m_e}{E_e} + \frac{\langle \vec{J} \rangle}{J} \cdot \left[ A \frac{\vec{p}_e}{E_e} + B \frac{\vec{p}_\nu}{E_\nu} + D \frac{\vec{p}_e \times \vec{p}_\nu}{E_e E_\nu} \right] \right. \\ & + \left[ \frac{J(J+1) - 3\langle (\vec{J} \cdot \hat{j})^2 \rangle}{J(2J-1)} \right] \left( c \left[ \frac{\vec{p}_e \times \vec{p}_\nu}{3E_e E_\nu} - \frac{(\vec{p}_e \cdot \hat{j})(\vec{p}_\nu \cdot \hat{j})}{E_e E_\nu} \right] + I \left[ \frac{1}{3} \frac{\vec{\sigma} \cdot \vec{p}_\nu}{E_\nu} - \frac{(\vec{\sigma} \cdot \hat{j})(\vec{p}_\nu \cdot \hat{j})}{E_\nu} \right] \right. \\ & + K' \frac{\vec{\sigma} \cdot \vec{p}_e}{E_e + m_e} \left[ \frac{1}{3} \frac{\vec{p}_e \cdot \vec{p}_\nu}{E_e E_\nu} - \frac{(\vec{p}_e \cdot \hat{j})(\vec{p}_\nu \cdot \hat{j})}{E_e E_\nu} \right] + M \left[ \frac{1}{3} \frac{\vec{\sigma} \cdot \vec{p}_e \times \vec{p}_\nu}{E_e E_\nu} - \frac{(\vec{\sigma} \cdot \hat{j})(\hat{j} \cdot \vec{p}_e \times \vec{p}_\nu)}{E_e E_\nu} \right] \Big) \\ & + \vec{\sigma} \cdot \left[ N \frac{\langle \vec{J} \rangle}{J} + Q \frac{\vec{p}_e}{E_e + m_e} \left( \frac{\langle \vec{J} \rangle}{J} \cdot \frac{\vec{p}_e}{E_e} \right) + R \frac{\langle \vec{J} \rangle}{J} \times \frac{\vec{p}_e}{E_e} + S \frac{\langle \vec{J} \rangle}{J} \frac{\vec{p}_e \cdot \vec{p}_\nu}{E_e E_\nu} \right. \\ & \left. + T \frac{\vec{p}_e}{E_e} \frac{\langle \vec{J} \rangle}{J} \cdot \frac{\vec{p}_\nu}{E_\nu} + U \frac{\vec{p}_\nu}{E_\nu} \frac{\langle \vec{J} \rangle}{J} \cdot \frac{\vec{p}_e}{E_e} + W \frac{\vec{p}_e}{E_e + m_e} \frac{\langle \vec{J} \rangle}{J} \cdot \frac{p_e \vec{x} p_\nu}{E_e E_\nu} \right] + V \frac{\langle \vec{J} \rangle}{J} \cdot \frac{\vec{\sigma} \times \vec{p}_\nu}{E_\nu} \Big) \end{aligned} \quad (1.4)$$

where  $F(\pm Z, E_e)$  is the Fermi function (a shape correction to the spectrum from coulomb interactions),  $E$  is the energy of a given particle,  $E^0$  is the endpoint energy of the electron,  $\vec{p}$  is the particle momentum,  $\vec{J}$  is the spin of the decaying nucleus (or nucleon), and  $\vec{\sigma}$  is the spin of the electron. All of the correlation coefficients are functions of the coupling constants in the weak Hamiltonian (see Equation 1.3), as is  $\xi$ . The correlation coefficients and  $\xi$  are also functions of Fermi and Gamow-Teller transition amplitudes <sup>1</sup>.

---

<sup>1</sup>For the complete definitions see [JTWJ57; JTW57; EF57]

Foreshadowing upcoming sections, we write down the definitions of  $\xi$  and  $A\xi$  (ignoring Coulomb corrections):

$$\xi = |M_F|^2(|C_S|^2 + |C_V|^2 + |C'_S|^2 + |C'_V|^2) + |M_{GT}|^2(|C_T|^2 + |C_A|^2 + |C'_T|^2 + |C'_A|^2) \quad (1.5)$$

and

$$A\xi = 2\text{Re} \left[ \pm |M_{GT}|^2 \lambda_{J'J} (C_T C'^*_T - C_A C'^*_A) + \delta_{J'J} M_F M_{GT} \left( \frac{J}{J+1} \right)^{\frac{1}{2}} (C_S C'^*_T + C'_S C^*_T - C_V C'^*_A - C'_V C^*_A) \right] \quad (1.6)$$

where

$$\lambda_{J'J} = \begin{cases} 1, & J \rightarrow J' = J-1 \\ \frac{1}{J+1}, & J \rightarrow J' = J \\ \frac{-J}{J+1}, & J \rightarrow J' = J+1 \end{cases} \quad (1.7)$$

and the  $\pm$  sign indicates  $\beta^-$ ( $\beta^+$ ) decay respectively (the plus sign goes with  $\beta^-$ , the  $-$  with  $\beta^+$  to be clear). The rest of the coefficients have varying combinations of the the complex coupling constants  $C$ ,  $C'$ , and the Fermi and Gamow-Teller amplitudes.

Jackson, Treiman, and Wyld concisely state the impact these terms have on tests of C, P, and T invariance:

Invariance with respect to space inversion implies that the coupling constants  $C'$  vanish (or alternatively the  $C$  vanish). Invariance with respect to charge conjugation implies that the constants  $C$  are real and the constants  $C'$  pure imaginary, up to an overall phase. Invariance under time reversal would imply that all coupling constants  $C$ ,  $C'$  are real, again up to an overall phase.

Measurements of the correlation parameters in nuclear systems shed light on the relationships between the different coupling constants, but it would take observations of the behavior of the observed neutrinos and electrons to determine the true structure of the interaction Hamiltonian.

#### 1.2.4 $V - A$ Structure

By 1956, the theory of the weak interaction had developed from a purely vector current-current process into a combination of all possible Lorentz invariant current-current interactions and finally to the potential mixture of current-current terms that

transform as scalars and pseudoscalars in order to accomodate parity violation. At this point, the theory needed to rely on experiment to determine which couplings were nonzero.

In early 1957, upon Wu reporting preliminary results regarding the large asymmetry seen in the  $\beta$ -decay of  $^{60}\text{Co}$  to Lee and Yang, the duo developed a two component theory of the neutrino where a massless neutrino exists in a predefined polarization, or that its spin is always oriented in the same direction with respect to its momentum [LY57]<sup>2</sup>. This was the first theory to indicate that the weak interaction coupled only to particles of a certain handedness, where right (left) handedness refers to eigenstates with eigenvalues of the chirality projection operator ( $P_{\pm} = (1 \pm \gamma^5)/2$ ) equal to  $+1(-1)$ . This operator should look familiar, as it is the term Lee and Yang inserted into Fermi's theory of  $\beta$ -decay when  $C_i = C'_i$ .

In 1958, Feynman and Gell-Mann [FGM58] (and separately Sudarshan and Marshak [SM58]) would report the currently accepted V-A (vector minus axial vector) theory of the weak interaction. The name derives from the form of the two currents in the current-current Hamiltonian. The new theory involved the coupling of the weak current to strictly left-handed particles and right-handed antiparticles. More simply, a massless neutrino will always have helicity  $\vec{\sigma} \cdot \vec{p}/p = -1$  while an anti-neutrino will have  $\vec{\sigma} \cdot \vec{p}/p = +1$ , where the fact that helicity and chirality are one in the same for massless particles is utilized. The form of the V-A interaction Hamiltonian

$$H = G_F \left( \bar{\psi}_n \gamma_\mu (1 - \gamma^5) \psi_p \right) \left( \bar{\psi}_{\bar{n}} \gamma^\mu (1 - \gamma^5) \psi_e \right), \quad (1.8)$$

where  $G_F$  is the Fermi coupling constant of the weak interaction, assumes that the V-A structure is universal within the weak interaction<sup>3</sup>.

The theories of Feynman and Gell-Mann (and Sudarshan and Marshak) explained the observations at that time regarding the weak interaction. Then, also in 1958, confirmation of the V-A theory arrived when Goldhaber, Gradzins, and Sunyar indirectly measured the helicity of the neutrino in electron capture on  $^{152}\text{Eu}$  and determined the emitted neutrino was indeed left-handed [GGS58; GMB96]. It should be noted that these two theories differed from that of Lee and Yang in the definition of the chirality of the particles (-) and anti-particles (+), where Lee and Yang had the opposite definition.

---

<sup>2</sup>Technically this only applies to neutrinos that interact via the weak interaction, but seeing as neutrinos are only observed to interact weakly, this can be generalized to all observable neutrinos. Also, Lee and Yang's theory had the wrong sign for the  $\vec{\sigma} \cdot \vec{p}$  of the neutrino.

<sup>3</sup>This is only strictly true for the charged weak interaction (so a change in charge occurs in each current), but at this time only the charged weak interaction was known.

Now one may be tempted to ask why only the vector and axial vector components of the original parity violating Hamiltonian remain, and this is easily answered by imagining that the left-handed coupling was discovered prior to modification of the Hamiltonian in equation 1.2 by Lee and Yang to account for parity violation. We can define the left-handed particle states as

$$\psi_L = \frac{1}{2}(1 - \gamma^5)\psi. \quad (1.9)$$

Then using this in the current yields

$$\bar{\psi}_{1,L} O_i \psi_{2,L} = \frac{1}{4} \overline{(1 - \gamma^5) \psi_1} O_i (1 - \gamma^5) \psi_2 \quad (1.10)$$

where  $O_i$  refers to all of the operators which produce S, V, T, A, and P bilinear covariants from Table 1.1 and subscript 1,2 refers to two different particle states. The  $O_i$  are those that are present in 1.2.

Table 1.2: The chirality projected operators.

Type	$O_i$	$O'_i$
S	1	0
P	$\gamma^5$	0
V	$\gamma^\mu$	$\frac{1}{2}\gamma^\mu(1 - \gamma^5)$
A	$\gamma^\mu\gamma^5$	$-\frac{1}{2}\gamma^\mu(1 - \gamma^5)$
T	$\sigma^{\mu\nu}$	0

Now it can be shown that

$$\begin{aligned}
\bar{\psi}_{1,L} O_i \psi_{2,L} &= \frac{1}{4} \overline{(1 - \gamma^5) \psi_1} O_i (1 - \gamma^5) \psi_2 \\
&= \frac{1}{4} \left( (1 - \gamma^5) \psi_1 \right)^\dagger \gamma^0 O_i (1 - \gamma^5) \psi_2 \\
&= \frac{1}{4} \psi_1^\dagger (1 - \gamma^5)^\dagger \gamma^0 O_i (1 - \gamma^5) \psi_2 \\
&= \frac{1}{4} \psi_1^\dagger (1 - \gamma^5) \gamma^0 O_i (1 - \gamma^5) \psi_2 \\
&= \frac{1}{4} \psi_1^\dagger \gamma^0 \frac{1 + \gamma^5}{2} O_i (1 - \gamma^5) \psi_2 \\
&= \frac{1}{4} \bar{\psi}_1 \frac{1 + \gamma^5}{2} O_i (1 - \gamma^5) \psi_2
\end{aligned}$$

where the relations  $\gamma^{5\dagger} = \gamma^5$  and  $\{\gamma^5, \gamma^i\} = 0$  were used.

Then, if we define

$$O'_i = \frac{1}{4}(1 + \gamma^5)O_i(1 - \gamma^5),$$

we can calculate how all of the S, V, T, A, and P operators transform. This is shown in table 1.2, where we see that only the vector and axial vector terms remain, and they appear with the same  $\gamma^\mu(1 - \gamma^5)$  factor up to a sign! Thus, these are the only currents that can contribute in the weak interaction Hamiltonian [GMB96].

### 1.2.5 Renormalizing the Hadronic Current

The forms of both the hadronic current ( $\bar{\psi}_p\gamma_\mu(1 - \gamma^5)\psi_n$ ) and leptonic current ( $\bar{\psi}_e\gamma_e(1 - \gamma^5)\psi_{\bar{\nu}}$ ) in 1.8 indicate that the vector and axial vector currents possess the same coupling constants, or that they contribute equally in the weak interaction. For the leptonic current this is the case as the particles participating are true point particles (and the equal relative strengths are what is meant by parity is violated maximally in the weak interaction), but what about the hadronic current? One must remember that the hadronic process that occurs is actually the decay of a single quark, and that the other two quarks (and the sea of quarks and gluons confined within the hadron) are spectators to the process. It is conceivable then that the spectator quarks could modify the couplings. To account for potential differences in the hadronic current, the Hamiltonian is modified slightly,

$$H = G_F \left( \bar{\psi}_p\gamma_\mu(g_V - g_A\gamma^5)\psi_n \right) \left( \bar{\psi}_e\gamma^\mu(1 - \gamma^5)\psi_{\bar{\nu}} \right), \quad (1.11)$$

which lends itself to the definition

$$\lambda \equiv \frac{g_A}{g_V}. \quad (1.12)$$

The presence of the spectator quarks in the hadron can effectively renormalize the interaction, creating nonzero values for  $g_V$  and  $g_A$ , and thus making them different from the couplings in the leptonic current.

#### 1.2.5.1 Conserved Vector Current Hypothesis

The observed measurements of the Fermi constant ( $G_F$ ) seemed universal when comparing measurements from purely leptonic interactions and purely Fermi transitions (vector transitions). Thus the vector portion, in analogy with electromagnetism, is taken to be conserved, as was postulated by Feynman and Gell-Mann in 1958 [FGM58].

The conservation of the vector current can be imagined by considering the dis-occision of the neutron into a proton and a  $\pi^-$  for a short period of time, until the proton absorbs the  $\pi^-$  and becomes a neutron again. If during this time when the proton and  $\pi^-$  exist separately the decay process is not allowed, then we would expect that the current would be renormalized. Instead, the  $\pi^-$  can weakly decay via  $\pi^- \rightarrow \pi^0 + e^- + \bar{\nu}$ , a Fermi transition as  $J^\pi = 0^- \rightarrow J^\pi = 0^-$ . This loop diagram and others like it contribute to the conservation of the vector current by projecting the potentiality of neutron decay onto the disassociated pion [GK90]. So, while one may naively think that the neutron could not decay while the pion exists, the probability of the pion also decaying via the same interaction and giving the same decay products conserves the vector current. This conservation of vector current is now called the Conserved Vector Current (CVC) hypothesis, and the value of  $g_V$  is taken to be unity ( $g_V = 1$ ).

The same conservation of coupling to the axial vector current can not be assumed, as was also considered by Feynman and Gell-Mann [FGM58]:

Now with present knowledge it is not so easy to say whether or not a pseudovector current like  $\bar{\psi} i\gamma^5 \gamma^\mu \tau^+ \psi$  can be arranged to be not renormalized. The present experiments in  $\beta$  decay indicate that the ratio of the coupling constant squared for Gamow-Teller (axial vector) and Fermi (vector) is about  $1.3 \pm 0.1$ . This departure from 1 might be a renormalization effect.

The value of  $g_A$  can then only be determined experimentally<sup>4</sup> and is directly related to measurements of the correlation coefficients in Section 1.2.3.

### 1.2.6 CKM Mixing Matrix

The weak interaction as introduced thus far describes, within the hadronic current, the transitions between quarks with charge  $-1/3$  and  $+2/3$ . This includes observed interactions between the heavier strange quark (charge  $-1/3$ ) and the up quark (charge  $+2/3$ ). A shortcoming of the interaction in Equation 1.11 was the inability to describe the decay rate of strangeness altering processes with respect to strangeness conserving decays, where the strangeness is measured by the number of strange quarks in the state of interest. This led Cabibbo [Cab63] to introduce the following correction to the hadronic current:

$$J_H^\mu = \cos \theta_C J_H^\mu (\Delta S = 0) + \sin \theta_C J_H^\mu (|\Delta S| = 1), \quad (1.13)$$

---

<sup>4</sup>Today it can also be calculated on a lattice as will be discussed in a few sections.

where  $J_H^\mu = \bar{\psi}_1 \gamma_\mu (g_V - g_A \gamma^5) \psi_2$  is the hadronic current between hadrons 1 and 2, and  $\theta_C$ , called the Cabibbo angle, quantifies the relative strength of the couplings to the strangeness conserving and strangeness altering processes. Cabibbo found that  $\theta_C \approx 13^\circ$  described the observed differences.

At the time Cabibbo introduced his modification, only the up, down and strange quarks were known to exist. Glashow, Iliopoulos, and Maiani proposed the existence of a fourth quark, the charm quark, with charge +2/3 as a complimentary particle in the weak doublet with the strange quark, to explain an observed discrepancy in the decay rate of  $K^0 \rightarrow \mu^+ + \mu^-$  [GIM70]. Validation of the GIM mechanism arrived with the discovery of the charm quark in 1974.

Even prior to the discovery of the charm quark, Kobayashi and Maskawa generalized the ideas of Cabibbo, Glashow, Iliopoulos, and Maiani to include three generations of quarks [KM73]. The single Cabibbo angle was replaced with three angles relating couplings between each generation of quarks and a complex phase. We now know that three generations of quarks exist, and they appear in the weak interaction as part of weak doublets rather than particle doublets, i.e.

$$\begin{pmatrix} u \\ d' \end{pmatrix}, \begin{pmatrix} c \\ s' \end{pmatrix}, \begin{pmatrix} t \\ b' \end{pmatrix}. \quad (1.14)$$

The weak states for the down ( $d$ ), strange ( $s$ ), and bottom ( $b$ ) quarks are related to the particle states by the CKM matrix:

$$\begin{pmatrix} d' \\ s' \\ b' \end{pmatrix} = \begin{pmatrix} V_{ud} & V_{us} & V_{ub} \\ V_{cd} & V_{cs} & V_{cb} \\ V_{td} & V_{ts} & V_{tb} \end{pmatrix} \begin{pmatrix} d \\ s \\ b \end{pmatrix}, \quad (1.15)$$

$$\begin{pmatrix} d' \\ s' \\ b' \end{pmatrix} = \begin{pmatrix} c_{12}c_{13} & s_{12}c_{13} & c_{13}e^{i\delta} \\ -s_{12}c_{23} - c_{12}s_{23}s_{13}e^{i\delta} & c_{12}c_{23} - s_{12}s_{23}s_{13}e^{i\delta} & s_{23}c_{13} \\ s_{12}s_{23} - c_{12}c_{23}s_{13}e^{i\delta} & -c_{12}s_{23} - s_{12}c_{23}s_{13}e^{i\delta} & c_{23}c_{13} \end{pmatrix} \begin{pmatrix} d \\ s \\ b \end{pmatrix}, \quad (1.16)$$

where  $c_{ij}$  ( $s_{ij}$ ) stand for  $\cos \theta_{ij}$  ( $\sin \theta_{ij}$ ),  $\theta_{ij}$  are the three angles  $\theta_{12}$ ,  $\theta_{13}$ , and  $\theta_{23}$  that relate the couplings between each quark generation, and  $\delta$  is a complex phase.

Each element of the CKM matrix,  $V_{ij}$ , quantifies the coupling of quark  $i$  to quark  $j$ , or in comparison to Cabibbo's modification to the hadronic current above, the CKM matrix elements take the place of the  $\cos \theta_C$  and  $\sin \theta_C$  when extended to three generations of quarks. As a matter of fact, if we assume no mixing with the third generation of quarks, the CKM matrix becomes the matrix developed by Glashow, Iliopoulos, and Maiani and the only quantity needed to fully determine the relationships between the weak states and the quark states is the Cabibbo angle  $\theta_{12} = \theta_C$ .

[Gri08]. Thus, direct comparison with Equation 1.13 indicates that the proper  $V_{ij}$  should accompany the hadronic current of the process being considered in the Hamiltonian, i.e.  $V_{ud}$  accompanies the hadronic current in neutron  $\beta$ -decay.

The existence of non-zero off diagonal terms means that there are non-zero probabilities for weak interactions between quarks of different generations, given that it is energetically allowed. The complex phase ( $\delta$ ) present in the CKM matrix also accounts for CP-violation in weak interactions. The elements of the CKM matrix must be measured experimentally, and the unitarity of the matrix is an important test of the Standard Model. If

$$|V_{ud}|^2 + |V_{us}|^2 + |V_{ub}|^2 = 1, \quad (1.17)$$

then the Standard Model contains only the three observed generations of quarks.

## 1.3 What does this mean for the neutron?

### 1.3.1 Matrix Element

The matrix element for  $\beta$ -decay is given by

$$\mathcal{M} = \frac{G_F V_{ud}}{\sqrt{2}} J^\mu L_\mu \quad (1.18)$$

where  $L_\mu = \bar{u}_e \gamma_\mu (1 - \gamma^5) u_\nu$  is the leptonic current and the hadronic current  $J^\mu$ , written in the style of [GZ01], is given by

$$J^\mu = \bar{u}_p \left[ f_1(q^2) - i \frac{f_2(q^2)}{M} \sigma^{\mu\nu} q_\nu + \frac{f_3(q^2)}{M} q^\mu + g_1(q^2) \gamma^5 - i \frac{g_2(q^2)}{M} \sigma^{\mu\nu} \gamma^5 q_\mu + \frac{g_3(q^2)}{M} \gamma^5 q^\mu \right] u_n \quad (1.19)$$

where the terms included are all those that satisfy translational and Lorentz invariance. Notice the usual  $f_1(0) = g_V$  and  $g_1(0) = -g_A$  terms from the earlier construction of the weak interaction (Equation 1.11). The rest of the couplings account for modifications to the hadronic current from other mechanisms (nuclear recoil and Coulomb for example) that may transform in ways not described by the typical axial vector and vector currents. Also note that all terms included in the current are either axial vector or vector, as is ensured by the proper inclusion of the momentum transfer  $q_\nu$ . This must be the case since all terms in the current-current multiplication  $J^\mu L_\mu$  must be scalar or pseudoscalar.

The  $f_2$  term is often called the weak magnetism contribution [GM58], as it, in the words of Gell-Mann, “bears the same relation to the allowed Fermi coupling that magnetism bears to electricity”. As  $q^2 \rightarrow 0$  and assuming the CVC hypothesis,  $f_2(0) = (\mu_p - \mu_n)/2$ , where  $\mu$  denotes the anomalous magnetic moment. The  $g_3$  term is the induced pseudoscalar term and is predicted to contribute to the energy spectrum at the order  $m_e^2/ME_e \approx 10^{-4}$  [Hol74; Pla+12].

The remaining  $f_3$  and  $g_2$  couplings are considered second-class currents [Wei58]. They arise from violations of  $G$  parity, defined as  $G = Ce^{i\pi I_2}$ . If  $G$  parity is conserved in weak interactions as it is in strong interactions, then  $f_3 = g_2 = 0$ . Even if nonzero, the effects from either are expected to be small, as they also contribute to the energy spectrum at order  $m_e^2/ME_e \approx 10^{-4}$  [Hol74; Pla+12].

### 1.3.2 Neutron $\beta$ -decay Asymmetry Parameter $A$

In the case of  $\beta$ -decay of polarized free neutrons and assuming the electron spin is undetectable, Equation 1.4 simplifies drastically,

$$\begin{aligned} \frac{d\Gamma}{dE_e dE_\nu d\Omega_e d\Omega_\nu} &= \frac{1}{2} \frac{F(\pm Z, E_e)}{(2\pi)^5} p_e E_e (E^0 - E_e)^2 \\ &\times \xi \left\{ 1 + a \frac{\vec{p}_e \cdot \vec{p}_\nu}{E_e E_\nu} + b \frac{m_e}{E_e} + \frac{\langle \vec{J} \rangle}{J} \cdot \left[ A \frac{\vec{p}_e}{E_e} + B \frac{\vec{p}_\nu}{E_\nu} + D \frac{\vec{p}_e \times \vec{p}_\nu}{E_e E_\nu} \right] \right\}. \end{aligned} \quad (1.20)$$

Now in the case of UCNA, only the polarization of the initial neutron population and the momentum of the decay electron are observable, which further simplifies Equation 1.20 to

$$\frac{d\Gamma}{dE_e dE_\nu d\Omega_e d\Omega_\nu} = \frac{1}{2} \frac{F(\pm Z, E_e)}{(2\pi)^5} p_e E_e (E^0 - E_e)^2 \times \xi \left\{ 1 + b \frac{m_e}{E_e} + A \frac{\langle \vec{J} \rangle}{J} \cdot \frac{\vec{p}_e}{E_e} \right\}. \quad (1.21)$$

The  $b$  term is known as the Fierz interference term, and, if nonzero, it presents itself within the electron energy spectrum as an energy shift. The other term is the asymmetry parameter  $A$  between the neutron spin and the electron momentum, the measurement of which is the topic of this thesis.

The Fierz interference term can be written as

$$b\xi = \pm 2\gamma \text{Re} \left[ |M_F|^2 \lambda_{J'J} (C_S C_V^* - C'_S C_V'^*) + |M_{GT}|^2 (C_T C_A^* - C'_T C_A'^*) \right] \quad (1.22)$$

where  $\gamma = (1 - \alpha^2 Z^2)^{1/2}$ ,  $\alpha$  is the fine structure constant, and  $\xi$  is given in Equation 1.5. From Equation 1.22, we see that  $b = 0$  under the V-A structure of the weak

interaction within the Standard Model, as  $C_S = C'_S = C_T = C'_T = 0$ . Measurements of  $b$  provide constraints on beyond Standard Model physics as they probe the existence of scalar and tensor currents, but these measurements are difficult because they require precise determination of the shape of the electron energy spectrum. A measurement of  $b$  using the 2010 UCNA energy spectrum exists, with a value of  $b_n = 0.067 \pm 0.005_{\text{stat}}^{+0.090}_{-0.091\text{syst}}$  [Hic+17], which is consistent with  $b = 0$ . A result using the energy spectra presented in this dissertation is currently under analysis by Xuan Sun of the California Institute of Technology, with intentions of reducing the systematic uncertainty from the previous result.

The asymmetry parameter  $A$  was given in Equation 1.6, but under the assumptions that the weak interaction is V-A and couples to left-handed fermions ( $C_A = C'_A$  and  $C_V = C'_V$ ), the couplings are pure real, and using the fact that  $\Delta J = \frac{1}{2}^+ - \frac{1}{2}^+ = 0$  we have

$$A\xi = 2 \left[ \frac{2}{3} |M_{GT}|^2 \left( -C_A^2 \right) + M_F M_{GT} \left( \frac{1}{3} \right)^{\frac{1}{2}} (-2C_V C_A) \right] \quad (1.23)$$

$$= -4 \left( \frac{1}{3} C_A^2 |M_{GT}|^2 + \frac{1}{\sqrt{3}} C_V C_A M_F M_{GT} \right) \quad (1.24)$$

and from 1.5 under the same assumptions,

$$\xi = 2|M_F|^2 C_V^2 + 2|M_{GT}|^2 C_A^2. \quad (1.25)$$

For the neutron, the Fermi and Gamow-Teller matrix elements are  $M_F = 1$  and  $M_{GT} = \sqrt{3}$ , with the simplicity resulting from there being no overlapping nucleon wavefunctions as there would be in nuclear  $\beta$ -decay [GK90]. Using this in the equations above we have

$$A = \frac{-4(C_A^2 + C_V C_A)}{2(C_V^2 + 3C_A^2)} \quad (1.26)$$

$$A = -2 \frac{\lambda(\lambda + 1)}{1 + 3\lambda^2} \quad (1.27)$$

where

$$\lambda = \frac{C_A}{C_V} = \frac{g_A}{g_V}. \quad (1.28)$$

This expression for  $A$  is free of recoil order and Coulomb corrections, and so it is often referred to as  $A_0$ . Thus we see that upon measuring the  $\beta$ -decay asymmetry parameter  $A$ , we must make modifications to the measured value to extract  $A_0$ . From  $A_0$ , a direct determination of  $\lambda = \frac{g_A}{g_V}$ , the ratio of the axial-vector to vector coupling constants in the hadronic weak interaction, follows. These corrections are below.

### 1.3.2.1 Recoil order corrections

Gardner and Zhang [GZ01] present the asymmetry parameter  $A$  upon considering recoil order effects from a finite mass nucleon. The treatment is completely general in that it includes all possible couplings (including induced couplings and second-class currents) from the hadronic current in Equation 1.19. Defining the parameters

$$\tilde{f}_i = f_i(0)/f_1(0), \quad \tilde{g}_i = g_i(0)/g_1(0), \quad R = \frac{E_e^{\max}}{M_n}, \quad x = \frac{E_e}{E_e^{\max}}, \quad \epsilon = \left(\frac{m_e}{M}\right)^2$$

where again  $f_1(0) = g_V$ ,  $g_1(0) = -g_A$ , and  $\lambda = g_A/g_V$ , Gardner and Zhang report:

$$\begin{aligned} A = A_0 + \frac{1}{(1+3\lambda^2)^2} & \left\{ \frac{\epsilon}{Rx} \left[ 4\lambda^2(1-|\lambda|)(1+|\lambda|+2\tilde{f}_2) + 4|\lambda|(1-|\lambda|)(|\lambda|\tilde{g}_2 - \tilde{f}_3) \right] \right. \\ & + R \left[ \frac{2}{3} [1+\lambda+2(\tilde{f}_2+\tilde{g}_2)] (3\lambda^2+2|\lambda|-1) \right] \\ & \left. + Rx \left[ \frac{2}{3} (1+|\lambda|+\tilde{f}_2) (1-5|\lambda|-9\lambda^2-3|\lambda|^3) + \frac{4}{3} \tilde{g}_2 (1+|\lambda|+3\lambda^2+3|\lambda|^3) \right] \right\} \\ & + O(R^2, \epsilon). \quad (1.29) \end{aligned}$$

The correction to  $A_0$  is energy dependent, as the  $x$  term is simply the electron energy divided by the endpoint energy. The above expression simplifies to the recoil order corrections presented elsewhere [Bil+60; Wil82] when the second-class currents are ignored. The correction as applied within this analysis, shown in Section 5.3.1, also ignores the second-class currents.

Gardner and Zhang provide a similar expression for  $a$  (the neutrino-electron correlation), which is also of the form  $d_0R + d_1Rx + d_{-1}\epsilon/(Rx)$  where the coefficients  $d_i$  are functions of the three unknowns  $\lambda$ ,  $\tilde{f}_2$ , and  $\tilde{g}_2$ . They point out that, via a determination of  $d_0$  and  $d_1$  (via the  $x^0$  and  $x^1$  energy dependence) from measurements of both  $A$  and  $a$ :

The system is over-constrained, so that we can infer the existence of physics beyond the SM (Standard Model), namely, presence of non- $(V-A)$  currents [JTWJ57], if the extracted coupling constants differ from SM bounds or if the values of the extracted couplings are not consistent with each other.

Current experimental limits are not yet at the precision needed to provide stringent limits on the beyond SM physics, but this is motivation to continue to measure neutron decay correlation parameters like  $A$ .

### 1.3.2.2 Electromagnetic Corrections

The decay electron is immersed in the Coulomb field of the proton, and thus the observed decay kinematics can be affected by both exchanging photons with the other constituents or Bremsstrahlung radiation as the electron moves through the field. Fermi initially accounted for modifications to the electron wavefunction from the presence of a point nucleus [Fer34b; Wil82], which appears as the Fermi correction to the phase space factor as seen the angular distribution in Equation 1.4.

The radiative correction of order  $\alpha$  (the fine structure constant) to the decay rate of unpolarized nuclei was established by Sirlin in 1967 [Sir67], and it takes the form:

$$G(E, E_0) = 1 + \frac{\alpha}{2\pi} g(E, E_0), \quad (1.30)$$

where the functional form of  $g(E, E_0)$  is given in [Sir67]. This appears as a multiplicative factor in the decay rate.

Shann then readdressed the radiative corrections of Sirlin, only he extended the correction to polarized nuclei in the context of the electron asymmetry, giving the correction factor [Sha71]:

$$A(E) = A_0 \left( 1 + \frac{\alpha}{2\pi} \left( h(E, E_0) - g(E, E_0) \right) \right), \quad (1.31)$$

where

$$\begin{aligned} h - g = 4 & \left( \frac{E_0 - E}{3E\beta^2} \right) \left( \frac{\tanh^{-1} \beta}{\beta} - 1 \right) \left( 1 - \beta^2 + \frac{E_0 - E}{8E} \right) \\ & + \frac{\tanh^{-1} \beta}{\beta} \left( 2 - 2\beta^2 - \frac{(E - E_0)^2}{6E^2} \right). \end{aligned} \quad (1.32)$$

The application of this correction within the context of this analysis is given in Section 5.3.2.

### 1.3.3 Neutron Lifetime

The neutron lifetime is another observable of the free neutron, and it is calculated using the matrix element in Equation 1.18 and then integrating over the allowable phase space for the decay. The neutron lifetime is given by

$$\frac{1}{\tau_n} = \frac{G_F^2 m_e^5}{2\pi^3} V_{ud}^2 (1 + 3\lambda^2) f (1 + \text{RC}) \quad (1.33)$$

where  $f$  is the phase space factor and  $(1 + \text{RC})$  accounts for recoil order corrections [CMS04]. If we take  $G_F$  to be known from muon decay and  $\lambda$  from measurements of

correlation parameters (like  $A$ ), then we see that upon measuring the neutron lifetime  $\tau_n$ , there is only one unknown: the CKM matrix element  $V_{ud}$ . We can rewrite the lifetime equation as

$$|V_{ud}|^2 = \frac{4908.7(1.9)\text{s}}{\tau_n} (1 + 3\lambda^2), \quad (1.34)$$

where the known values from  $G_F$ ,  $f$ , and  $(1 + \text{RC})$  have been combined. The uncertainty on the numerator comes from the combined uncertainties on the recoil corrections and the small uncertainty on  $G_F$ . Here we see that by measuring the neutron lifetime and  $\lambda$  from free neutron decay, one can determine  $V_{ud}$  solely from neutron decay. To date, the most precise determination of  $V_{ud}$  come from nuclear  $\beta$ -decay of  $0^+ \rightarrow 0^+$  which is purely a vector interaction and thus does not contain the axial-vector renormalization  $g_A$ .

## 1.4 Ultracold Neutrons

While neutrons have a magnetic moment and mass, the typical energy scale of a free neutron is much larger than any potential energy associated with the interaction of the neutron with materials, gravitational fields, or magnetic fields. But what happens if the neutron is cooled down to where its kinetic energy almost vanishes? The neutron begins to interact quite differently than typically expected!

In the UCNA experiment, neutrons with kinetic energies  $< 350$  neV and speeds  $< 8$  m/s are utilized to measure the neutron  $\beta$ -decay asymmetry parameter  $A$ . Neutron's of such energies are called ultracold neutrons, and will often be referred to simply as UCN. The low energy of these neutrons means they can be trapped in material bottles, manipulated with magnetic fields, and even affected by gravity.

### 1.4.0.1 Fermi Potential

As mentioned, UCN can be confined within material bottles, meaning that they are totally internally reflected from certain surfaces no matter the angle of incidence. Thus the slow moving neutrons behave more like a diffuse gas than a typical neutron beam.

UCN see an effective Fermi potential when encountering a surface, given by

$$V_{\text{eff}} = \frac{2\pi\hbar^2}{m} Na, \quad (1.35)$$

where  $a$  is the bound atom coherent scattering length of the material and  $N$  is the number density of the material. This potential can be treated as a one-dimensional

non-relativistic quantum mechanics problem, and what one finds is that when the energy of the incoming wave is less than  $V_{\text{eff}}$ , the neutron will be totally reflected, although there is a transmitted component of the wave function which penetrates the material. This transmitted component can lead to losses of UCN via interactions with the nuclei through neutron capture or upscattering [GRL91]. A table of typical effective potentials is seen in Table 1.3. By constructing the critical guides and other components of the UCNA experiment using materials with high Fermi potentials, UCN can be guided to the experimental volume and then held until they decay.

Table 1.3: Effective potentials for some UCN reflecting materials.

Material	$V_{\text{eff}}$ (neV)
$^{58}\text{Ni}$	342
Stainless Steel	189
Cu	168
Fe	210
Be	252

#### 1.4.0.2 Gravity

As in classical physics, the neutron possesses gravitational potential energy of the form

$$V_g = m_n g h \approx (102 \text{ neV/m}) \cdot h. \quad (1.36)$$

Normally this is inconsequential for a neutron with typical energies on the MeV scale, but for UCN with energies comparable to the potential energy associated with only a few meters change in height, gravity can have a great influence. One might consider using a change in height to lower the UCN energy to a regime which can be guided by certain materials as seen in Section 1.4.0.1, or they can be accelerated using a decrease in height to assist in detection of the UCN [GRL91].

#### 1.4.0.3 Magnetic Fields

The neutron has an intrinsic magnetic moment given by  $\mu_n = -1.91304272(45)\mu_N$  [PG+16] which arises from the quark makeup of the neutron. The negative sign indicates that the neutron magnetic moment is anti-aligned with its spin.

A magnetic moment interacts with a magnetic field through the  $-\vec{\mu} \cdot \vec{B}$  potential, so for a neutron we have

$$V_m = -\vec{\mu}_n \cdot \vec{B} = \mu_n \hat{\sigma} \cdot \vec{B} \approx \pm (60 \text{ neV/T}) \hat{\sigma} \cdot \vec{B}, \quad (1.37)$$

where  $\hat{\sigma}$  is a unit vector in the direction of the spin. From this it is apparent that a spin which is aligned to the field will feel a repulsive force from the potential, while a spin of the opposite orientation will see an attractive potential. The strength of the potential also indicates that a modest magnet of several Tesla will completely reflect a spin aligned with the field. We'll return to this in the next chapter.

## 1.5 Motivation in a nutshell

The focus of this thesis is describing in detail a new precision measurement of the neutron  $\beta$ -decay asymmetry parameter  $A_0$ . While a measurement of  $A_0$  is alone interesting as it presents a measure of parity violation within the weak interaction, the necessity for continued measurements of  $A_0$  may not be so obvious, given that we already know parity is violated maximally in the weak interaction. The motivation becomes apparent though when considering the relationships between all of the  $\beta$ -decay correlations and the coupling constants of Lee and Yang's version of Fermi's theory of  $\beta$ -decay (first derived by Jackson, Treiman, and Wyld [JTWJ57] and described in Section 1.2.3). From this relationship we see that precision measurements of any  $\beta$ -decay observable (i.e.  $A_0$ ) either produces a measurement of the couplings known to exist ( $g_A$  and  $g_V$  or the ratio  $\lambda = g_A/g_V$ ), or tests the couplings believed to not exist within the Standard Model (scalar, pseudoscalar, tensor).

### 1.5.1 Why determine $\lambda$ ?

Determining  $\lambda$  from measurements of the correlation coefficients is more fundamental to weak interaction physics, as the value is not determined within the theory. Therefore, theoretical calculations involving the weak interaction use as input the experimentally determined value for  $\lambda$ , and the precision of the calculation is limited by the precision of the experimental value. One may have even noticed that the recoil order corrections to the asymmetry parameter in Section 1.3.2.1 are themselves dependent on  $\lambda$ .

Precision measurements of  $\lambda$  not only allow for more reliable theoretical calculations, but they also serve as complimentary benchmarks for lattice QCD (LQCD) calculations, where the continuous field theory of the strong interaction (Quantum Chromodynamics, hence QCD) is discretized on a finite four-dimensional lattice (space and time). By solving the theory on the lattice and extrapolating to an infinitely large lattice with lattice spacing of zero and physical masses for the particles, one can,

for example, extract the coupling constants in the hadronic current (Equation 1.19). The limiting factor for lattice QCD determinations of any parameter is the statistical precision from finite Monte Carlo sampling and systematic uncertainties associated with the extrapolations, but recent improvements in LQCD calculations [Col+16; Cap+17; Ber+17] show promise in soon reaching comparable precision for  $g_A$  in relation to experiment. As such, comparison between the measured and LQCD results will allow for limits on beyond Standard Model right-handed currents in the weak interaction, as what is actually measured experimentally is  $g'_A = g_A(1 - 2\epsilon_R)$ , where  $\epsilon_R$  denotes the effective right-handed coupling if present [CGH13; GAC16; Ali+17].

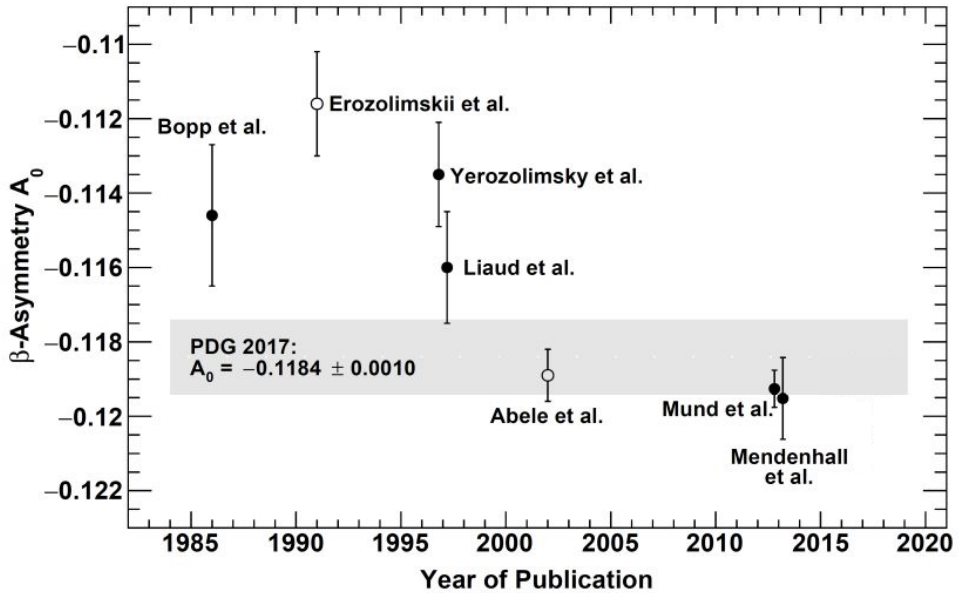


Figure 1.4: Historical plot of  $A_0$  measurements prior to the analysis presented within this thesis [Bop+86; Ero+91; Yer+97; Lia+97; Abe+02; Mun+13; Men+13]. The shaded band indicates the Particle Data Group average value [PG+16] for the asymmetry parameter, where the solid data points are included in the average. Thank you to Dr. Plaster for inclusion of this plot.

### 1.5.2 Current status of $A_0$ measurements

Measurements of  $A_0$  provide the most sensitive value of  $\lambda = g_A/g_V$ , which we now see has profound impact within the physics community. Measurements of  $a_0$ , the correlation between the electron momentum and neutrino momentum, are of comparable sensitivity, but such measurements are inherently more difficult. They require either the reconstruction of the neutrino momentum through measurement of the

recoil proton kinetic energy [Dar+17], which is less than 760 eV compared to the  $\sim 782$  keV endpoint of the electron, or through direct measurement of the proton energy spectrum [Byr+02]. The most precise measurement of  $a_0$  to date is at the sub-4% precision level, while current  $A_0$  measurements are sub-1% precision, thus providing better determination of  $\lambda$  for the time being.

Figure 1.4 shows the evolution of  $A_0$  measurements for the neutron dating back to 1986 and not including the most recent result which is the topic of this thesis. We see that with time not only has the precision increased, but a dichotomy has arisen between older measurements (pre-2002) and more recent measurements. The difference between the two groups may be attributed to the relatively large systematic corrections applied for the older pre-2002 results ( $> 10\%$ ) compared to all corrections being  $< 2\%$  for the newer post-2002 results [Bro+17].

The Mendenhall *et al.* result [Men+13] is the UCNA predecessor to the current analysis presented within this thesis. It should be noted that all measurements prior to Mendenhall *et al.* used cold neutron beams, whereas UCNA utilizes ultracold neutrons, and thus necessitates far different systematic corrections to the measured asymmetry compared to the other experiments. This makes the UCNA experiment a great compliment to the other measurements to ensure no unforeseen systematic bias to the experimentally determined value of  $A_0$  and  $\lambda$  from cold neutron techniques. Present results from UCNA already confirm that the shift in  $A_0$  values seems to be motivated by better experimental techniques as a whole and that post-2002 results are perhaps more aligned with the underlying value. From this point on, we focus on a new analysis of UCNA data in an attempt at further reducing the uncertainty on the  $\beta$ -decay asymmetry parameter  $A_0$  using UCN, thereby improving the precision on  $\lambda = g_A/g_V$ .

Copyright<sup>©</sup> Michael A-P Brown, 2018.

# Chapter 2

## UCNA Experiment

The UCNA Experiment is a mature experiment, having taken data from 2007-2013, that aims to precisely determine  $A_0$ , the neutron  $\beta$ -decay asymmetry parameter. Here a description of the experimental apparatus is given.

The description which follows applies to data taken from Fall 2011 through Spring 2013. The analysis is split into two separate data sets, denoted 2011-2012 (data taken from Fall 2011 through Spring 2012) and 2012-2013 (data taken from Fall 2012 through Spring 2013), due to minor changes in the decay trap geometries. Although small, any changes in the geometry require new simulations, and so a separate analysis is carried out. From now on, any part of the experiment or analysis which is different for the two data sets will be indicated.

### 2.1 Overview

Ultracold neutrons are produced in a solid deuterium source which is fed neutrons via a spallation source at the end of an 800 MeV proton beam. These UCN are then guided towards a material trap where they decay. During travel, the UCN pass through a series of polarizing magnets which allows the experimenter to control the spin state of the neutrons being loaded into the decay trap during any run. Utilizing a 1 T magnetic field along the central axis of the decay trap, decay electrons spiral towards detectors at either end of the spectrometer where their energy can be reconstructed. From knowledge about the initial direction and the energy of the electron, one can construct an energy dependent asymmetry and determine a value for  $A_0$ .

## 2.2 Ultracold Neutron Source and Guide System

Detailed descriptions of the UCN source can be found in [Sau+04; Mor+02; Sau+13], with more recent improvements given in [Ito+17]. The state of the UCN source today is different than what is described hereafter, with a substantial increase in UCN production.

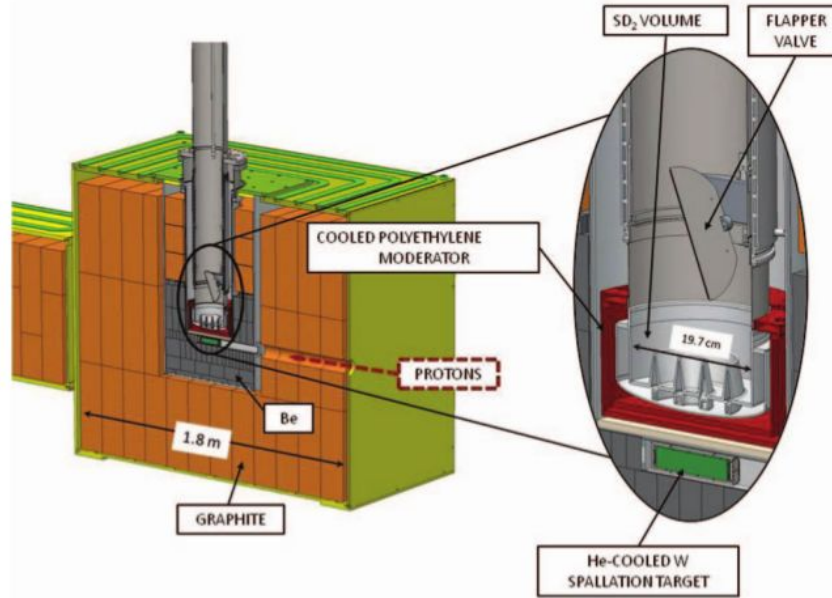


Figure 2.1: UCN source schematic. Inlay is a zoom in on the SD<sub>2</sub> cell [Sau+13].

A schematic to assist in the understanding of the source at the time of data-taking for this analysis is found in Figure 2.1. The process begins with delivery of protons from the 800 MeV proton accelerator operated in pulsed mode, with pulses repeated at a rate of 0.2 Hz. The protons strike a helium-cooled tungsten target (12 cm long) and produce spallation neutrons at roughly 20 MeV. The spallation target is surrounded by a room temperature beryllium reflector to help direct as many neutrons as possible towards the UCN source. The solid deuterium (SD<sub>2</sub>) UCN source is located directly above the tungsten target, housed in a liquid helium cooled cryostat. Prior to entering the SD<sub>2</sub> source, neutrons pass through a 1 cm thick moderator made of polyethylene beads cooled with the boil off gas from the cooling of the SD<sub>2</sub> source in the cryostat. UCN are produced using the superthermal interaction of a cold neutron with the SD<sub>2</sub>, which transfers most of the neutron's energy to a phonon in the crystal [GRL91].

The SD<sub>2</sub> source is a cylinder 19.7 cm in diameter and 5.7 cm tall. There is a

collection of “fins”, or vertical teeth-like structures, located in the bottom of the aluminum cryostat to increase the surface area of contact between the  $\text{SD}_2$  and the liquid helium cooled surface. The surface of the cryostat is coated with beryllium to reflect as many UCN as possible within the UCN source. Above the  $\text{SD}_2$  is a flapper valve which opens to let UCN out of the source and prevent UCN from re-entering the  $\text{SD}_2$  to reduce upscattering and loss of UCN.

Once a UCN passes the flapper, it is guided along a 1 m vertical guide coated with  $^{58}\text{Ni}$ . At this point, the UCN enter stainless steel horizontal guides for transportation from the biological shielding that surrounds the source. The higher 342 neV potential of the  $^{58}\text{Ni}$  ensures that all neutrons which are capable of being guided by the stainless steel (189 neV potential) are confined within the entirety of the vertical guide [Sau+13]. Upon looking at Figure 2.2, one sees that there are two 45° bends in the stainless steel guides to remove neutrons still exceeding the UCN regime [Pla+12].

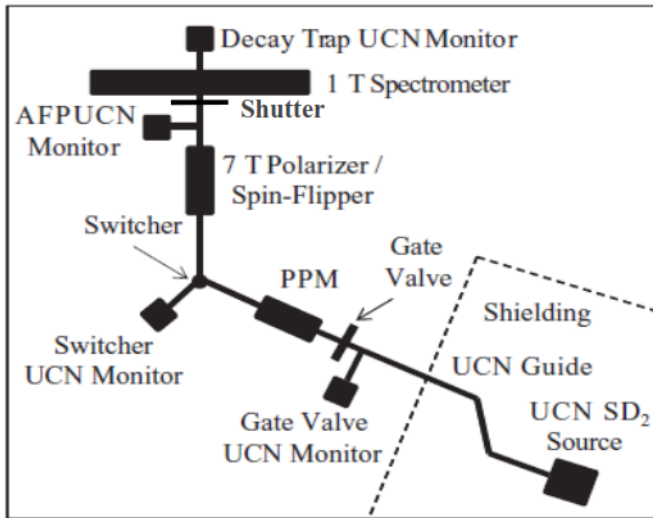


Figure 2.2: Schematic of guides and layout of the UCNA experiment [Pla+12].

Once the UCN exit the shielding, they are guided along stainless steel guides through a gate valve which allows for separation of the UCNA apparatus from the UCN source while the proton beam is on, thus allowing for background measurements in the spectrometer during  $\beta$ -decay running conditions (proton beam operating, but void of UCN). Beyond the gate valve is a 6 T pre-polarizing magnet (PPM). The purpose of the PPM is to minimize the loss of UCN during transport through the Zr foil used to separate the vacuum in the UCN source from the vacuum in the rest of the apparatus. The neutrons are nominally polarized longitudinally after passing through the PPM’s longitudinal field.

Beyond the PPM, the guides switch to electropolished copper (168 neV potential) to maintain the initial polarization of the neutrons. Just downstream of the PPM is the “switcher” valve. When the valve is open, the downstream guides are connected to the guides coming from the PPM carrying UCN. Upon closing the switcher valve, the downstream guides are redirected to a  ${}^3\text{He}$  UCN detector [Mor+09] used in polarimetry measurements.

Upon bypassing the switcher, the UCN are guided through the 7 T primary polarizing magnet (or AFP magnet). At this point the guides switch to 100 cm of diamondlike carbon coated quartz guides [Mam10] for passage through the Adiabatic Fast Passage (AFP) spin flipper [Hol+12a]. The guides then switch back to circular copper guides before coupling to a rectangular (4 cm width  $\times$  7 cm height) copper guide which transports the neutrons into the 1 T field inside the Superconducting Spectrometer (SCS).

Prior to the beginning of running in 2011, a shutter was installed between the decay trap and the guides used to close the decay trap off from the guides. During normal  $\beta$ -decay runs, the shutter is open allowing neutrons to flow into (and out of) the decay trap as they are created in the source. The shutter then closes at the beginning of a depolarization run, which immediately follows every  $\beta$ -decay run, to allow for draining of the guides prior to a depolarization measurement. This will be discussed in more detail later.

## 2.3 Neutron Polarization

The neutrons are initially polarized utilizing the  $-\vec{\mu} \cdot \vec{B} \approx \pm 60$  neV/T potential. The UCN pass through the 6 T pre-polarizing magnet and then through the 7 T primary AFP polarizing magnet. Neutrons with spin aligned to the field (remember that the magnetic moment of the neutron is negative and so is antialigned to the spin) see a positive (repulsive) potential of 420 neV from the 7 T magnet, and thus all UCN in this spin state are reflected. The opposite spin state sees an attractive potential and is transmitted, thus producing a completely polarized population of UCN beyond the AFP magnet. At this point, the neutrons pass through the AFP spin flipper. If the spin flipper is on, the spins undergo a  $\pi$  spin-flip before being loaded into the decay trap, and when off, the spins are loaded in the same state that was selected by the AFP magnet.

A detailed description of the spin flipper can be found in [Hol+12a]. In short, the flipper works under the premise of nuclear magnetic resonance (NMR) and utilizes

a sinusoidally varying magnetic field ( $B_1$ ) that is transverse to the primary holding field ( $B_0 \approx 1$  T). If there is a finite region where the  $B_1$  field exists, i.e. it is zero outside this region and only the  $B_0$  holding field exists, it can be shown that as a spin passes through this region it will undergo a  $\pi$  spin-flip if at some point on the interval the frequency  $\omega$  of the rotating field  $B_1$  is equal to the Larmor precession frequency  $\omega_L$  of the spin about the holding field  $B_0$ . To ensure that  $\omega = \omega_L$  at some point on the neutron's trajectory through this interval, a gradient is introduced in the holding field  $B_0$  while the frequency of the rotating field is held constant. With proper tuning, the resonance condition is met, and as long as adiabaticity is maintained, the spin flips direction. The conditions for adiabaticity defined in terms of pertinent field parameters for this setup can be found in [Hol+12a]. Testing of the apparatus indicates an efficiency of  $0.9985 \pm 0.0004$  [Hol+12a].

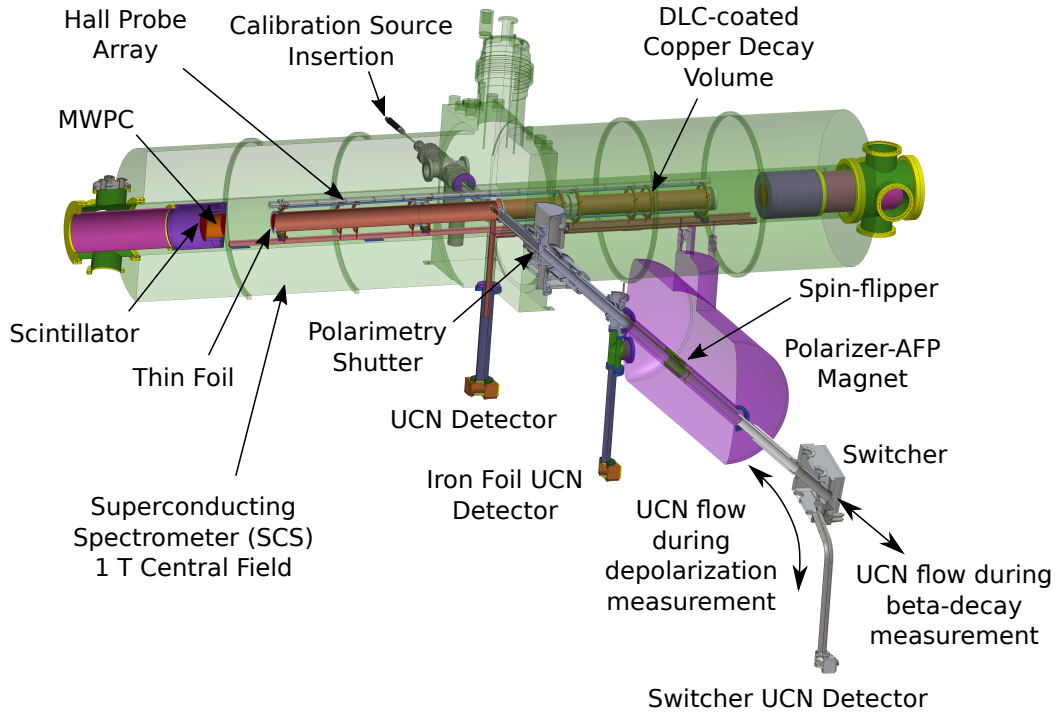


Figure 2.3: Detailed rendering of the experimental area.

## 2.4 Super-conducting Solenoidal Spectrometer

The spectrometer consists mainly of the superconducting solenoidal magnet designed to produce the 1 T central field, a decay trap to contain the UCN until they decay, and

detector packages located at each end of the spectrometer to detect decay electrons after they spiral about the field lines towards either detector. The detectors are referred to as East and West based on their orientation in the experimental area. Brief descriptions of the main components follow.

### 2.4.1 Decay Trap

The decay trap is situated at the center of the spectrometer within the 1 T magnetic field. The cylindrical 300 cm in length, 12.4 cm in width decay trap is made of electropolished Cu to confine as many UCN as possible. Typically the vacuum within the decay trap and the guides upstream to the Zr foil which separated the source vacuum from the experimental apparatus was about  $10^{-5}$  Torr. The density of UCN in the decay trap was monitored using a  $^3\text{He}$  UCN detector directly below a 0.64 cm hole in the decay trap.

One of the main differences between the 2011-2012 and 2012-2013 run periods was the thickness and material of the decay trap endcaps. In both geometries the endcaps were coated with 150 nm of Be (potential 252 neV) to aid in reflecting neutrons to confine them. The 2011-2012 endcaps were 500 nm Mylar on both the East and West detectors, while the 2012-2013 endcaps were made of 6F6F [Hoe03] and were 130 nm (East) and 180 nm (West) thick. The change in endcap thickness is the primary reason for analyzing the two sets of data separately, as this changes the systematics involving electron backscattering.

### 2.4.2 Magnetic Field

The general requirements for the magnetic field within the decay trap was that it must be aligned with the axis of the decay trap to define the axis of polarization, strong enough to confine the larmor radius of the decay electrons as they spiral toward the detectors, and uniform enough that electrons will not be reflected.

The necessity for a uniform magnetic field follows from consideration of the flux contained within the spiral of the electron around the magnetic field lines. From [Jac99] we know the flux,  $B r_e^2$ , is an adiabatic invariant, which means so is  $p_\perp^2/B$  where  $p_\perp$  is the transverse momentum of the spiraling electron and  $p = \sqrt{p_\perp^2 + p_\parallel^2}$ . Given this, there exists a condition for reflection when an electron originates in a field  $B_0$  with initial momentum  $p_0 = \sqrt{p_{0,\perp}^2 + p_{0,\parallel}^2}$  and encounters a field  $B_{\max}$ ,

$$\frac{B_{\max} - B_0}{B_0} > \frac{p_{0,\parallel}^2}{p_{0,\perp}^2}. \quad (2.1)$$

A field uniformity of  $10^{-4}$  was determined sufficient to remove appreciable effect on the asymmetry [Pla+08].

The magnet, constructed by American Magnetics, Inc., is a warm-bore 35 cm diameter, 4.5 m long superconducting solenoid (SCS magnet). Technical details of the magnet can be found in [Pla+08; Pla+12]. An important aspect of the magnetic field not mentioned previously is the field expansion from 1 T to 0.6 T beyond the decay trap windows but prior to the wirechambers. This field expansion decreases the pitch angle of the electron, defined as  $\theta = \cos^{-1}(p_{\parallel}/p)$ , as it enters the detector package as seen from the earlier stated adiabatic invariant  $p_{\perp}^2/B$  coupled with conservation of momentum. Decreasing the pitch angle decreases the probability of backscattering substantially. One should note here that transverse positions measured using the MWPC within the field expansion region need to be converted to decay trap coordinates, which is within the 1 T field region, using  $x_{\text{trap}} = \sqrt{0.6} \times x_{\text{MWPC}}$ .

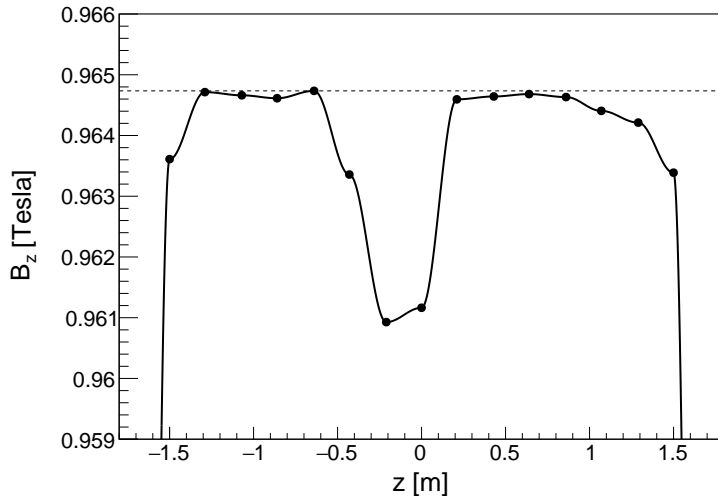


Figure 2.4: Typical field profile from 2011-2012 run period. The smooth interpolation between discrete values utilizes a half-wave of a cosine as defined in 3.4.2.3.

In 2011-2012 and 2012-2013, the magnetic field was not as uniform as reported in [Pla+08] due to damage to the shim coil persistence heater switches caused by multiple magnet quenches [Pla+12]. A typical field profile can be seen in Figure 2.4, where the uniformity is at the  $10^{-3}$  level, but there is pronounced dip in the center. Electrons that originate in the dip region can become trapped if the condition in equation 2.1 is satisfied. The electron then only exits the field dip upon scattering from the residual gas in the decay trap which randomizes the direction of the electron. The effect on the asymmetry from the field dip is addressed as a systematic uncertainty in Section 5.2.6.3.

## 2.4.3 Detector Packages

### 2.4.3.1 Multiwire Proportional Chamber

The multiwire proportional chamber (MWPC, or sometimes simply called the wirechamber) [Ito+07; Pla+12] is utilized to reconstruct the position of the electron events and to reduce the ambient backgrounds. The MWPC consists of an anode plane in between two cathode planes, with the cathode planes oriented perpendicular to one another to allow for position reconstruction in both directions transverse to the axis of the SCS. There are 64 wires in each plane with 2.54 mm spacing between each wire. The spatial extent of the MWPC is  $16.3 \times 16.3 \text{ cm}^2$  which maps to  $(\sqrt{0.6} \times 16.3) \times (\sqrt{0.6} \times 16.3) \text{ cm}^2 = 12.6 \times 12.6 \text{ cm}^2$  coverage within the decay trap (remember the decay trap is within the 1 T field while the detectors are in the field expansion region with field of 0.6 T), thus the wirechamber covers the full decay trap exit. The anode wires are 10  $\mu\text{m}$  in diameter while the cathode wires are 78.2  $\mu\text{m}$  in diameter, with the diameter of the cathode wires slightly larger than in previous run periods (50  $\mu\text{m}$ ).

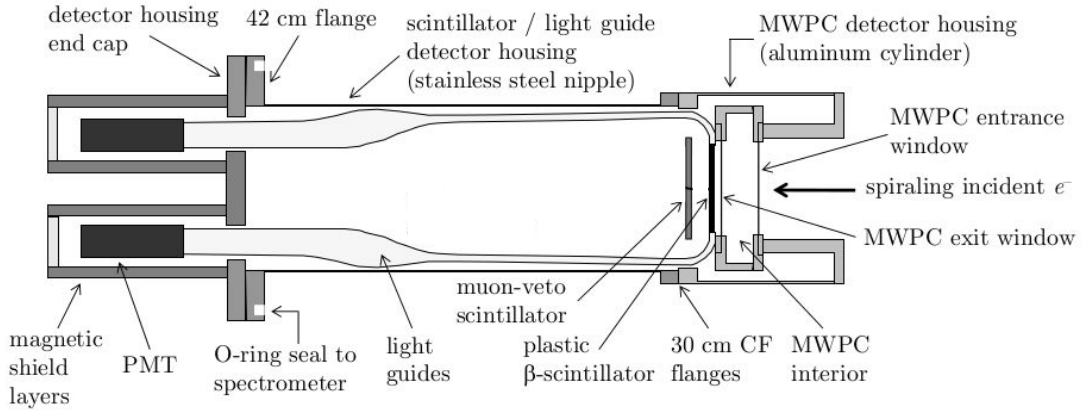


Figure 2.5: Schematic of the detector packages [Pla+12].

Charged particles passing the MWPC ionize the gas, and the  $\sim 2700$  V bias between the anode and cathode plains causes the ions and electrons to drift towards the cathode and anode respectively, inducing a signal in the wires proportional to the ionization created by the traversing charged particle. The anode wires are read out as a summed signal, with all 64 wire signals summed corresponding to a single ADC channel. This signal is typically used in relating the total signal in the MWPC to an energy deposited within the wirechamber. The cathode wires are read out in groups of four consecutive wires, so there are 16 ADC channels for each wirechamber

cathode plane. These 16 “wires” (as we will call them from now on) are used for position reconstruction. Either signal can be effectively used for the MWPC software trigger.

The fill gas chosen for the MWPC should be low Z (low atomic number) to minimize the backscattering from heavy nuclei, but also electron dense to increase the ionization efficiency. Thus complex large molecules made up of low Z nuclei are good candidates. The MWPC during running was primarily filled with neopentane ( $C_5H_{12}$ ) gas at a pressure of 100 Torr, chosen to ensure enough gain for electrons within the  $\beta$ -decay spectrum. For a short time period in 2012-2013, the neopentane ran out and isobutane ( $C_5H_{10}$ ) was used instead. Separate simulations were used for the isobutane runs, but no appreciable difference was noticed.

The windows on the wirechamber are made as thin as possible so as to reduce backscattering, but still retain their integrity under the 100 T pressure difference between the SCS and the wirechamber. Events that scatter off of the entrance window are particularly troublesome as they become missed backscattering events. The chosen front window material is 6  $\mu m$  of aluminized Mylar reinforced with Kevlar strings placed at 5 mm increments, and the exit window is also 6  $\mu m$  of aluminized Mylar [Men14].

The importance of the MWPC should not be understated. First of all, the position reconstruction allows for the definition of a fiducial volume within the decay trap so that we can cut out events which may have interacted with the decay trap walls. Such interactions change the energy/direction of the electron, so simply removing them reduces the systematic correction necessary. Secondly, the scintillator’s energy response is position dependent, so the position of each event is needed to properly assign a reconstructed initial energy to each electron event. The MWPC is also vital in identifying backscattering events by looking at the energy deposited within the wirechamber, i.e. an event that backscatters off of the dead layer of the scintillator will deposit energy in the MWPC above some software cut and can be identified. And last of all, the wirechamber is highly insensitive to gamma rays, so by including a coincidence trigger between the wirechamber and the scintillator the majority of the gamma background is removed.

#### 2.4.3.2 Scintillator

A 15 cm diameter, 3.5 mm thick plastic scintillator [Pla+12] from Eljen Technology (EJ-204) is located beyond the MWPC. The maximum stopping distance for an endpoint (782 keV) electron is 3.1 mm, so the scintillator is capable of reconstructing

the entire energy spectrum. To transport the scintillation light out of the 0.6 T field to the photomultiplier tubes (PMT), located about 1 m from the scintillator where the field is  $\sim 0.03$  T, twelve light guides are coupled to the edge of the scintillator using optical grease. From there, the twelve guides are adiabatically merged into four larger guides which are attached to four Hamamatsu R7725 PMTs with custom bases [Hic13]. The light guides are merged and coupled to the PMTs in such a way that each PMT effectively covers one quadrant of the scintillator. A hardware two-fold trigger, or two PMTs above discriminator threshold, is required for a global trigger to be issued from the PMTs.

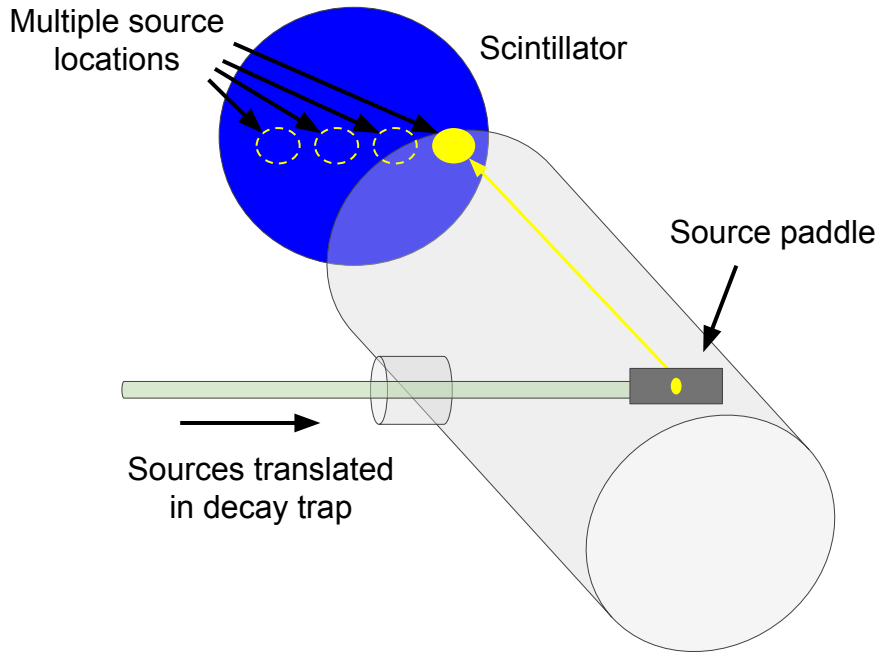


Figure 2.6: Schematic showing the mechanics of the scintillator calibration. The sources are located on a source paddle, which is inserted into the decay trap while under vacuum. The sources are then translated across the face of the detector, and a calibration run is completed at each stationary point. There are generally far more than four positions sampled, but for demonstrations sake only four points are included in the figure.

#### 2.4.3.3 Scintillator Energy Calibration

The scintillator energy calibration utilized the conversion electron lines from (with dominant K-shell energies listed)  $^{137}\text{Ce}$  (130.3 keV),  $^{113}\text{Sn}$  (363.8 keV), and  $^{207}\text{Bi}$  (481.7 keV and 975.7 keV) sources. As depicted in Figure 2.6, these sources are

placed on a source paddle and inserted into the side of the decay trap while under vacuum, and then they are translated across the horizontal axis of the decay trap. This method probes the position dependence of the scintillator, but only along one axis and at discrete points. The full position response is captured using another method as will be described later. Also detailed later in Section 3.2.2, the gain of the PMTs is monitored and drifts corrected on a run-by-run basis using a  $^{207}\text{Bi}$  “pulser” system [MBM76].

#### 2.4.3.4 Muon Veto System

Cosmic ray muons can create a scintillator two-fold trigger and pass the software trigger in the MWPC, so they trigger the same components of the detector as a  $\beta$ -decay electron. By identifying the muons through means other than the scintillator or wirechamber, the muon events can be vetoed during analysis. The first veto mechanism used is an argon/ethane sealed drift tube system [Rio+11]. The drift tube veto sits above the spectrometer, partially wrapped around the sides. Muons ionize the gas inside the tube, and thus by checking for a coincidence in the drift tube, one can remove muons and events from secondary electrons created by the muons. The second method of monitoring muon events is the use of scintillators placed directly behind the primary electron scintillator as seen in Figure 2.5. The primary detector stops all  $\beta$ -decay electrons, so a coincident signal in the “backing veto” indicates that a muon or some other event passed through the detector package.

## 2.5 Data Signals and Trigger Logic

Details regarding the data acquisition system can be found in [Pla+12; Men14], so the electronics will be left out of this discussion. Instead, what is more important for understanding the work contained within this thesis is the primary logic used to determine an electron event, and the terminology used when discussing different signals.

The two primary types of signals mentioned are ADC and TDC signals. An ADC signal is a number related to a voltage output by a detector component, and this signal may either be an integrated signal or a peak sensing signal. Either way, it is related to the “strength” of the signal as seen by the detector component, which is the energy deposited in most cases. An example of an ADC signal can be seen in Figure 2.7, where we show the detector output over one run for a single PMT during a  $\beta$ -decay run. The second signal used is a TDC signal, which for our purposes is just

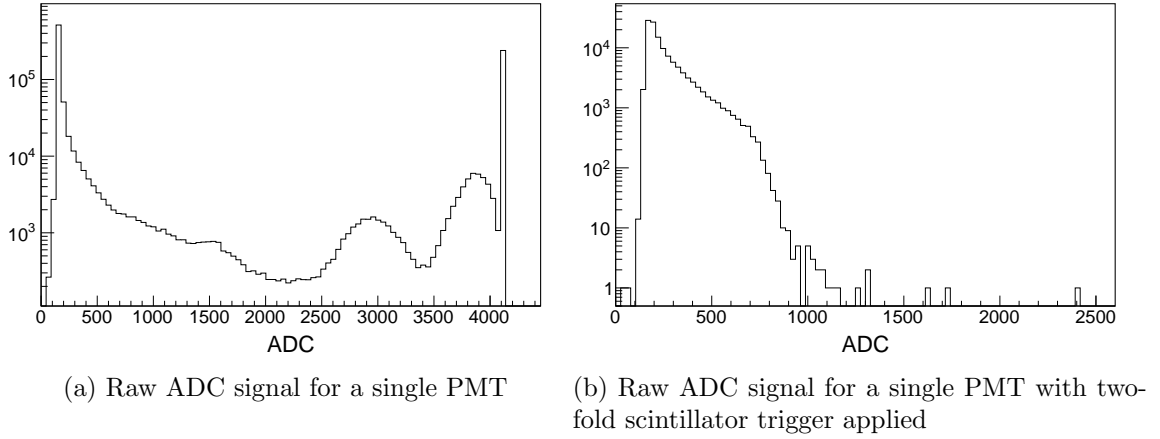


Figure 2.7: Comparison of the raw ADC signal from a single PMT for any global trigger in panel a.) and upon requiring a two-fold PMT trigger on the side of the PMT of interest in panel b.). This type of cut is part of the electron trigger along with a coincidence with the wirechamber.

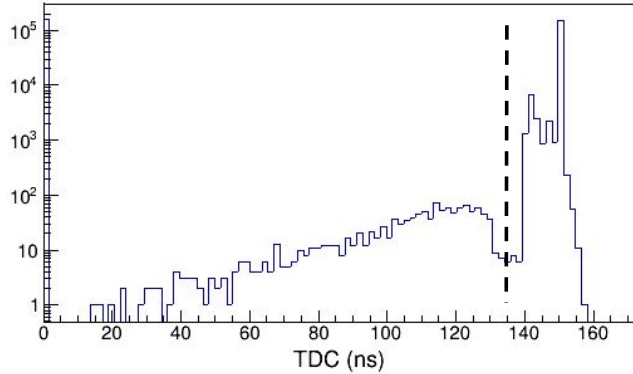


Figure 2.8: Example TDC signal (converted to nanoseconds) from a  $\beta$ -decay run for a single detector. Note that the horizontal axis is technically the time elapsed since a trigger occurred, so a longer time indicates an earlier trigger. The dashed line indicates the cut used to separate a self-trigger (right of the dashed line) from a backscattering trigger (left of the dashed line). The events at  $t = 0$  are events which did not create a self-trigger.

a timing signal to indicate when a detector component triggered, or if it triggered at all. An example TDC signal can be seen in Figure 2.8.

Several types of signals can generate a global trigger, where the data acquisition system (DAQ) reads all possible inputs. These include:

- UCN monitor – used to monitor the UCN production at various stages along the experimental apparatus.

- $^{207}\text{Bi}$  pulser event – This is a high threshold, single PMT trigger, so if one PMT has a trigger above a preset high threshold, but no other PMT has any trigger, this indicates the pulser created the trigger at the PMT and not the scintillator. This will be addressed more in the next chapter.
- LED pulser – An LED system was in place to assist in correcting any non-linearity in the PMT response. This was not utilized in this analysis, but still results in a global trigger.
- Two-fold PMT trigger – at least two of the four PMTs on one side must have signal above a pre-set threshold. This two-fold trigger indicates a particle deposited energy in the scintillator, distinguishing it from noise in a single PMT, a  $^{207}\text{Bi}$  pulser event, or an LED event.

The two-fold PMT trigger is of most importance for the analysis that follows, as this indicates that there was sufficient energy deposition in the scintillator to be an electron event. The hardware trigger does not discriminate between what type of event may have created the trigger though, so any particle that can deposit energy in the scintillator could have been the culprit. To remedy this, we rely on methods already highlighted in above sections. By applying a software trigger to the wirechamber, we can require that any event that created a two-fold scintillator trigger in detector 1 must also pass the software trigger in MWPC 1. This almost entirely removes the gamma background, as the wirechamber is virtually transparent to a gamma. Then by checking for muon veto signals above some software threshold we eliminate cosmic ray muon backgrounds, leaving primarily electron events. Of course some background events make it into the analysis, but these are accounted for via background subtraction as will be discussed.

Along with ADC signals proportional to energy deposition, all PMTs also report hardware trigger timing information (TDC signal). Along with the individual TDC signals, a two-fold TDC signal for each detector is recorded when there is a global trigger. For backscattering events which trigger both detectors, we use the two-fold TDC signals to determine the primary side, or the initial direction of the electron. This can be seen in Figure 2.8. The dashed line indicates the position of a cut to separate a primary trigger from a backscattering trigger. An acceptable event either has a single primary trigger or a primary trigger on one side and a backscattering trigger on the other side.

## 2.6 Data Taking Structure

The data is broken into three types of run periods, namely  $\beta$ -decay data, source calibration, and Xe position mapping. The latter two determine the parameters of the energy calibration to be applied to the data runs. The source calibration and Xe position mapping run periods occur periodically throughout each data set and are applied to surrounding  $\beta$ -decay runs. This creates different subsets of data to which each calibration is applied, as will be illustrated throughout the rest of this dissertation. Here we simply highlight the structure of the  $\beta$ -decay runs, and one should take note that the source calibrations and Xe position map periods are spaced throughout.

### 2.6.1 $\beta$ -decay run structure

We utilize what we call an octet run structure, where each octet contains a total of twenty-four runs, eight of which are  $\beta$ -decay data runs, eight of which are background runs, and eight of which are depolarization runs. The octet is further split into two halves, A and B, which define the order of the runs within them as seen in table 2.1. Whether the A structure or the B structure comes first within an octet is determined randomly. There are four  $\beta$ -decay runs of each spin-state (aligned and anti-aligned to the magnetic field in the spectrometer), and their accompanying background runs allow for background subtraction.

Table 2.1: Octet structure, where  $\pm$  indicates spin flipper on/off, B refers to background run, D refers to depolarization run, and  $\beta$  refers to  $\beta$ -decay runs.

A1	A2	A3	A4	A5	A6	A7	A8	A9	A10	A11	A12
B <sup>-</sup>	$\beta$ <sup>-</sup>	D <sup>-</sup>	B <sup>+</sup>	$\beta$ <sup>+</sup>	D <sup>+</sup>	$\beta$ <sup>+</sup>	D <sup>+</sup>	B <sup>+</sup>	$\beta$ <sup>-</sup>	D <sup>-</sup>	B <sup>-</sup>
B1	B2	B3	B4	B5	B6	B7	B8	B9	B10	B11	B12
B <sup>+</sup>	$\beta$ <sup>+</sup>	D <sup>+</sup>	B <sup>-</sup>	$\beta$ <sup>-</sup>	D <sup>-</sup>	$\beta$ <sup>-</sup>	D <sup>-</sup>	B <sup>-</sup>	$\beta$ <sup>+</sup>	D <sup>+</sup>	B <sup>+</sup>

## 2.7 Backscattering

Before moving forward, it is important to formally introduce the different backscattering events, as they will be referenced often. A backscattering event is an electron event initially emitted towards one detector, but that is scattered through a large enough angle that its momentum is reversed and it travels to the opposite detector.

Some of these events are backscattered by a detector component and can therefore be identified as having backscattered due to energy deposition on both sides of the spectrometer, while others backscatter without depositing enough energy (or backscatter prior to reaching the detector) and therefore become what we call “missed” backscattering events. Missed backscattering events are problematic as they are assigned the wrong initial direction and therefore systematically effect the asymmetry.

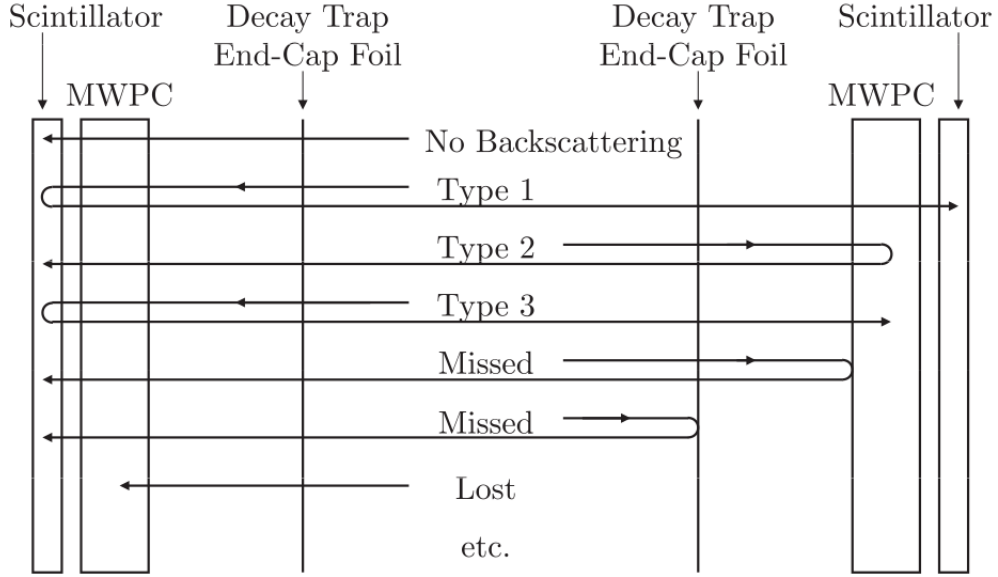


Figure 2.9: Schematic of different event types and the trigger logic involved with identifying each type [Pla+12].

Based on which detector components trigger, we classify events into those that do not backscatter (Type 0) and those that do backscatter (Types 1, 2, and 3) [Pla+12]. A schematic of the different event types can be seen in Figure 2.9. Type 0 events trigger one scintillator and one MWPC on the same side, while Type 1 events trigger both scintillators and both MWPCs. For such events, we assign the initial direction to the triggering detector for Type 0 and to the earlier triggering detector for Type 1. Type 2/3 events comprise a class of events that backscatter and trigger both MWPCs, but only trigger a single scintillator. Since the MWPCs do not contain any timing information, the initial direction of such events can not be determined from trigger logic alone, as can be demonstrated by considering two events which look identical under trigger logic. For example, let “Event 1” denote an event that initially backscatters off of MWPC 1 before reaching scintillator 1 and then traverses the length of the decay trap to trigger both MWPC 2 and scintillator 2 on the opposite side. Then, suppose “Event 2” denotes another event emitted in the

opposite direction to event 1. Suppose this event triggers MWPC 2 and scintillator 2 only to backscatter from the scintillator and travel to MWPC 1 and stop short of scintillator 1. Both events trigger MWPC 1 and 2 and scintillator 2, but the two events had opposite initial directions, so inclusion of the two events without further knowledge of their initial direction creates a dilution to the asymmetry.

An important distinction, however, does exist between Type 2 and Type 3 events: Type 2 events only pass through the MWPC on the triggering scintillator side once, whereas Type 3 events scatter from the scintillator, and therefore pass through the MWPC twice on the triggering side. We can consequently apply a cut on the energy deposited in the MWPC on the triggering side to statistically assign Type 2/3 events to the correct side. This drastically reduces Monte Carlo corrections for such backscattering events as simulation indicates we properly identify > 80% of all Type 2/3 events across all energies using this technique, a marked improvement over the roughly 50% misidentification rate without separation.

Copyright<sup>©</sup> Michael A-P Brown, 2018.

# Chapter 3

## UCNA Analysis

This chapter is dedicated to introducing important aspects of the analysis that is not strictly tied to calibrations and asymmetry extraction, but rather data collection and processing to turn raw detector signals into values that can be calibrated and analyzed.

### 3.1 Outline of Analysis Steps

To preface the rest of this chapter, we can highlight the general process of the analysis beginning with a raw detector ADC value from each PMT and finishing with an asymmetry. Below are the general steps:

- Determine pedestals for each PMT and subtract the pedestal from each data event.
- Measure the gain of each PMT and divide the drifts out of the signal.
- Apply a PMT-by-PMT calibration to determine the expected position dependent energy deposited in the scintillator for each event.
- Correct for the position dependent response of each PMT to return a visible energy as seen by each PMT,  $E_{\text{vis},i}$ .
- Combine the four PMT energies into a single deposited energy,  $E_{\text{vis}}$ .
- Convert this combined estimate of the energy deposition to a final reconstructed energy,  $E_{\text{recon}}$ , to use in analysis.
- Calculate an asymmetry and apply all systematic corrections.

It is important to point out early on the difference between  $E_{\text{vis}}$  and  $E_{\text{recon}}$ . The deposited or visible energy,  $E_{\text{vis}}$ , is an estimate of the energy physically deposited in the scintillator by a particle, while the reconstructed energy,  $E_{\text{recon}}$ , is an estimate of the true initial energy of an event. The two are different due to the electron losing energy as it traverses through the windows of the decay trap, the windows of the MWPC, the MWPC itself, and the dead layer of the scintillator. Of course the analysis could be done in terms of  $E_{\text{vis}}$ , but it is more convenient to express the results in terms of the true electron energy spectrum, and also the energy dependent theory modifications are in terms of the true initial energy of an event.

## 3.2 Time-dependent Detector Corrections

Obviously the system is not immune to drifts in signals due to variations in time. There are many sources of such drifts, ranging from simple electronic noise to changes in temperature. We deal with such time-dependent effects using pedestal subtraction, gain correction, and constant monitoring of backgrounds.

### 3.2.1 Pedestal Subtraction

The pedestal is a measure of the inherent detector signal, or baseline, upon which all other data signals lie. In terms of PMT signals, you can imagine the pedestal as a non-zero ADC value corresponding to zero input, or an offset. You might say that the experiment can be run without caring about an offset because the calibration will take this into account, which would be the case if the pedestals were constant or if we calibrated each run against itself, but neither is the case. We use a collection of subsequent runs to form our calibration sets, and these sets then calibrate data which is often taken hours, or even days, earlier or later. Thus changing pedestals can be worrisome, and care must be taken to determine the pedestals and subtract them from data.

To determine a pedestal, events must be chosen where there was a global trigger, but the PMT of interest does not trigger and preferably there is no signal whatsoever in the scintillator on that side. Obvious choices for these events are UCN monitor triggers, opposite side two-fold PMT triggers, and high-threshold  $^{207}\text{Bi}$  pulser triggers from other PMTs. Once there is a global trigger, we can use the individual TDC to ensure there was no individual trigger, and the events can be histogrammed for the PMT of interest. The mean of pedestal peak can be taken as the average pedestal

for a single run, and this value can be subtracted from every subsequent reading of this PMT.

One interesting thing to note is that the discriminators, which determine whether a component triggers, for all PMTs are housed together, which leads to correlations between the PMT triggers. In a perfect world, each PMT would have one pedestal, and that pedestal wouldn't care about other PMT's signals. Instead, what we see is that the pedestals can be dependent on the type of events that are chosen to construct the pedestal, and the effect can be  $\tilde{10}$  channels for some PMTs. This indicates that the pedestal for one PMT may be dependent on the signal present in another PMT. These shifts are important as a pedestal shift of 5-10 channels maps to an offset of roughly 5-10 keV, as the PMTs show roughly 1:1 correspondence between ADC and keV.

The influence of event type on pedestal values means we must carefully choose which events to use when calculating the pedestal. The best choice would be UCN monitor events due to there being zero signal in the electronics box housing the PMT electronics, and these thus would give the cleanest measurement of the PMT pedestal. These are unfortunately the first event type we can eliminate as they are only present during  $\beta$ -decay runs (when UCN are produced and thus create UCN monitor triggers) and not during calibration runs (taken during the day when the beam is off). Of the remaining two options, the choice was made to use the two-fold PMT triggers from the opposite detector rather than  $^{207}\text{Bi}$  pulser events. The choice is somewhat arbitrary, because what is important is that we choose a consistent subset of data for both calibration and  $\beta$ -decay data, but the opposite side two-fold triggers do better represent the baseline present in each PMT for data events when compared to the much higher signal present from the  $^{207}\text{Bi}$  pulser.

With the event type chosen, we extract the mean and RMS of the pedestal peak for each PMT in every run. The pedestal mean (referred to as simply the pedestal) is then subtracted from the ADC values for all events. This effectively removes the time-dependent baseline from the detector signals. The time dependence of the pedestals can be seen for the East PMTs from 2011-2012 in Figure 3.2. Most of the PMTs have pedestals which remain quite stable, but PMT East 3 shows the importance of a run-by-run pedestal subtraction.

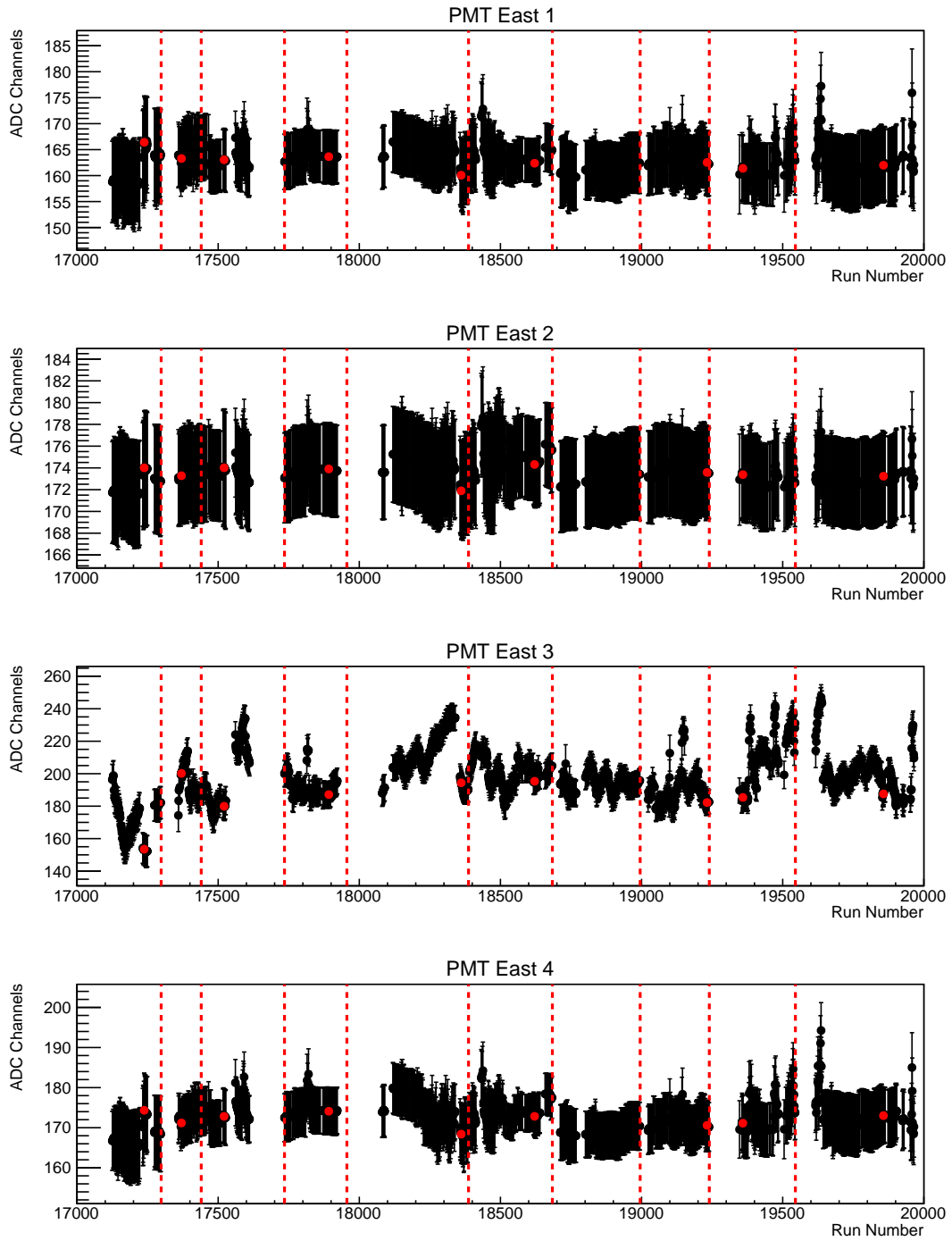


Figure 3.1: Pedestal means as a function of run number for 2011-2012 East Detectors. Error bars are the RMS of the measured pedestal. The red lines indicate what ranges of runs belong to different calibration periods, and the red marker is the calibration reference run, which will be discussed in later sections.

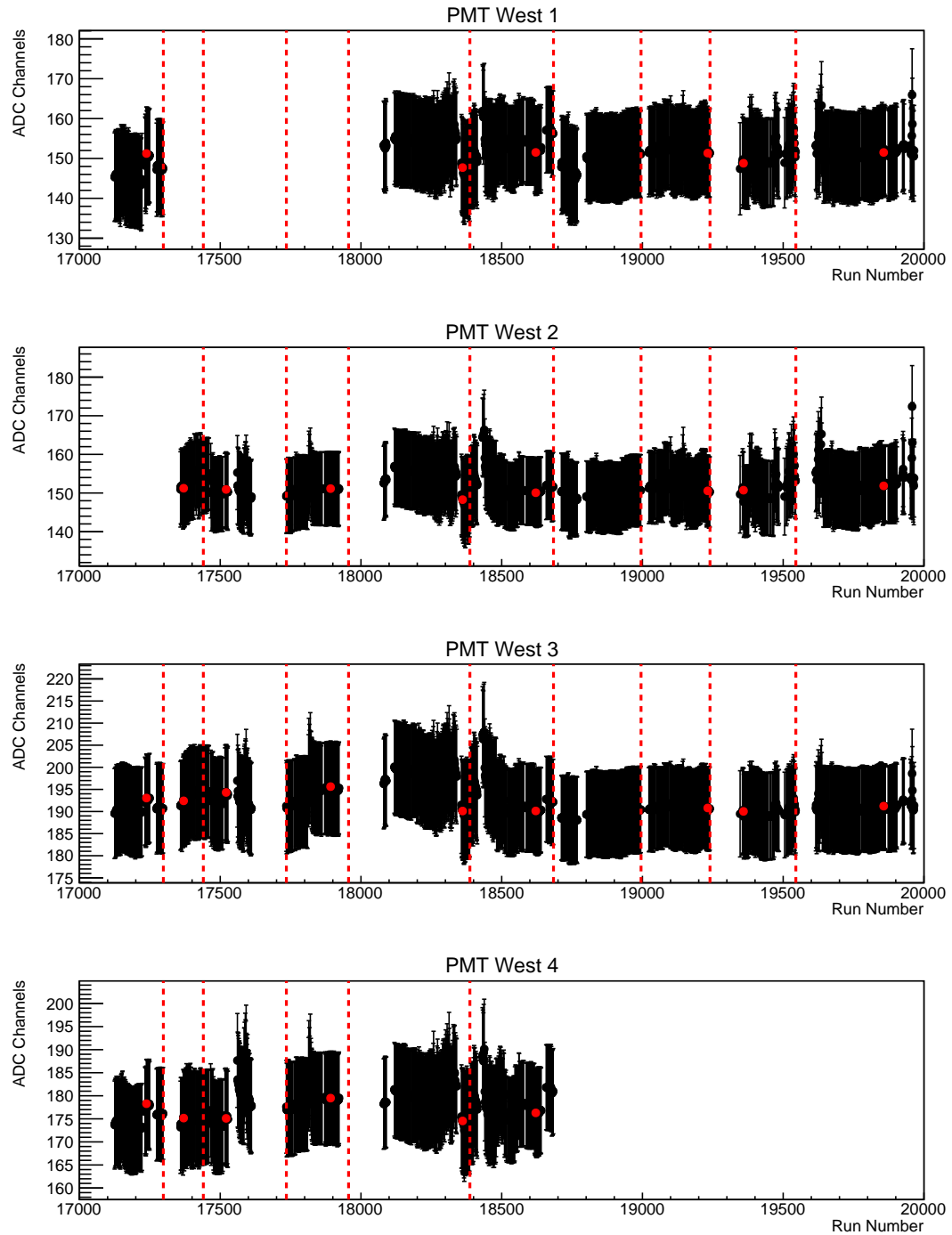


Figure 3.2: Pedestal means as a function of run number for 2011-2012 West Detectors. Error bars are the RMS of the measured pedestal. The red lines indicate what ranges of runs belong to different calibration periods, and the red marker is the calibration reference run, which will be discussed in later sections.

### 3.2.2 Gain Correction

#### 3.2.2.1 $^{207}\text{Bi}$ Pulser

The primary gain monitoring system consists of a small amount  $^{207}\text{Bi}$  deposited within a small block of scintillator. The scintillator was surrounded by light reflecting material on three sides, with the fourth side covered with an optical attenuator to attempt to match the light output of the  $\tilde{1}$  MeV conversion line in the  $^{207}\text{Bi}$  to the light output of 1 MeV of energy deposited in the detector scintillator. The pulser was then attached directly to the PMT next to where the light guides attached to the PMT. To allow for a single-PMT high threshold trigger, the signal was split off to a different discriminator than the one used when determining a two-fold trigger. These high threshold discriminators then allowed for pulser triggers with a distinct pulser identification [Men14].

An unfortunate but low impact issue with the pulser involves the amount of attenuation applied to the pulser signal. The pulser peak lies well beyond the equivalent of 1 MeV of light as would be produced in the detector scintillator, and therefore far outside the range of the  $\beta$ -decay spectrum. This is not a serious issue as the PMTs seem to be quite linear, so even a peak well outside the energy range of interest should suffice.

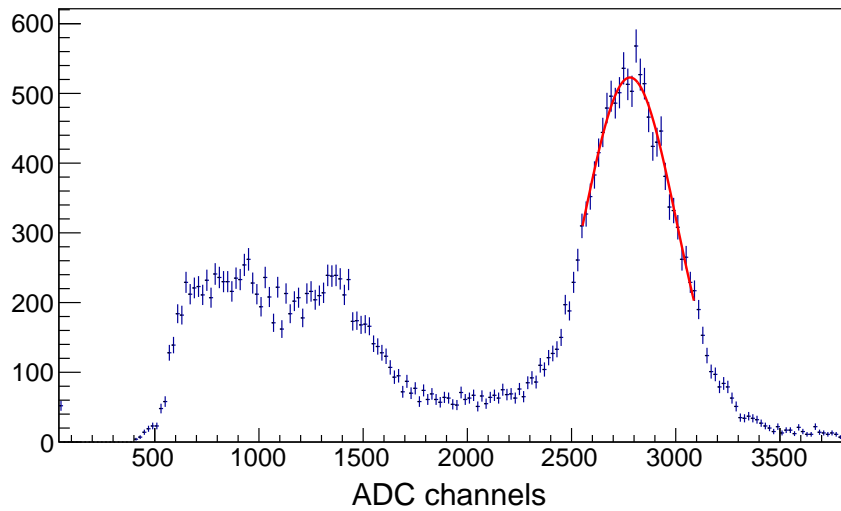


Figure 3.3: Example  $^{207}\text{Bi}$  spectrum and fit for a single PMT over the course of a run. The upper and lower bismuth conversion electron peaks are seen, along with a distribution from decay gammas. Note that the gamma rays are visible because the pulser is attached directly to PMT and there is no type of veto (like the MWPC) to remove them.

The  $^{207}\text{Bi}$  pulser peak is fit by a Gaussian on a run-by-run basis, allowing for gain corrections on the time scale of a single run. The fit was done iteratively, with the initial guesses for mean and fit range determined by stepping backwards from the last bin and using a self-written algorithm to search for the peak. Then the peak was fit five times consecutively, with each successive fit being fed the previous fits mean and sigma. This made sure the fit converged as best as possible on the mean of the pulser peak. An example pulser peak and fit can be seen in Figure 3.3. The asymmetric fit (range extends farther above the peak than below) is actually a characteristic part of the iterative fitting algorithm developed for use throughout this analysis. For Gaussian like peaks occurring as a result of a process like energy loss in a scintillator followed by PMT amplification, the upper end of the peak is inherently more Gaussian due to the lower end having a tail from extraneous energy losses.

The method for applying the gain correction is as follows. First, a reference gain must be determined to normalize all other gains against. This was chosen to be what is called the “reference run”, and it typically consists of a manually inspected source run within each source calibration period. The gain factor is then calculated as the ratio of the pulser peak in a given run divided by the pulser peak in the reference run, or

$$g_i = \frac{\mu_i}{\mu_{\text{ref}}} \quad (3.1)$$

This automatically defines the gain of the reference run to be  $g_{\text{ref}} = 1$ . Then all other runs which are calibrated by a certain run period have gain factors which vary based on the fitted pulser value. The time dependence of the gain values in 2011-2012 can be seen in figures 3.4 and 3.5. The behavior is similar in 2012-2013.

Some problems with the  $^{207}\text{Bi}$  pulser did occur. There were several periods where the pulser simply did not work for a certain PMT. This was always limited to a single PMT not working, and when this was the case the PMT without a pulser signal was not used when reconstructing the energy. This has minimal effect on the energy reconstruction though, as the “bad” PMT is still used when determining a two-fold trigger, and the remaining three PMTs contain sufficient information for reconstructing the energy deposited. Periods where  $^{207}\text{Bi}$  pulser information is missing are evident in figures 3.5 where there is missing data for certain PMTs over extended ranges. It should be noted that in 2012-2013, West PMT4 never had a functioning pulser.

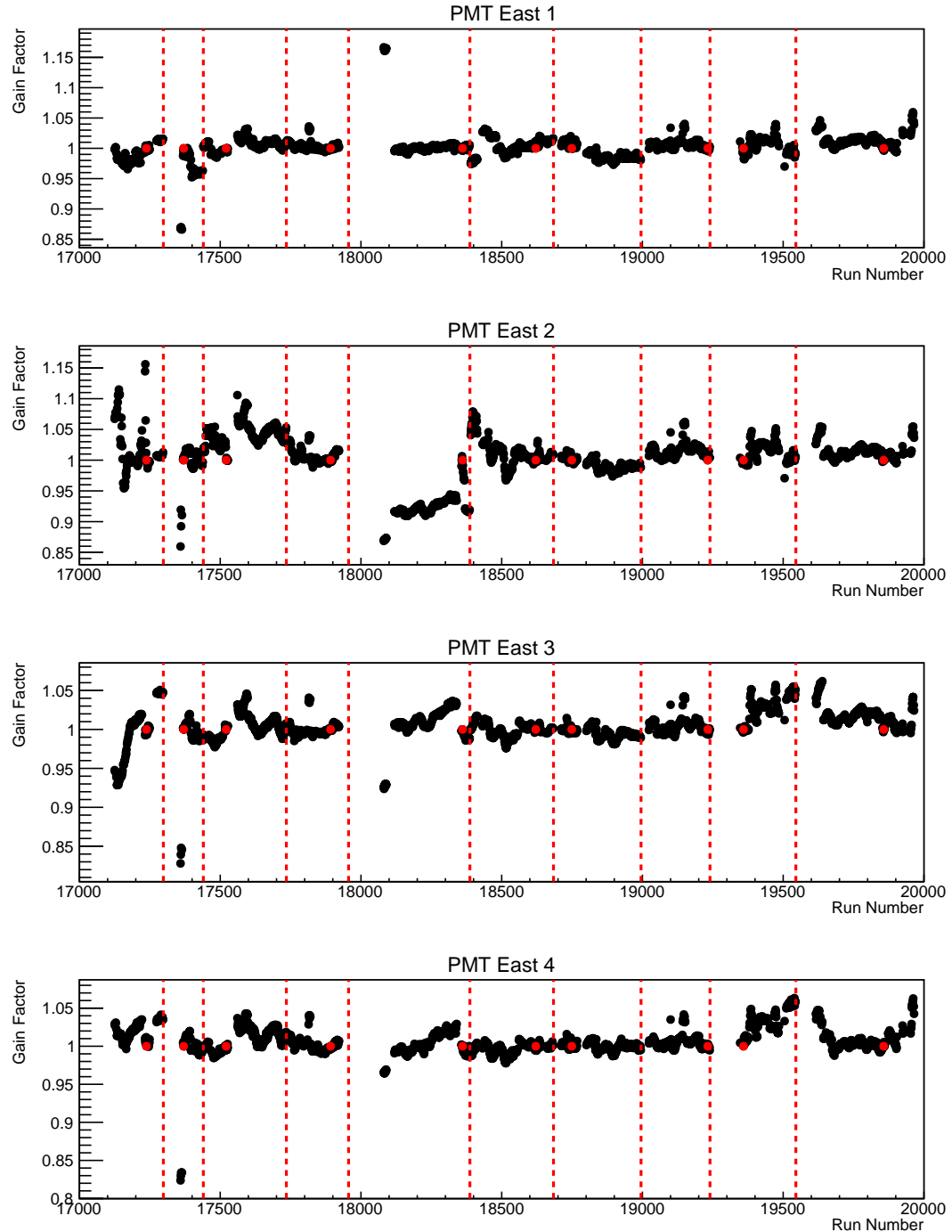


Figure 3.4: Gain factors,  $g_i$ , as a function of run number for 2011-2012 East Detectors. The red lines indicate what ranges of runs belong to different calibration periods, and the red marker is the calibration reference run.

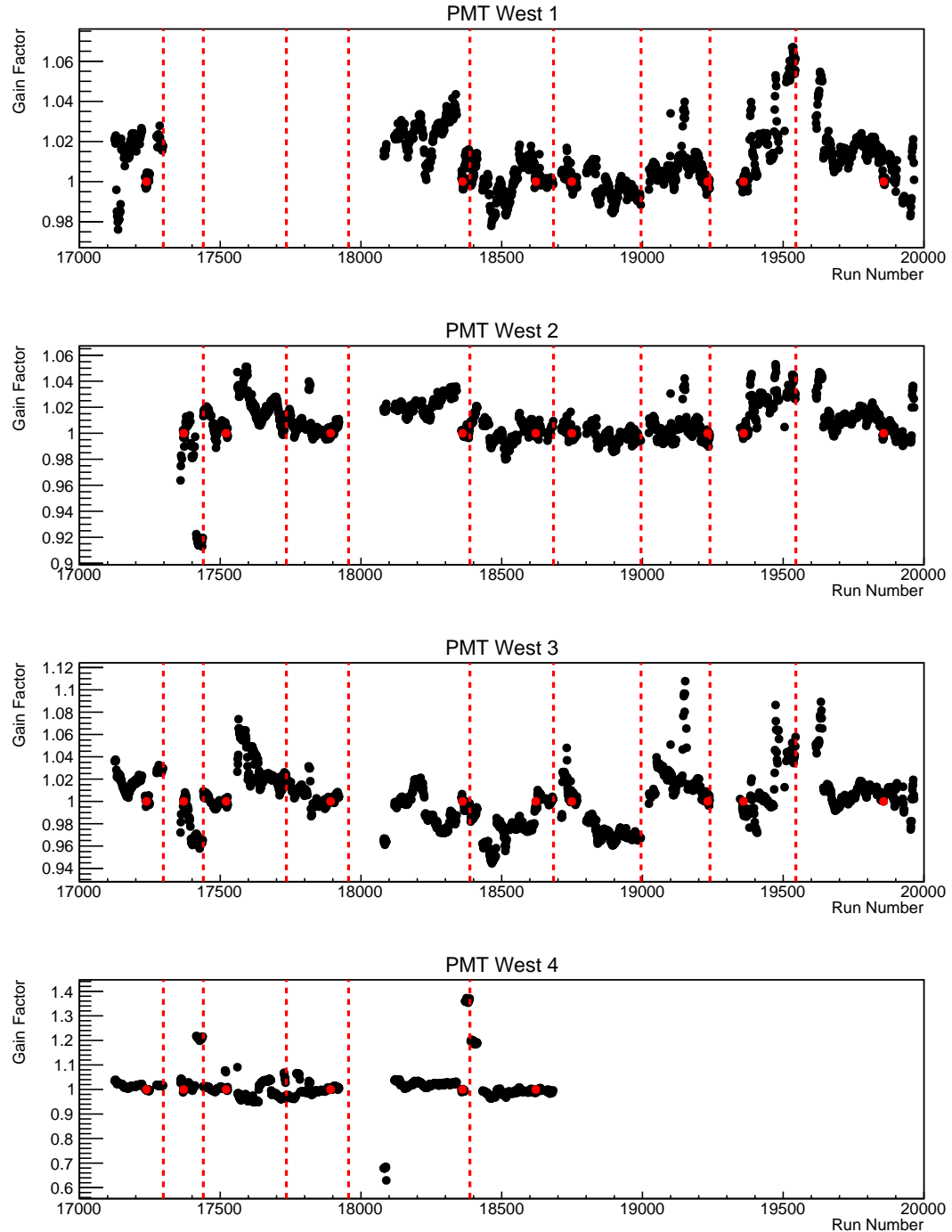


Figure 3.5: Gain factors,  $g_i$ , as a function of run number for 2011-2012 West Detectors. The red lines indicate what ranges of runs belong to different calibration periods, and the red marker is the calibration reference run.

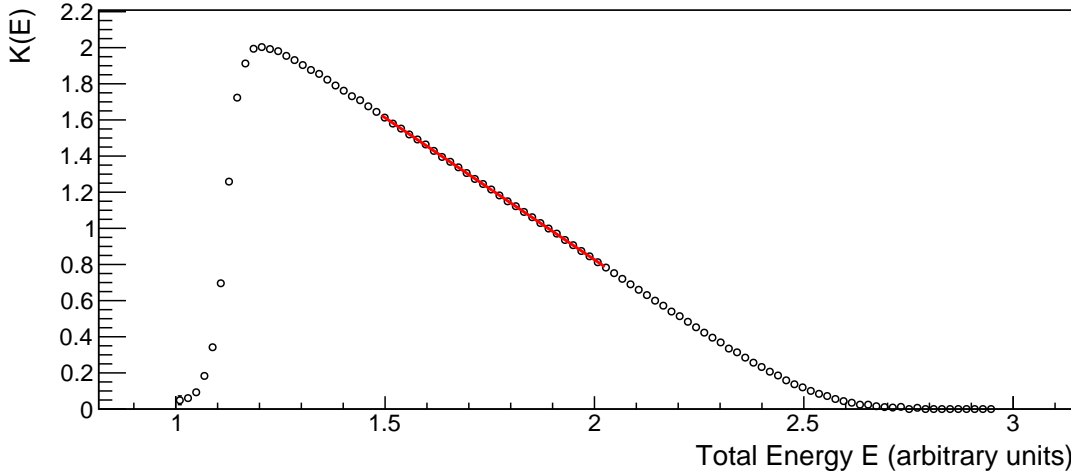


Figure 3.6: Example Kurie plot with linear fit to extract the y-intercept, which is the endpoint energy. The deviations from a straight line are due to the trigger efficiency at low energies and finite resolution at high energies. Care must be taken to fit in a region which more appropriately characterizes the true underlying electron energy spectrum.

### 3.2.2.2 Endpoint Stabilization

There are unexplained longer term gain fluctuations that do not seem to be captured by the  $^{207}\text{Bi}$  gain monitoring system that can be seen by monitoring the endpoint of the  $\beta$ -decay spectrum. These are corrected by applying a second gain factor,  $g_{\text{ep},i}$  for PMT  $i$ , as the last step in the calibration process. This endpoint gain factor is determined by comparing the endpoints as seen by each calibrated PMT to the expected endpoint from the simulation. The final energy for each PMT is then multiplied by this factor. This does not force the final reconstructed energy endpoint to match the final reconstructed simulation endpoint exactly, as the final spectra are the weighted average of the four PMT responses, but rather it corrects some systematically shifted periods of data which consistently exhibited endpoints  $> 30$  keV away from the expected endpoint.

The method for calculating  $g_{\text{ep}}$  was developed previously by M. Mendenhall in section 5.2.2 of [Men14]. For the sake of clarity, the process is repeated here.

The endpoints are fit using a Kurie plot [KRP36], which linearizes the energy response making for easy determination of the endpoint energy. If we approximate the decay rate as the phase space factor for the neutron, then we can write down the decay rate as a function of the electron total energy  $E$ , endpoint energy  $E_0$ , and

momentum  $p$  as

$$S(E) = pE(E_0 - E)^2 \quad (3.2)$$

From this we see that a linear equation (the Kurie plot) can be formed:

$$K(E) = \sqrt{\frac{S(E)}{pE}} = E_0 - E \quad (3.3)$$

where the  $y$ -intercept and  $x$ -intercept both determine the endpoint energy  $E_0$ . An example Kurie plot can be seen in Figure 3.6.

Now we assume that the measured kinetic energy spectrum  $T_{\text{meas}}$  is different from the expected kinetic energy spectrum  $T_{\text{sim}}$  by the gain factor  $g_{\text{ep}}$  such that

$$T_{\text{sim}} = g_{\text{ep}} T_{\text{meas}}. \quad (3.4)$$

Then we can write the measured total energy as

$$E_{\text{meas}} = m_e + g_{\text{ep}} T_{\text{meas}} \quad (3.5)$$

where  $c = 1$  is used. The extracted endpoint for the data is now a function of  $g_{\text{ep}}$  since

$$K(E_{\text{meas}}) = \sqrt{\frac{S(E_{\text{meas}})}{pE_{\text{meas}}}} = E_{0,\text{meas}} - E_{\text{meas}}, \quad (3.6)$$

and upon proper choice of  $g_{\text{ep}}$ ,  $E_{\text{meas}} = E_{\text{sim}}$ . To solve for the proper gain factor, the data endpoint is iteratively fit with the gain factor adjusted upon each iteration according to

$$g'_{\text{ep}} = \frac{E_{0,\text{meas}} - m_e}{E_{0,\text{sim}} - m_e} g_{\text{ep}} = \frac{T_{0,\text{meas}}}{T_{0,\text{sim}}} g_{\text{ep}}, \quad (3.7)$$

where  $E_{0,\text{meas}}$  is the extracted endpoint energy from the data with gain factor  $g_{\text{ep}}$  applied,  $E_{0,\text{sim}}$  is the expected endpoint energy extracted from simulation,  $T_0$  is the endpoint kinetic energy, and  $g'_{\text{ep}}$  is the guess for the next iteration of endpoint fitting. Once the condition  $1 - \frac{g'_{\text{ep}}}{g_{\text{ep}}} < 10^{-7}$  is met, the value of  $g'_{\text{ep}}$  is taken as the final endpoint gain factor and is saved to the calibration database. This process is carried out for each PMT for every  $\beta$ -decay run, and then every event is reprocessed with the new gain factor applied to the visible energy from PMT  $i$  according to

$$E_{\text{vis},i}^{\text{FINAL}} = g_{\text{ep},i} E_{\text{vis},i}. \quad (3.8)$$

Then  $E_{\text{recon}}$  is calculated using the final visible energies from the available PMTs.

### 3.2.3 Time-dependent backgrounds

Background events which may have some time dependence are removed from the analysis via dedicated background runs that accompany every  $\beta$ -decay run. Subtracting these background rates from the data rates accounts for backgrounds with roughly a one hour time variation. Any backgrounds that vary at the sub one hour level may go unnoticed, but with a signal to background better than 50:1 the contribution from such is minimal. The background run scheme will be addressed later in this chapter, with the background subtraction addressed in chapter 5.

## 3.3 Trigger Thresholds

Looking ahead to the detector response model that will be implemented when processing the simulated data, we need to determine the trigger thresholds for each of the PMTs. With each PMT attached to a leading edge discriminator, the amount of charge in a pulse that can create a trigger is randomized. The ADC signal is an integrated signal, so two signals with integrated charge at roughly the trigger threshold may have different amplitudes and therefore different likelihoods of passing the discriminator threshold. Measurement of these thresholds is important for the detector response model within the simulation in order to properly model the low energy behavior of the measured spectrum.

### 3.3.1 General Model for Trigger Determination

The most important part of determining the trigger threshold shape for any detector is the availability of data which was collected no matter if the detector or component (PMT) produced a trigger. If such a subset of data is available and plentiful, it is straightforward to estimate the trigger probability by binning the data in some unit proportional to energy (whether in energy or something like it isn't important) and taking the bin-by-bin ratio of those events that triggered to all of the events in the sample. Plotting these ratios as a function of whatever energy-like metric was chosen tells you how probable an event of some value is to create a trigger. Once you have mapped this probability, you can then sample these curves within simulation to apply your true trigger threshold to simulated data.

### 3.3.2 Trigger Data Selection

As mentioned before, the data used for constructing trigger thresholds must not be biased towards triggering the PMT of interest. Thus that PMT must not be a mandatory component of the global trigger for that event, so care must be taken to choose only events which would trigger regardless of the behavior of the PMT of interest. One other stipulation placed on these events is that they have an opportunity to deposit energy in a particular scintillator. The best choice of events which satisfy these conditions are those which have a two-fold trigger on the opposite side and then backscatter and those which trigger at least three PMTs on the side of interest, which guarantees that the scintillator would have triggered with or without the PMT of interest.

### 3.3.3 Determining the Trigger Probability

One option for determining the trigger probability function (and probably the most straightforward) is to calculate the trigger probability for an entire detector as a whole as a function of the energy deposited by an event. What you get is a function that provides the probability that an event of energy  $E_i$  produces some sort of trigger, either 2-fold, 3-fold, or 4-fold, in that detector. Initially this method was used for sake of simplicity, and it produced reasonable agreement between simulation and data, but there is one glaring concern: Determining this trigger function from data requires that the data be calibrated first. At first glance this may not seem like much of an issue, but the calibration hinges upon the simulated peaks at low energy, which in turn rely on the trigger functions. This cyclical dependence hinders one from truly understanding any discrepancy between simulation and data at low energies, which is exactly the reason this method was abandoned.

Instead, similarly to previous analyses, we decided to calculate the trigger function on a PMT-by-PMT basis as a function of ADC channels above pedestal. This encompasses a true characteristic of each component of the detector rather than some average effect as seen by a detector package, which is what the aforementioned method produces. A typical trigger threshold is seen in Figure 3.7. As illustrated in Section 3.3.1, the ratio of triggering events to all events was taken in each ADC bin and then fit using the method described in the following section.

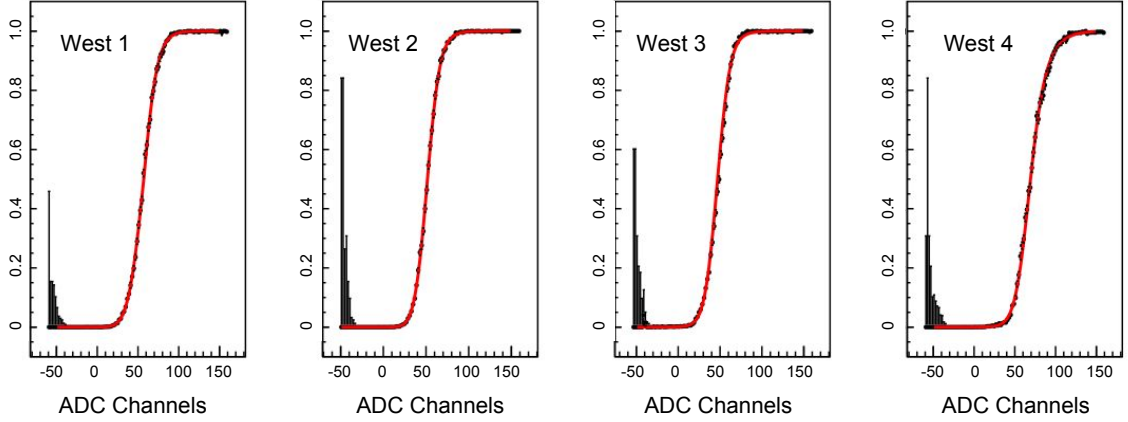


Figure 3.7: Typical trigger thresholds as a function of pedestal subtracted ADC values from the West PMTs with fits shown in red. The y-axis is a probability of triggering given some ADC signal.

### 3.3.3.1 Functional Fit of the Trigger Threshold

From the sigmoid shape of the threshold data in Figure 3.7, one might guess the shape of the curve to be a hyperbolic tangent or an error function. The data tends to show a sharper turn on at lower ADC channels and a softer levelling off to unit probability, which prompted the use of both the  $\text{erf}(x)$  (lower end of transition region) and  $\tanh(x)$  (upper end of transition region), with a continuous transition between the two provided by a smoothing function  $S_{\pm}$  defined as

$$S_{\pm}(x; x_0, R) \cdot f(x) = \frac{1}{2} \left( 1 \pm \tanh \left( \frac{x - x_0}{R} \right) \right) \cdot f(x), \quad (3.9)$$

which acts to “turn on/off” (+/-) a function  $f(x)$  around the pivot point  $x_0$  and with the severity of the on/off transition determined by the width parameter  $R$ . The functional fit  $F(q)$  then becomes (note that the  $\text{erf}(x)$  and  $\tanh(x)$  have the range (-1,1), so they must be shifted and the range halved to accommodate  $0 < F(q) < 1$ ):

$$F(q) = \frac{1}{2} \left[ S_{-}(q; \mu, R) \left( 1 + \text{erf} \left( \frac{q - \mu}{w_1} \right) \right) + S_{+}(q; \mu, R) \left( 1 + \tanh \left( \frac{q - \mu}{w_2} \right) \right) \right] \quad (3.10)$$

where  $q$  is the ADC value and the free parameters are  $\mu$  ( $f(q = \mu) \approx 0.5$ ),  $w_1$  (width of  $\text{erf}$ ),  $w_2$  (width of  $\tanh$ ), and  $R$  (severity of turn on/off). This function, while motivated purely by inspection of the shape of the trigger threshold, fits the data quite well with only these four free parameters. An example of the fits for a single  $\beta$ -decay run can be seen in Figure 3.7.

## 3.4 Simulation

The simulations and application of the detector response model provide a suitable starting point for discussing the analysis, as the calibration of the data hinges strongly on the simulation results. There is a notable dependence of the response model on data, but this will be addressed as needed when describing the calibration.

The simulation work for this thesis was completed using the Geant4 simulation software package. The geometry of the apparatus was duplicated to the best precision possible and benchmarked against data after the detector response model was applied. The structure of the simulation code did not change from those in the previous analysis as described in [Men14], although minor changes were made to the geometry to reflect real adjustments to the experimental apparatus.

### 3.4.1 Input

#### 3.4.1.1 Conversion Electron Sources

make sure to show figures or a table with the conversion lines

#### 3.4.1.2 Activated Xenon

#### 3.4.1.3 $\beta$ -decay Electrons

### 3.4.2 Output

The Geant4 simulation provides adequate trajectory tracking along with the energy deposition along these tracks. Obviously we have access to far more information in the simulation than we do with actual data, so the first task is to construct observables related to those coming from the detectors.

#### 3.4.2.1 Energy Deposition

By tallying the energy deposited along an entire track within some subset of the geometry, one can reconstruct the energy deposited anywhere within the SCS. The areas of highest interest for the sake of analysis are the wirechambers and the scintillators. The energy deposited in the scintillator is of utmost importance, as the analysis can be completed without knowledge of the energy deposition in the wirechamber, where determination of energy deposition is only used for type II/III separation. From here on, the energy lost in the scintillator, as determined from simulation, will be referred

to as  $E_{dep}$ . This is the maximum energy which could be detectable for an event in the data if no inconspicuous energy losses existed.

### 3.4.2.2 Quenched Energy

Show Birk's law. Talk about MPM and jianglai's analysis to determine quenching parameters. Then talk about the modification using BradF's note and show the shift to the functional form. Also show a figure which shows the quenched energy vs Edep.

### 3.4.2.3 Magnetic Field

### 3.4.2.4 Position of Detector hits

Talk briefly of importance of position dependence, and maybe address the way the position for the wirechamber and scintillator are calculated. I believe this was a weighted average of the track positions where the weights are given by the energy deposition.

## 3.4.3 Simulating Detector Response

While all pertinent components of the experimental apparatus were included in the simulation, the detector response is not inherent within our output. You may notice from (figure with quenched energy) that this doesn't resemble the gaussian peaks normally seen in a detector signal. The gaussian-like peaks arise from finite resolution effects and must be put in defacto using parameters calculated from real data. The better we understand the conversion from a pure simulation energy output to a response which mimics that from our actual detectors, the more credence we can put in our calibration. For the time being, the model will be introduced with parameter determination addressed as it arises.

## 3.4.4 Detector Response Model

Recall from Section ?? that we can relate a digital signal in a PMT,  $ADC_i$ , to the energy deposited in the scintillator using Equation ???. By reverse engineering this process, we can use a purely simulated  $E_Q$  and simulate an ADC channel, so that we can process the simulated data in exactly the same way we process real data. The following equation comes directly from ??:

$$ADC_i = f_i^{-1} (\eta_i(x, y) \cdot E_Q) / g_i(t) + p_i(t) + \delta p_i(t) \quad (3.11)$$

This relationship is somewhat incomplete though, as it does not address the stochastic nature of the PMTs themselves. Let's rewrite \*\*\*\*\*To properly incorporate this into our model we must utilize the fact that a PMT consists of several dynodes, each of which introduces stochasticity into the final voltage read out.

## 3.5 Energy Response from Detector Response

Following the process outlined in the previous section, we can derive an expression which takes a detector signal to an energy estimate for each PMT. The visible energy  $E_{\text{vis},i}$  deposited in the scintillator as seen by a single PMT  $i$  for an event at position  $(x, y)$  is given by the following:

$$E_{\text{vis},i} = \eta_i^{-1}(x, y) \cdot f_i \left( (\text{ADC}_i - p_i(t)) \cdot g_i(t) \right), \quad (3.12)$$

where

$f_i$  = linearity relation from ADC channels to light output (proportional to energy),  
 $\eta_i(x, y)$  = PMT position map factor to correct for position dependence of light response,  
 $p(t)$  = mean pedestal value for PMT  $i$ ,  
 $g(t)$  = gain correction factor for PMT  $i$ .

This expression is exact in the case where all values are determined with infinite precision and without stochastic fluctuations. Unfortunately, each parameter on the right side of this equation is either stochastic in itself (as is the ADC response), or it was determined via observation of a random process (the gain and pedestal), and so the underlying value for any given event may not be the same as the value applied in the above expression. Thus what we really resolve is an approximation to the energy, which comes with some uncertainty. This uncertainty will be addressed later in Section 5.2.4. For the time being, keep in mind the above list of input parameters which take us from an ADC signal (detector signal) to an energy signal.

### 3.5.1 Combining PMT Responses

For every two-fold trigger, all four PMTs from each side (eight in total) are read out by the DAQ. Upon application of the individual detector calibrations, this yields eight visible energies,  $E_{\text{vis},i}^{\text{E,W}}$ , where  $i$  runs from 1 to 4 for the four PMTs on each side. For each detector, the four available energies should be combined to create a visible

energy for each side,  $E_{\text{vis}}^{\text{E,W}}$ . While the majority of events only strike one scintillator so only one of E/W visible energies will be useful, the Type 1 events will have a usable energy on each side.

Now not all PMTs are created equal. Some PMTs have better resolution than others, thus these PMTs should contribute more to the average energy. A simple average would not account for this, but a weighted average, upon definition of the weights, will suffice:

$$E_{\text{vis}}^{\text{E,W}} = \frac{\sum_{i=1}^4 w_i E_{\text{vis},i}^{\text{E,W}}}{\sum_{i=1}^4 w_i}, \quad (3.13)$$

where  $w_i = \frac{1}{\sigma_i^2}$  are the weights for each  $E_{\text{vis},i}^{\text{E,W}}$ . We will drop the superscript E/W for now, understanding that what follows is done for each detector.

Now let's assume that the  $E_{\text{vis},i}$  from Equation 3.12 is an approximation for an event which deposited exactly the energy  $E_Q$  (the  $Q$  stands for “quenched”, which will be described in Section 3.4.2.2). A certain amount of this  $E_Q$  is visible to each PMT, given by  $\eta_i(x, y)E_Q$ , as each PMT only captures a portion of the total number of photons produced in the scintillator. Now if we want to relate this to the signal read out by the DAQ from the PMT, we must multiply by a PMT resolution factor  $\alpha_i$  to convert from energy to photoelectrons, giving  $N_i = \alpha_i \eta_i(x, y)E_Q$ . These PMT resolution factors are calculated during the calibration process and will be discussed in Section 4.2.4, but for now, assume they are known.

The number of photoelectrons produced by a PMT is a stochastic process, so we can write the actual measured number of photoelectrons as  $\bar{N}_i = N_i \pm \sqrt{N_i}$ . The fractional uncertainty is then  $1/\sqrt{N_i} = 1/\sqrt{\alpha_i \eta_i(x, y)E_Q}$ . Now, since the measured number of photoelectrons,  $\bar{N}_i$ , is directly proportional to the ADC signal of the PMT and thus also the visible energy of the PMT by Equation 3.12, we have

$$E_{\text{vis},i} = E_Q \pm \frac{E_Q}{\sqrt{\alpha_i \eta_i(x, y)E_Q}} = E_Q \pm \sqrt{\frac{E_Q}{\alpha_i \eta_i(x, y)}}. \quad (3.14)$$

The measured value of  $E_{\text{vis},i}$  is actually sampled from a distribution with  $\mu$  and  $\sigma$  given by the above equation, but we can assume that the best weight is given by  $w_i = \frac{1}{\sigma_i^2} = \frac{\alpha_i \eta_i(x, y)}{E_Q}$ . Then the final combined  $E_{\text{vis}}$  for a single detector becomes

$$E_{\text{vis}} = \frac{\sum_{i=1}^4 \frac{\alpha_i \eta_i(x, y)}{E_Q} E_{\text{vis},i}}{\sum_{i=1}^4 \frac{\alpha_i \eta_i(x, y)}{E_Q}} = \frac{\sum_{i=1}^4 \alpha_i \eta_i(x, y) E_{\text{vis},i}}{\sum_{i=1}^4 \alpha_i \eta_i(x, y)} = \frac{\sum_{i=1}^4 \alpha_i f_i(q)}{\sum_{i=1}^4 \alpha_i \eta_i(x, y)} \quad (3.15)$$

where we have used Equation 3.12 with  $q = (\text{ADC}_i - p_i(t)) \cdot g_i(t)$ . The uncertainty on the final weighted average above is given by

$$\delta E_{\text{vis}} = \frac{1}{\sqrt{\sum_{i=1}^4 w_i}} = \frac{1}{\sqrt{\sum_{i=1}^4 \frac{\alpha_i \eta_i(x,y)}{E_Q}}} \approx \sqrt{\frac{E_{\text{vis}}}{\sum_{i=1}^4 \alpha_i \eta_i(x,y)}}. \quad (3.16)$$

As pointed out in [Men14], the position map values only enter into the weighted average as part of the sum in the denominator and multiplied by the  $\alpha_i$  conversion factors, which is a smoother function of position than the individual position map values, and thus sensitivity to uncertainty in position map values  $\eta_i$  should be minimized.

### 3.5.2 $E_{\text{vis}}$ to $E_{\text{recon}}$

As mentioned in Section 3.1,  $E_{\text{vis}}$  is an estimate of the energy visible to the PMT from deposition in the scintillator. The more meaningful initial energy of the particle must be determined using a separate parameterization. To determine such a parameterization, simulated data is used so that the initial energies of the events are known precisely, and then the response of the detector to different event energies and types can be modeled.

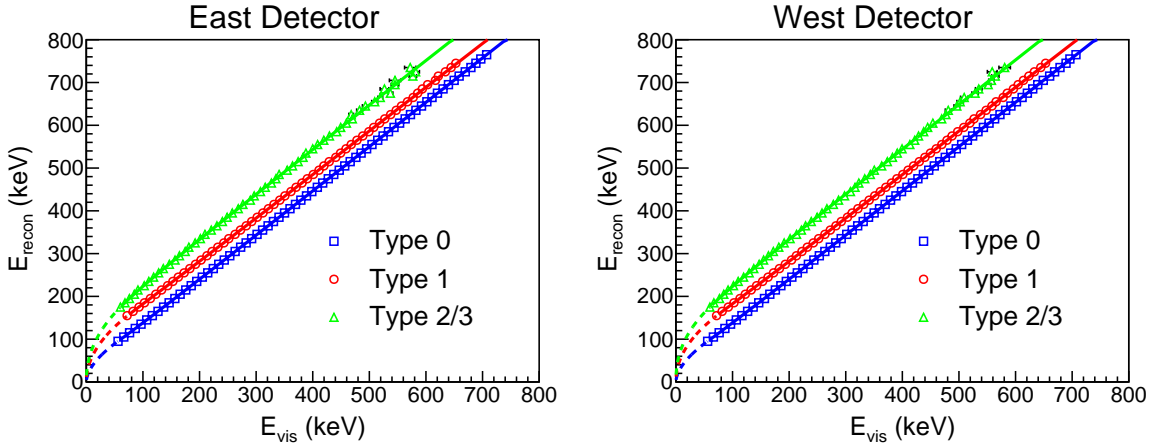


Figure 3.8: Parameterization between  $E_{\text{vis}}$  and  $E_{\text{recon}}$  for 2011-2012. The mapping for the other geometries are very similar and thus are not shown.

The mapping between  $E_{\text{vis}}$  and  $E_{\text{recon}}$  is determined separately for 2011-2012, 2012-2013, and 2012-2013 with isobutane in the wirechamber. Using the simulated  $\beta$ -decay spectrum and a characteristic set of detector response variables, the simulated events are processed in the same manner as they would be for data. They are identified as

Type 0,1, or 2/3, and their  $E_{\text{vis}}$  values for each detector are determined. Then the events are grouped into histograms using their initial energy (we will call it  $E_{\text{recon}}$ , but really this is the true energy of the events), with the histograms corresponding to 10 keV groups from 0 keV to 790 keV. Then each of these histograms are fit to determine the average  $E_{\text{vis}}$  value for a given  $E_{\text{recon}}$ . The results of these fits for each event type in each detector for 2011-2012 is shown as the data points in Figure 3.8. The other geometries look very similar and thus are left out. Data points with low statistics at low energies were dropped.

The fit to the data is of the form

$$E_{\text{recon}} = C_1 + C_2 E_{\text{vis}} + \frac{C_3}{E_{\text{vis}}} + \frac{C_4}{E_{\text{vis}}^2}, \quad (3.17)$$

and then the fit is extrapolated continuously to zero from the lowest energy data point using

$$E_{\text{recon}} = C_5 E_{\text{vis}}^{C_6} \quad (3.18)$$

with the parameters  $C_5$  and  $C_6$  determined by ensuring the two equations are equal at the transition point along with their first derivatives.

Using the fitted parameters, an  $E_{\text{recon}}$  value is determined for every event by plugging its weighted average  $E_{\text{vis}}$  into the proper equation. It should be noted that for Type 1 events, the visible energies of both the East and West detectors are added together when determining the parameterization, so the same is done when applying the above parameterization to data. This is done to utilize as much detector information as possible. The side for a Type 1 event is set to the detector with the earlier trigger, making it the primary detector. Thus, for a Type 1 event, one would plug  $E_{\text{vis}} = E_{\text{vis}}^E + E_{\text{vis}}^W$  into the  $E_{\text{recon}}$  equation for the side that triggered first.

## 3.6 Calibration Overview

In the next chapter, we will take an in depth look at the calibrations of both the wirechamber and the scintillator. Here we simply highlight their use in the analysis.

### 3.6.1 PMT Calibration

The PMT calibration, as mentioned in Section 2.4.3.3, uses well known conversion electron sources to understand the detector response to there well-defined energies. By comparing the detector response (coupling both ADC values and position map values) to simulated responses, we can map ADC signals from each PMT to visible

energies deposited in the scintillator. These calibrations parameterize the detector response so that the functional form of the calibration can be applied to the  $\beta$ -decay data.

### 3.6.2 Wirechamber Calibration

The wirechamber calibration relates the anode signal in the MWPC to an energy deposited in the MWPC. This is primarily useful for separating the Type 2/3 backscattering events, as the energy deposition in the MWPC is not used within the reconstruction of an electron's initial energy. This separation is important though as it drastically reduces the systematic correction for these backscattering events.

## 3.7 Polarimetry

The polarimetry analysis was carried out Eric Dees of North Carolina State University and deserves the attention of an entire dissertation itself. The previous polarimetry measurement is described in detail in a dissertation by Adam Holley [Hol+12b]. A major difference between the previous depolarization measurement and the current depolarization hinges upon the installation of the shutter between the spin flipper and decay trap. An update of the new polarimetry measurement method can be found in the publication of the result presented within this dissertation [Bro+17].

Here is a brief description of the polarimetry measurement. The polarimetry measurement determines the average neutron polarization in each spin state using the depolarization runs that follow every  $\beta$ -decay run. As detailed in section 2.3, the neutrons are initially polarized by traversing the 7 T primary polarizing magnet, and then the desired spin is chosen using the AFP spin flipper.

After a  $\beta$ -decay run, the depolarization run begins by closing the shutter and changing the switcher state to allow the UCN to flow into the switcher detector for measurement of UCN populations. The switcher signal as a function of time can be found in Figure 3.9. The guides are cleaned of UCN while the UCN population in the trap remains contained. Then the spin flipper state is changed allowing the neutrons that were trapped between the 7 T magnet and the decay trap to pass back through the high field region (these trapped neutrons result from UCN who underwent an unwanted spin flip after passing the high field region, subsequently keeping them passing the 7 T field). Now that the guides are cleaned, the shutter is opened and all UCN with spins not equal to the desired loaded spin are emptied (remember that

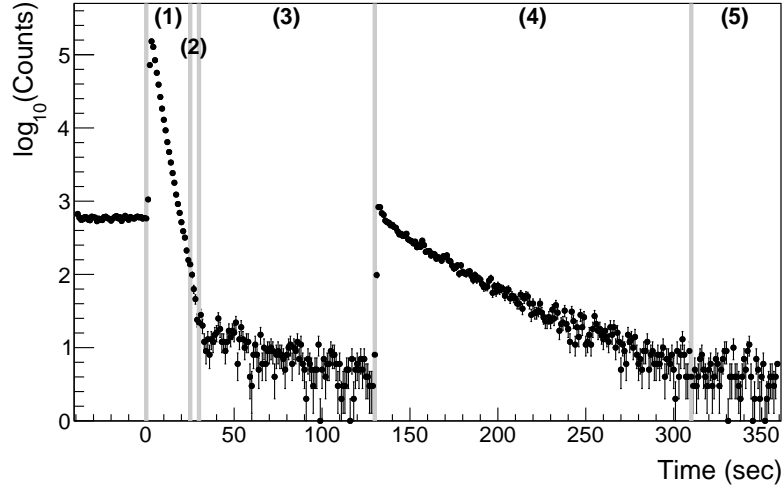


Figure 3.9: Figure courtesy of E. Dees and A. R. Young as published in [Bro+17]. “Switcher signal as a function of time, during “D”-type runs: (1) the shutter closes and the switcher state changes, permitting UCN in the guide outside the decay volume to drain to the switcher UCN detector, (2) the AFP spin-flipper changes state, allowing depolarized neutrons in the guides outside the decay volume to drain to the switcher, (3) the shutter opens, permitting depolarized neutrons within the decay volume to drain to the switcher detector, (4) the AFP spin-flipper returns to its initial state, allowing the initially loaded spin state to drain from the decay volume, (5) backgrounds are measured after the UCN population in the decay volume has drained away. The presented data were taken in 2011 and UCN loaded into the decay volume with the spin-flipper off.”

the spin flipper is switched from its original state). Once this population has been measured in the switcher detector, the spin-flipper state is again changed back to its original state, and the properly polarized UCN population is measured in the switcher detector. This process is followed by a short background measurement in the switcher detector.

The ratio of these populations is then extrapolated back to the equilibrium population as established during  $\beta$ -decay running by utilizing further *ex situ* measurements and comparisons with simulation. The results of these measurements as well as the correction to the uncertainty resulting from imperfect polarization ( $P < 1$ ) can be found in Section 5.2.3.

Copyright<sup>©</sup> Michael A-P Brown, 2018.

# Chapter 4

## UCNA Calibrations

Detector calibrations are a beautiful combination of simulation and data manipulation which allows one to extract the energy of an event based solely on some electronic signal. Imagine a baseball pitcher throwing a fastball into a sheet, and the observer behind the sheet must determine the velocity of the ball from only seeing the impression the pitch made on the sheet. This is the task every nuclear physics experiment is faced with, only the baseball is a particle and the sheet is our detector system. Below we focus on the energy calibration of our apparatus.

This chapter will begin by discussing the position reconstruction algorithm, which relies on signals from the wirechamber (MWPC). Then we will describe the energy calibration of the scintillators which utilizes the position of the events, as each individual PMT response is highly position dependent. Last of all, an energy calibration of the wirechamber will be discussed, which, while not imperative to the analysis, provides the ability to distinguish between a Type 2 and Type 3 backscattering event more effectively.

### 4.1 Wirechamber Position Reconstruction

#### 4.1.1 Wirechamber signals

The wirechamber signals for each detector include a summed anode signal, and two collections of cathode signals consisting of 16 individual “wire” readings. Again we use the term wire loosely, as there are technically 64 wires in a plane, but they are read out in groups of four. The position of each wire group is taken to be the midpoint of the grouping (between the two center wires). The two sets of cathode signal collections come from perpendicular planes, so the position can be reconstructed along both the

$x$ -axis and  $y$ -axis.

The signal is read out by a peak sensing ADC, so the maximum value of the signal is recorded for each event. The pedestal is determined using the bismuth pulser events (different from the PMT pedestals) and is subtracted from the ADC signal for every event. For the cathodes, a software threshold for each wire is set at 100 channels above pedestal, so only wires above this threshold will be used in the position reconstruction.

#### 4.1.1.1 Wirechamber trigger

As mentioned in sections 2.4.3.1 and 2.7, a wirechamber software trigger is set and used to eliminate the gamma background and to identify different backscattering events. One could use either the summed anode signal or a signal formed from the cathode signals. The best trigger is one that separates the pedestal furthest from the triggering data. For this analysis, this was found to be the sum of the maximum cathode signals from the two wire planes. (Add figure of the two signals?)

#### 4.1.1.2 Cathode wire clipping

Low energy events deposit a substantial amount of energy in the MWPC, and thus create large signals in one or more wires in cathode planes. This can create a signal which is beyond the range of the ADC, producing an overflow event which is read out as the max value of the ADC regardless of how much actual charge was deposited in the wirechamber. These events are called “clipped” events. A plot of the typical ratio of clipped events and the number of clipped wires can be seen in Figure 4.1.

A clipped event poses a problem in the position reconstruction because the true signal is no longer known, only that it was above the maximum ADC value. Using this wire in the position reconstruction will not properly account for the strength of the signal at the position of the clipped wire.

### 4.1.2 Wirechamber position reconstruction

Determining the position of the spiraling electrons is vital for every component of the analysis that follows. Before now, the gain, pedestals, and trigger thresholds are determined with no knowledge of the position of an event, but rather basic trigger logic. As will be seen in the Section 4.2.2, the actual response of the PMT is position dependent, and so we introduce the position reconstruction algorithm now.

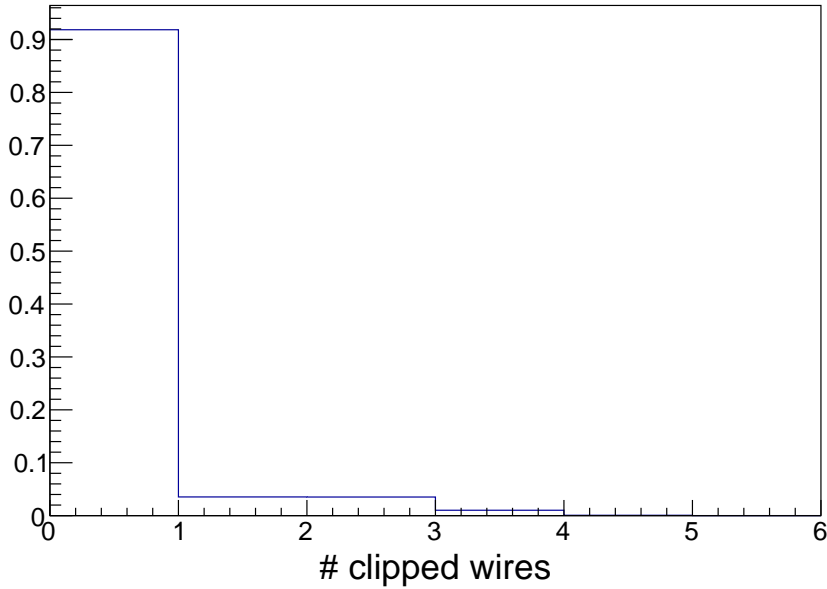


Figure 4.1: Number of clipped wires in the  $x$ -plane of the East detector. Most of the events (92 %) exhibit no clipping.

#### 4.1.2.1 Events with no cathode clipping

The algorithm developed for reconstructing the positions of the events for this analysis is meant to be as simple of possible, with more complex measures taken for special events. If we have an event that passes through the MWPC, creates a software trigger, and has no clipped wires, then the position is calculated as the average position of the signals:

$$\bar{x} = \frac{\sum q_i x_i}{q_i}, \quad (4.1)$$

where the sum runs over wires above the individual pedestal subtracted threshold,  $q_i$  are the pedestal subtracted wire signals, and  $x_i$  are the positions of the wires. This can be interpreted either as a weighted average of the wire positions with the weights equal to the wire signals, or it can be seen as a simple average where each unit of the signal is seen as an event entering into the average with a value equal to the wire position. The final position of the event is then given by  $(\bar{x}, \bar{y})$ , where  $\bar{y}$  is calculated in the same manner.

For well-behaved wires (no clipping, no missing or “dead” wire segments), this method produces a continuous reconstruction of the events based on where they pass through the wirechamber. An example of the position dependence can be seen in Figure 4.2.

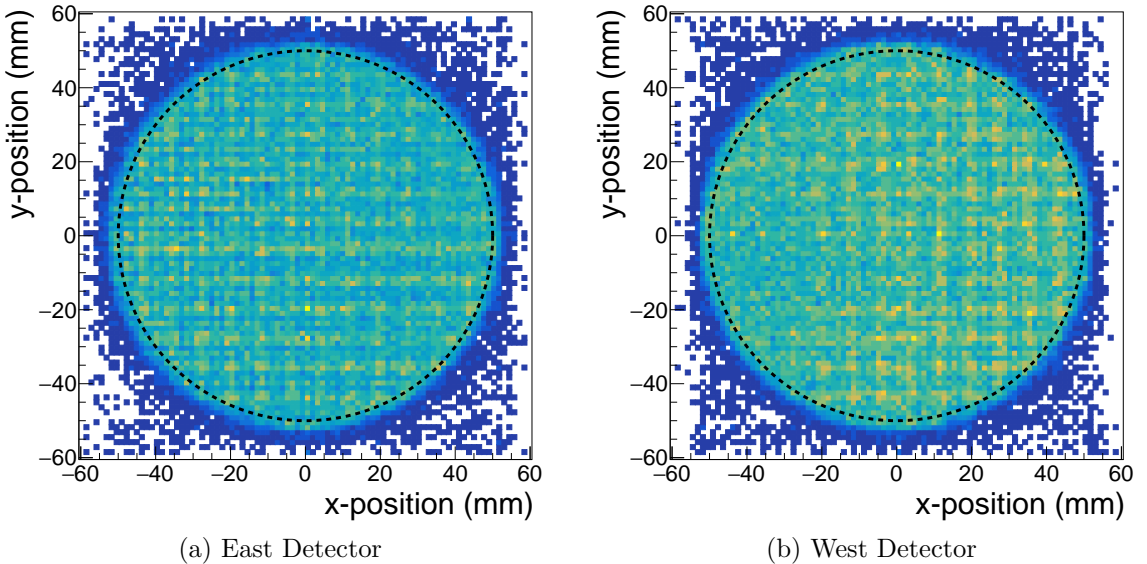


Figure 4.2: Wirechamber reconstructed positions for all electron events in a single octet of  $\beta$ -decay data. The black dashed line indicates the 50 mm fiducial cut applied to the data during asymmetry extraction.

#### 4.1.2.2 Events with cathode clipping or missing wire signals

In the event of a clipped wire or the rare case of a missing wire signal, the basic average method shown above will not suffice. Using the clipped wire in the average can systematically shift the reconstructed position if the signal is not symmetric about the clipped wire, and the same can be said of a missing signal. While this may not appear as a visible distortion to the position distribution, the method loses its integrity.

To handle these types of events, a method similar to that used in the previous analysis [Men14] was adopted. By assuming that the wirechamber charge cloud (or ionization cloud) takes a Gaussian shape in the MWPC, we can expect that the signals in the wires should also sit on a Gaussian given by

$$q = N e^{(x-\bar{x})^2/\sigma^2}, \quad (4.2)$$

where  $q$  is the signal as a function of position,  $x$  is the position of the signal, and  $N$

is a scaling parameter. If we take the log of this expression we have

$$\ln(q) = \ln(N) + \frac{(x - \bar{x})^2}{\sigma^2} \quad (4.3)$$

$$\ln(q) = \frac{1}{\sigma^2}x^2 - \frac{2\bar{x}}{\sigma^2}x + \left( \ln(N) + \frac{\bar{x}^2}{\sigma^2} \right) \quad (4.4)$$

$$\ln(q) = Ax^2 + Bx + C \quad (4.5)$$

with

$$A = \frac{1}{\sigma^2}, \quad B = -\frac{2\bar{x}}{\sigma^2}, \quad C = \ln(N) + \frac{\bar{x}^2}{\sigma^2}. \quad (4.6)$$

This equation has three unknowns, thus with three “good” wires giving three points on the Gaussian, the unknowns are fully determined. The three chosen wires are the maximum non-clipped wire and the next two largest signals surrounding this maximum signal. These two wires can be on one side of the maximum wire, as would be the case if the maximum wire were the edge wire. The extraction of the mean is the approximation of the center of the event.

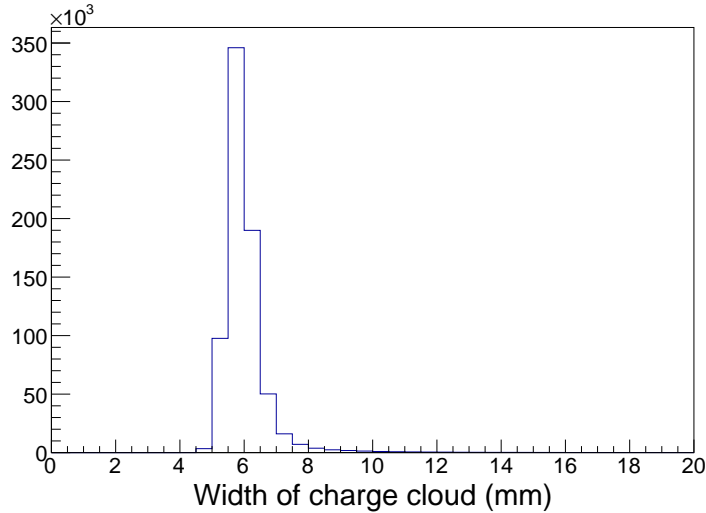


Figure 4.3: Collection of extracted  $\sigma$  values for the Gaussian determination of event position. The average of this distribution is an estimate of the characteristic width of the wirechamber charge cloud,  $\sigma_c$ , used when only two wires are usable in the position reconstruction.

Now there is also the special case where there are only two usable wires above the individual cathode wire threshold. If they are consecutive wires, the average method is applied, but if they are not consecutive wires (so they are separated by a clipped wire(s)), a new approximation must be applied. The expression in equation 4.3 requires three wire signals to estimate a position, so we must eliminate one of the unknowns to use this method. Again, if we assume that all signals follow a typical

Gaussian shape, then the width of the charge cloud should be roughly constant. Thus we can determine a characteristic width,  $\sigma_c$ , from the mean extracted  $\sigma$  from the rest of the events (including the non-clipped events). A histogram of the extracted  $\sigma$  values can be seen in Figure 4.3. A value of  $\sigma_c = 6$  mm was used for these type events, and then the mean was calculated by solving 4.3 with two unknowns.

Last of all, there is the situation where only one wire was above the individual threshold. For this type of event, the only reasonable choice is to set the position of the event to the position of this wire.

### 4.1.3 Simulation of wirechamber positions

In order to reduce any unforeseen systematic effects, an attempt at including every aspect of the experiment within the simulated data is made. Thus for the wirechamber position reconstruction, we would like to employ the methods outlined above for every simulation event also.

Embedded within the simulation by M. Mendenhall during the previous analysis is a model for the charge collection within the wirechamber based on the work from [Mat91]. In summary, based on the wirechamber geometry, an estimate of the charge cloud as seen by the cathode and anode can be calculated for an event that deposits energy  $E_{\text{MWPC}}$  in the wirechamber. The agreement between data and simulation was shown to be good ([Men14] section 6.3.6), and thus the charge collection model was used in this analysis.

A new contribution to the model is the application of the observed wirechamber thresholds and clipping conditions to each of the cathode wires. The model already included is simply an estimation of the charge collection on the range from 0 to  $\infty$ . This could be used in the simple average method for “good” events with no clipping and no missing wires, but then any systematic effects from wire clipping would go unnoticed.

#### 4.1.3.1 Wire model

For each wire in each plane, the response can be characterized by two values: a clipping threshold and a trigger threshold. Recall that we apply an individual software trigger threshold of 100 ADC channels for each wire, so a model parameter must be determined for this. Also, in the simulation model, the signal on each cathode is not bound, so an artificial clipping parameter must be introduced.

To determine the trigger threshold  $E_T$  for a single cathode wire in a given plane, the ratio of events with signal above the software trigger threshold for that wire to the total number of electron events identified by that detector is calculated as

$$R_T = \frac{N_T}{N_{ALL}}, \quad (4.7)$$

where  $N_T$  indicates “trigger” events and  $N_{ALL}$  refers to the total number of electron events.

Then for the corresponding simulation of this wirechamber cathode wire, the trigger threshold  $E_T$  is applied starting at  $E_T = 0.01$  keV and the same ratio as above is calculated for the simulation,  $R_T^{\text{sim}}$ . The threshold is incrementally increased by 0.01 keV and the ratio is recalculated until  $R_T^{\text{sim}} = R_T$ . The value for  $E_T$  is saved for application within the new simulation model.

Now with the knowledge of the low energy threshold, a similar method for the high energy clipping threshold  $E_C$  can be applied for this wire. The ratio of events from data becomes

$$R_C = \frac{N_C}{N_T}, \quad (4.8)$$

so that this is now the ratio of clipped events to triggered events for the wire of interest. Then within the simulation, the clipping threshold can be scanned down from an arbitrarily high threshold until  $R_C^{\text{sim}} = R_C$ . It was found that starting the clipping threshold at  $E_C = 9$  keV and incrementing by  $-0.1$  keV provided nice enough agreement while not using exceptionally high computation times, as this process is carried out for every wire grouping (64/run) in every  $\beta$ -decay run ( $\sim 1000$ ).

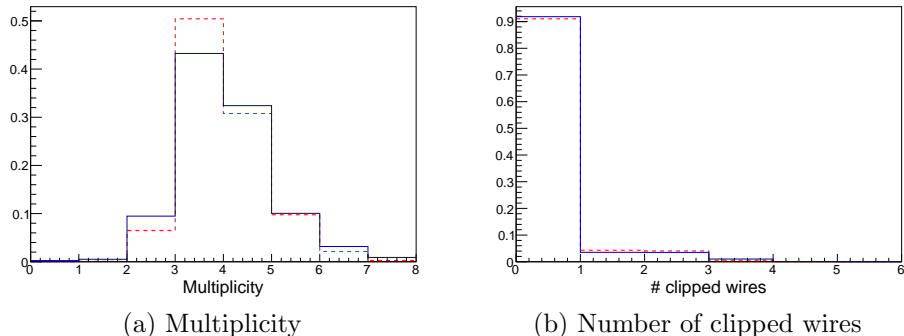


Figure 4.4: Comparisons between data (blue line) and simulation (red dashed line) after the application of the single wire trigger and clipping model. There is a discrepancy in the multiplicity, but the general features are captured. The number of clipped wires in data and simulation is in better agreement.

#### 4.1.3.2 Results of individual wire model

The agreement between data and simulation from application of the trigger threshold can be seen in Figure 4.4 a.), where the multiplicity of triggered wires for both data and simulation is shown. Without the the application of a nonzero individual trigger threshold, the multiplicity would generally be much higher for the simulation.

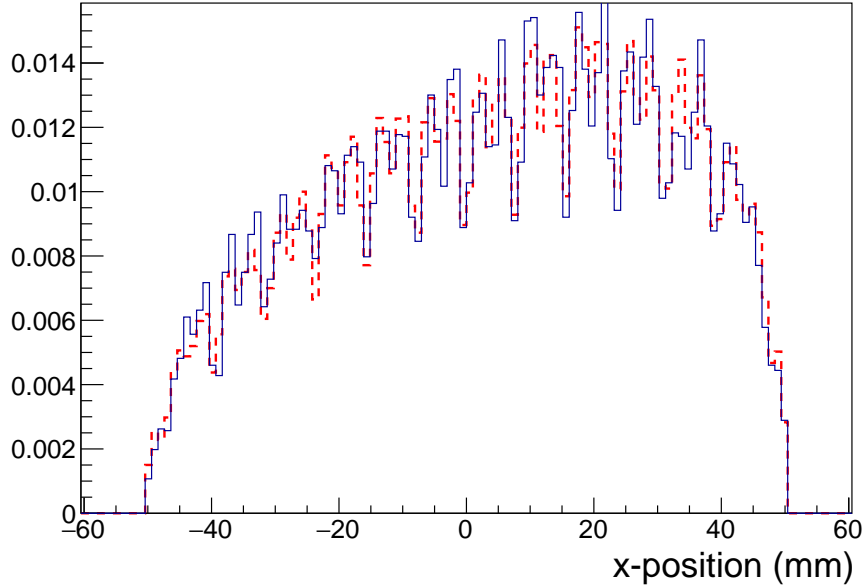


Figure 4.5: Position dependence of clipped events for data (blue line) and simulation (red dashed line) after the application of the single wire trigger and clipping model to the simulation. The model captures the position dependence of the clipping nicely.

The application of the clipping threshold to the simulation also provides nice agreement as seen in Figure 4.4 b.). More importantly, the position dependence of the clipped events is properly accounted for in the simulation as shown in figure 4.5.

With these effects accounted for within the simulation, effects regarding position reconstruction should be accounted for within the systematic corrections. Any subsequent MWPC systematic effects from the efficiency of the MWPC trigger described in section 4.1.1.1 is accounted for separately as will be shown in Section 5.2.6.1.

## 4.2 Scintillator Energy Calibration

### 4.2.1 Method

The goal of the energy calibration is to provide a means for taking as input an ADC value from a PMT and returning as output an estimate of the energy deposited in the

scintillator to which the PMT is coupled. For a given event, one will have up to four estimates from a single detector from the four PMTs on each side (less than four if a PMT is not functioning properly). Then, given the event type and the method for combining multiple PMT responses in Section 3.5, we can produce a single estimate of the initial energy of the event.

The energy calibration is briefly highlighted in Sections 2.4.3.3 and 3.6.1. Figure 2.6 nicely depicts in a cartoon how the conversion electron sources are translated across the detector face using a source paddle. The different source locations sample different regions of the PMT light transport maps, thus providing markedly different PMT responses from an individual source. This allows one to characterize the ADC response to a broad range of light exposure using only three conversion sources. The entire process takes place without breaking vacuum, so the calibrations can be done intermittently during  $\beta$ -decay running.

Up to this point, the parameters that enter the calibration have been well-defined and only need to be determined once (pedestals, gain, event positions, etc.). To determine the relationship between the ADC response in a PMT and the energy deposited, we instead turn to a cyclical process which depends on both the relationship between ADC and the scintillation light that reaches a PMT, what we will call the linearity curves, and the PMT resolution factors  $\alpha_i$  (first introduced in Section 3.5.1), which relate the number of photoelectrons produced by a PMT to the incoming light from an event. While the data inherently includes the resolution factors given the observed widths of the source peaks, the detector response model takes the resolution factors as input, and therefore the linearity curves, which compare simulation to data, depend on the  $\alpha_i$  values. An easy way to determine the  $\alpha_i$  values is to compare the observed calibrated data peak widths to the simulated widths, wherein lies the problem that the data needs to first be calibrated. To mitigate this inherent dependence of one aspect on the other, we simply guess at an initial set of calibration parameters (both the linearity curves and resolution factors for each PMT), and then we analyze the resulting simulated peak widths with respect to the calibrated data peak widths. By tweaking the  $\alpha_i$  values in such a way as to create better agreement between simulation and data peak widths, the simulation data can then be re-processed in the detector response model, and we can calculate a new set of linearity curves. This process is repeated until the agreement is satisfactory, as will be discussed in the upcoming sections.

One last component that was left out of the above cyclical discussion is the determination of the position dependent response of each PMT to events that occur

at different  $(x, y)$  locations of the scintillator. In the past, these position dependent light transport maps were also part of the cycle, as they were determined from an  $E_{\text{recon}}$  spectrum of xenon which is dependent on the calibration, but in this analysis we decided to make a single determination of the position dependent response. The position dependent response is thus another “well-defined” input parameter of the calibration and is the topic of the next section.

In general, the entire scintillator energy calibration process proceeds as follows:

- Determine the position dependent light transport maps for each PMT,  $\eta_i(x, y)$ .
- Approximate the PMT resolution factors,  $\alpha_i$ .
- For each source peak in a given calibration period,
  - Fit the ADC peak from the data.
  - Apply the detector response model to the simulation to emulate the data taking conditions.
  - Fit the  $E_{\text{vis}}$  peak from the simulation.
- Relate the ADC peaks to the simulation  $E_{\text{vis}}$  to produce an energy calibration.

Every step beyond the first is then repeated to converge on the best approximation of the resolution factors and linearity curves.

### 4.2.2 Position Dependent Light Transport Maps

As mentioned in the experimental description, each PMT is coupled to a quadrant of the scintillator and collects the most light from this quadrant. The light collection is therefore position dependent, and an individual PMT will receive a different amount of light for an event of energy  $E_i$  depending on where that event strikes the scintillator. To properly map the PMT signal to energy, this position dependence must be accounted for on a PMT-by-PMT basis. The collection of values that correct for this dependence will often be called position maps from here on.

#### 4.2.2.1 Activated Xenon

To map the position response of the scintillator, signals must be present across the entire face of the detector. The  $\beta$ -decay spectrum is an obvious option as the UCN fill the entire decay volume, and was used for these position maps prior to 2010, but the event rate is low when divided into small position bins across the scintillator.

Prior to running in 2010, a method using activated xenon was developed to provide a higher event rate with the required full fiducial coverage.

The xenon is activated by placing a small amount of natural xenon in the volume that normally holds the  $\text{SD}_2$  source, freezing it, and then exposing it to the moderated neutron flux for several minutes. This produces a plethora of radioactive isotopes with various half-lives. The xenon is then warmed up to a gas and stored. The gas is then released into the spectrometer during position mapping periods, and the decay products are detected [Men14]. The various radioactive isotopes provide several features to fit for comparison with one another across the entire detector surface.

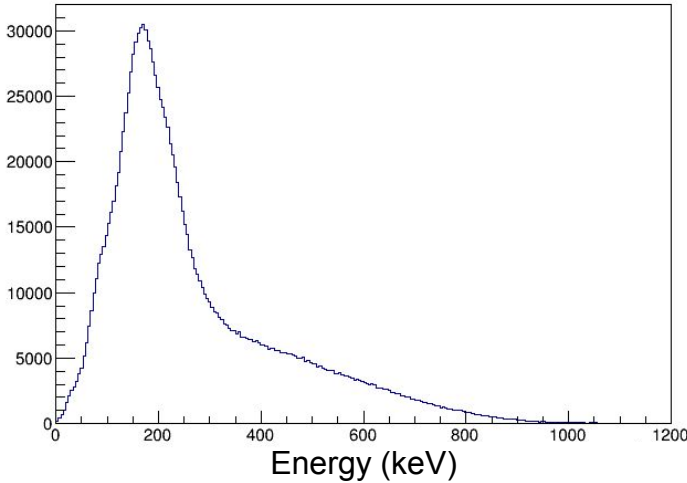


Figure 4.6: Example energy spectrum of the neutron-activated xenon used for position map determination.

The spectral shape of the activated xenon changes with time due to the different half-lives of the isotopes, but this is not a concern as the PMT will see the same shape at all positions across the detector, just with different ADC scales due to the position dependence of the light collection. Therefore one only needs to choose a feature of the spectrum to fit in different positions to map the relative response.

#### 4.2.2.2 Position Maps

The scintillator is divided into a grid of  $5 \times 5 \text{ mm}^2$  squares (in the 1 T decay trap coordinates) with one square directly in the center, and the xenon events are collected for each of these “pixels”. A key feature from the spectrum is then chosen and fit in every pixel, with the position dependent response factor in pixel  $i$  for a single PMT

defined as

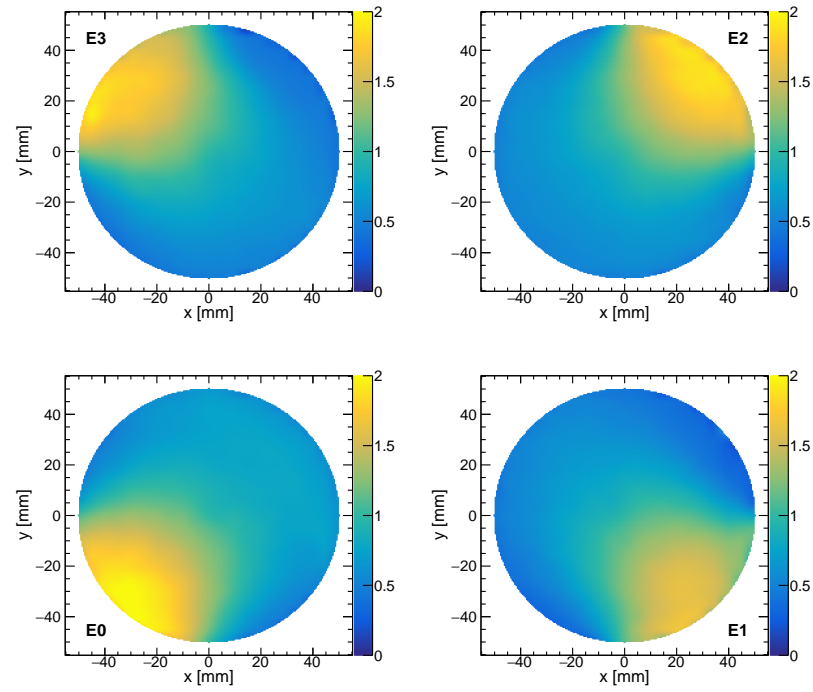
$$\eta_i = \frac{Q_i}{Q_0}, \quad (4.9)$$

where  $Q_i$  is the fitted ADC value of the feature in pixel  $i$  and  $Q_0$  is the fitted ADC value of the feature in the center pixel. This normalizes the position response for a PMT to the center pixel. The position response at some position  $(x, y)$ , referred to as the continuous variable  $\eta(x, y)$ , is then calculated via a two-dimensional Catmull-Rom cubic interpolating spline [CR74]. The same interpolation is used to produce the smooth plots of the position dependence in Figure 4.7.

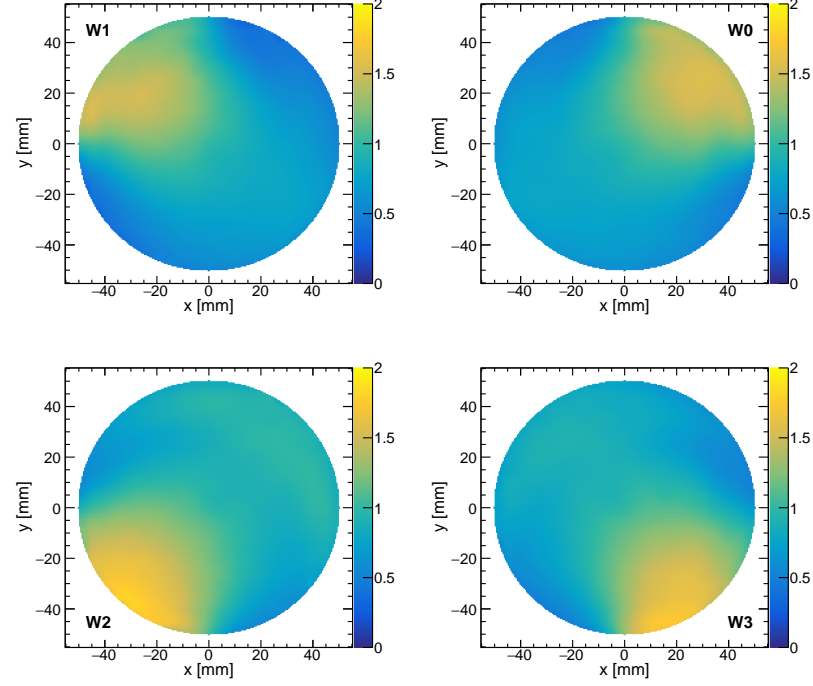
A typical xenon energy spectrum can be seen in Figure 4.6. The two obvious features one could fit are the peak between 100 keV and 200 keV or the 915 keV  $\beta$ -decay endpoint. The peak is a superposition of several isotopes, while the endpoint comes from the  $^{135}\text{Xe}$   $\frac{3}{2}^+$  isotope. The position maps are fit in terms of pedestal and gain corrected ADC, so unfortunately the luxury of knowing an initial guess for the feature position is not afforded as it would be if the fit was done in the energy domain. This makes fitting the peak more reliable upon first inspection, as the endpoint fit (done via a Kurie plot as described in Section 3.2.2.2) is more sensitive to the range of the fit, especially when the spectrum is not purely a  $\beta$ -spectrum. There is a problem with using the peak though, as areas with low light collection for a given PMT lose a portion of the peak below the trigger threshold. This changes the feature shape compared to regions of higher light output, thus biasing the position map. The better choice is then the  $^{135}\text{Xe}$   $\frac{3}{2}^+$  endpoint.

The problem with fitting the endpoint in pixels with different light collection efficiencies is illustrated by imagining that every pixel sees the same xenon energy spectrum (as in Figure 4.6), but that the spectrum is compressed or stretched when compared to the spectrum in the center pixel depending on where the pixel is located. Since each pixel has the same ADC range, choosing the proper fit range becomes difficult as it is different in every pixel. To avoid this issue, a secondary feature was derived to be used as a seed to the endpoint fit range. This secondary feature is calculated by first fitting the peak with a Gaussian and extracting the mean ( $\mu$ ) and sigma ( $\sigma$ ), and then calculating the average ADC value,  $\xi$ , of the spectrum from  $\mu + 1.5\sigma$  and beyond. Then the endpoint fit is done over the range  $(\xi, 2\xi)$ . The range used to calculate  $\xi$  and the range over which the endpoint were fit were determined via trial and error, and produce consistent results across the entire detector.

It should also be noted that the position maps were calculated using both the peak and the endpoint as the key feature, and the differences are noticeable for the



(a) East Detector



(b) East Detector

Figure 4.7: Typical set of position maps from a xenon position mapping period. The position maps remain fairly constant throughout the two run periods.

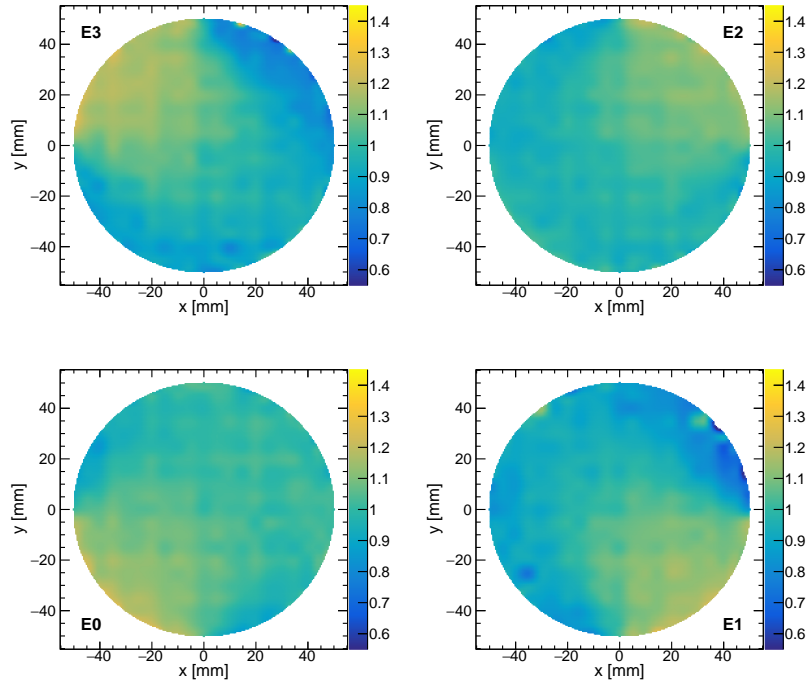


Figure 4.8: Ratio of  $\eta_{\text{peak}}/\eta_{\text{endpoint}}$  for the East side PMTs. The differences are most pronounced in areas of high and low light collection. The West side shows more consistency when comparing maps calculated using the different features.

East detector. This is illustrated in Figure 4.8, where the ratio of the two methods is plotted.

### 4.2.3 Linearity Curves

After determining the position dependent light transport maps for each PMT, the next step in the scintillator energy calibration process is relating a gain and pedestal subtracted ADC signal to an energy. In our case, we choose to relate the signal as seen in a single PMT to a quantity that is proportional to the light that would have reached the PMT. This quantity is of course related to the deposited energy by the position response factor, and thus we calibrate to  $\eta_i(x, y)E_{\text{vis}}$ , where  $E_{\text{vis}}$  in this case comes from simulation.

#### 4.2.3.1 Fitting the source peaks

Typical single PMT energy spectra for simulation and data from the  $^{137}\text{Ce}$ ,  $^{113}\text{Sn}$ , and  $^{207}\text{Bi}$  sources can be found in Figures 4.13, 4.14, and 4.15 respectively. These

spectra were produced using the final calibration, and at this point should only be inspected for their general shape to understand the type of fit required.

An iterative peak fitting procedure like that from Section 3.2.2 is used to extract the final mean of each peak to be used in the calculation of the linearity curves, where the fit is performed five times taking the previous mean and sigma as input parameters for the next fit. For the  $^{137}\text{Ce}$  and  $^{113}\text{Sn}$  sources, which have a single electron peak, a single Gaussian with an asymmetric fit range extended farther above the mean is used. Again this is to weight the fit more heavily on the portion of the spectrum which exhibits the most Gaussian-like structure. The lower tail of the energy distribution has a contribution from events detected that have lost energy elsewhere in the spectrometer and is thus broadened compared to the upper tail. For the  $^{207}\text{Bi}$  source, the two Gaussian peaks are fit simultaneously by the summation of two Gaussian functions, so that the effect of one on the other is taken into account by the fit, and the proper mean is extracted from each. This helps remove effects from possible use of inaccurate resolution factors.

#### 4.2.3.2 Extracting the PMT response

As mentioned above, we calibrate the PMT ADC response to a quantity proportional to the light incoming into the PMT, or  $\eta_i(x, y)E_{\text{vis}}$ , so we need to plot  $\eta_i(x, y)E_{\text{vis}}$  vs. ADC response. Above we described how we fit the mean of the expected visible energy  $E_{\text{vis}}$  from simulated spectra and the observed ADC response for each PMT. The value of  $\eta$  used for each source peak is determined from the average position of the events in the peak. For each source calibration run period, all of the data points are plotted for each PMT and the response is fit with a quadratic response function,

$$f(x) = C_1 + C_2x + C_3x^2, \quad (4.10)$$

where  $x$  is the gain corrected ADC signal and  $f$  is equivalent to  $\eta(x, y)E_{\text{vis}}$ . The quadratic term is constrained to  $|C_3| < 7.5 \times 10^{-5}$ , which is small compared to  $C_2 \approx 1$ . The  $C_1$  offset allows for imperfections in the pedestal subtraction. If the pedestal subtraction were perfect, one would expect  $C_1 \approx 0$ . Allowing  $C_1$  to be a free parameter generally produces better Monte Carlo to Data agreement at low energies.

Example calibration fits for a single calibration run period in 2011-2012 are illustrated in Figures 4.9 and 4.10 for the East and West PMTs respectively. Beneath each calibration plot are the calibration residuals for each data point compared to the fit line reported as a percent residual. The parameters of each linearity curve are written to file to be accessed when applying the calibration to data.

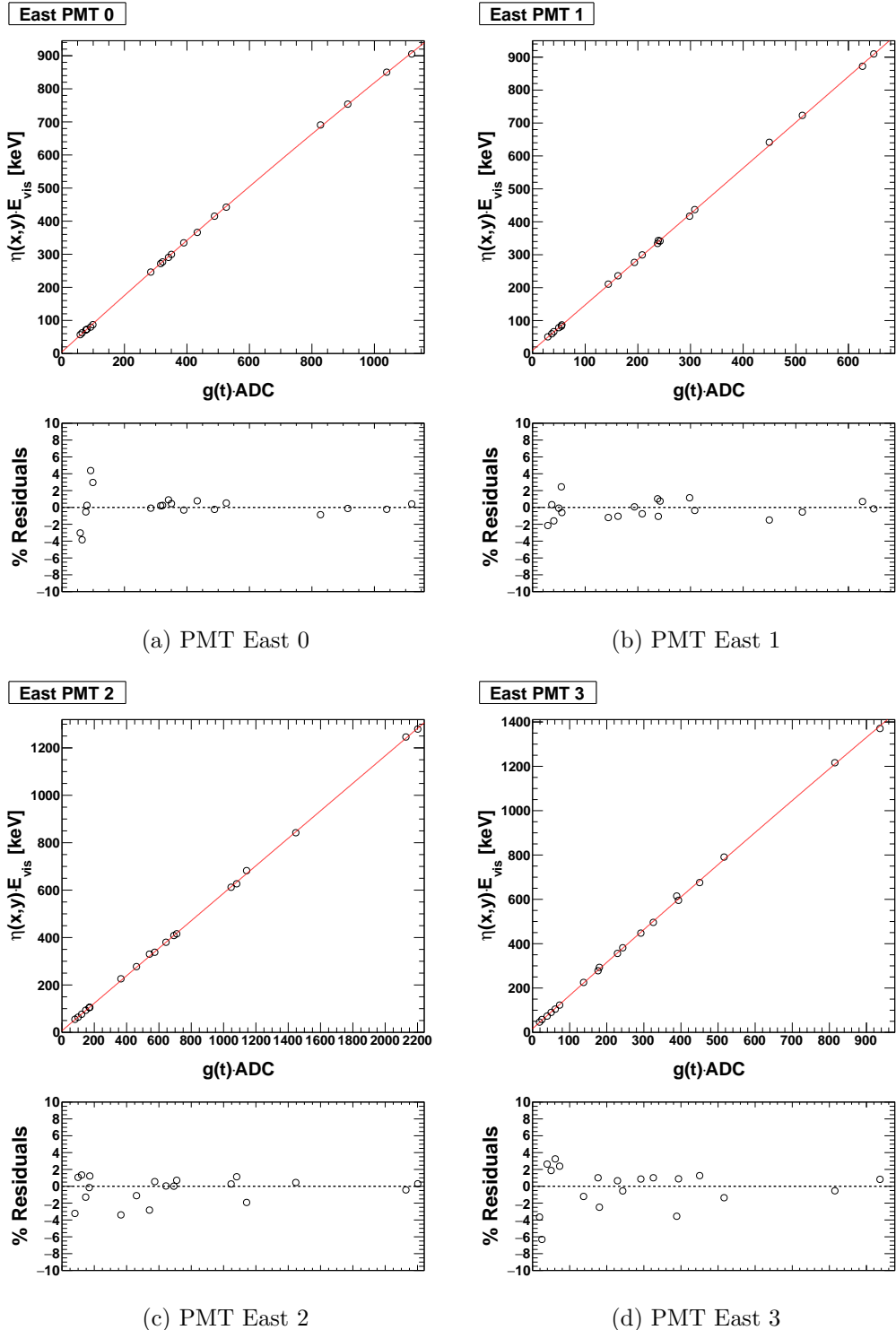


Figure 4.9: East linearity response curves for a single calibration run period in 2011-2012. The residuals reported are calculated as  $100 \times (fit - data)/fit$ . The error bars on the points are the error on the extracted mean from the fits of the data and simulation peaks, but they are smaller than the markers.

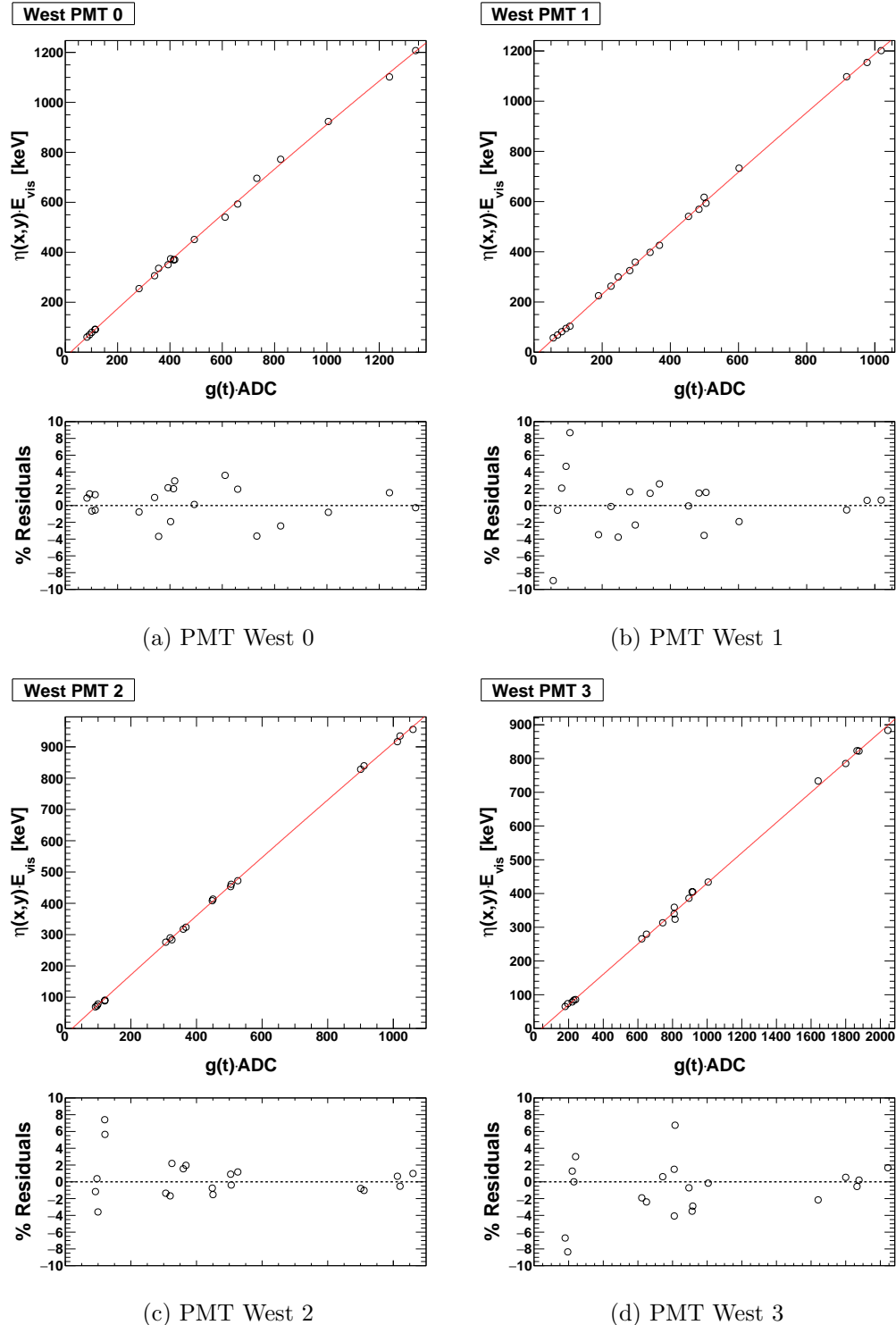


Figure 4.10: West linearity response curves for a single calibration run period in 2011-2012. The residuals reported are calculated as  $100 \times (fit - data)/fit$ . The error bars on the points are the error on the extracted mean from the fits of the data and simulation peaks, but they are smaller than the markers.

#### 4.2.4 PMT Resolution Factors

The PMT resolution factors are key inputs into the detector response model, making them especially important to the calibration. They directly affect the observed width of the simulated conversion electron peaks, and improper simulated peak widths present a possible bias in the calibration by changing the shape of the peak being fit.

As mentioned earlier, a “guess” is made for the initial resolution factors for the first iteration of the energy calibration. This guess is set to a higher resolution for each PMT than is typically observed so that the simulation peaks do not suffer from extreme broadening which can make fitting unreliable, especially for the double Gaussian peak of  $^{207}\text{Bi}$ . After the calibration curves are determined, we can assess whether or not the resolution factors are correct for each individual calibration run period. This involves comparing the widths of the data peaks to the widths of the simulation peaks, both in the energy domain. The widths of the simulation peaks come directly from the fits used in calculating the linearity curves, as the simulated  $E_{\text{vis}}$  spectra were already fitted, but recall that the PMT ADC spectra were used in determining the linearity curves. Thus, in order to extract the data  $E_{\text{vis}}$  widths, the energy calibration for each run period must be applied to the conversion electron events themselves (the method for applying the calibration is briefly described in the following section). This provides  $E_{\text{vis}}$  spectra for each PMT as well as an  $E_{\text{recon}}$  spectrum from the combination of the individual PMT energies.

With the source widths from both the data and simulation in hand, we plot the simulated widths vs. the data widths. If the resolution factors are correct, there will be a 1:1 ratio of the peaks. On the contrary, if the  $\alpha_i$  values are incorrect, the slope of the relationship indicates whether or not the resolution is set too high or to low. Figure 4.11 exemplifies the desired relationship between the simulation and data peak widths. The slope is extracted from a linear fit, and this is carried out for each PMT in a calibration period. The data points represent every source run in the respective source calibration period.

A slope of  $\sim 1$  is not achieved after one iteration of the calibration, but rather several. After extracting the slopes,  $m_i$ , for each PMT following an intermediate iteration of the calibration, a new set of resolution factors are determined in the same manner as in the previous analysis, namely from

$$\alpha_i = m^2 \alpha'_i, \quad (4.11)$$

where  $\alpha'_i$  are the new estimates for the resolution factors.

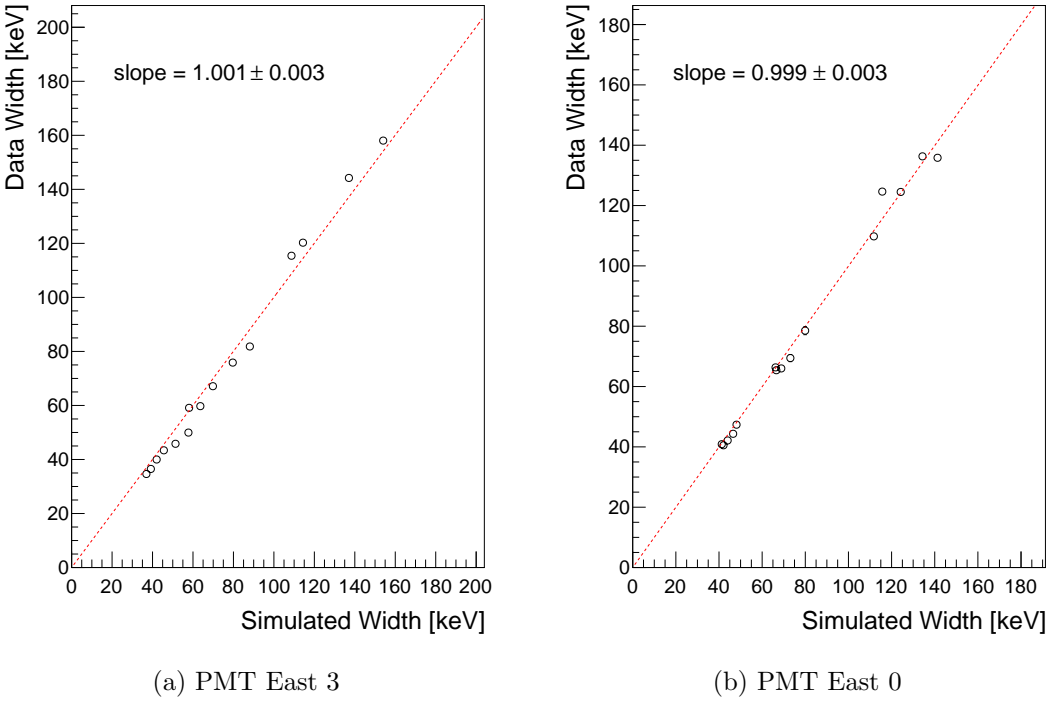


Figure 4.11: Plots of the data source widths vs. the simulated source widths for a single PMT on each side of the detector used for determination of the proper PMT resolution factors. When the slope  $\approx 1$ , the resolution factors are recorded to be used in the final calibration.

Once the slopes approach unity for all PMTs, the resolution factors are recorded and the linearity curves are calculated as the last step so that they use the best  $\alpha_i$  values. This completes the calibration, and at this point final  $E_{\text{recon}}$  spectra for each source peak exist. The widths of these spectra, which are the culmination of all of the PMT information combined, provide a idea as to how well the final combined widths agree between simulation and data. Figure 4.12 shows this agreement for a single run period.

#### 4.2.5 Applying the calibration

Application of the calibration to an electron event of any kind requires first reading from the collection of calibration variables for each PMT: the position dependent response (interpolated to the exact position of the event), the resolution parameters  $\alpha_i$ , and the linearity curve parameters  $C_1$ ,  $C_2$ , and  $C_3$ . Then, by inserting the gain corrected ADC response of each PMT into Equation 4.10 with the proper parameters, the linearity curve returns an estimate of the scintillation light as viewed from a

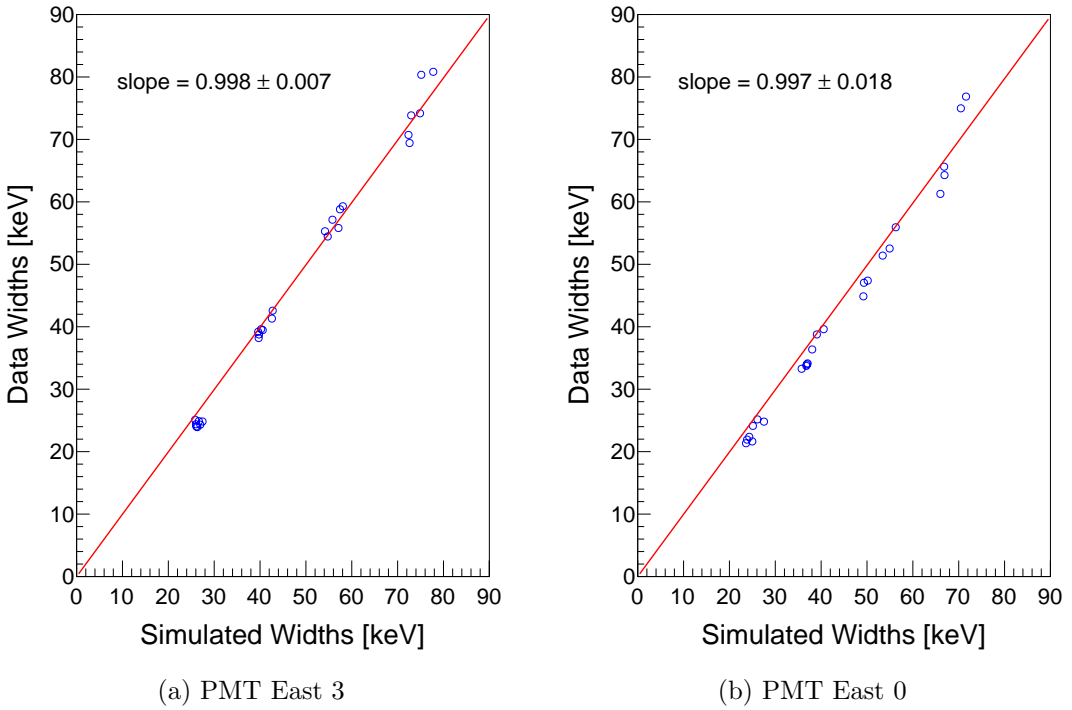


Figure 4.12: Plots of the data source widths vs. the simulated source widths for the final  $E_{\text{recon}}$  source spectra on each side of the detector. This is a measure of how well the individual PMT resolution factors combine to produce agreement between the final reconstructed energy spectra. The slopes of nearly unity indicate the final detector resolutions were very good for this calibration period.

given PMT. To reach an estimate of  $E_{\text{vis}}$  from the returned value  $f$  (remember that  $f = \eta(x, y)E_{\text{vis}}$ ), one simply divides by the position map value for that event. With a value for  $E_{\text{vis}}$  from each PMT, a final  $E_{\text{recon}}$  value is constructed using the methods of Section 3.5.1, which rely on  $\alpha_i$ . Examples of the individual calibrated PMT responses for simulation and data can be found in Figures 4.13, 4.14, and 4.15. These spectra came from a single calibration run that included all three sources within the fiducial volume at the same time.

#### 4.2.6 Monte Carlo to Data Agreement

A final measure of the agreement between Monte Carlo and data is best observed by comparing the  $E_{\text{recon}}$  spectra of the data (after applying the calibration) to the  $E_{\text{recon}}$  spectra of the simulation (with the full detector response model applied). Figure ?? shows the typical agreement for each source. The agreement of all of the source peaks is further analyzed when determining the energy uncertainty contribution to the final

asymmetry in Section 5.2.4.

## 4.3 Wirechamber Energy Calibration

### 4.3.1 Method

The goal of the wirechamber energy calibration is to provide an estimate of the energy deposited within the MWPC,  $E_{\text{MWPC}}$ , depending on the response of the wirechamber. The available information from the wirechamber includes the summed anode signal, which is proportional to the total amount of ionization within the MWPC gas and thus the total energy deposited, and the reconstructed position from the cathode signals. Also available is the reconstructed initial energy of all events,  $E_{\text{recon}}$ , as a result of the previously described scintillator energy calibration. This is important as higher energy events deposit less energy in the wirechamber than lower energy events, and thus subsets of events with different  $E_{\text{recon}}$  will provide different distributions of  $E_{\text{MWPC}}$ . With this in mind, the general idea for calibrating the wirechamber is as follows:

- Map out the position dependence of the anode signals in a similar manner to the PMT light transport maps.
- Separate data into subsets based on  $E_{\text{recon}}$  to provide several different distributions of wirechamber signals (anode for data and  $E_{\text{MWPC}}$  for simulation).
- For each  $E_{\text{recon}}$  subset, fit the wirechamber ADC signals for the data.
- For each  $E_{\text{recon}}$  subset, fit the simulated wirechamber deposited energy,  $E_{\text{MWPC}}$ .
- Plot the extracted ADC values from the data vs. the extracted  $E_{\text{MWPC}}$  from the simulation to determine the parameterization from anode signal to wirechamber deposited energy.

The energy calibration of the wirechamber is carried out for every individual  $\beta$ -decay run, rather than using the periodic source calibration runs as was done for the scintillator energy calibration. This is advantageous as it automatically corrects for any changes in the anode gain on the run-by-run time scale.

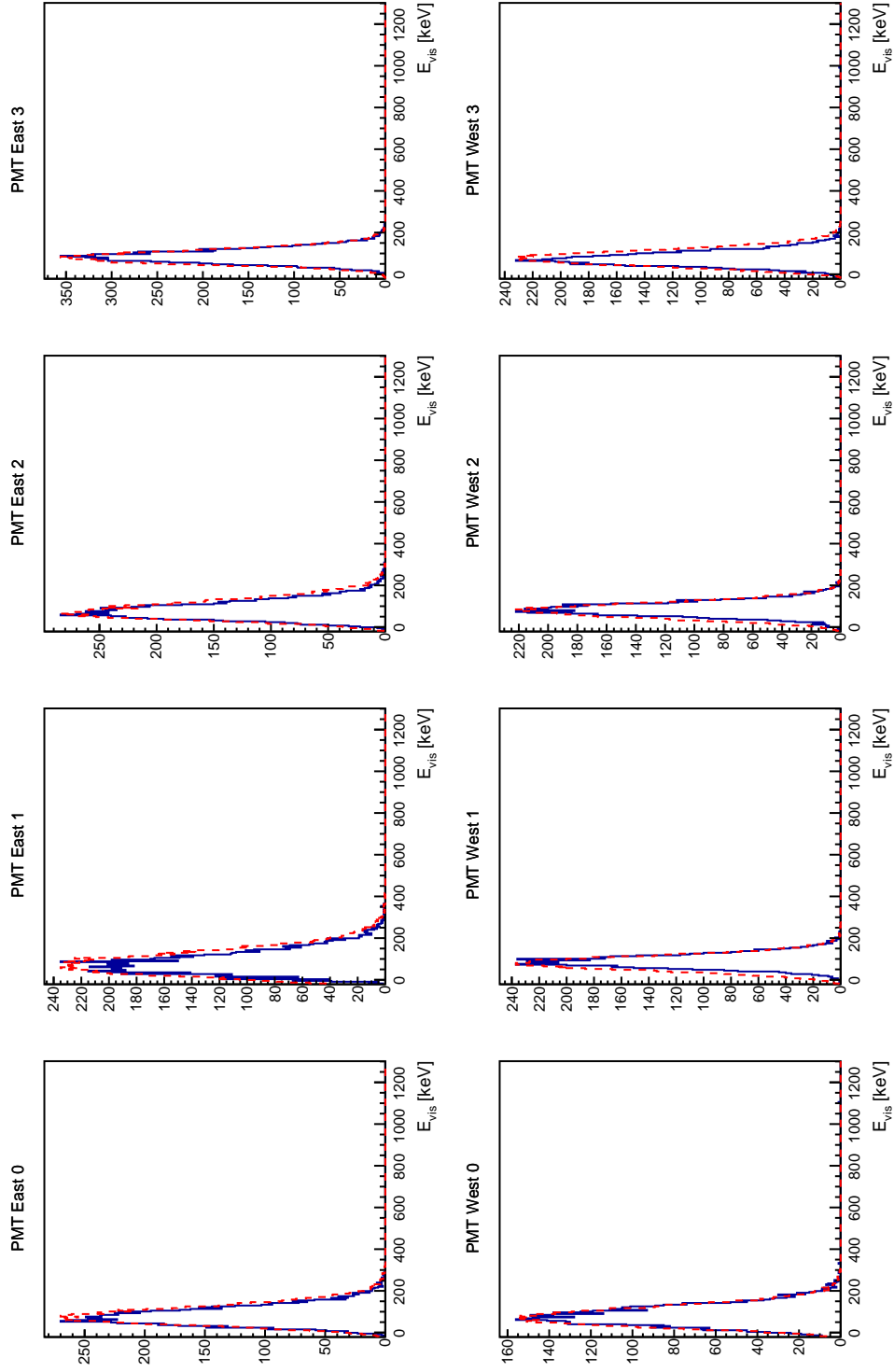


Figure 4.13: Example spectra from each PMT for simulation (red dashed line) and data (blue line) for  $^{137}\text{Ce}$  conversion electron source after application of the calibration. This is for a random run that included all three sources within the fiducial volume at the same time.

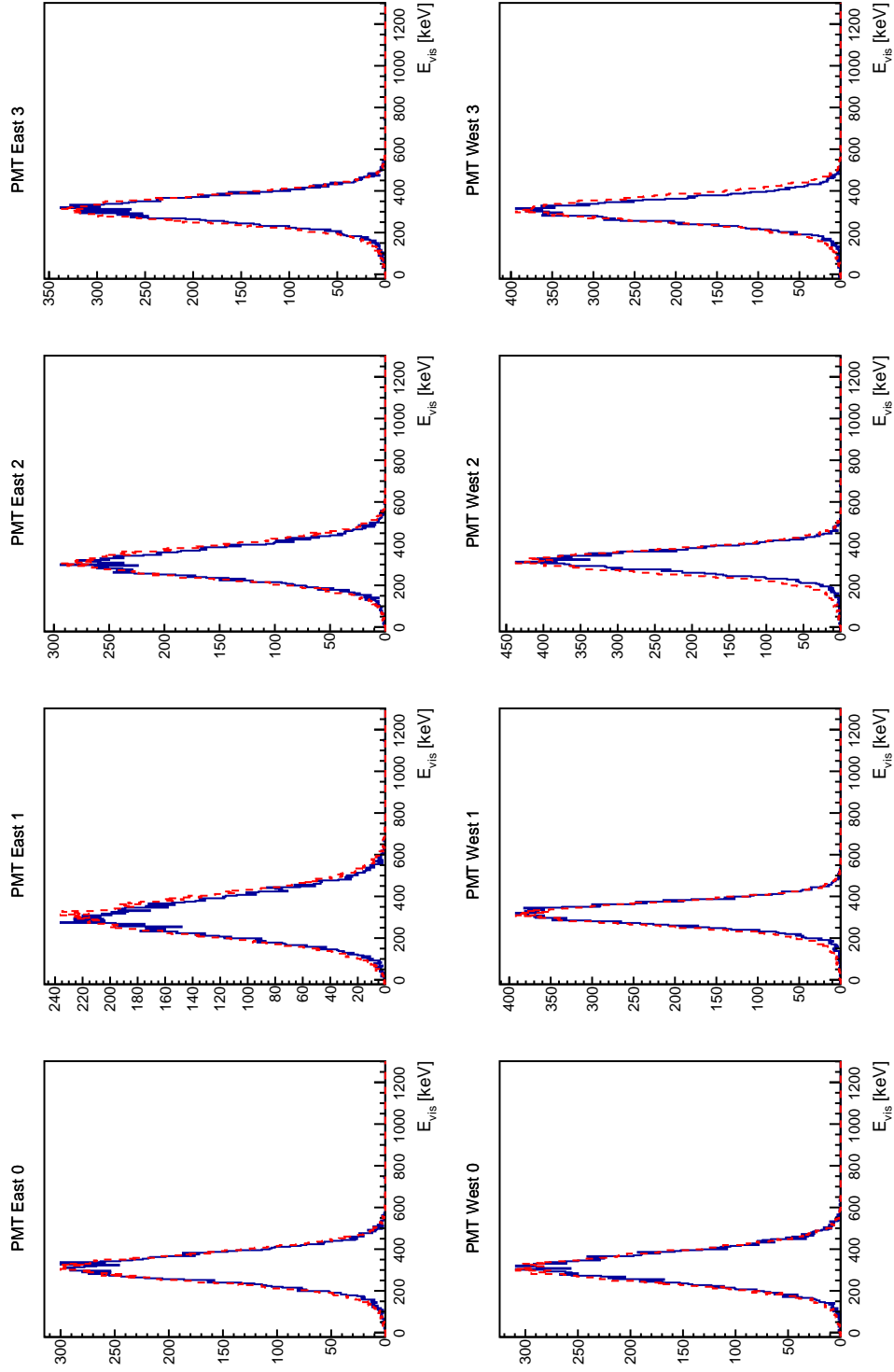


Figure 4.14: Example spectra from each PMT for simulation (red dashed line) and data (blue line) for  $^{113}\text{Sn}$  conversion electron source after application of the calibration. This is for a random run that included all three sources within the fiducial volume at the same time.

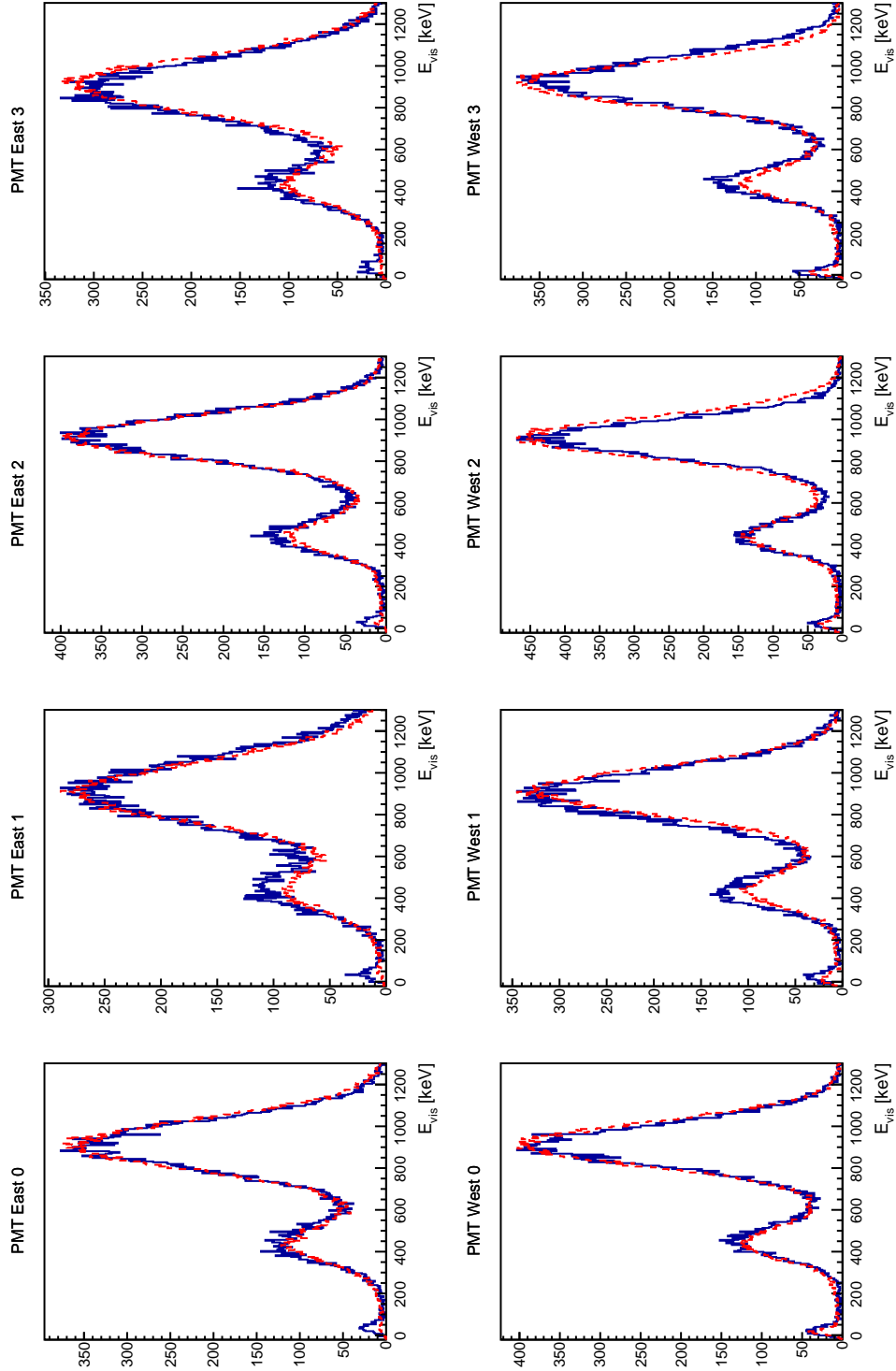


Figure 4.15: Example spectra from each PMT for simulation (red dashed line) and data (blue line) for  $^{207}\text{Bi}$  conversion electron source after application of the calibration. This is for a random run that included all three sources within the fiducial volume at the same time.

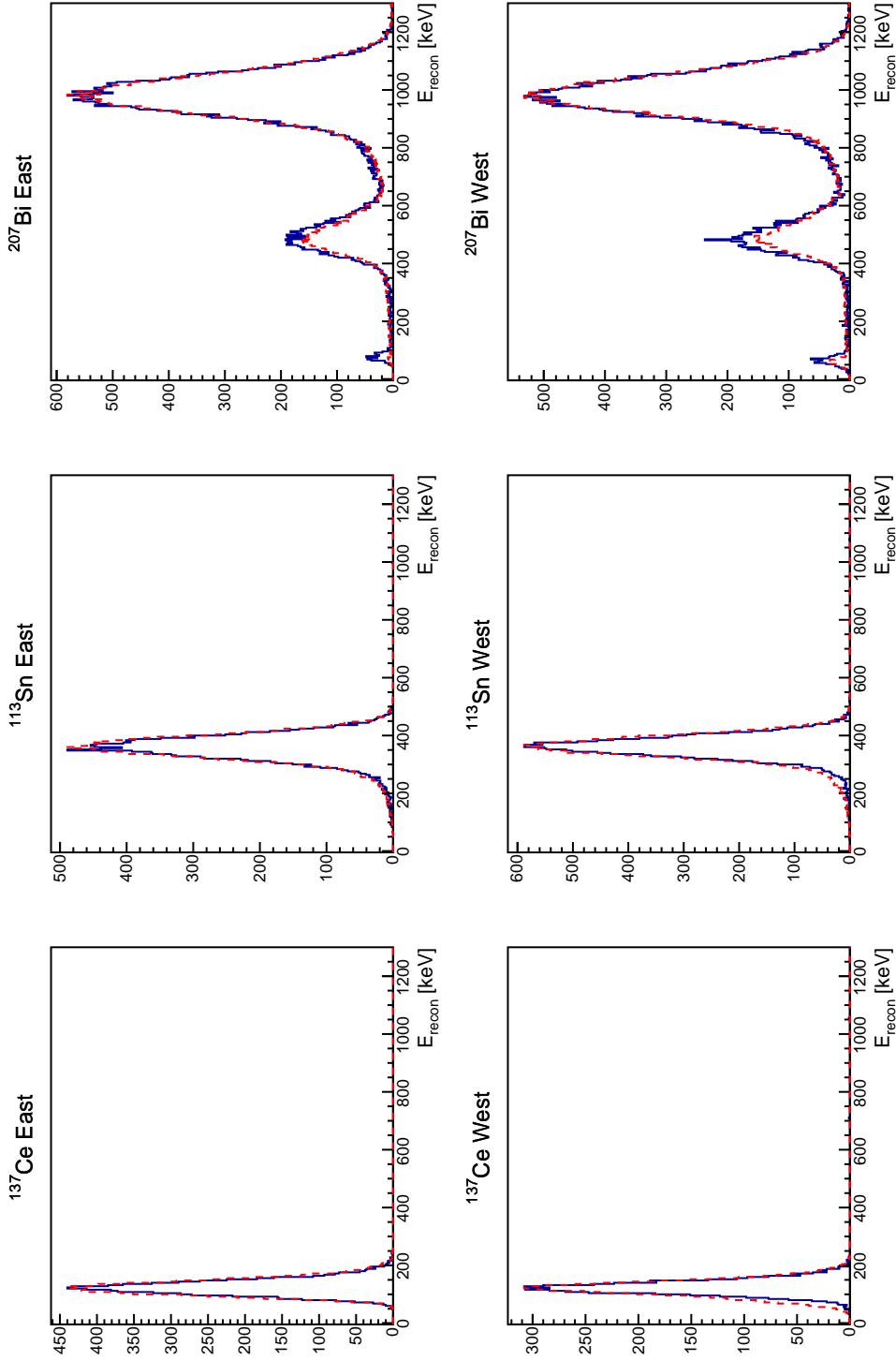


Figure 4.16: Example  $E_{\text{recon}}$  spectra from combined PMT response for simulation (red dashed line) and data (blue line) for all conversion electron sources after application of the calibration. This plot is from the same run as the plots of the previous individual PMT spectra, showing how the spectra combine to produce a single final energy estimate.

### 4.3.2 Position dependence of anode signal

While the wirechamber is constructed to be as homogeneous as possible, a residual position dependence to the anode signal still exists. The cause of such position dependence is undetermined, but it only affects the energy calibration of the wirechamber, which is a non-essential component of the analysis. Also, by mapping the position dependence in a manner similar to the PMT position maps (Section 4.2.2.2), we can remove any effects altogether.

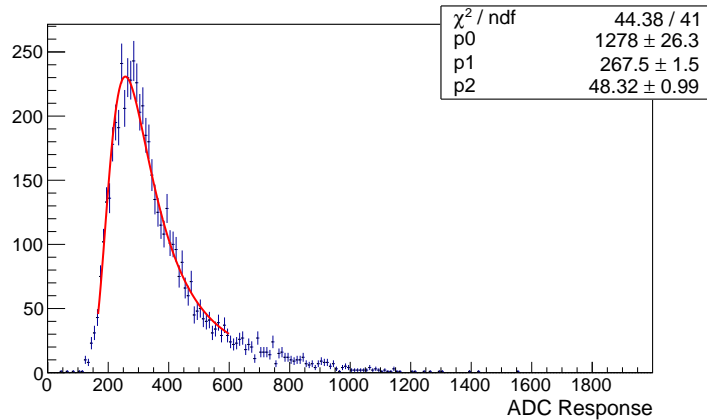


Figure 4.17: Typical wirechamber anode signal for a xenon calibration run in a single pixel. The fit function is a TMath::Landau function from the ROOT Data Analysis Framework, and the extracted value is the MPV (most probable value) from the distribution.

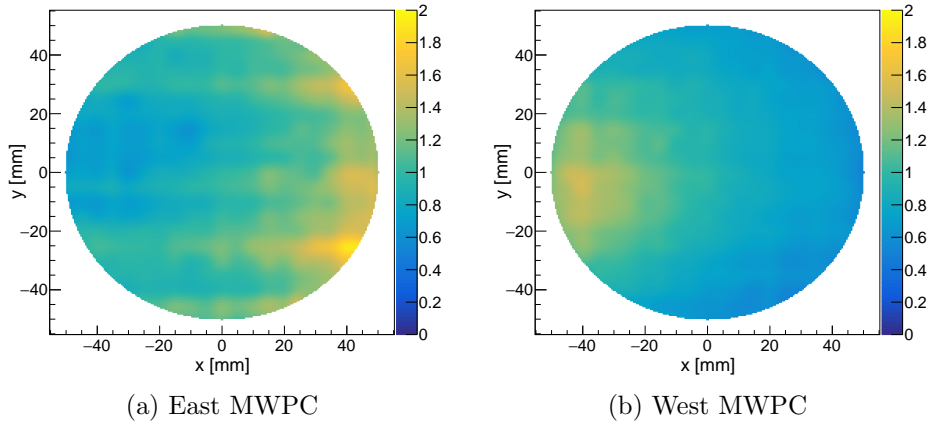


Figure 4.18: Example position dependent anode response for each MWPC. These MWPC position maps were created using electrons with  $300 \text{ keV} < E_{\text{recon}} < 350 \text{ keV}$ .

The dedicated xenon calibration runs were used to determine the MWPC position

maps. The wirechamber anode signal was histogrammed in  $5 \text{ mm} \times 5 \text{ mm}$  position bins (pixels) across the detector, giving distributions like the one seen in Figure 4.17. Only Type 0 events were used for the position dependence of the wirechamber, as these only pass through the wirechamber once and are a better representation of the amount of energy deposition as a function of initial event energy. The distribution in each pixel is fit with a TMath::Landau function from the ROOT Data Analysis Framework. The most probable value of the distribution is returned from the fit for every pixel, and then the position dependent response factor is formed via

$$\eta_i^{\text{MWPC}} = \frac{\text{MPV}_i}{\text{MPV}_0}, \quad (4.12)$$

where  $\text{MPV}_0$  is the most probable value of the center pixel. The continuous values plotted in Figure 4.18 are determined as they were in Section 4.2.2.2. The position dependent response factor is divided out of the anode signal prior to determining the wirechamber calibration, and thus also prior to applying the wirechamber calibration to the data.

One should note that the MWPC position maps can be determined for different initial energies of the electrons, since the scintillator calibration has already been applied. The position response plots in Figure 4.18 were made using electrons with  $300 \text{ keV} < E_{\text{recon}} < 350 \text{ keV}$ , although the position maps are stable for any 50 keV window chosen. For ease of application, the MWPC position maps from the above energy range were used for electrons of all initial energies.

### 4.3.3 Relating Anode Signal to $E_{\text{MWPC}}$

As mentioned above, the wirechamber energy calibration is carried out on a run-by-run basis, so the discussion that follows applies to every individual  $\beta$ -decay run. After dividing out the MWPC position dependent response from the anode signals of all electron events, we can attempt to relate the anode response to the expected wirechamber response from simulation (again we only use Type 0 events for the energy calibration). To do this, we first separate the electron events by their  $E_{\text{recon}}$  into 50 keV energy bins beginning at 100 keV and ending at 800 keV, giving twelve separate collections of electron events. The lower bound is chosen to avoid any possible effects from differences between the simulated and actual scintillator thresholds. The upper bound is just beyond the endpoint energy of the  $\beta$ -decay electrons.

The twelve electron energy groupings provide twelve different distributions to be fit with a Landau distribution, and the MPV of each should be different. This is a

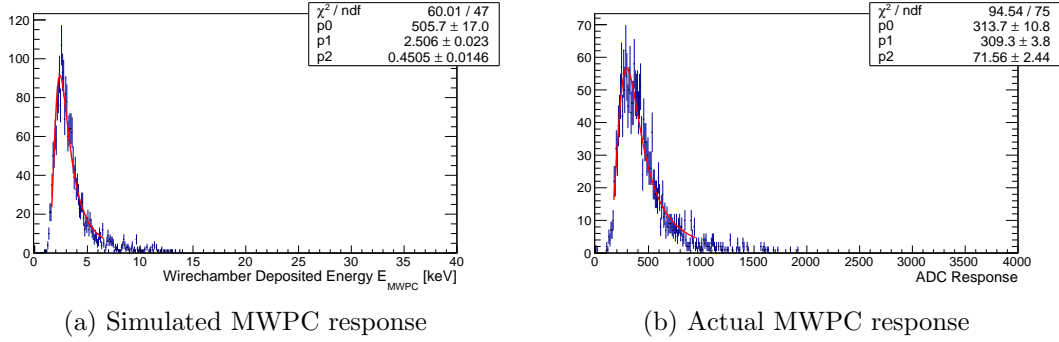


Figure 4.19: TMath::Landau fit of both simulation and data for electron events which deposited between 300-400 keV in the west scintillator. The fitted MPV (p1 in the statistics box) from each plot make up a single data point in the wirechamber energy calibration plot below (Figure 4.20).

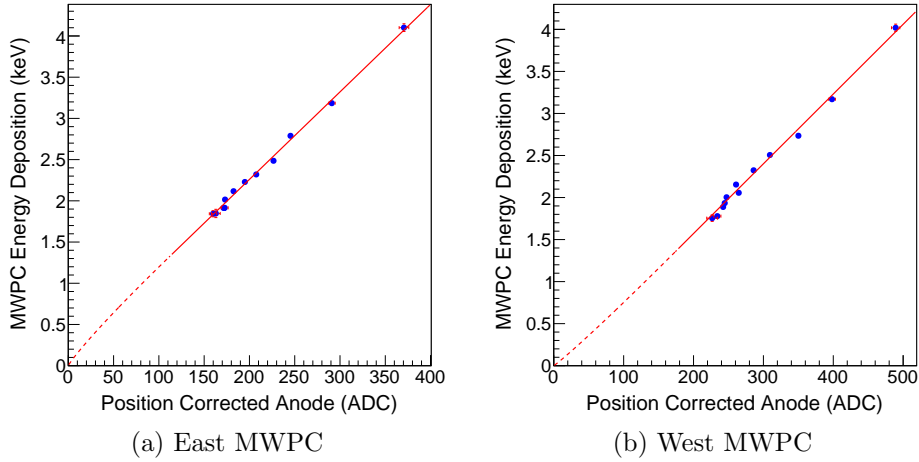


Figure 4.20: Example MWPC calibration curve for a single run in 2011-2012. A calibration like this one is carried out for every  $\beta$ -decay run.

result of the electrons of interest lying in an energy range such that interactions with the wirechamber fill gas produce more energy loss per unit length for less energetic electrons, or in other words the lower energy electrons fall below the minimum ionizing particle energy for the fill gas. A nice summary of particle interactions with matter can be found in [PG+16], but the important takeaway from this is that the twelve different initial energy groupings yield twelve different energy deposition distributions in the wirechamber, which provides twelve data points to use when comparing simulation with data.

For the simulation, the MPV is extracted in the energy domain, where the energy is the amount of energy deposited within the wirechamber gas. For the data, the

MPV is an ADC value. Examples of each fit for a single  $E_{\text{recon}}$  grouping can be seen in Figure 4.19. If we have modeled the wirechamber correctly and as long as the MWPC anode signal is proportional to the total ionization created in the wirechamber, then we expect a linear relationship between the simulated energy deposition and the anode signal for each of the  $E_{\text{recon}}$  groupings. By plotting the MPVs from data and simulation and fitting with a straight line, we define the conversion from (position corrected) MWPC anode signal to energy deposited within the wirechamber. An example calibration is demonstrated in Figure 4.20. The calibration fit is of the form

$$E_{\text{MWPC}}(\text{ADC}) = C_1 + C_2 \cdot \text{ADC}, \quad (4.13)$$

and the fit is extrapolated to the origin in a continuous manner using

$$E_{\text{MWPC}} = C_3 \cdot \text{ADC}^{C_4} \quad (4.14)$$

with the parameters  $C_3$  and  $C_4$  determined by ensuring the two equations are equal at the transition point along with their first derivatives. The transition point is defined as 50 ADC channels below the lowest data point.

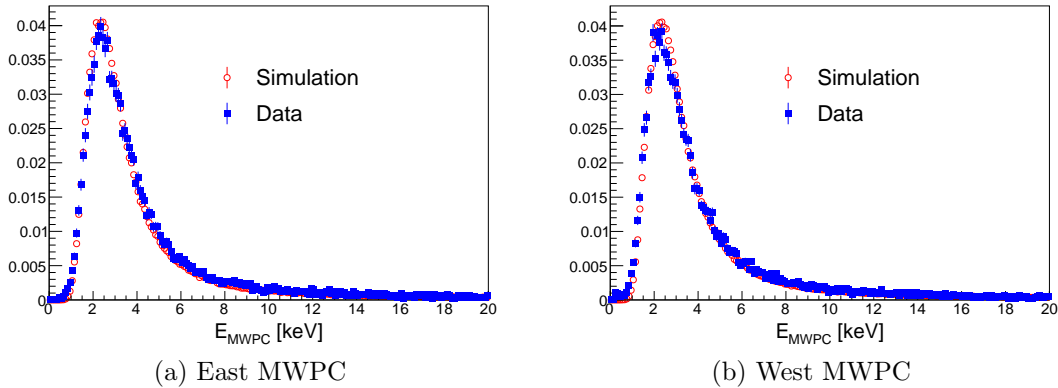


Figure 4.21: Simulation vs. Data after application of the wirechamber calibration for a single run in 2011-2012. This plot includes only Type 0 events.

Including the  $C_1$  parameter ( $y$ -intercept) allows for imperfections in the MWPC anode pedestal subtraction. The extrapolation to the origin produces better agreement with simulation, as data events with very low energy deposition in the wirechamber could otherwise be assigned negative energies if only Equation 4.13 is used and the  $y$ -intercept is negative. Comparison between simulation and data of the final calibrated energy deposition for a single run is shown in Figure 4.21, where we see very nice agreement for both detectors.

#### 4.3.4 Backscattering Separation for Type 2/3 Events

The primary reason for performing the wirechamber energy calibration is to allow for comparison with simulation in order to separate the Type 2 and Type 3 backscattering events. Recall from Section 2.7 that the Type 2/3 backscattering events are indistinguishable using only detector trigger logic, but that their energy deposition in the primary wirechamber is different due to Type 2 events passing through the primary MWPC once and Type 3 passing through twice. Thus there should exist an energy cut that most effectively distinguishes the Type 2 from the Type 3 events.

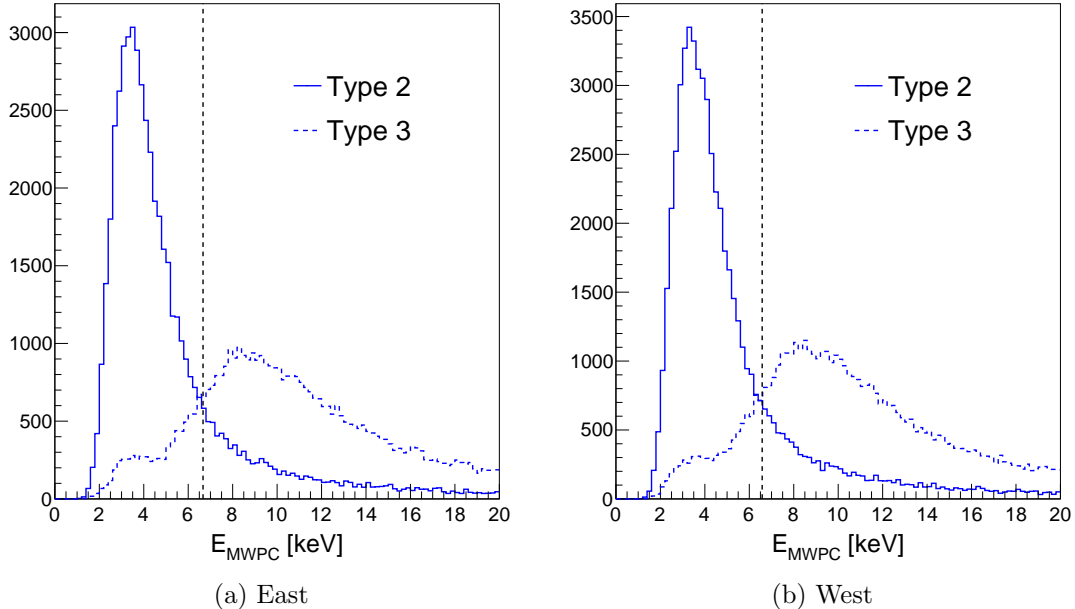


Figure 4.22: 2011-2012 simulated wirechamber energy deposition of Type 2 and Type 3 events with  $200 \text{ keV} < E_{\text{recon}} < 300 \text{ keV}$ . The vertical dashed line indicates the optimal cut on the wirechamber energy deposition to separate the two otherwise identical backscattering events. The position of this cut varies with  $E_{\text{recon}}$ . The distributions for the other geometries are similar.

##### 4.3.4.1 Monte Carlo Study

Monte Carlo studies provide the means for applying the most efficient cuts on the energy deposition in the wirechamber to separate the Type 2/3 backscattering events due to the fact that the true initial direction of each event is known, and thus so is the true type of the event. With this knowledge, one can analyze the fraction of events that are assigned the proper side as a function of different separation cuts.

When we say we are applying cuts to separate the two event types, we mean choosing a wirechamber deposited energy where any events above the cut value will be assigned one event type (and thus a certain side), while an event below the chosen cut will be identified as the other event type (and the opposite side). An example of the wirechamber energy deposition for the two types of events can be seen in Figure 4.22, with the location of the optimal cut indicated by the vertical line. Note that this plot uses only electron events satisfying  $200 \text{ keV} < E_{\text{recon}} < 300 \text{ keV}$ . From this plot we see that an event with  $E_{\text{MWPC}}$  below the cut would be identified as a Type 2 event, while an event lying above the cut would be a Type 3 event. One can also see from this plot that the separation is not perfect, as the two event type distributions overlap.

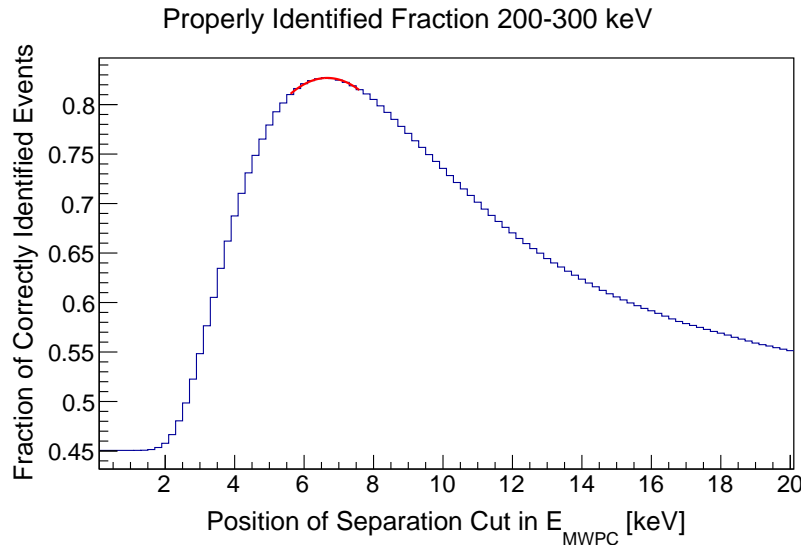


Figure 4.23: Fraction of properly identified events where  $200 \text{ keV} < E_{\text{recon}} < 300 \text{ keV}$  as a function of the separation cut. The polynomial fit to the maximum is indicated by the solid red line, from which the location of the most effective separation cut is extacted.

The position of the optimal cut in Figure 4.22, while arguably obvious to the keen observer, is determined quantitatively for eight different groups of  $E_{\text{recon}}$  events in 100 keV increments from 0 – 800 keV. For each  $E_{\text{recon}}$  group, the cut is incremented from 0 keV to 20 keV in 1 keV steps, and then the fraction of properly identified events given each different cut is calculated. The fraction of properly identified events for each value of the separation cut is plotted as a function of the position of the cut as shown in Figure 4.23. The goal is then to extract the maximum of this distribution, which indicates the optimal cut. To determine the maximum, the peak is fit with a

second-order polynomial of the form

$$f(x) = C_1 + C_2(x - C_3) + C_4(x - C_3)^2, \quad (4.15)$$

and then the maximum is extracted using the derivative of the fit function. The location of this maximum is the optimal cut for separating Type 2/3 events within the  $E_{\text{recon}}$  range being analyzed.

#### 4.3.4.2 Determining a continuous separation cut

After fitting the location of the optimal cuts of the eight  $E_{\text{recon}}$  groups, a continuous wirechamber cut can be extracted by plotting the location of the cuts vs. the midpoint of the  $E_{\text{recon}}$  group, i.e. for the electron events with  $200 \text{ keV} < E_{\text{recon}} < 300 \text{ keV}$  we use 250 keV. Such plots are shown in Figure 4.24 for the 2011-2012 and 2012-2013 data sets. Due to the consistency between the two detectors, a fit to the average of the data points from each side is carried out, with the fit taking the functional form

$$f(x) = C_1 + C_2 e^{-C_3 x}. \quad (4.16)$$

Then, with the fit parameters saved for each geometry, a continuously varying separation cut can be calculated depending on the  $E_{\text{recon}}$  of an individual event.

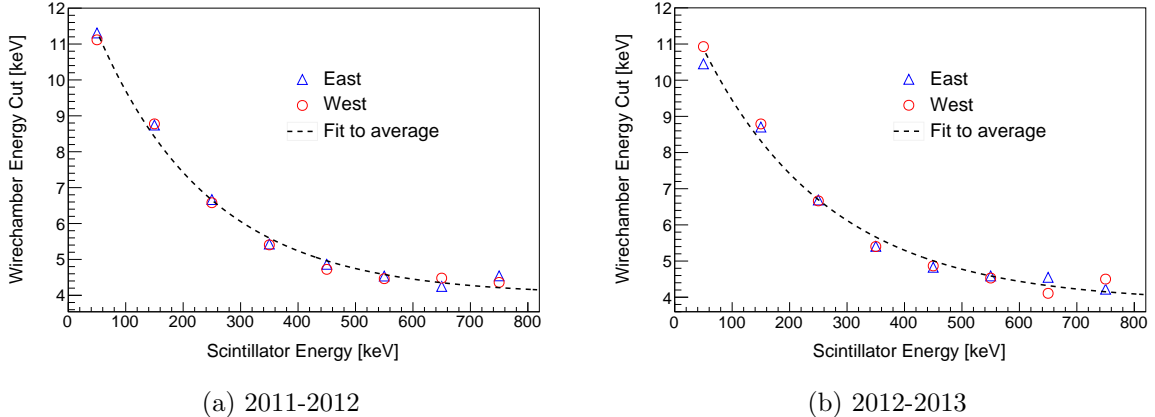


Figure 4.24: Plot of optimal cuts for each detector from 2011-2012 and 2012-2013. The eight data points for each detector are a result of dividing the simulation data into 100 keV  $E_{\text{recon}}$  groups from 0 – 800 keV. The average of the two detector sides are fit to determine a continuous function describing the optimal Type 2/3 separation cuts.

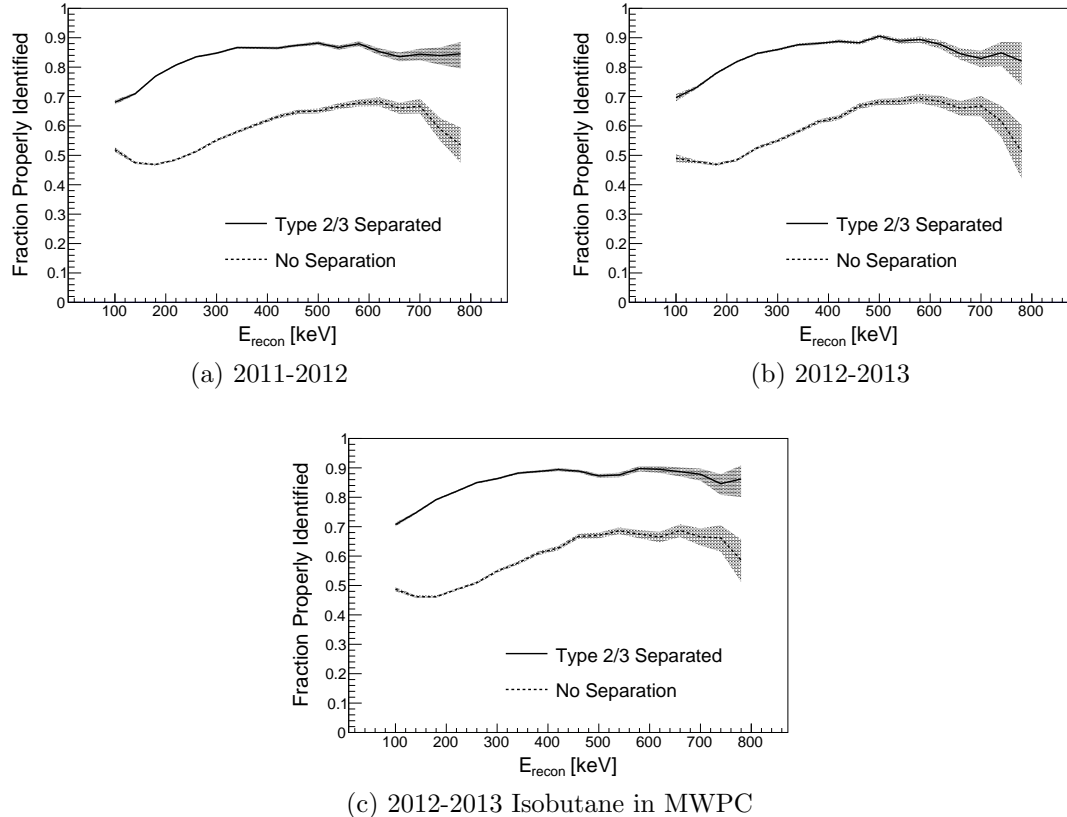


Figure 4.25: Fraction of properly identified events when the Type 2/3 separation is applied compared to when it is not applied. The results are shown for a single octet from all possible geometries. The shaded error band is purely statistical.

### 4.3.4.3 Results

By applying the continuous cut to the processed simulation, we can assess the effectiveness of the Type 2/3 separation procedure. Figure 4.25 shows the fraction of the events that are assigned to the correct side of the detector as a function of reconstructed initial energy. The plot shows a vast improvement in properly assigning the initial direction of the events when using the Type 2/3 separation highlighted above (solid line), rather than using no separation at all (dashed line). Upon integrating across all energies, the Type 2/3 separation method yields  $> 81\%$  proper identification of the Type 2/3 events, compared to the  $\sim 53\%$  when no separation is applied. This improvement is very important if all event types are to be included in the final analysis, as it drastically reduces the Monte Carlo systematic corrections that must be applied to the backscattering events. This will be shown in detail in the following chapter.

Copyright<sup>©</sup> Michael A-P Brown, 2018.

# Chapter 5

## UCNA Results

### 5.1 Constructing an Asymmetry

#### 5.1.1 Decay Rate Model

As discussed in earlier in section 1.3.2, the nominal decay rate for polarized neutrons with no detection of final-state spins is expressed in terms of the spin vector of the neutron and all possible correlations to the products [JTWJ57]. For simplicity, we begin by writing the differential decay rate for the case where only the electron momentum is detectable (and assuming no BSM terms):

$$\Gamma(E, \Omega) = C \cdot S(E) \cdot (1 + A(E)\beta \cos \theta), \quad (5.1)$$

where  $S(E)$  is the Standard Model differential decay rate for unpolarized  $\beta$ -decay,  $C$  is a constant which encompasses anything not included in  $S(E)$  and serves the purpose of absorbing other constants,  $A(E)$  is the energy dependent electron asymmetry parameter,  $\beta \equiv v/c$  is the electron velocity, and  $\theta$  is the angle between the spin of the neutron and the electron momentum.

We can also introduce an average polarization of the neutrons, giving

$$\Gamma(E, \Omega) = C \cdot S(E) \cdot \epsilon \cdot (1 + \langle P \rangle \cdot A(E)\beta \cos \theta), \quad (5.2)$$

where  $\epsilon$  is the loading efficiency of neutrons in this spin state which I haven't absorbed into the constant for reasons to be seen, and  $\langle P \rangle$  is the polarization, i.e. a number between 0 and 1 (very close to 1 in our case).

At this point, assumptions can be made regarding the experimental setup utilized to further express the decay rate in terms of detector rates. Due to the spins being aligned with the 1 T magnetic field in the decay trap, electrons emitted with a

momentum component along the spin will spiral towards one detector, while electrons with a component of momentum opposite the spin will be detected in the opposite detector. If we fix the  $z$ -axis using the static position of our apparatus, we can call the detector at  $\theta = 0$  detector 1 and the opposite detector 2.

Now, all electrons with  $0 < \theta < \pi/2$  will head towards detector 1 and those with  $\pi/2 < \theta < \pi$  will be directed towards detector 2. The solid angle can then be integrated out for each detector by integrating  $\phi$  from  $(0, 2\pi)$  and  $\cos\theta$  over the intervals given, where the integral of  $\cos\theta$  over detectors 1 and 2 yields  $+1/2$  and  $-1/2$  respectively:

$$\Gamma_{1,2}(E) = 2\pi \cdot C \cdot S(E) \cdot \epsilon \cdot \eta_{1,2}(E) \left[ 1 + \langle P \rangle \cdot A(E) \beta \left( \pm_{1,2} \frac{1}{2} \right) \right], \quad (5.3)$$

$$\Gamma_{1,2}(E) = C' \cdot S(E) \cdot \epsilon \cdot \eta_{1,2}(E) \left[ 1 \pm_{1,2} \langle P \rangle \cdot A(E) \frac{\beta}{2} \right], \quad (5.4)$$

with  $\eta_{1,2}(E)$  signifying energy dependent electron detection efficiencies for detectors 1 and 2.

Thus far we have assumed a fixed polarization, but in UCNA we have the ability to flip the spin of the neutrons prior to loading. We call these states flipper on (+) and flipper off (-), denoted by  $\langle P \rangle_{\pm}$ . The flipper on state introduces a negative in front of the polarization efficiency due to the fact that the spin  $\vec{\sigma}$  is now aligned with  $-\hat{z}$ , thus reversing the sign of  $\vec{\sigma} \cdot \vec{p}_e$  with respect to the prior assumption of  $\vec{\sigma}$  in  $+\hat{z}$ :

$$\Gamma_{1,2}^{\pm}(E) = C' \cdot S(E) \cdot \epsilon_{\pm} \cdot \eta_{1,2} \left[ 1 \pm_{1,2} (\mp \langle P \rangle_{\pm}) \cdot A(E) \frac{\beta}{2} \right], \quad (5.5)$$

where  $\epsilon_{\pm}$  accounts for differing loading efficiencies for different spin states.

If we now assume that we are equally as efficient at polarizing in either spin state, we can say  $\langle P \rangle_+ = \langle P \rangle_- = \langle P \rangle$  (extraction of the asymmetry under the super-ratio technique not assuming this condition can be found later in Section 5.2.3.1) giving:

$$\Gamma_{1,2}^{\pm}(E) = C' \cdot S(E) \cdot \epsilon_{\pm} \cdot \eta_{1,2} \left[ 1 \pm_{1,2} (\mp \langle P \rangle) \cdot A(E) \frac{\beta}{2} \right]. \quad (5.6)$$

### 5.1.2 Super-Ratio

A simple asymmetry over some energy bin for a single polarization state can be defined as

$$A_{\text{simple}} = \frac{\Gamma_1 - \Gamma_2}{\Gamma_1 + \Gamma_2}, \quad (5.7)$$

and assuming that the efficiencies  $\eta_1$  and  $\eta_2$  are the same one finds

$$A_{\text{simple}} = \langle P \rangle \cdot A(E) \cdot \frac{\beta}{2}, \quad (5.8)$$

where  $\beta$  is calculated as either the velocity associated with the energy at the center of the bin or the average energy of the bin. The distinction is unimportant as this is later corrected for as part of the angular acceptance correction detailed in Section 5.2.2.2.

In reality we cannot assume with certainty that the detectors are identical, but we can utilize the fact that we can flip the spins to cancel differing efficiencies. If we take two runs with opposite polarizations, we can define the super-ratio asymmetry in some energy range as:

$$A_{\text{SR}} = \frac{1 - \sqrt{R}}{1 + \sqrt{R}}, \quad (5.9)$$

where

$$R = \frac{\Gamma_1^+ \cdot \Gamma_2^-}{\Gamma_1^- \cdot \Gamma_2^+}. \quad (5.10)$$

Some algebra yields an identical expression to Equation 5.8,

$$\begin{aligned} R &= \frac{\left[ C' S(E) \epsilon_+ \eta_1 \left[ 1 + (-\langle P \rangle) A(E) \frac{\beta}{2} \right] \right] \left[ C' S(E) \epsilon_- \eta_2 \left[ 1 - (+\langle P \rangle) A(E) \frac{\beta}{2} \right] \right]}{\left[ C' S(E) \epsilon_- \eta_1 \left[ 1 + (+\langle P \rangle) A(E) \frac{\beta}{2} \right] \right] \left[ C' S(E) \epsilon_+ \eta_2 \left[ 1 - (-\langle P \rangle) A(E) \frac{\beta}{2} \right] \right]}, \\ R &= \frac{\left[ 1 + (-\langle P \rangle) A(E) \frac{\beta}{2} \right] \left[ 1 - (+\langle P \rangle) A(E) \frac{\beta}{2} \right]}{\left[ 1 + (+\langle P \rangle) A(E) \frac{\beta}{2} \right] \left[ 1 - (-\langle P \rangle) A(E) \frac{\beta}{2} \right]}, \\ R &= \frac{\left[ 1 - \langle P \rangle A(E) \frac{\beta}{2} \right]^2}{\left[ 1 + \langle P \rangle A(E) \frac{\beta}{2} \right]^2}, \end{aligned}$$

and plugging into  $A_{\text{SR}}$

$$\begin{aligned} A_{\text{SR}} &= \frac{1 - \frac{\left[ 1 - \langle P \rangle A(E) \frac{\beta}{2} \right]}{\left[ 1 + \langle P \rangle A(E) \frac{\beta}{2} \right]}}{1 + \frac{\left[ 1 - \langle P \rangle A(E) \frac{\beta}{2} \right]}{\left[ 1 + \langle P \rangle A(E) \frac{\beta}{2} \right]}}, \\ A_{\text{SR}} &= \frac{2 \langle P \rangle A(E) \frac{\beta}{2}}{2}, \\ A_{\text{SR}} &= \langle P \rangle A(E) \frac{\beta}{2}. \end{aligned} \quad (5.11)$$

The super-ratio not only cancels the detector efficiencies, but any difference between the integrated rates between the two spin states also cancel.

### 5.1.3 Extracting $A_0$

The quantity of interest is not the raw measured asymmetry, or even  $A(E)$ , but rather  $A_0$ , which is directly proportional to  $\lambda = g_A/g_V$ , yielding a direct measurement of the axial vector coupling constant if the CVC hypothesis is assumed.

$A_0$  manifests itself in our measured asymmetry as:

$$A_0 = A(E) \cdot (1 + \Delta(E)), \quad (5.12)$$

where  $\Delta(E)$  is the energy dependent correction to the measured asymmetry from theory corrections and experimental systematic effects, all of which will be described in detail in 5.2. The modifications from theory were also mentioned in chapter 1.

Solving 5.2.3.1 for  $A(E)$  and inserting into the above expression, we have

$$A_0 = \frac{(1 + \Delta(E)) \cdot A_{\text{SR}}(E)}{\langle P \rangle \cdot \beta / 2}, \quad (5.13)$$

where again  $\beta = v/c$ .

With an energy dependent expression for  $A_0$ , we can bin our data in discrete energy bins, evaluate  $\beta$  at the midpoint of the bin, apply appropriate energy dependent corrections, and then fit the resulting collection of  $A_0$  values with a constant. Careful selection of the energy range to fit over is discussed in 5.4.3.2.

## 5.2 Systematic Corrections and Uncertainties

Measuring any quantity without imparting a systematic shift in the result due to imperfect experimental techniques is nearly impossible; but what is more dangerous to the result is not understanding these shifts. This section discusses how well we understand the theoretical and experimental effects present in the UCNA experiment that cause us to measure an asymmetry that is not directly equal to the parameter of interest, thus requiring corrections.

### 5.2.1 Definition of $\Delta$

We adopt a similar formalism for systematic corrections as previously defined in [Men14], at least as far as the definition of the correction is concerned. If we have an asymmetry  $A(E)$  measured without some correction  $i$ , then we can define  $A'(E)$  as

$$A'(E) = (1 + \Delta_i(E)) \cdot A(E), \quad (5.14)$$

where  $A'(E)$  is the new corrected asymmetry with systematic effect  $i$  removed. Rearrangement of the above equation provides a definition for  $\Delta_i$ :

$$\Delta_i(E) = \frac{A'(E)}{A(E)} - 1 \quad (5.15)$$

This is useful as most corrections are determined by studying the effect on the asymmetry from some aspect of the experiment via Monte Carlo, so energy dependent corrections can be constructed and applied to data.

If the uncertainty on correction  $\delta\Delta_i$ , denoted  $\delta\Delta_i$ , has been determined, we can also define the uncertainty on the resulting asymmetry  $\delta A'(E)$  via normal error propagation techniques as

$$\delta A'(E) = A(E) \cdot \delta\Delta_i(E), \quad (5.16)$$

$$\frac{\delta A'(E)}{A'(E)} = \frac{\delta\Delta_i(E)}{1 + \Delta_i(E)}. \quad (5.17)$$

Now the collection of all corrections, if extracted independently, will commute, and thus provides

$$1 + \Delta(E) = (1 + \Delta_1(E))(1 + \Delta_2(E))(1 + \Delta_3(E)) \dots, \quad (5.18)$$

such that a final corrected asymmetry  $A''' \dots$  can be written as

$$\begin{aligned} A''' \dots (E) &= (1 + \Delta(E)) \cdot A(E), \\ A''' \dots (E) &= \left( \prod_i (1 + \Delta_i(E)) \right) \cdot A(E). \end{aligned} \quad (5.19)$$

The rest of this section is dedicated to determining all applicable  $\Delta_i$  and their associated uncertainties.

### 5.2.2 Energy Dependent Monte Carlo Corrections

The Monte Carlo corrections are calculated by forming asymmetries from simulated data with the entirety of the detector response model applied. For each individual data run, the conditions of the apparatus (calibration, pedestal, resolution, etc) are determined and a subset of the simulation data (roughly  $16 \times$  the data run) is processed using such conditions. This produces a higher statistics simulation of the individual runs, and therefore allows one to run the simulated octets through the asymmetry analysis in the exact same manner as the data. The fact that we know everything about each individual event in the simulation allows us to correct for effects to the asymmetries from the experimental conditions. Via Equation 5.15, the asymmetry before and after a given correction can be used to determine the value of the correction to be applied to the data.

The Monte Carlo corrections are also further separated into corrections from misidentification of backscattering types,  $\Delta_2$ , and from angular acceptance effects,  $\Delta_3$ . In [UCNA2017],  $\Delta_2$  and  $\Delta_3$  correspond to  $\Delta_{\text{backscattering}}$  and  $\Delta_{\cos\theta}$  respectively.

### 5.2.2.1 Backscattering Misidentification, $\Delta_2$

Imagine an event which initially heads towards the east detector, but it backscatters off of the decay trap window and never reaches a sensitive detector on the East side. The electron then heads towards the West detector where it is detected. Using only triggering information, this event would be improperly identified as a Type 0 event with initial Western momentum. Experimental data possess no way of properly identifying such events, so we rely on simulation. As mentioned previously, we have access to all initial conditions of each simulated event, so upon forming an asymmetry one can properly identify all events which were detected as Type 0 and assure they are assigned to their proper initial direction. The comparison of the asymmetry before and after such a correction defines the Monte Carlo correction due to backscattering misidentification of Type 0 events. Let's call this  $\Delta_{2,0}$ , where the subscript 0 refers to the backscattering correction for Type 0 events. One can imagine that the same process can be repeated for each of the detected event types, giving us the following definition for the total  $\Delta_2$  correction:

$$1 + \Delta_2 = (1 + \Delta_{2,3})(1 + \Delta_{2,2})(1 + \Delta_{2,1})(1 + \Delta_{2,0}) \quad (5.20)$$

The corrections as a function of electron energy can be seen in figure 5.1. Application of the correction increases the magnitude of the measured asymmetry as it should, as missed backscattering events dilute the measured asymmetry. The uncertainties seen in the figure will be discussed in Section 5.2.2.3. The leading contribution to the backscattering correction comes from Type 0 events due to them accounting for roughly 95% of the data. The other event types have much smaller contributions to the backscattering correction when all event types are included in the analysis due primarily to the little statistical weight they carry. If the Type 0 events are ignored, the backscattering corrections become very large for the Type 1, 2, and 3 events. This will be illustrated when showing asymmetries for different combinations of event types later in this chapter.

The difference between 2011-2012 and 2012-2013 corrections arises from the thinner decay trap windows in 2012-2013, which substantially reduces the  $\Delta_{2,0}$  correction for misidentified Type 0 events. There is almost no effect on the other event types, as should be expected due to no dramatic change in event type fractions or triggering efficiencies for the two detector sides. Another way to think of this is that once an event passes through the decay trap endcap, its likelihood of triggering the detector approaches 100% fairly quickly (see Figure 5.2) and is not dependent on the changing geometry, so the corrections for backscattering events are robust. Differing endcap

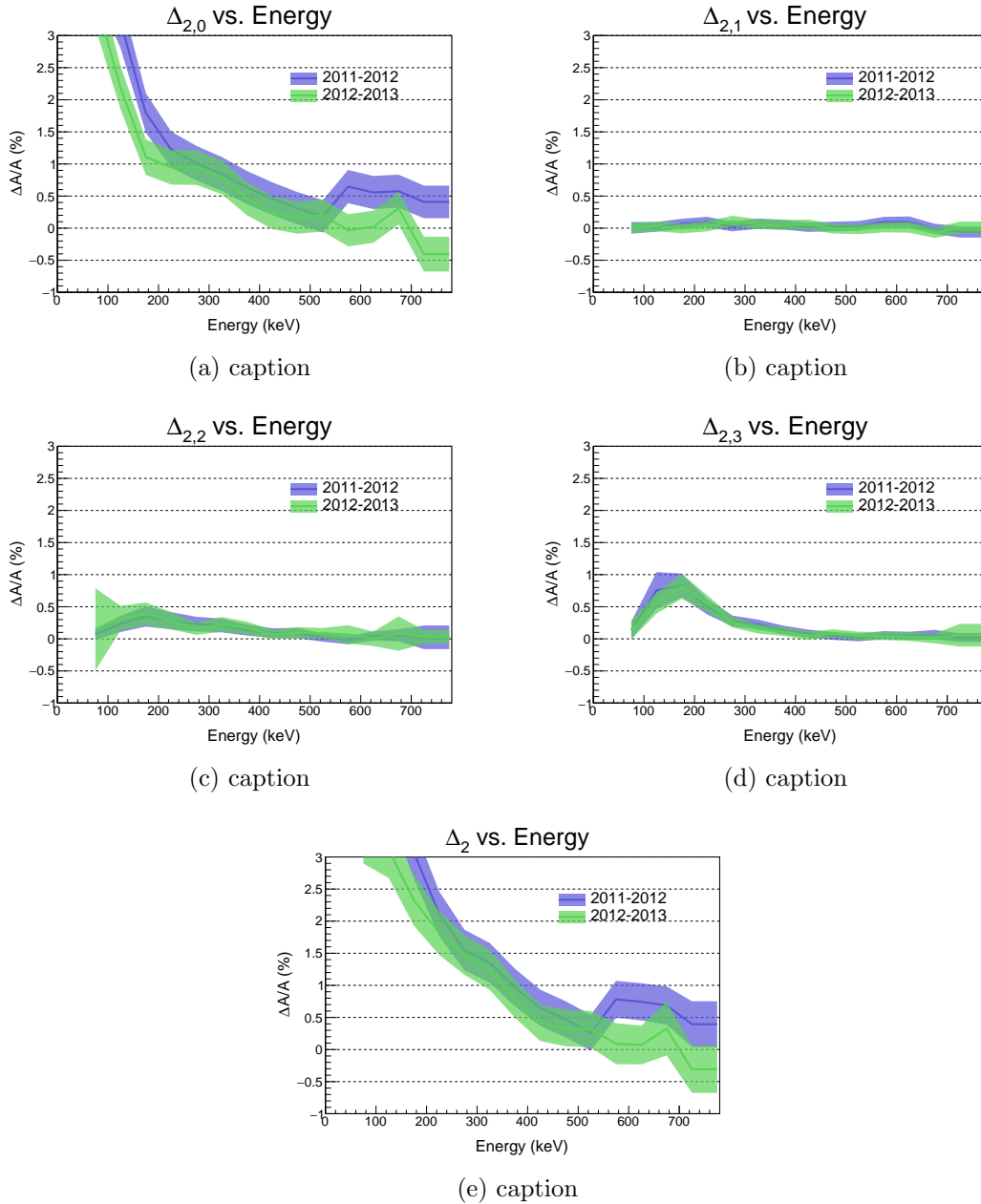


Figure 5.1: Backscattering corrections for analysis choice used in final asymmetry extraction (All event types included with 2/3 separated using the MWPC energy calibration).

thicknesses do however modify the number of misidentified Type 0 events, decreasing them in the case of thinner windows as more electrons should pass through without scattering, thus decreasing the magnitude of the  $\Delta_{2,0}$  correction by definition.

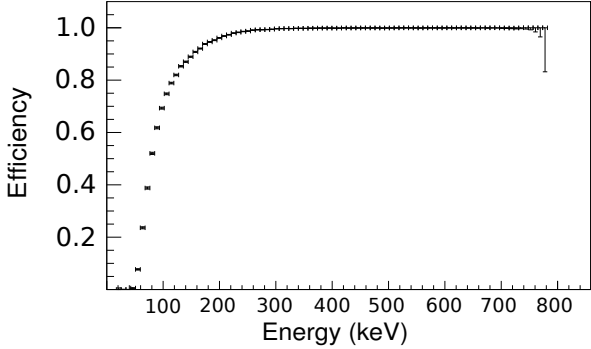


Figure 5.2: Simulated detector efficiency as a function of electron energy for electrons which pass through the decay trap endcaps.

### 5.2.2.2 Angular Acceptance, $\Delta_3$

Remember from Equation 5.1 that the asymmetric component of the decay rate depends on  $\beta \cos \theta$  and that we proceeded to integrate over one hemisphere of the detector giving  $\langle \cos \theta \rangle = 1/2$ . We also use the midpoint of the energy bin of interest when evaluating  $\beta = v/c$ , which isn't equal to the average value in a single bin due to the non-constant shape of the electron energy spectrum. What is described is an approximation of the form  $\langle \beta \cos \theta \rangle \approx \beta_{\text{mid}}/2$ . The actual value of  $\langle \beta \cos \theta \rangle$  must be determined using simulated data, as events are lost in an energy and angle dependent manner, with lower energy and high pitch angle events being most likely to be lost.  $\Delta_3$  attempts to remove this angular dependence on event acceptance while also correcting for the slight systematic effect of approximating  $\beta$  at the midpoint.

If we define the asymmetry which properly accounts for the true  $\langle \beta \cos \theta \rangle$  as  $A'$  and the asymmetry which uses our approximation  $\langle \beta \cos \theta \rangle \approx \beta_{\text{mid}}/2$  as  $A$ , then we see from 5.2.3.1 that

$$A' = \frac{A_{\text{SR}}}{\langle \beta \cos \theta \rangle \langle P \rangle} \quad (5.21)$$

and

$$A = \frac{A_{\text{SR}}}{\frac{\beta}{2} \langle P \rangle}. \quad (5.22)$$

Then from our generic definition for a systematic correction, equation 5.15, we have

$$\Delta_3(E) = \frac{A'}{A} - 1$$

and upon use of equations 5.21 and 5.22,

$$\Delta_3(E) = \frac{\frac{\beta}{2}}{\langle \beta \cos \theta \rangle} - 1. \quad (5.23)$$

From this, we see that it is sufficient to determine  $\langle \beta \cos \theta \rangle$  from simulation and calculate the energy dependent corrections.

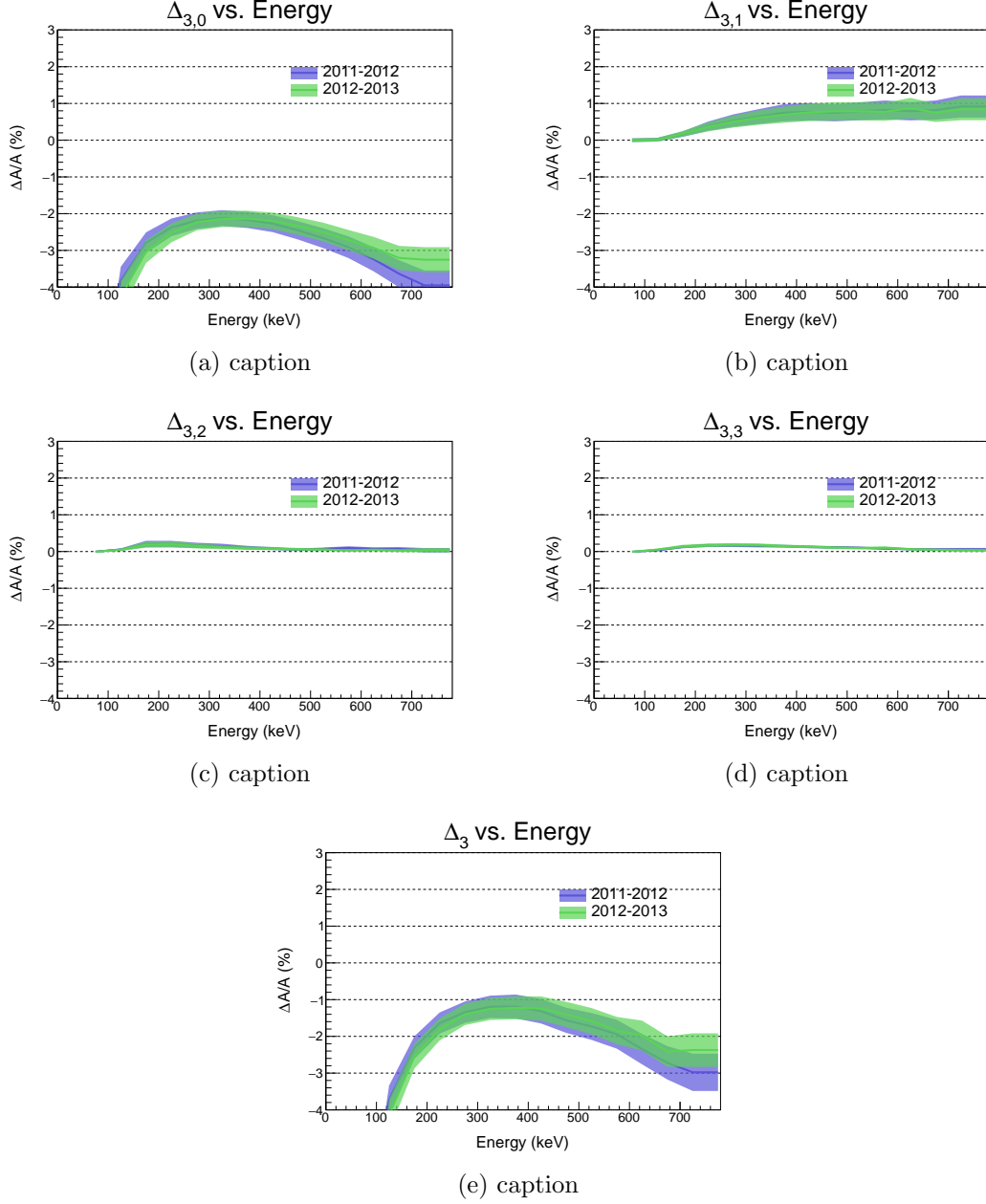


Figure 5.3:  $\cos \theta$  corrections for analysis choice used in final asymmetry extraction (All event types included with 2/3 separated using the MWPC energy calibration).

In previous analyses, this correction was done for the event population as a whole, producing only a single correction  $\Delta_3$ . New work specific to this thesis allows for

separation of this correction into individual contributions from each event type,

$$1 + \Delta_3 = (1 + \Delta_{3,3})(1 + \Delta_{3,2})(1 + \Delta_{3,1})(1 + \Delta_{3,0}). \quad (5.24)$$

This is more difficult than separating  $\Delta_2$ , as it requires more than a simple event-by-event reassignment to the proper initial direction. This requires evaluation of an average observable in the simulation, so we need a way to realize the contribution of each event type to the average. The key is to use the individual asymmetry of each event type and its respective angular correction, and then define the total correction as a function of the individual corrections.

Determination of the  $\Delta_{3,i}$  corrections starts with a new definition of the uncorrected combined asymmetry<sup>1</sup> involving the individual asymmetries of each event type. The following definitions will be useful in this derivation.

$$\begin{aligned} A &\equiv \text{Uncorrected total asymmetry} \\ A^i &\equiv \text{Asymmetry for event type } i \\ f^i &\equiv \text{Statistical weight for event type } i \\ \Delta_3^i &\equiv \text{Angle correction to } A^i \text{ for event type } i \\ A^{\text{corr},i} &\equiv \text{Corrected asymmetry for event type } i \\ A_{\text{corr},i} &\equiv \text{Total asymmetry corrected for event type } i \\ \Delta_{3,i} &\equiv \text{Angle correction to total asymmetry } A \text{ for event type } i \end{aligned}$$

Now we can define the uncorrected total asymmetry as

$$A = \sum_i f^i A^i \quad (5.25)$$

where the sum runs over the event types that are to be included in the determination of the asymmetry. As will be seen in 5.4.2.3, one can include any combination of event types to produce many different asymmetries, so this definition allows for use across any choice of event types.

Next we can define  $\Delta_3^i$ , or the angle correction to the asymmetry when only including type  $i$  events, using Equation 5.23 and only including type  $i$  events when calculating  $\langle \beta \cos \theta \rangle$ . Then we can write down an expression for the corrected asymmetry for that event type as

$$A^{\text{corr},i} = (1 + \Delta_3^i) A^i. \quad (5.26)$$

---

<sup>1</sup>This definition of the asymmetry is only used for analysis of this correction, and not for extraction of the final asymmetry.

It then follows that the total asymmetry corrected for the same event type  $i$  becomes

$$A_{\text{corr},i} = A^{\text{corr},i} + \sum_{j \neq i} f^j A^j. \quad (5.27)$$

With these relationships at hand, it is straightforward to follow the prescription to write down an expression for  $\Delta_{3,i}$  in terms of known values:

$$\begin{aligned} \Delta_{3,i} &= \frac{A_{\text{corr},i}}{A} - 1 = \frac{A_{\text{corr},i} - A}{A} = \frac{f^i(A^{\text{corr},i} - A^i)}{A} \\ &\Rightarrow \Delta_{3,i} = \frac{f^i A^i}{A} \Delta_3^i. \end{aligned} \quad (5.28)$$

The energy dependent  $\Delta_{3,i}$  corrections are shown in Figure 5.3. The impact of applying the combined  $\Delta_3$  correction is to decrease the magnitude of the measured asymmetry. This comes from the dominance of the  $\Delta_{3,0}$  portion, or the correction due to the acceptance of Type 0 events. Type 0 events are more likely lost when they are high pitch angle, low energy events. Such events carry little asymmetry information ( $\beta \cos \theta$  gets small) as seen in Equation 5.1. Measurement of an asymmetry which has these low-asymmetry events removed yields a larger magnitude asymmetry, thus necessitating a correction which decreases the magnitude of the measured asymmetry. The contribution of the backscattering events to the angular correction have the opposite sign and act to increase the magnitude of the measured asymmetry. While this may seem counterintuitive due to the detectors nominally preferentially selecting low pitch angle, high energy events, this sign is due to the backscattering events being overwhelmingly high pitch angle events. Therefore  $|\langle \cos \theta \rangle|$  over one hemisphere of the decay trap will be less than the nominal value 1/2 for all backscattering events types, calling for a correction which increases the magnitude of the measured asymmetry.

### 5.2.2.3 Uncertainty in $\Delta_{\text{MC}}$

In the analysis of the previous 2010 data set [Men+13] a conservative 25% uncertainty was applied to all Monte Carlo corrections, where the 25% came from the observed discrepancy between data and Monte Carlo backscattering fractions. The issue with such a correction is obvious when the correction itself is zero, as any percent uncertainty on that correction would also be zero. One might argue that the absence of a correction would imply the absence of an uncertainty in that correction, but we must remember that the corrections are determined using Monte Carlo simulations of finite statistics, thus even a 0% correction comes with an uncertainty. Another concern is that not all event type fractions disagree with Monte Carlo by 25%, and

the backscattering spectra that do disagree contribute little statistically to the asymmetry. Also, the asymmetry is no longer dominated by statistical uncertainty, and, as will be seen in Section 5.2.4, the uncertainty due to energy reconstruction has been reduced, thus the ultra conservative worst-case scenario may artificially limit our result. With these concerns taken into consideration, a new method was developed to assess the uncertainty on the Monte Carlo corrections motivated by the fractional discrepancies between data and simulation for each event type, denoted by  $\delta_{\text{frac}}\Delta_{i,j}$ , and the statistical fluctuations in the corrections themselves,  $\delta_{\text{stat}}\Delta_{i,j}$ .

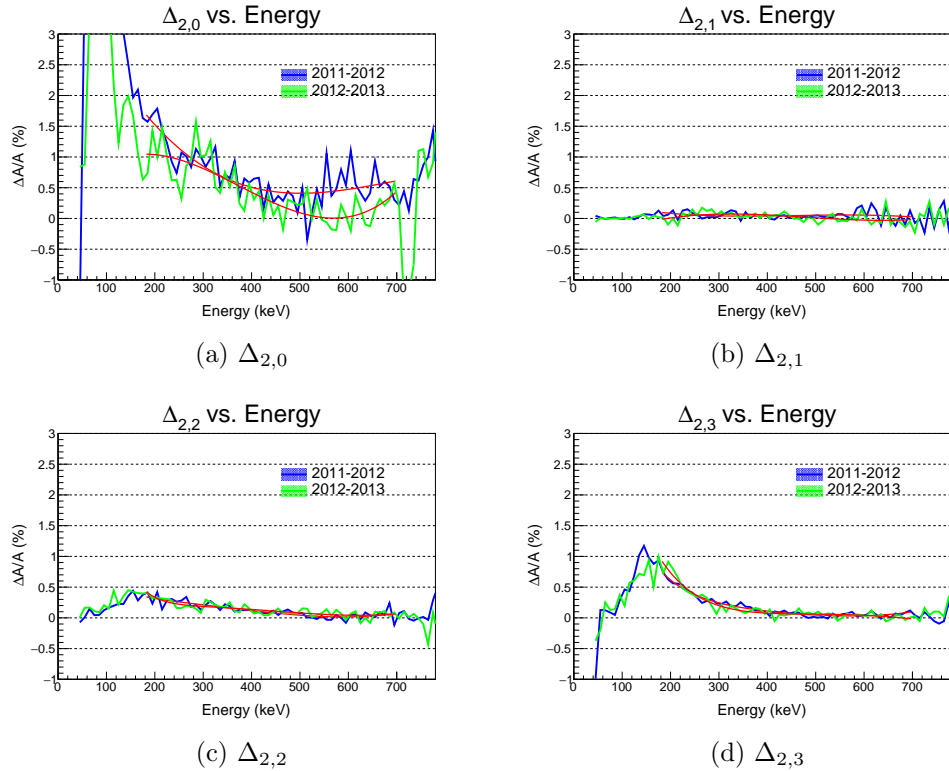


Figure 5.4: Bin-by-bin  $\Delta_2$  corrections with polynomial fit shown in red.

We further break up the statistical uncertainty into two parts and add these in quadrature to get  $\delta_{\text{stat}}\Delta_{i,j}$ . There is an obvious uncertainty that comes from simply propagating the statistics of the simulation through the correction, which we will call  $\delta_{\text{stat}}^{\text{pure}}\Delta_{i,j}$ . This uncertainty doesn't seem to account for the fluctuations we see in the correction though, as seen in Figure 5.4 panel (a) where the correction, when plotted for each energy bin, oscillates at the roughly 0.25% correction level at higher energies. This oscillation may be due to correlations between the Monte Carlo events used to simulate each run, as there are only 200 million events for each geometry and the events are chosen randomly from this pool of events. Regardless of the cause,

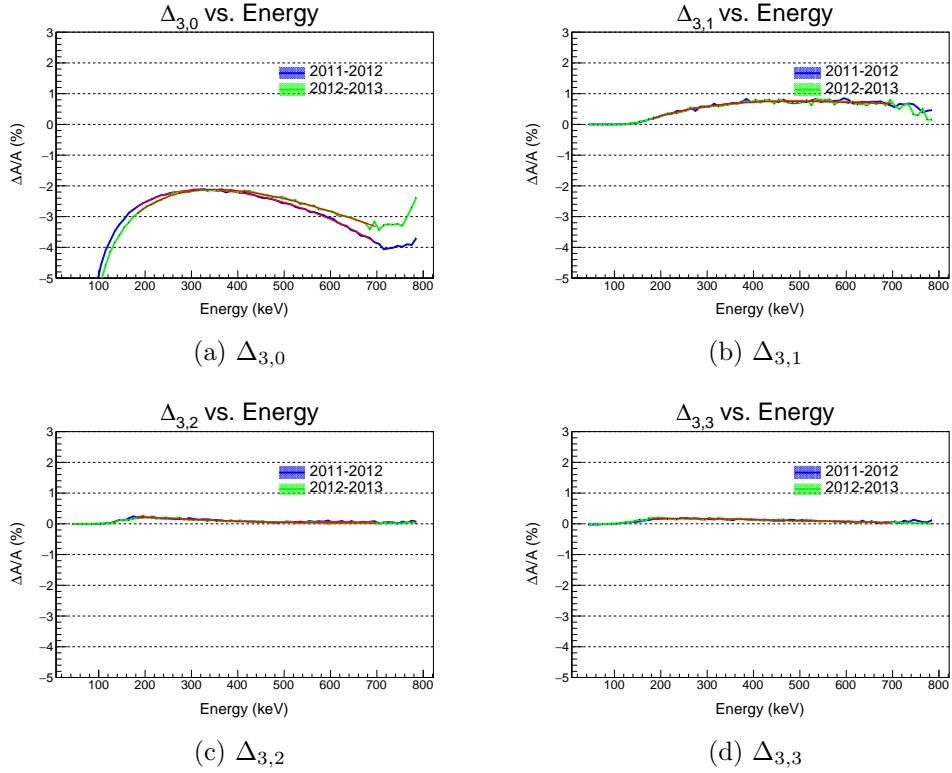


Figure 5.5: Bin-by-bin  $\Delta_3$  corrections with polynomial fit shown in red.

we account for this observed statistical fluctuation using what we call the effective statistical uncertainty, or  $\delta_{\text{stat}}^{\text{eff}} \Delta_{i,j}$ , which gives us

$$\delta \Delta_{i,j} = \sqrt{(\delta_{\text{frac}} \Delta_{i,j})^2 + (\delta_{\text{stat}} \Delta_{i,j})^2}$$

$$\delta \Delta_{i,j} = \sqrt{(\delta_{\text{frac}} \Delta_{i,j})^2 + (\delta_{\text{stat}}^{\text{pure}} \Delta_{i,j})^2 + (\delta_{\text{stat}}^{\text{eff}} \Delta_{i,j})^2}. \quad (5.29)$$

To determine the effective statistical uncertainty  $\delta_{\text{stat}}^{\text{eff}} \Delta_{i,j}$ , we begin by fitting the bin-by-bin Monte Carlo corrections with the combination of a decaying exponential and a third-order polynomial,

$$f(E) = C_0 e^{-C_1 E} + C_2 + C_3 E + C_4 E^2 + C_5 E^3. \quad (5.30)$$

The decaying exponential is included to describe the expected larger correction at low energies for backscattering which tapers off as energy increases (remember that the lower energy events are more likely to backscatter). The polynomial is included to account for any other observed shape in the corrections. The function was initially developed for use on the  $\Delta_2$  corrections, but the same functional fit worked well for  $\Delta_3$  and thus was adopted for both corrections.

Table 5.1: Values for the effective statistical uncertainties from each event type. The value is reported as the uncertainty on  $\frac{\Delta A}{A}$ .

% Uncert.	
$\delta_{\text{stat}}^{\text{eff}} \Delta_{2,0}$	$\pm 0.25$
$\delta_{\text{stat}}^{\text{eff}} \Delta_{2,1}$	$\pm 0.074$
$\delta_{\text{stat}}^{\text{eff}} \Delta_{2,2}$	$\pm 0.062$
$\delta_{\text{stat}}^{\text{eff}} \Delta_{2,3}$	$\pm 0.059$
$\delta_{\text{stat}}^{\text{eff}} \Delta_{3,0}$	$\pm 0.04$
$\delta_{\text{stat}}^{\text{eff}} \Delta_{3,1}$	$\pm 0.04$
$\delta_{\text{stat}}^{\text{eff}} \Delta_{3,2}$	$\pm 0.02$
$\delta_{\text{stat}}^{\text{eff}} \Delta_{3,3}$	$\pm 0.02$

After fitting the corrections, one can form residuals for every energy bin by subtracting the actual value of the correction from the value given by the fit. The RMS of the residuals was then calculated separately for each  $\Delta_{i,j}$  and each geometry. The effective statistical uncertainty was set to the larger RMS from the two geometries for each  $\Delta_{i,j}$  to be conservative. The values for  $\delta_{\text{stat}}^{\text{eff}} \Delta_{i,j}$  can be found in table 5.1.

Table 5.2: Values for the fractional uncertainties from each event type. The value is reported as the uncertainty on  $\frac{\Delta A}{A}$ .

% Uncert.	
$\delta_{\text{frac}} \Delta_{2,0}$	$\pm 0.10$
$\delta_{\text{frac}} \Delta_{2,1}$	$\pm 0.30$
$\delta_{\text{frac}} \Delta_{2,2}$	$\pm 0.40$
$\delta_{\text{frac}} \Delta_{2,3}$	$\pm 0.20$
$\delta_{\text{frac}} \Delta_{3,0}$	$\pm 0.10$
$\delta_{\text{frac}} \Delta_{3,1}$	$\pm 0.30$
$\delta_{\text{frac}} \Delta_{3,2}$	$\pm 0.40$
$\delta_{\text{frac}} \Delta_{3,3}$	$\pm 0.20$

Assigning values for the fractional uncertainties on each correction is more straightforward and comes from looking at the spectral discrepancies of each event type. We have a Monte Carlo predicted spectrum and a data spectrum for each of our event types, so we can construct a fractional residual between these spectra as seen in Figure 5.6 simply using  $\frac{\text{MC}}{\text{Data}} - 1$ . Then by choosing approximately the maximum fractional

Table 5.3: Actual integrated event type fractions as percent of total events. Also reported is the % difference between Monte Carlo and data spectra for each event type. These are calculated over an energy window of 190-740 keV, chosen to minimize the total uncertainty as will be shown.

	Type 0	Type 1	Type 2	Type 3
Data	94.44	3.31	1.09	1.15
MC	94.86	3.30	0.78	1.06
% Diff.	0.44	-0.29	-28.24	-7.91

residual over energies of interest (180-700 keV, starting at roughly the lower limit on our analysis energy window and ending when the statistics drop below 10% of the maximum rate), we conservatively set the fractional discrepancy of our corrections. The values of  $\delta_{\text{frac}}\Delta_{i,j}$  are tabulated in table 5.2. One should note that the integrated agreement between Monte Carlo and data is much better than these conservative fractional uncertainties, as seen in table 5.3.

#### 5.2.2.4 Fidelity of Corrections

As mentioned in Section 3.4.1.3, an asymmetry equal to the 2017 PDG value ( $A_0 = -0.1184$ ) was incorporated into the Monte Carlo event generator, along with all radiative and recoil order effects. This allows us to extract the Monte Carlo corrections from event distributions which mimic our measurement populations, but it also allows us to apply our corrections to the Monte Carlo rates to see what we extract for  $A_0$ . Because we process the simulations such that we have complementary simulated data for every  $\beta$ -decay run (with the Monte Carlo having  $\approx 16 \times$  data statistics), we can run the simulated data through the same asymmetry extraction method and compare the extracted fully-corrected asymmetries to the PDG input value. Figure 5.7 shows the Monte Carlo corrected asymmetries for all analysis choices. The agreement across all event types indicates the energy dependent Monte Carlo corrections are self-consistent.

### 5.2.3 Polarimetry Correction

As mentioned in Section 3.7, an equilibrium population of neutron spins develops within the decay trap during a  $\beta$ -decay run. While this population is dominated by the spin-state of choice (> 99%), precise determination of the average polarization is important as it directly affects the final extracted asymmetry as shown in equation

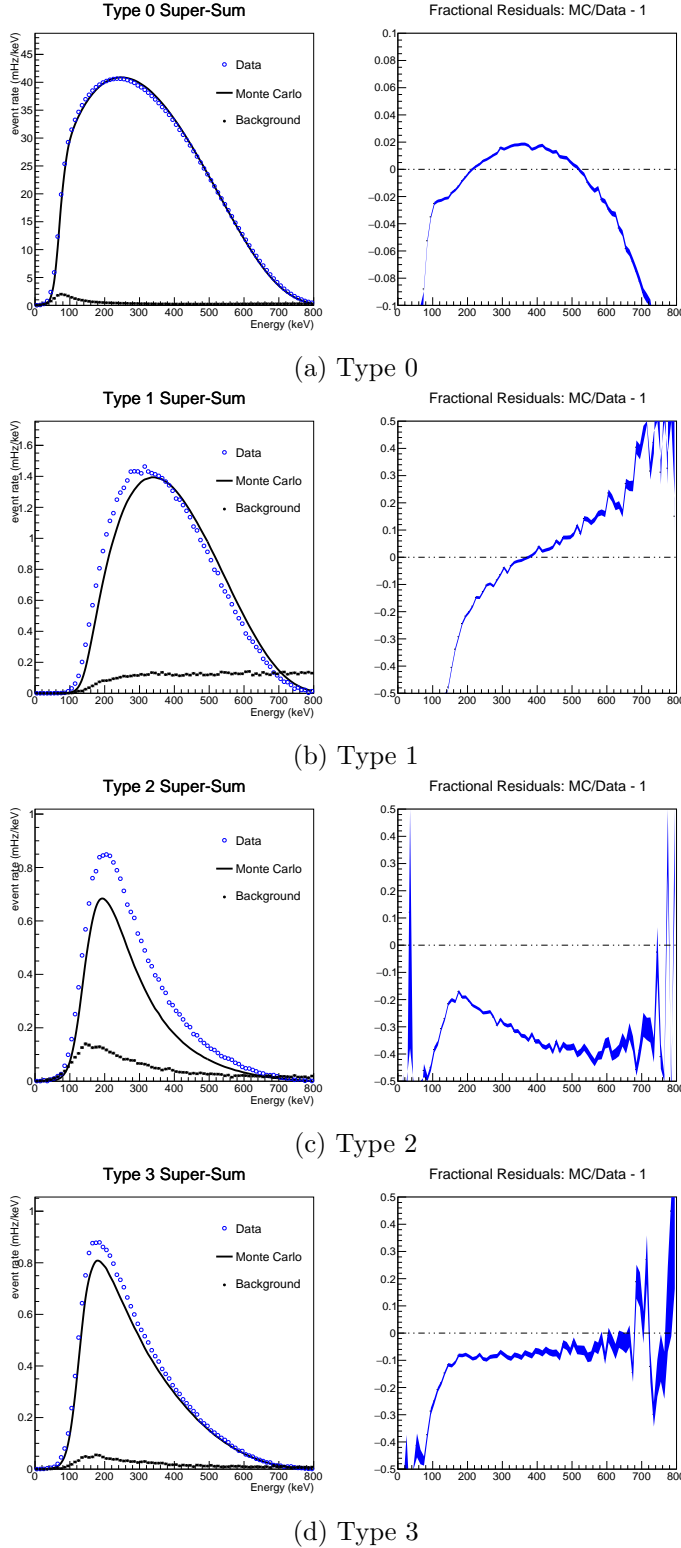
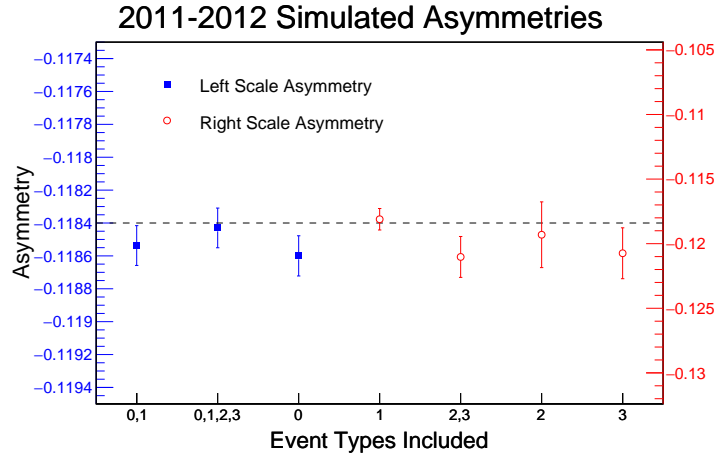
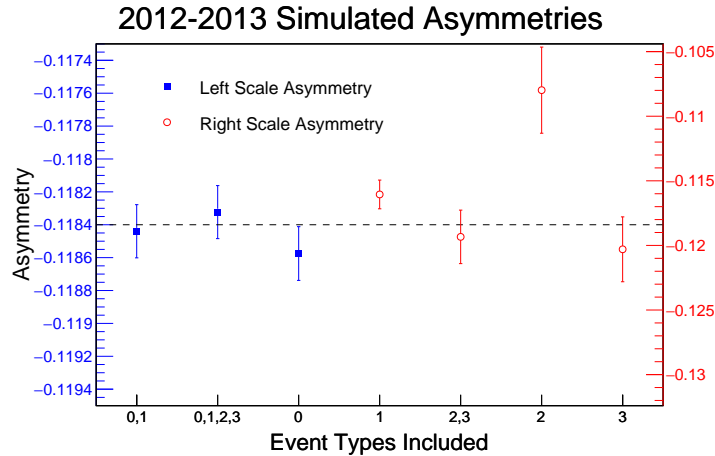


Figure 5.6: Subfigures are broken into each event type. Left of each subfigure shows electron energy spectra for background subtracted data (blue open circles), Monte Carlo (black solid line), and the background (black closed circles). The right plot in each subfigure shows the fractional residual between background subtracted data and Monte Carlo, which is used when applying the conservative fractional uncertainty on the Monte Carlo corrections.



(a) 2011-2012



(b) 2012-2013

Figure 5.7: Extracted asymmetries from Monte Carlo data processed to mimic the experimental data. The dashed line indicates the 2017 PDG value  $A_0 = -0.1184$  which was input into the simulation, thus the goal upon extraction of the final asymmetry parameter. The blue closed points indicate analysis choices that include type 0 events and utilize the scale on the left vertical axis values. The red open circles include only backscattering event types and use the right vertical axis values.

5.13. The determination of the polarization values was carried out in a separate analysis by Eric Dees of North Carolina State University. The values for the  $\pm$  spin-flipper states for each geometry are given in table 5.4.

There are two options for applying a polarization correction, namely calculate an average polarization  $\langle P \rangle$  which is averaged over both spin states and simply divide this out of the measured asymmetry as shown in Equation 5.13, or utilize the separate

Table 5.4: Results for average polarization fractions for each dataset in spin-flipper off (–) and spin-flipper on (+) states.

2011-2012		2012-2013	
$\langle P \rangle_-$	$\langle P \rangle_+$	$\langle P \rangle_-$	$\langle P \rangle_+$
0.9970(30)	0.9939(25)	0.9979(15)	0.9952(20)

$\langle P \rangle_\pm$  values. The second method is not a simple division of either term but rather a more complicated combination due to the usage of the super-ratio. This second method was adopted for this analysis and is described below.

### 5.2.3.1 Extraction of $A_0$ using $\langle P \rangle_+$ and $\langle P \rangle_-$

Using each of the  $\langle P \rangle_\pm$  values requires modification of our initial asymmetry formalism from 5.1 [You17]. We can no longer make the assumption that  $\langle P \rangle_+ = \langle P \rangle_-$  if we want to treat them separately. Let us start our new derivation from Equation 5.6, which now becomes

$$\Gamma_{1,2}^\pm(E) = C' \cdot S(E) \cdot \epsilon_\pm \cdot \eta_{1,2} \left[ 1 \pm_{1,2} (\mp \langle P \rangle_\pm) \cdot A(E) \frac{\beta}{2} \right] \quad (5.31)$$

under the substitution  $\langle P \rangle \rightarrow \langle P \rangle_\pm$ .

The super-ratio now must be written as

$$R = \frac{\Gamma_1^+ \cdot \Gamma_2^-}{\Gamma_1^- \cdot \Gamma_2^+} = \frac{\left[ 1 + (-\langle P \rangle_+) A(E) \frac{\beta}{2} \right] \left[ 1 - (+\langle P \rangle_-) A(E) \frac{\beta}{2} \right]}{\left[ 1 + (+\langle P \rangle_-) A(E) \frac{\beta}{2} \right] \left[ 1 - (-\langle P \rangle_+) A(E) \frac{\beta}{2} \right]},$$

and upon letting  $\xi = A(E) \frac{\beta}{2}$  we have

$$R = \frac{(1 - \xi \langle P \rangle_+) (1 - \xi \langle P \rangle_-)}{(1 + \xi \langle P \rangle_-) (1 + \xi \langle P \rangle_+)} \quad (5.32)$$

We are interested in solving for  $A(E)$ , or  $\xi$ , so we can rearrange 5.32 to give

$$\begin{aligned} R (1 + \xi \langle P \rangle_-) (1 + \xi \langle P \rangle_+) &= (1 - \xi \langle P \rangle_+) (1 - \xi \langle P \rangle_-), \\ R (1 + \xi (\langle P \rangle_- + \langle P \rangle_+) + \xi^2 \langle P \rangle_- \langle P \rangle_+) &= (1 - \xi (\langle P \rangle_- + \langle P \rangle_+) + \xi^2 \langle P \rangle_- \langle P \rangle_+), \\ 0 &= \xi^2 \langle P \rangle_- \langle P \rangle_+ (1 - R) - \xi (\langle P \rangle_- + \langle P \rangle_+) (1 + R) + (1 - R), \end{aligned}$$

and

$$0 = \xi^2 \langle P \rangle_- \langle P \rangle_+ - \xi (\langle P \rangle_- + \langle P \rangle_+) \left( \frac{1 + R}{1 - R} \right) + 1, \quad (5.33)$$

which has roots (let  $\gamma = \frac{1+R}{1-R}$ )

$$\xi = \frac{\gamma(\langle P \rangle_- + \langle P \rangle_+) \pm \sqrt{\gamma^2(\langle P \rangle_- + \langle P \rangle_+)^2 - 4\langle P \rangle_-\langle P \rangle_+}}{2\langle P \rangle_-\langle P \rangle_+}. \quad (5.34)$$

To choose the proper root, we set  $\langle P \rangle_- = \langle P \rangle_+ = \langle P \rangle$  and determine which root returns the original expression for the super-ratio as given in equations 5.9 and 5.2.3.1, namely

$$A_{\text{SR}} = \frac{1 - \sqrt{R}}{1 + \sqrt{R}} = \langle P \rangle A(E) \frac{\beta}{2}.$$

Upon doing so, we find that the negative root is the correct solution, which results in a new expression for  $A(E)$  of

$$A(E) = \frac{\gamma(\langle P \rangle_- + \langle P \rangle_+) - \sqrt{\gamma^2(\langle P \rangle_- + \langle P \rangle_+)^2 - 4\langle P \rangle_-\langle P \rangle_+}}{\beta\langle P \rangle_-\langle P \rangle_+}. \quad (5.35)$$

The uncertainty on  $A(E)$  from such an application of the polarization is determined via the usual error propagation,

$$\delta_P A(E) = \sqrt{\left(\frac{\partial A(E)}{\partial \langle P \rangle_+}\right)^2 (\delta \langle P \rangle_+)^2 + \left(\frac{\partial A(E)}{\partial \langle P \rangle_-}\right)^2 (\delta \langle P \rangle_-)^2}. \quad (5.36)$$

Although this method of determining the measured asymmetry is more rigorous than using a polarimetry value averaged over the two spin states, the effect on the asymmetry is at the  $\Delta A \approx 10^{-6}$  level as shown by K. Hickerson in [Hic13]. A change in the asymmetry of this magnitude is small compared to the uncertainty from the polarization alone and inconsequential compared to the final uncertainty on the asymmetry.

#### 5.2.4 Energy Reconstruction

The energy enters the calculation of the asymmetry in the  $\beta$  term ( $v/c$  of the electron) in Equation 5.2.3.1, and thus it is essential to assess how well we can reconstruct the initial energy of an electron. The obvious choice for determining the efficacy of our energy calibration is to use the calibration peaks themselves and compare to Monte Carlo simulation. We apply the calibrations from Chapter 4 to the data source peaks in all individual source runs, which maps the detector response to a reconstructed peak energy ( $E_{\text{recon}}^{\text{data}}$ ), and then we apply our detector response model to the simulation peaks and extract a Monte Carlo reconstructed peak energy ( $E_{\text{recon}}^{\text{MC}}$ ). We can then calculate a residual for every single run (and each conversion peak within that run)

via Residual =  $E_{\text{recon}}^{\text{data}} - E_{\text{recon}}^{\text{MC}}$ . Upon collecting all of the residuals for each of the conversion electron peaks (Figures 5.8 and 5.9), we calculate <sup>2</sup> the mean and sigma of the distributions, with values reported in table 5.5, and use them as the data points seen in Figure 5.10. These points are a measure of the accuracy of the energy calibration at four discrete energies, the mean energies of the conversion electron lines themselves.

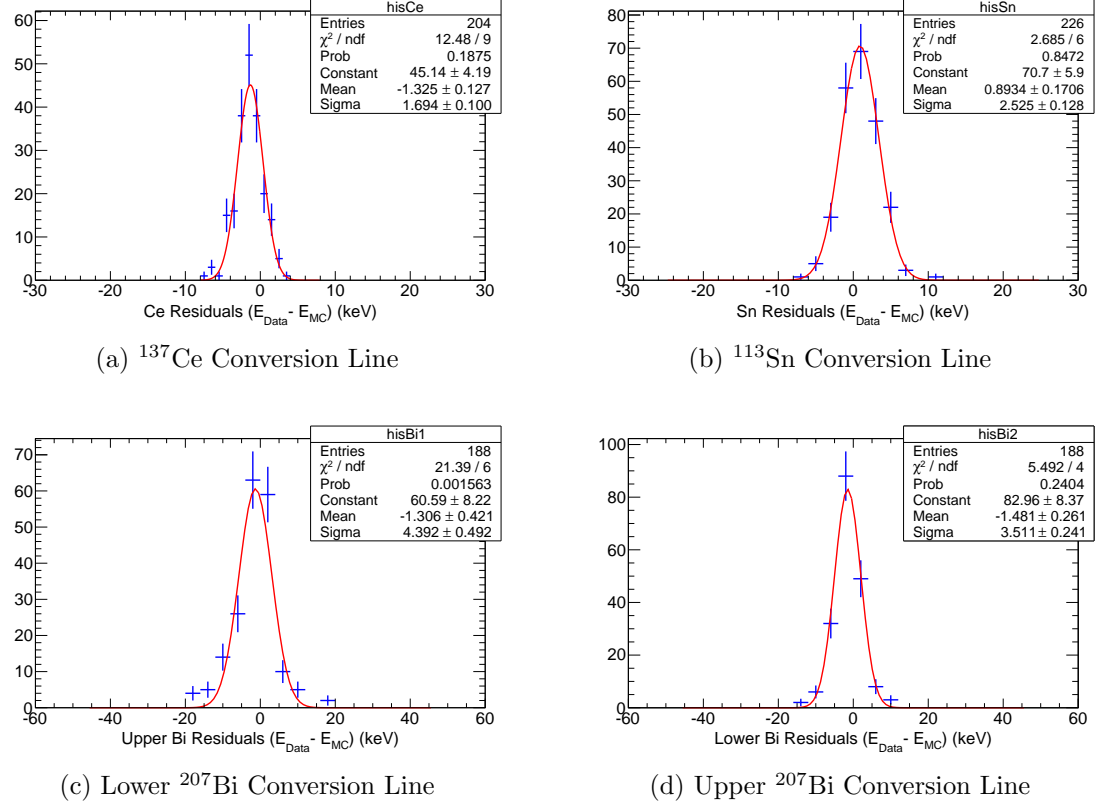


Figure 5.8: Distributions of the residuals for each conversion electron source line used in the 2011-2012 calibration. The mean and sigma reported in the fit box are not the same as those used in the energy uncertainty, as they are the results of the fit and not the calculated mean.

The residuals at these discrete energies do not themselves tell us how well we do at intermediate energies. In the past, a conservative uncertainty envelope was drawn to encompass the calibration points [Men+13; Men14]. For the analysis presented here, a more quantitative determination of the uncertainty envelope was employed via methods developed by K. Hickerson for determination of limits on  $b_n$  from the previous

<sup>2</sup> The mean and sigma are calculated rather than fitted so as to not neglect any non-Gaussian tails in the distributions.

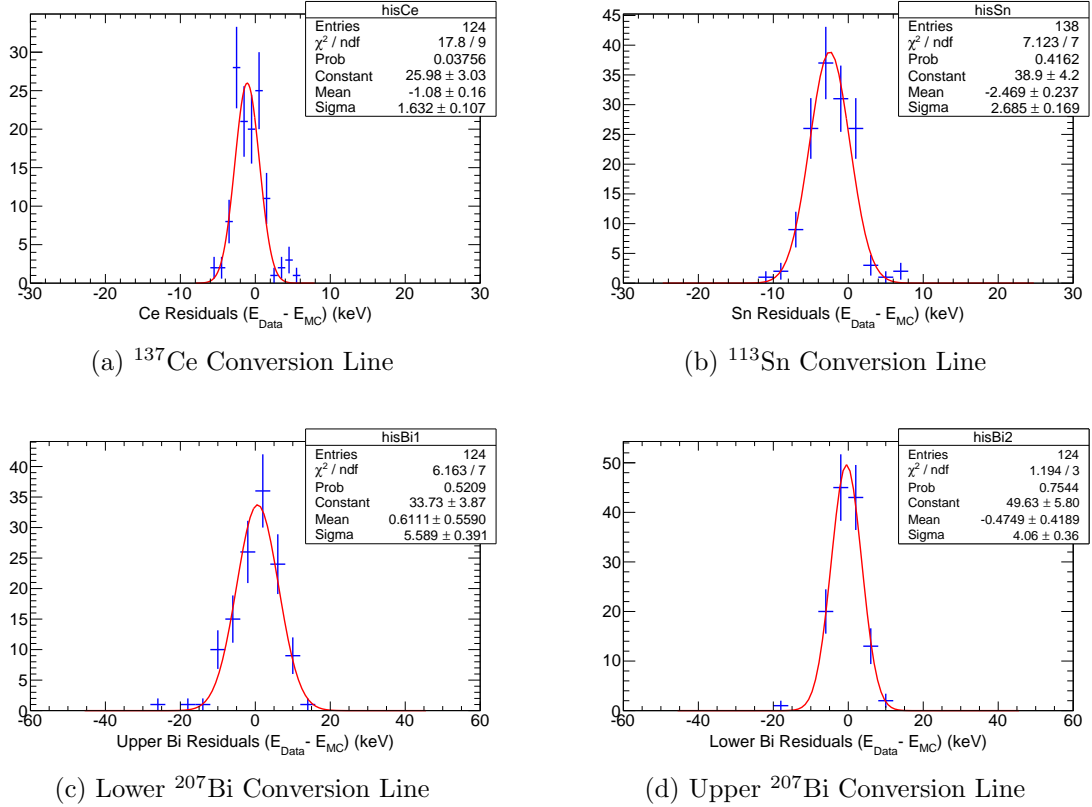


Figure 5.9: Distributions of the residuals for each conversion electron source line used in the 2012-2013 calibration. The mean and sigma reported in the fit box are not the same as those used in the energy uncertainty, as they are the results of the fit and not the calculated mean.

Table 5.5: Mean and  $\sigma$  of each conversion electron residual distribution as used in the energy uncertainty, Figure 5.10.

	2011-2012	2011-2012
$^{137}\text{Ce}$	$-1.43 \pm 1.81 \text{ keV}$	$-0.80 \pm 2.00 \text{ keV}$
$^{113}\text{Sn}$	$0.91 \pm 2.52 \text{ keV}$	$-2.24 \pm 2.87 \text{ keV}$
$^{207}\text{Bi}$ (lower)	$-1.36 \pm 3.81 \text{ keV}$	$-0.39 \pm 3.90 \text{ keV}$
$^{207}\text{Bi}$ (upper)	$-1.55 \pm 5.77 \text{ keV}$	$0.01 \pm 6.40 \text{ keV}$

UCNA spectrum ([Hic+17]). In short, the envelope is produced by sampling the coefficients of a quadratic,  $f(E_{\text{recon}})$ , from distributions that reproduce the residual data points seen in Figure 5.10 with  $1\sigma$  deviation. This obviously results in an asymmetric uncertainty band due to the asymmetric distribution of the data points about zero, but our conservative approach is to take the worst case uncertainty at every energy and use this as our symmetric final uncertainty. This produces the

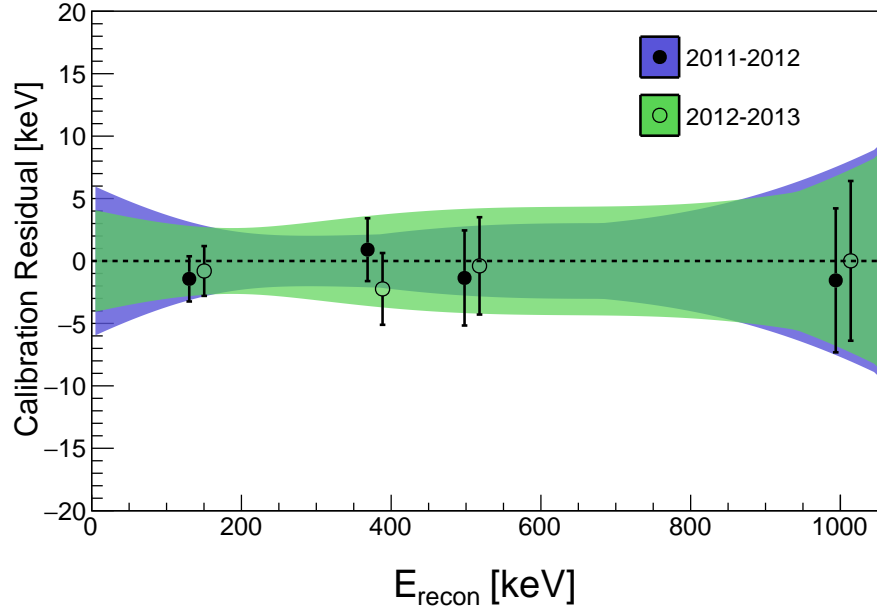


Figure 5.10: Plot of energy uncertainty vs. reconstructed energy. The points plotted are the mean and  $\sigma$  of all reconstructed calibration peaks of  $^{137}\text{Ce}$ ,  $^{113}\text{Sn}$ , and the lower and upper  $^{207}\text{Bi}$  peaks in that order. The  $x$ -axis offset in the 2011-2012 and 2012-2013 points is artificial and only meant for visualization. The bands represent the energy uncertainty at any given electron energy for the two data sets.

symmetric uncertainty band in Figure 5.10.

The symmetric worst case uncertainty band allows us to report a systematic uncertainty rather than a correction and an uncertainty from the energy reconstruction. The energy dependent uncertainty on  $A_0$  for the maximal energy uncertainty (outer edge of the uncertainty envelope) is shown in Figure 5.11. The uncertainty is then weighted by the data statistics in each bin to determine the total uncertainty in the final asymmetry, producing energy uncertainties of 0.17% and 0.25% for 2011-2012 and 2012-2013 respectively.

### 5.2.5 Background Contributions

The desired events (foreground) are superposed with background triggering events from something other than a neutron  $\beta$ -decay within the decay trap. Such unwanted events include background ambient gamma rays, cosmic rays, and other unforeseen events which trigger the detector. Gamma ray events are highly suppressed due to the requirement of a coincidence trigger between the MWPC and the scintillator, and cosmic ray muon events are removed using a series of muon veto detection packages,

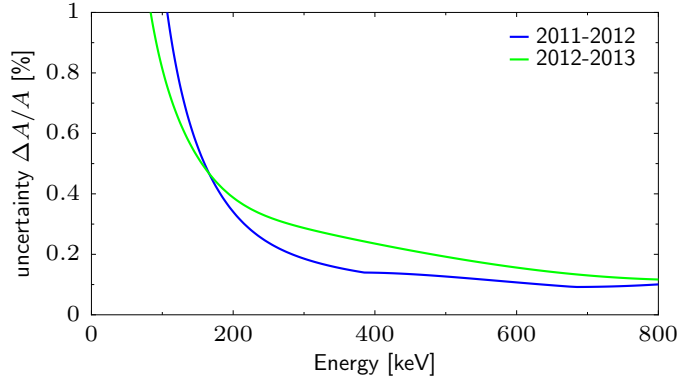


Figure 5.11: Plot of uncertainty on  $A_0$  from the energy calibration vs. reconstructed energy for each of the 2011-2012 and 2012-2013 geometries. Weighting the energy dependent uncertainties shown here by the experimental statistics in each energy bin produces the final uncertainty on the extracted asymmetries.

which leaves the rest of the background to be subtracted using direct measurements of the electron spectrum in the absence of neutrons in the decay trap.

#### 5.2.5.1 Background Subtraction

Accompanying every  $\beta$ -decay run is a dedicated background run roughly 1/4 the length of the data taking run. The background events are processed in an identical manner to the data events and the rates are subtracted from the data rates. The uncertainties are propagated into the final rate, so in the absence of any non-statistical background fluctuations, the uncertainties from the backgrounds are inherently included in the extraction of the asymmetry. The background spectra for the different event types can be seen in figures 5.12 and 5.13.

The typical ratio between data and background rates is roughly 70:1 in 2011-2012 and 40:1 in 2012-2013 when integrated over the electron energy range 190-740 keV, with the difference attributed to source performance issues. Figures 5.14 and 5.15 show the integrated rates in  $\beta$ -decay runs and background runs for the two geometries. The splitting in the  $\beta$  run rates is due to the difference between a spin-flipper “on” vs. spin-flipper “off” run, as the flipper “on” loading efficiency is  $\sim 2/3$  that of a flipper “off” run. This difference results from electrons being boosted by roughly 120 neV from the change in potential associated with a spin flip in the  $\sim 1$  T field in the AFP spin-flipper, which moves a portion of the neutrons out of the UCN energy regime and thus they are no longer confined within the decay trap.

The background subtraction transforms the rates in every bin in the following

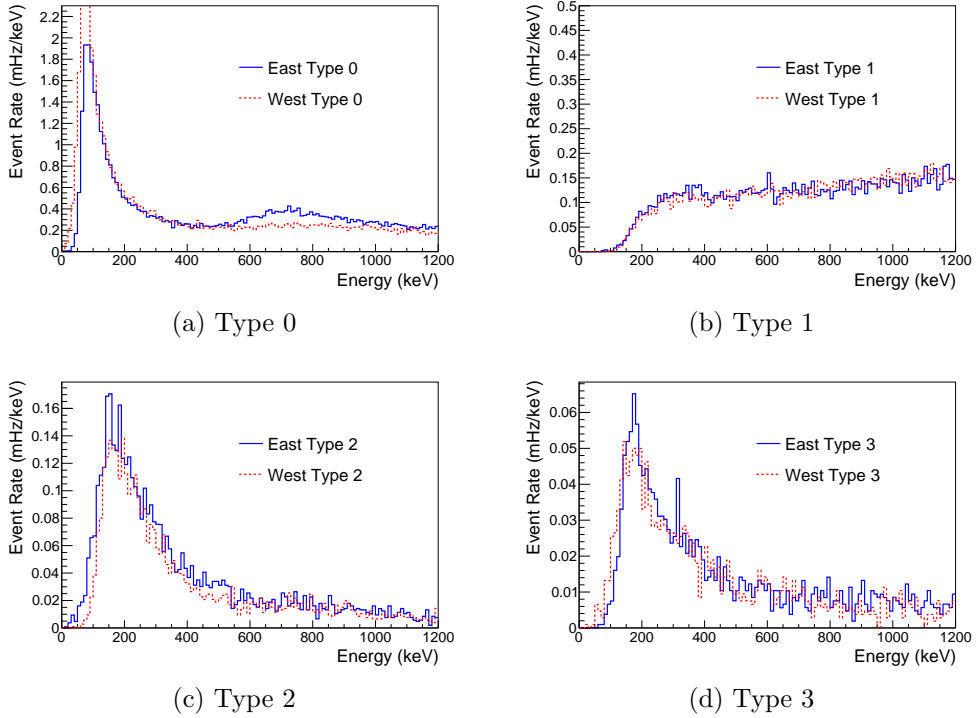


Figure 5.12: Total background spectra summed over all background runs for each event type in 2011-2012.

manner:

$$r_{\text{final},i} = \left( \frac{N_{\text{data},i}}{T_{\text{data}}} - \frac{N_{\text{bg},i}}{T_{\text{bg}}} \right) \pm \sqrt{\left( \frac{\sqrt{N_{\text{data},i}}}{T_{\text{data}}} \right)^2 + \left( \frac{\sqrt{N_{\text{bg},i}}}{T_{\text{bg}}} \right)^2} \quad (5.37)$$

where  $r_{\text{final},i}$  is the background subtracted rate in bin  $i$ ,  $N$  refers to counts,  $T$  is the total time of a given run, and the subscript “data/bg” indicates whether the quantity comes from either the  $\beta$ -decay run or the background run. Equation 5.37 holds true as long as the counts in both the data and background run are large enough so that Poisson statistics may be assumed. Below some count threshold ( $N < 25$  for this analysis), we resort to an estimate of the uncertainty in a given bin. To do this, we utilize higher statistics reference spectra created by summing over all background runs for each spin state ( $\pm$ ) and detector side (1,2) and apply the same data selection cuts (5.4.2.1) used for asymmetry analysis. The reference spectra are essentially combinations of those seen in figures 5.12 and 5.13. The expected background rate to be used in properly determining the background uncertainty is then determined by multiplying the reference background fraction in some energy bin by the total

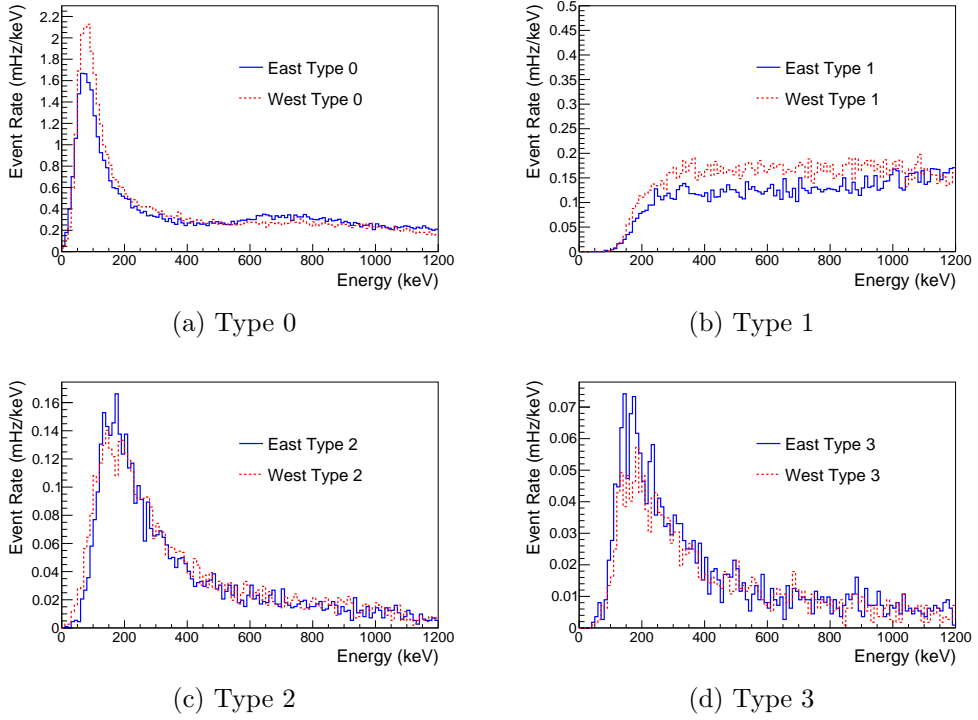


Figure 5.13: Total background spectra summed over all background runs for each event type in 2011-2012.

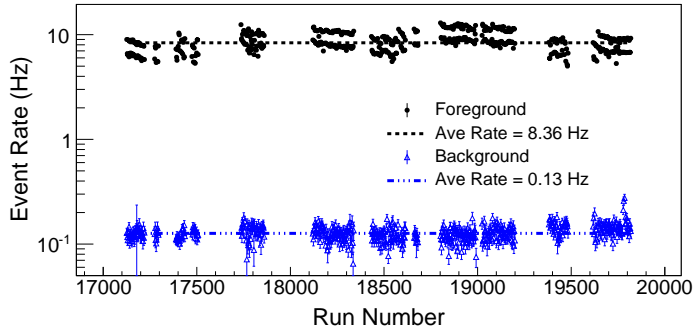
background counts in the background run, or

$$r_{\text{bg},i} = \frac{1}{T_{\text{bg}}} \left( N_{\text{bg},i} \pm \sqrt{N_{\text{bg,tot}} \frac{N_{\text{ref},i}}{N_{\text{ref,tot}}}} \right), \quad (5.38)$$

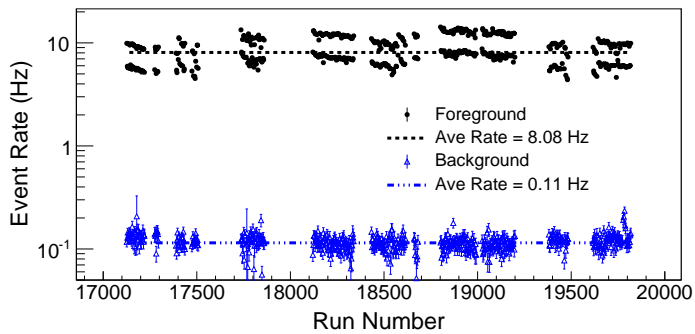
where subscript “ref” refers to the reference spectrum of background counts and subscript “tot” refers to the integrated total counts in the respective spectrum. This new background rate and uncertainty (note that only the uncertainty changes when  $N < 25$ ) are then used in Equation 5.37. This method removes large statistical variation in the background uncertainties when the counts are low and gives an uncertainty to background rates that could be zero for a given bin.

### 5.2.5.2 Neutron Generated Backgrounds

Substantial work done previously by M. Mendenhall pioneered a thorough determination of the systematic correction to  $A_0$  from neutron generated backgrounds, as can be found in [Men14]. Neutron generated backgrounds cannot be accounted for using normal background subtraction as the decay trap is void of neutrons during background runs. The correction comes mainly from UCN that escape the decay



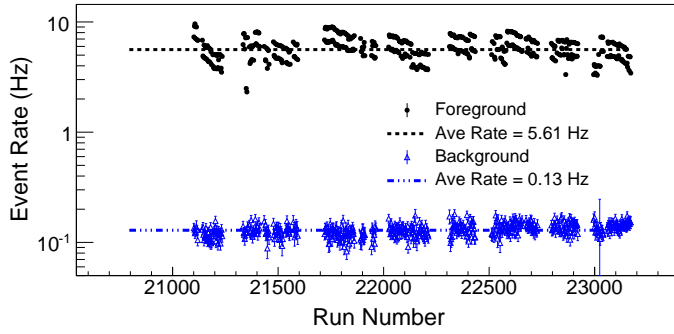
(a) East Side



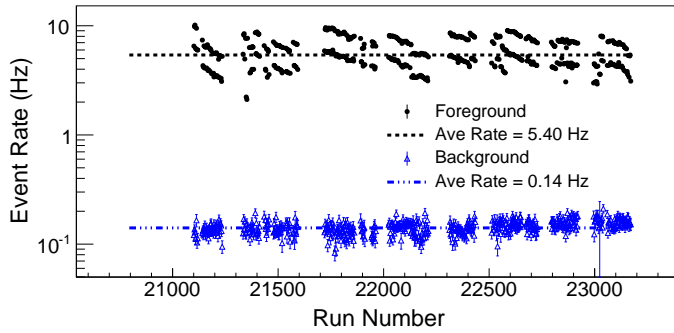
(b) West Side

Figure 5.14: Integrated event rates for 2011-2012 East and West sides. The splitting in the  $\beta$  run rates is due to the difference between a spin-flipper “on” vs. spin-flipper “off” run, as the flipper “on” loading efficiency is approximately 2/3 that of a flipper “off” run.

trap and interact with other components of the apparatus. The two main mechanisms studied were neutron capture on the aluminum wirechamber entrance and exit windows ( $n + ^{27}\text{Al} \rightarrow ^{28}\text{Al}$ ) and on hydrogen in the scintillators ( $n + ^1\text{H} \rightarrow ^2\text{H}$ ).  $^{28}\text{Al}$  subsequently  $\beta$ -decays (2863 keV endpoint) into an excited state of  $^{28}\text{Si}$  which emits a 1779 keV gamma upon relaxing to the ground state. The excited deuteron falls to its ground state via emission of a 2223 keV gamma. Each of these decay products can interact with the scintillator, so the presence of such interactions would create a small excess of events in the background subtracted spectra above the  $\beta$ -decay endpoint, a common characteristic seen in both 2010 (used in [Men14]) and in the current analysis. Since the beyond endpoint rates agree within statistics and no changes were made to hardware outside the decay trap, adoption of the previously determined correction  $\Delta A/A = 0.01(2)\%$  is assumed for this analysis.



(a) East Side



(b) West Side

Figure 5.15: Integrated event rates for 2012-2013 East and West sides. The splitting in the  $\beta$  run rates is due to the difference between a spin-flipper “on” vs. spin-flipper “off” run, as the flipper “on” loading efficiency is approximately 2/3 that of a flipper “off” run.

### 5.2.5.3 Veto Efficiency Uncertainty

Gamma events and muon events that are vetoed by checking for coincidence between the scintillators and another detector of the experiment could contribute an uncertainty to the asymmetry if the detector used for determining a coincidence behaves erratically. If all components are fairly stable in time, then even events which pass the veto due to inefficiency would be subtracted out using the typical background subtraction method mentioned above. To be conservative though, the uncertainty from the previous analysis of  $\pm 0.03\%$  was applied to the final asymmetry in case of any non-statistical fluctuations in the background rates.

## 5.2.6 Miscellaneous Systematic Corrections and Uncertainties

While the core Monte Carlo corrections described above make up the majority of the simulation-motivated corrections due to effects from the apparatus, there are several corrections and/or uncertainties determined from other Monte Carlo studies. These systematic effects are not determined on an energy dependent basis, but rather integrated over the final analysis window.

### 5.2.6.1 Wirechamber Efficiency

Since a dual trigger between the MWPC and the scintillator is required to differentiate between a background gamma ray and an electron (remember the MWPC is highly insensitive to gammas), electron events that fail to trigger the MWPC but trigger the scintillator will be misidentified as a gamma and will not be included in the asymmetry analysis. Higher energy, lower pitch angle events deposit less energy in the MWPC, thus these events suffer misidentification more often from MWPC efficiencies < 100%. These same higher energy, lower pitch angle events contribute more to the raw asymmetry as seen by rewriting Equation 5.2.3.1 and leaving the  $\cos \theta$  dependence in,

$$A_{\text{SR}} = \langle P \rangle A(E) \beta \langle \cos \theta \rangle. \quad (5.39)$$

Missing these events effectively decreases the measured asymmetry, thus a systematic correction for such an effect should act to increase the magnitude of the measured asymmetry.

The goal for determining such a correction is to use simulated data to model the effect the efficiency of our MWPCs has on our measured asymmetry. First we need to determine the efficiency from data. A set of long  $^{113}\text{Sn}$  runs with accompanying background runs were conducted at the end of the 2011-2012 run period. Using the background subtracted rates for MWPC triggering events (identified as an electron) and non-MWPC triggering events (identified as a gamma ray), one can set a lower limit on the wirechamber efficiency at the energy of the  $^{113}\text{Sn}$  peak by calculating the ratio

$$\eta_{\text{MWPC}} = \frac{r_{\text{trigger}}}{r_{\text{trigger}} + r_{\text{NoTrigger}}}. \quad (5.40)$$

This is a lower limit because there could be contamination from actual gamma rays emitted by the  $^{113}\text{Sn}$  source, but this contribution is quite small due to the gammas not being confined within the decay trap by the 1 T magnetic field and the small solid

angle acceptance of the detectors for gammas originating at the center of the decay trap. The efficiencies found were  $\eta_{\text{MWPC}} = 0.99912(40)$  and  $\eta_{\text{MWPC}} = 0.99974(36)$  for the East and West detectors respectively.

The above efficiencies are only valid at the energy of the  $^{113}\text{Sn}$  source, which is not ideal for use in the simulation as it stands. Instead, one would like to convert this into an energy deposition trigger threshold within the wirechamber. Using an MWPC energy threshold rather than an efficiency automatically creates an energy dependent efficiency, as the higher energy, lower pitch angle electrons will deposit less energy in the MWPC and will be less likely to trigger. Determining the threshold is done using simulations of the long  $^{113}\text{Sn}$  runs. By scanning the MWPC threshold up from 0 keV, one can calculate the point at which the simulated wirechamber efficiency matches the wirechamber efficiency found using the data. The energy thresholds for the East and West MWPCs occur at roughly 0.969 keV and 0.874 keV respectively.

At this point, the integrated asymmetry is calculated for  $\beta$ -decay simulations with and without the MWPC efficiency in place, and then the correction is calculated in the usual way,

$$\Delta_{\text{MWPC}} = \frac{A_{\text{noThresh}}}{A_{\text{Thresh}}} - 1, \quad (5.41)$$

where the corrected asymmetry is that without the threshold since we want to remove the dependence on the MWPC efficiency. This was done for fifty independent batches of simulations, and the resulting fifty corrections were histogrammed and fit with a Gaussian. The mean of this Gaussian gives the correction, and the error on the mean gives the uncertainty. The final  $\Delta_{\text{MWPC}}$  corrections are  $+0.13(1)\%$  and  $+0.11(1)\%$  for 2011-2012 and 2012-2013.

### 5.2.6.2 Gain Uncertainty

Gain corrections are applied on a run-by-run basis, so variations of the gain within each run will present themselves as an additional energy uncertainty. To study this effect, the individual endpoint values of every run from the data were histogrammed and the  $1\sigma$  spread in the distribution was attributed to possible uncertainty in the gain during an individual run. Assuming that the gain is a non-energy-dependent multiplicative factor, one can extract the fractional energy uncertainty for all energies by calculating the ratio of the uncertainty at the endpoint to the endpoint energy. The spread of the endpoint values was determined to be  $\approx 5$  keV, which, upon accounting for the 782 keV endpoint energy, is a 0.0064% uncertainty on the energy. Assuming the same constant energy uncertainty across all electron energies and weighting by the

experimentally observed spectrum as was done in Section 5.2.4, we find uncertainties of  $\pm 0.16\%$  (2011-2012) and  $\pm 0.17\%$  (2012-2013) from variations in PMT gain.

### 5.2.6.3 Magnetic Field Nonuniformity

As shown in Section 2.4.2, the magnetic field is not uniform near the center of the decay trap, but rather has a dip surrounded by local maxima. Such conditions yield precarious scenarios for electrons with small longitudinal momentum (along the decay trap axis), as electrons with total momentum  $p = \sqrt{p_{\parallel}^2 + p_{\perp}^2}$  in a magnetic field  $B_0$  will be reflected if encountering a local maxima  $B_{\max}$  such that

$$B_{\max} > B_{\text{crit}} \equiv \left( \frac{p^2}{p_{\perp}^2} \right) B_0, \quad (5.42)$$

where  $B_{\text{crit}}$  is the critical condition for reflection. Thus a local field maximum will reflect a certain fraction of electrons, and a local field minimum, or field dip as we refer to it, will trap a certain fraction of electrons which originate within the dip.

The potential effect of nonuniform fields on the measured asymmetry is demonstrated quantitatively in appendix A. Qualitatively we understand the effect on the measured asymmetry using two ideal cases and considering the use of the super-ratio for extracting asymmetries. We also assume we have perfect detection efficiency in these cases.

The first nonuniformity we will consider is a central symmetric local maximum only. By central and symmetric we mean the field profile is identical on both sides of the maximum, which is at the center of the decay trap. A certain fraction of electrons both to the left and right of the maximum will be reflected back towards their initial location, changing the detected rates in each detector. Now spin state dependent and detector dependent acceptances nominally cancel in the super-ratio, but this modification to the rate is tied to the distribution itself, thus its effect is seen in the measured super-ratio asymmetry. This specific situation, in the context of appendix A, yields a dilution to the asymmetry that is dependent on the magnitude of the central maximum only.

The second scenario we will consider is that of a central symmetric field minimum (field dip). A field dip can trap  $\beta$ -decay electrons that originate in the lower field region if their longitudinal momentum is below some critical momentum, leaving them reflecting back and forth in the dip until they scatter off of the residual gas and gain enough momentum to escape. Such a scattering process randomizes the detected direction of the outgoing electron, thereby diluting the asymmetry.

Each ideal scenario alone produces a dilution to the asymmetry, and one would suspect that a correction to the asymmetry should be applied to increase the magnitude of the measured asymmetry, but simulation has shown the potential for nonuniform fields like those we measure to create an enhancement in the asymmetry. This very fact led to the calculation in appendix A, which shows that the position and shape of a field maximum or dip can create either enhancement or dilution to the asymmetry. This is not even considering that a field dip changes the angular distribution of the electrons it traps, which in turn changes the angular acceptance of the detected electrons, making electrons that never would have been detected before due to high pitch angle and low energy detectable by upscattering.

In conclusion, the intertwined dependence of the magnetic field correction on the shapes and positions of the nonuniformity and on the detector detection efficiencies prompted us to apply only an uncertainty from the field nonuniformity rather than a correction. Also, we only had reliable field data from 2011-2012, so a correction could not have been properly calculated for 2012-2013 without assumptions for the field profile. The uncertainty was determined by choosing a typical field profile and running fifty independent simulations with and without the field profile implemented for the 2011-2012 geometry. Both simulations were run with an increase in vacuum pressure from  $10^{-5}$  Torr to  $10^{-3}$  Torr in order to encourage upscattering from the field dip region, otherwise electron propagation time within the dip would have been far too computationally expensive. Since we are only studying the relative effect on the asymmetry, such a modification is acceptable. Upon histogramming the corrections to the asymmetry from the fifty independent simulations, one can extract the mean and error on the mean from a Gaussian fit to the distribution, giving the mean correction to be applied of  $-0.01(12)\%$ , but as mentioned we will only apply an uncertainty and no correction, so for both geometries the uncertainty from the field nonuniformity is  $\pm 0.12\%$ .

In the future, the issues encountered with the present determination of the field nonuniformity correction can be avoided. This uncertainty is strictly statistics limited, so with larger simulations the uncertainty can be reduced. Also, if the maps are taken often (and checked for quality), a credible time dependent correction to the asymmetry can be determined.

## 5.3 Theory Modifications

The  $\beta$ -decay asymmetry parameter of interest,  $A_0$ , is free of effects from the recoil of the decay proton (or the daughter nucleus in the case of a nuclear decay) and from Coulomb interactions between the charged products. What is measured experimentally obviously includes such effects, as they cannot be disentangled simply through observation of the decay electron momentum. The Monte Carlo corrections above are meant to correct for any geometry and detector dependent corrections, but to resolve  $A_0$ , we rely on theory calculations.

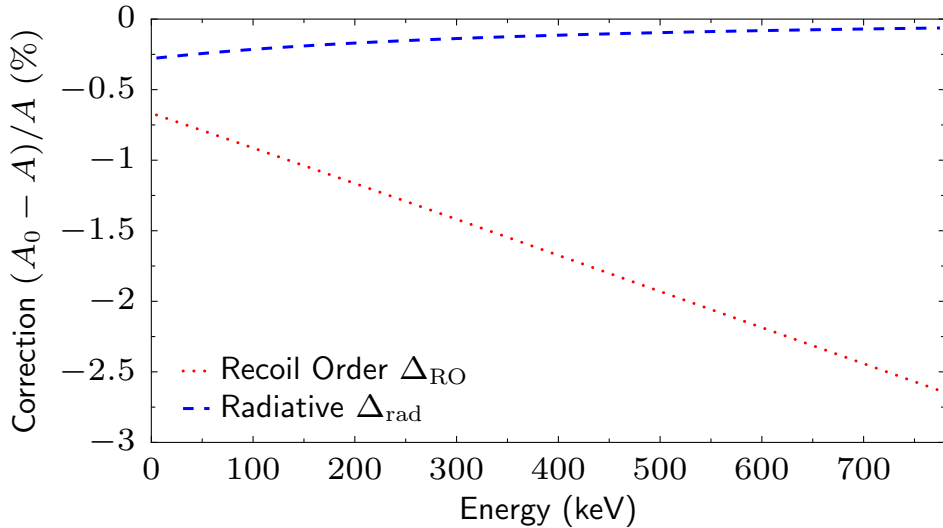


Figure 5.16: Radiative and Recoil Order theory corrections to the measured asymmetry due to finite mass and non-zero charge of the final state proton.

The theoretical effects come in two flavors: recoil-order modifications to address the finite mass of the final state proton and radiative corrections to remove effects from the electron interacting with the field of the proton. With all known systematic corrections from the experimental setup already addressed, we can write the final extracted value of  $A_0$  as  $A_0 = (1 + \Delta_{\text{RO}})(1 + \Delta_{\text{rad}})A$ . The energy dependence of each can be seen in 5.16.

### 5.3.1 Recoil Order Modification $\Delta_{\text{RO}}$

The recoil order and weak magnetism modification applied are those from Bilen'kii *et al.* [Bil+60] and further upheld by Wilkinson [Wil82]. The correction takes the

form

$$A(E) = A_0 \left( 1 + \frac{\lambda + \mu}{\lambda(1 - \lambda)(1 + 3\lambda^2)} \frac{1}{M} \left( \lambda^2 + \frac{2}{3}\lambda - \frac{1}{3} \right) E_0 - \left( \lambda^3 + 3\lambda^2 + \frac{5}{3}\lambda - \frac{1}{3} \right) E + \left( 2\lambda^2(1 - \lambda) \right) \frac{1}{E} \right), \quad (5.43)$$

where  $E$  is the electron total energy,  $E_0$  is the endpoint energy of the electron,  $\lambda \equiv \frac{g_A}{g_V}$ , and  $\mu \equiv \mu_p - \mu_n$ .

The correction to the asymmetry, when integrated over the analysis window and weighted by statistics, is -1.68(3)% and -1.67(3)% for 2011-2012 and 2012-2013 respectively. The uncertainties are conservative and carried over from the previous analysis.

It should be noted that the formalism above includes only the usual vector and axial vector terms in the hadronic current, as well as the weak magnetism coupling. Other work from Gardner and Zhang [GZ01], as discussed in Section 1.3.2.1, includes all potential interaction terms. The results agree with those from Bilen'kiĭ *et al.* and Wilkinson when the second class terms are neglected.

### 5.3.2 Radiative Modification $\Delta_{\text{rad}}$

Sirlin first calculated the  $O(\alpha)$  corrections to the unpolarized neutron  $\beta$ -decay electron energy spectrum [Sir67], followed a few years later by Shann's [Sha71] extension of the formalism for polarized neutrons. The asymmetry is modified by the amount  $(1 + \frac{\alpha}{2\pi}(h - g))$ , or

$$A(E) = A_0 \left( 1 + \frac{\alpha}{2\pi} (h(E, E_0) - g(E, E_0)) \right), \quad (5.44)$$

where

$$\begin{aligned} h - g = 4 \left( \frac{E_0 - E}{3E\beta^2} \right) & \left( \frac{\tanh^{-1} \beta}{\beta} - 1 \right) \left( 1 - \beta^2 + \frac{E_0 - E}{8E} \right) \\ & + \frac{\tanh^{-1} \beta}{\beta} \left( 2 - 2\beta^2 - \frac{(E - E_0)^2}{6E^2} \right). \end{aligned} \quad (5.45)$$

$E$  and  $E_0$  are the electron energy and endpoint energy, and  $\beta \equiv v/c$ . The correction over the analysis energy window is -0.12(5)% for both 2011-2012 and 2012-2013.

## 5.4 Final Asymmetries

The last step in determining the asymmetry parameter is, of course, extracting the asymmetry from the  $\beta$ -decay data. Application of all described Monte Carlo cor-

rections and uncertainties to the measured asymmetry produces a value for  $A_0$  and thereby determines the ratio of the axial vector to vector coupling constants in the weak interaction,  $\lambda \equiv \frac{g_A}{g_V}$ .

The general process includes choosing the proper subset of our data for the asymmetry extraction, making analysis cuts, optimizing our final analysis energy window to minimize uncertainties, and finally unveiling the result. This section is dedicated to these steps.

### 5.4.1 Blinding

All of the analysis discussed up until this point, and even all stages of the asymmetry extraction up until revealing the final result, are completed using blinded data, making this entire analysis a blind analysis. The idea behind blind analyses is to introduce a bias to your data in some way that would not allow anyone to know the final answer during all systematic studies. This removes the human temptation to skew corrections in such a way that the new result converges towards a personally desired result. This could be an attempt to achieve agreement with previous results or to move further from a null hypothesis to achieve discovery. Either way, avoiding this temptation makes for better science.

For this analysis, blinding was achieved by modifying the time stamps of every event in such a way that the the blinding factor (as part of the detector rates) would not cancel in the super-ratio. This required altered time stamps which are spin-state and detector dependent and do not cancel in the super-ratio. We produce two independent random blinding factors,  $f_{1,2}$ , such that

$$t_{1,2}^{\pm} = (1 \pm f_{1,2}) \cdot t \quad (5.46)$$

where  $t$  is the global time and  $t_{1,2}^{\pm}$  are the blinded times for each detector in each spin state. We completed detector calibrations, all systematic corrections, and the polarimetry analysis prior to unblinding, at which point all rates were recalculated using the proper global time  $t$ , generating the final unblinded asymmetries.

### 5.4.2 Data Selection and Processing

The data selection step generally involves choosing events that are “good” electron events, trying to preserve as many as possible to increase the statistical power while avoiding unforeseen systematic effects from questionable events. These cuts are also

applied to the simulated data when determining systematic corrections for consistency. Thus, if the model appropriately accounts for all experimentally induced deviations from the ideal asymmetry, the asymmetries from data and Monte Carlo should be consistent.

#### 5.4.2.1 Cuts

The first cut applied is a fiducial cut selecting events within 50 mm of the center of the decay trap. The fiducial cut removes events that could have potentially interacted with the decay trap wall, as the maximum radius of the electron’s spiral around the magnetic field is 7.76 mm and the wall of the decay trap is 62.2 mm from the center. Interactions with the walls of the decay trap can modify the energy and direction of the electron, thereby affecting the measured asymmetry. While the Monte Carlo model should be able to correct for this, avoiding the interactions altogether is advantageous.

We also remove from data and background runs any events that occur when the proton beam is dropped, which means no neutrons are being produced. Since we use the rate over an entire run in the super-ratio, using time periods with few events reduces the average rate. The real issue with this comes from the background subtraction, which is meant to account for backgrounds that could stem from beam related interactions. If either the  $\beta$ -decay or background run has a highly disproportionate amount of run time with the proton beam missing, the background subtraction for that run is not as effective. To illustrate this effect, imagine a background run where the proton beam was off for its entirety. The beam related background would thus be “zero” for the  $\beta$ -decay run that accompanies this background run, and the subsequent subtraction of the background run would leave the  $\beta$ -decay rates unaffected. While the extreme case is never observed, it is useful to remove periods of the runs where the proton beam is missing. A running monitor of the UCN production is used to determine when to cut intervals of data, dropping the events when the UCN rate in UCN Monitor 1 (the first monitor beyond the UCN source) falls below 2 Hz. The rate for all data was generally  $> 20$  Hz. Any events that occur within 0.05 s of the proton beam burst are also cut to improve the signal to background ratio.

Two wirechamber cuts, beyond the position cut, were also applied. The first is a cut on the “shape” of the wirechamber signal based on an algorithm developed by a collaborator C. Swank from Caltech. By shape we simply mean what the collection of cathode ADC signals look like when plotted as a function of position. While the algorithm classifies events as one of eight shapes based on the magnitude of the

signal on each wire group, the cut is used to remove non-physical shapes like multiple positions in one wirechamber. The second wirechamber cut simply checks that at least one cathode wire group in each plane was above threshold so that a position can be assigned to that event. Since a model of the cathode response was developed for the Monte Carlo in this analysis, these same cuts could be applied to the simulation to account for any systematic effect if these events are not simply random.

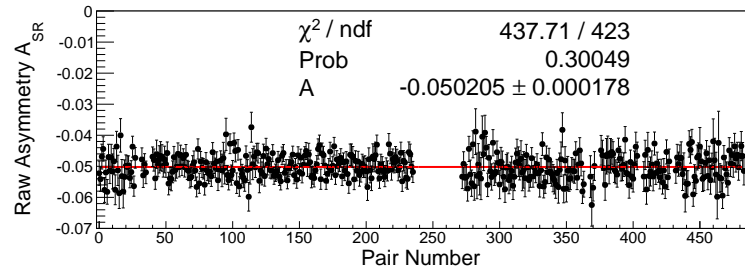
The last cut applied is an energy cut where we check that each event lies within the energy range  $190 \text{ keV} < T_e < 740 \text{ keV}$ . Within this energy range, the events are further separated into 10 keV energy bins for energy dependent asymmetry extraction. The determination of this analysis energy window is described below in Section 5.4.3.2. All asymmetries shown from now on will be fit or integrated over this energy range.

#### 5.4.2.2 Data Taking Structure

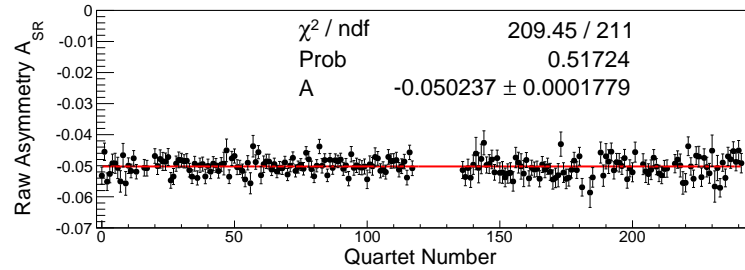
For use of the super-ratio technique, one must use at least two runs with differing loaded neutron spin states. For the UCNA experiment, we utilize what we call an octet data structure, consisting of eight  $\beta$ -decay runs, eight background runs, and eight depolarization runs, with the spin-state changing in such a way that produces four runs from each  $\pm$  spin state. The details of this method can be found in [Pla+12]. This method allows for construction of three different super-ratio asymmetries: octet asymmetries (utilizing all eight background subtracted  $\beta$ -decay runs in the asymmetry), quartet asymmetries (using four consecutive spin-flipped runs in the asymmetry), and pair asymmetries (using two consecutive spin-flipped runs). Each octet can potentially produce four pair asymmetries and two quartet asymmetries. We use the octet asymmetries in the extraction of the final asymmetry, as this structure lends to more efficient cancellation of time varying backgrounds. Figure 5.17 shows the raw asymmetries extracted from all three types of data groups. The results are consistent within statistical uncertainties, and the  $\chi^2/\text{NDF}$  indicates the fluctuations are statistical.

#### 5.4.2.3 Analysis Choices

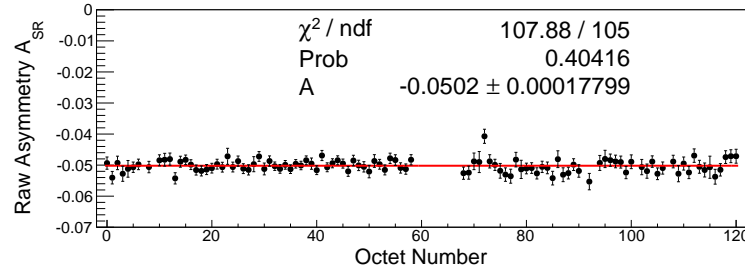
We have identified four detected electron event types thus far in this analysis, namely Type 0, 1, 2, and 3. In summary, Type 0 events are those which are identified as single detector events, meaning they trigger one detector package only, and they make up almost 95% of detected events. Types 1, 2, and 3 are identified as backscattering



(a) Pair Asymmetries



(b) Quartet Asymmetries



(c) Octet Asymmetries

Figure 5.17: All raw super-ratio asymmetries as a function of group number, whether octet, quartet, or pair. There are no systematic corrections applied, and the asymmetries are integrated over the analysis window 190-740 keV. The split in the data is a batch of data from 2012-2013 that had to be discarded due to bad timing information.

events, with Type 1 events triggering both scintillators, while 2 and 3 trigger both wirechambers but only one scintillator. Based on solely trigger logic, a Type 2 cannot be distinguished from a Type 3, but a delineation can be made between them given their energy deposition in the MWPC. See Section 2.7 for a detailed description of the backscattering events and Section 4.3.4 for implementation of the MWPC calibration used to separate the Type 2 and Type 3 events.

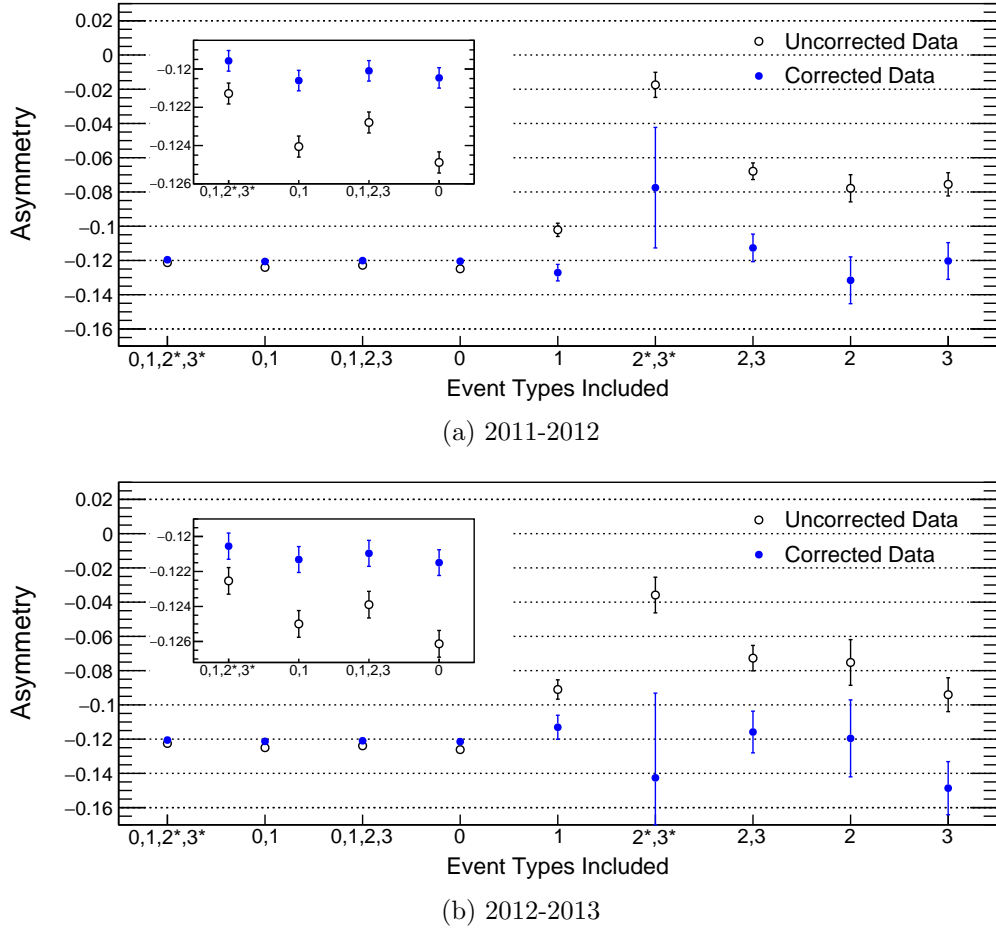


Figure 5.18: Asymmetries for different subsets of data. The \* signifies unseparated Type 2 and Type 3 events. The inset shows the asymmetries that include Type 0 events, as the uncertainties are too small to see in the main figure. The only corrections applied to these asymmetries are the energy dependent Monte Carlo corrections and the polarization correction. The error bars are purely statistical, so the observed agreement between asymmetries is a lower limit.

Inclusion of any subset of the aforementioned event types in the analysis produces different asymmetries, where any choices that have like event types are correlated at the level of the fractional statistical uncertainty of the like types. One may also decide to include the Type 2/3 events as unseparated or separated by the MWPC energy

cut, giving yet another set of analysis choices. For this analysis, we used all event types with the Type 2 and Type 3 separated. This choice utilizes maximal statistics, while separating the Type 2/3 events requires smaller systematic corrections and uncertainties than leaving them unseparated.

Figure 5.18 shows the asymmetries for all analysis choices considered, with the event types included in the asymmetry extraction listed on the horizontal axis. There is a noticeable improvement in the agreement across all analysis choices compared to previous analyses, indicating improvement in the Monte Carlo corrections, namely  $\Delta_2$  and  $\Delta_3$ . The uncertainties in the figure are purely statistical, so the agreement seen is a worst case scenario as inclusion of systematic uncertainties inflates the error bars.

### 5.4.3 Determining $A_0$

#### 5.4.3.1 Combining Results

After selecting the data to be used in the final determination of the asymmetry, one is left with two separate blinded results, one from each geometry (2011-2012 and 2012-2013). The results are then combined via a method developed for the previous analysis by M. Mendenhall [Men14]. In summary, the combination is a modified weighted average that takes into account correlations between all uncertainties. Uncorrelated uncertainties will improve the final uncertainty, while correlated uncertainties cannot. The method inherently solves for the weighting factors that minimize the total uncertainty of the combined final result.

For this analysis, the individual systematic uncertainties from each geometry (i.e.  $\Delta_2$  from 2011-2012 and 2012-2013) are taken to be completely correlated, but they are uncorrelated with all other uncertainties. The statistical uncertainty of one geometry is the only uncertainty treated as uncorrelated with its counterpart from the other geometry, as we would like to take advantage of the combined statistical power of each result.

#### 5.4.3.2 Optimization of energy range

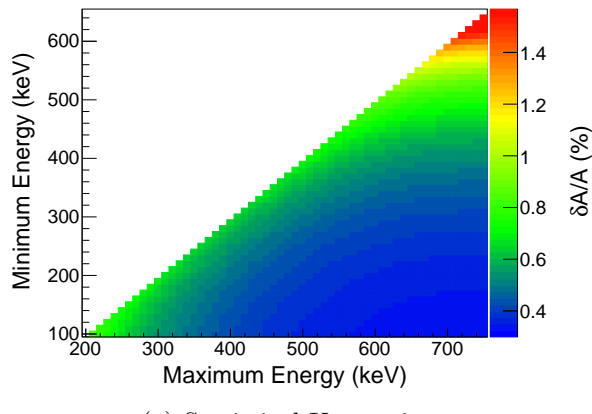
Once the framework for combining results is in place, the energy analysis window must be determined. Ideally, the analysis window should be one that minimizes the total uncertainty given the subset of data chosen for the final result, but, because several of the integrated corrections require the analysis window as input, we only consider

the uncertainties from statistics, energy reconstruction, and energy dependent Monte Carlo corrections during minimization.

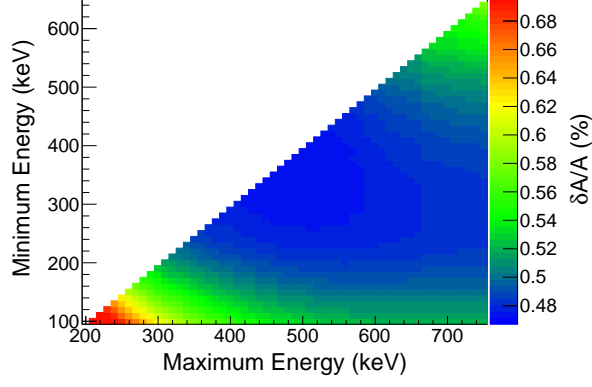
The final energy window is calculated by scanning all possible energy windows in 10 keV increments, with a minimum lower bound at  $> 100$  keV and a maximum upper bound of  $< 780$  keV. The total width of the energy window is set to start at 100 keV to save on computation time but is not limited beyond that. Upon exploring all energy windows, the minimum combined uncertainty occurs at  $190 \text{ keV} < T_e < 740 \text{ keV}$  shown. Figure 5.19 shows the uncertainty contributions as a function of energy window. The final plot shows the combined uncertainty from all three contributions, and we see that the window  $190 \text{ keV} < T_e < 740 \text{ keV}$  falls within the area of the minimum uncertainty. Once we choose the minimum edge of our window, we can view the dependence of the final uncertainty as a function of the upper edge of the analysis window as seen in Figure 5.20. Here we see the total uncertainty becomes essentially constant beyond an upper window cut of 690 keV. The dependence of the asymmetry on energy window can be seen in Figure 5.21 panel (a), where the ratio  $(A - A_{\min})/\delta A$  is plotted. The asymmetry is consistent with the minimum energy window asymmetry ( $A_{\min}$ ) within a  $1\sigma$  uncertainty over a large portion of the sampled analysis windows. Figure 5.21 panel (b) shows all of the energy windows that produce a  $1\sigma$  agreement. The minimum energy window chosen is indicated in the figure by the black dashed circle, well within a region where the asymmetry is stable.

#### 5.4.3.3 Unblinded Result

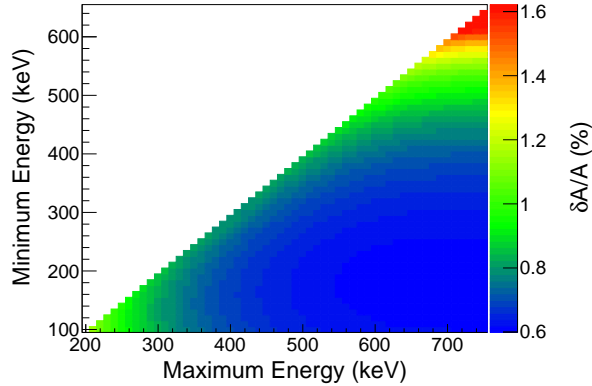
On August 16, 2017, upon completion of all systematic studies and the asymmetry analysis code, the data was unblinded and the asymmetries recalculated using the proper time stamps. The energy dependent asymmetries and final asymmetries for the two geometries, 2011-2012 and 2012-2013, are shown in Figure 5.23, with fits over the final analysis window of  $190 \text{ keV} < T_e < 740 \text{ keV}$ . The unblinded asymmetries with both statistical and systematic uncertainties accounted for are  $A_0 = -0.12026(54)_{\text{stat}}(67)_{\text{syst}}$  and  $A_0 = -0.12111(74)_{\text{stat}}(69)_{\text{syst}}$  for 2011-2012 and 2012-2013 respectively. Utilizing the method described in section 5.4.3.1 for combining results, the 2011-2012 and 2012-2013 asymmetries were combined with weights of 0.67 (2011-2012) and 0.33 (2012-2013), yielding a final value of  $A_0 = -0.12054(44)_{\text{stat}}(68)_{\text{syst}}$  corresponding to a value for the ratio of the axial-vector to vector coupling constants of  $\lambda \equiv \frac{g_A}{g_V} = -1.2783(22)$ , where the statistical and systematic uncertainties have been added in quadrature. Figure 5.24 shows schematically where the present result lies in comparison to previous measurements



(a) Statistical Uncertainty



(b) Systematic Uncertainty (Combined Energy Uncertainty and Monte Carlo uncertainty)



(c) Combined systematic and statistical uncertainty

Figure 5.19: Plots of the fractional uncertainty on the extracted asymmetry for given minimum and maximum limits on the analysis window. The minimum of the combined systematic and statistical uncertainty is used for the final analysis window,  $190 \text{ keV} < T_e < 740 \text{ keV}$ .

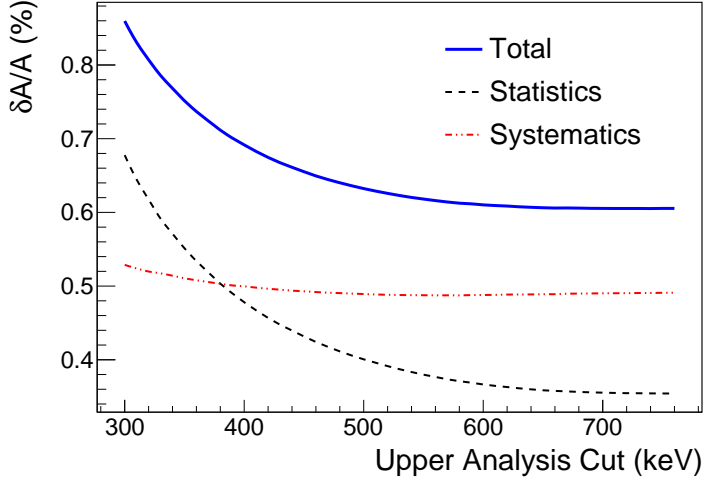


Figure 5.20: Statistical and systematic errors used in minimization of the energy window. This is a projection of Figure 5.19 about the minimum window cut of 190 keV to show the dependence on energy cut more effectively.

of  $A_0$ .

We also report a combined result using our previous measurement [Men+13] and a similar weighting method as above, only now we set all systematic uncertainties to the smallest reported value between the two measurements and treat them as completely correlated. This in turn means we do not benefit beyond the best measurement of any systematic uncertainty, but that we take advantage of the increased statistics. This culminates in the combined UCNA results of  $A_0 = -0.12015(34)_{\text{stat}}(63)_{\text{syst}}$  and  $\lambda \equiv \frac{g_A}{g_V} = -1.2772(20)$ , with weights of 0.39 for the previous result [Men+13] and 0.61 for the result from this analysis.

## 5.5 Future Outlook for UCNA and $A_0$ Measurements

While this measurement concludes results for  $A_0$  from the UCNA experiment in its current capacity, there are hopes for a next generation UCNA+ experiment. The uncertainties described within this thesis, namely the backscattering,  $\cos \theta$ , and energy reconstruction uncertainties, limit the UCNA Experiment as currently configured to the present precision.

With this in mind, UCNA+ intends to take actions to drastically reduce  $\Delta_3$ , or the  $\cos \theta$  correction, which can be achieved by decreasing the fraction of electrons that are lost due to inefficiencies within the spectrometer. These mainly come from

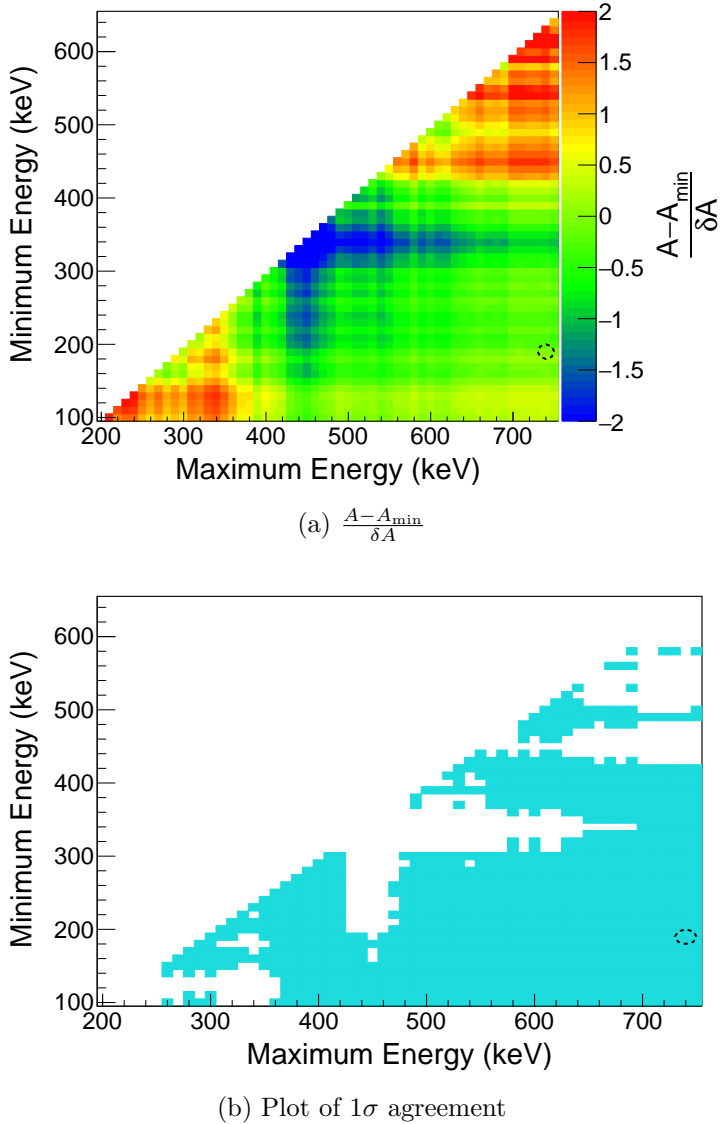


Figure 5.21: Panel (a) shows the ratio of  $(A - A_{\min})$  to  $\delta A$ , where  $\delta A$  is the  $1\sigma$  total uncertainty taken from Figure 5.19 panel (c). The  $z$ -axis is a measure of agreement between the asymmetry in a bin with the overall minimum uncertainty bin,  $A_{\min}$ , in units of  $\sigma$  of the bin being used. Values between  $-1$  and  $+1$  indicate that the asymmetry in the bin is in agreement with  $A_{\min}$  at the  $1\sigma$  level. Panel (b) shows the bins for which this  $1\sigma$  agreement is met. The black circle in each figure indicates the location of  $A_{\min}$ .

the existence of the foils at the end of the decay trap, so the idea is to remove the foils and no longer confine the neutrons within the decay volume. With the recent upgrades in the UCN source performance, trapping the neutrons within the decay volume is less important than it was during previous UCNA runs. Another interesting proposal is to have annular endcaps with a hole in the middle. This would

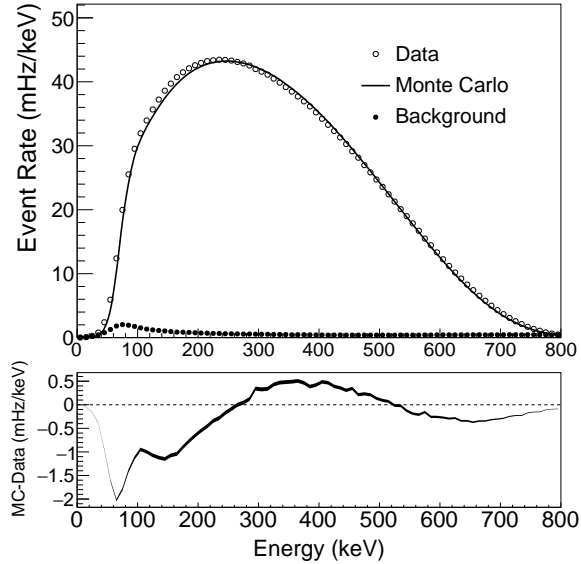


Figure 5.22: Final beta decay spectrum from data (open circles), Monte Carlo (solid line), and the subtracted background (closed circles). The bottom shows the difference between the Monte Carlo spectrum and the data.

allow one to make a radial position cut on the electron events to use events which either originated in the region with effectively no endcap or in the outer region where the electron would see an endcap. Comparisons between these two types of events sheds light on the behavior of the correction from data itself, and when compared to Monte Carlo can help determine the level at which the Monte Carlo corrections are accurate. This comparison with Monte Carlo may improve both the backscattering and  $\cos \theta$  systematic uncertainties.

As for the energy reconstruction, detectors with better linearity and perhaps a self-position-reconstructing scintillator would be useful. With position reconstruction accomplished within the scintillator, the wirechambers could be removed thus reducing the  $\cos \theta$  correction further. Another potential improvement, although admittedly difficult, would be the development of a calibration method which samples the entire fiducial volume, or at least a larger fraction of the detector face. The activated xenon spectrum highlights the promise of such a method, as it fills the entire spectrometer during position map calibration runs, but the existence of discrete conversion lines within the calibration gas would create a completely determined calibration for every “pixel” of the detector. This would remove the need for position maps altogether and would avoid any potential bias from measuring the position dependence of the detector with a characteristic of the xenon spectrum that is beyond the endpoint of the electron spectrum, an imperfect method when the detector shows any non-linear be-

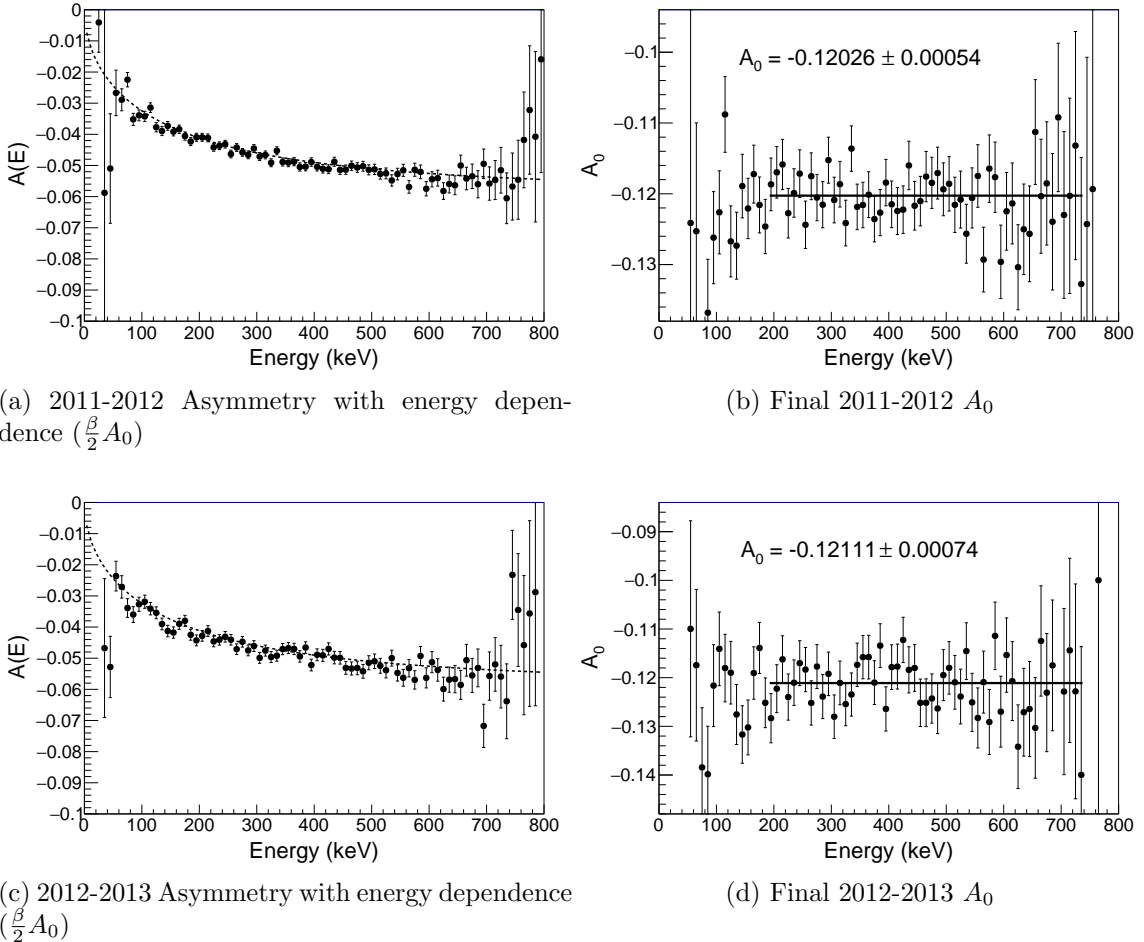


Figure 5.23: Final unblinded 2011-2012 and 2012-2013 asymmetry with all systematic corrections applied. The dashed line in a.) and c.) uses PDG  $A_0 = -0.1184$  for comparison. The fits in b.) and d.) are over the final analysis window,  $190 \text{ keV} < T_e < 740 \text{ keV}$ . The uncertainties are statistical only.

havior. Obviously a method like this, especially one that fills the entire spectrometer rather than just the decay trap, would require systematic studies of its own.

The future of  $A_0$  and  $\lambda$  measurements is quite promising given the status of recent results. Figure 5.25 illustrates the current dilemma facing the experimental nuclear physics community regarding weak interactions and the neutron itself. Of measurements included in the current 2017 Particle Data Group (PDG) average, there is a several  $\sigma$  discrepancy between  $\lambda$  measurements prior to 2002 and those after 2002. One also sees from the figure that a similar splitting of neutron lifetime values has occurred, with the difference seemingly arising between experiments using neutron beams [Yue+13; Byr+96] and those using UCN (both material bottle [Ser+05; Arz+15; Ste+12; Pic+10; Mam+93] and magnetic bottle [PJ+17] measure-

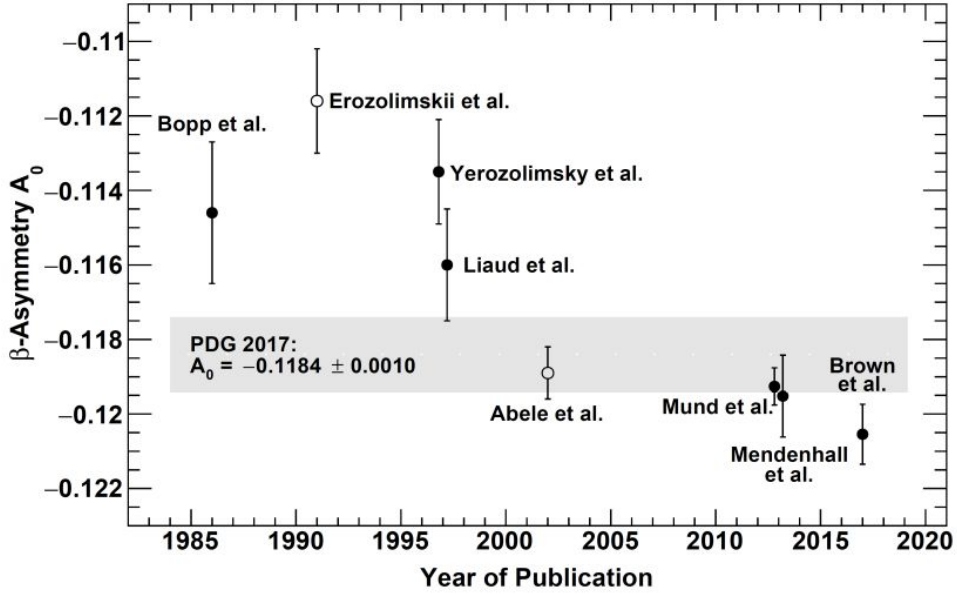


Figure 5.24: Historical plot of  $A_0$  measurements including the measurement resulting from this analysis [Bop+86; Ero+91; Yer+97; Lia+97; Abe+02; Mun+13; Men+13; Bro+17]. The shaded band indicates the Particle Data Group average value [PG+16] for the asymmetry parameter, where the solid data points are included in the average (not including the Brown *et al.* point, as this will be included in future averages). Thank you to Dr. Plaster for inclusion of this plot.

ments). When combined with measurements of the CKM matrix element  $V_{ud}$  from superallowed  $0^+ \rightarrow 0^+$  nuclear  $\beta$ -decays, a clearly favorable scenario presents itself, and further precision measurements of both  $\lambda$  and  $\tau_n$  will assist in settling the matter.

The older pre-2002 measurements of  $\lambda$  prompt the PDG to apply a scale factor of 2.2 to the uncertainty on the global average for  $\lambda$  (and a scale factor of 2.4 to  $A_0$ ). The PDG only includes in the calculation of the scale factor those measurements that satisfy

$$\delta x_i < 3\sqrt{N}\delta\bar{x}, \quad (5.47)$$

where  $x_i$  refers to one measurement of quantity  $x$  out of  $N$  measurements and  $\delta\bar{x}$  is the non-scaled error on the weighted average  $\bar{x}$  [PG+16]. So while the older measurements carry very little weight in the average value and the non-scaled uncertainty, they drastically affect the  $\chi^2$ . One solution to this issue is to improve the uncertainty on modern  $A_0$  and  $\lambda$  measurements, as inclusion of a 0.1% result for  $A_0$  (yielding a 0.025% result for  $\lambda$ ), removes the pre-2002 results for  $\lambda$  from those that enter the calculation of the scale factor. An expected result from PERKEOII is expected

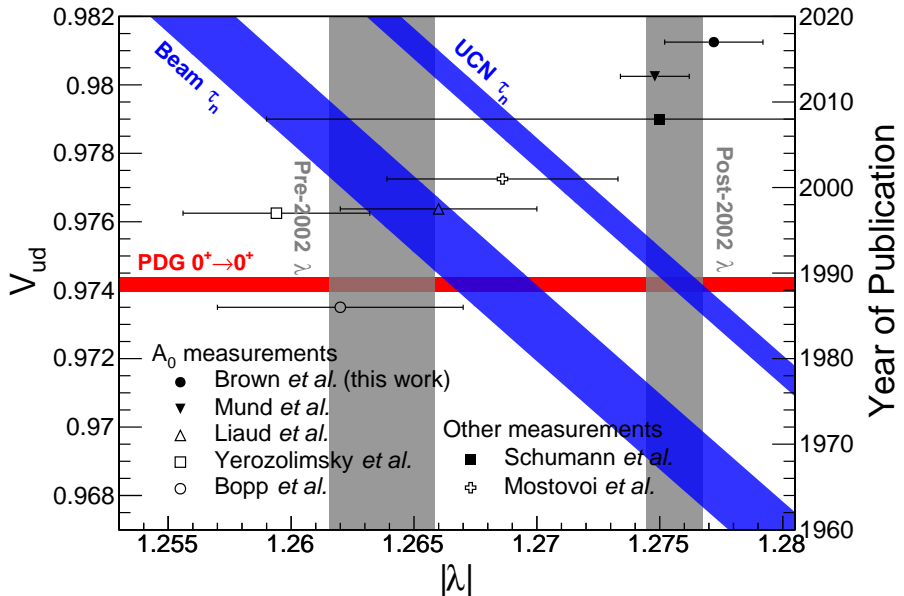


Figure 5.25: Status of  $V_{ud}$ , the neutron lifetime, and  $\lambda$  measurements. The  $\lambda$  result bands (vertical) are divided into pre-2002 [Bop+86; Yer+97; Lia+97] and post-2002 [Mos+01; Sch+08; Mun+13; Men+13] results, where the distinction is made using the date of the most recent result from each experiment. The right axis shows publication year for the individual lambda measurements included in the calculation of the  $\lambda$  bands (closed markers for post-2002, open markers for pre-2002). Note that the result of this work (Brown *et al.*) is the combined UCNA result from [Men+13] and the current analysis, and the Mund *et al.* result is the combined PERKEOII result from [Abe+02; Mun+13]. The diagonal bands are derived from neutron lifetime measurements and are separated into neutron beam [Yue+13; Byr+96] and UCN bottle experiments, which consist of material bottle storage [Ser+05; Arz+15; Ste+12; Pic+10; Mam+93] and magnetic bottle storage [PJ+17]. The  $V_{ud}$  band (horizontal) comes from superallowed  $0^+ \rightarrow 0^+$  nuclear  $\beta$ -decay measurements [PG+16]. The error bands include scale factors as prescribed by the Particle Data Group [PG+16].

to have an uncertainty  $< 0.3\%$  on  $A_0$ , and hopefully a next generation UCNA+ experiment can contribute the desired precision to remove the scale factor from the PDG average values for  $A_0$  and  $\lambda$  altogether.

Copyright<sup>©</sup> Michael A-P Brown, 2018.

## **Appendix A**

### **Magnetic Field Non-Uniformity and the Super-Ratio**

Copyright<sup>©</sup> Michael A-P Brown, 2018.

# References

- [Abe+02] Hartmut Abele et al. “Is the unitarity of the quark-mixing CKM matrix violated in neutron  $\beta$ -decay?” In: *Physical Review Letters* 88.21 (2002), p. 211801.
- [Ali+17] Simone Alioli et al. “Right-handed charged currents in the era of the Large Hadron Collider”. In: *Journal of High Energy Physics* 2017.5 (2017), p. 86.
- [Arz+15] S Arzumanov et al. “A measurement of the neutron lifetime using the method of storage of ultracold neutrons and detection of inelastically up-scattered neutrons”. In: *Physics Letters B* 745 (2015), pp. 79–89.
- [Ber+17] Evan Berkowitz et al. “An accurate calculation of the nucleon axial charge with lattice QCD”. In: *arXiv preprint arXiv:1704.01114* (2017).
- [Bil+60] SM Bilenkii et al. “On the theory of neutron beta-decay”. In: *SOVIET PHYSICS JETP-USSR* 10.6 (1960), pp. 1241–1244.
- [Bop+86] Peter Bopp et al. “Beta-Decay Asymmetry of the Neutron and g A g V”. In: *Physical Review Letters* 56.9 (1986), p. 919.
- [Bro+17] M. A.-P. Brown et al. “New result for the neutron  $\beta$ -asymmetry parameter  $A_0$  from UCNA”. In: *arXiv preprint arXiv:1712.00884* (2017).
- [Byr+02] J Byrne et al. “Determination of the electron–antineutrino angular correlation coefficient  $a_0$  and the parameter—  $\lambda$ —— GA/GV— in free neutron  $\beta$ -decay from measurements of the integrated energy spectrum of recoil protons stored in an ion trap”. In: *Journal of Physics G: Nuclear and Particle Physics* 28.6 (2002), p. 1325.
- [Byr+96] J Byrne et al. “A revised value for the neutron lifetime measured using a Penning trap”. In: *EPL (Europhysics Letters)* 33.3 (1996), p. 187.
- [Cab63] Nicola Cabibbo. “Unitary symmetry and leptonic decays”. In: *Physical Review Letters* 10.12 (1963), p. 531.

- [Cap+17] Stefano Capitani et al. “Iso-vector axial form factors of the nucleon in two-flavour lattice QCD”. In: *arXiv preprint arXiv:1705.06186* (2017).
- [CGH13] Vincenzo Cirigliano, Susan Gardner, and Barry R Holstein. “Beta decays and non-standard interactions in the LHC era”. In: *Progress in Particle and Nuclear Physics* 71 (2013), pp. 93–118.
- [CJ+56] CL Cowan Jr et al. “Detection of the Free Neutrino: A Confirmation”. In: *Science* 124 (1956), pp. 103–104.
- [CMS04] Andrzej Czarnecki, William J Marciano, and Alberto Sirlin. “Precision measurements and CKM unitarity”. In: *Physical Review D* 70.9 (2004), p. 093006.
- [Col+16] Precision Neutron Decay Matrix Elements PNDME Collaboration et al. “Axial, scalar, and tensor charges of the nucleon from 2+ 1+ 1-flavor Lattice QCD”. In: *Physical Review D* 94.5 (2016), p. 054508.
- [CR74] Edwin Catmull and Raphael Rom. “A class of local interpolating splines”. In: *Computer aided geometric design*. Elsevier, 1974, pp. 317–326.
- [Dar+17] G Darius et al. “Measurement of the Electron-Antineutrino Angular Correlation in Neutron  $\beta$  Decay”. In: *Physical Review Letters* 119.4 (2017), p. 042502.
- [EF57] ME Ebel and G Feldman. “Further remarks on Coulomb corrections in allowed beta transitions”. In: *Nuclear Physics* 4 (1957), pp. 213–214.
- [Ero+91] BG Erozolimskii et al. “New measurements of the electron-neutron spin asymmetry in neutron beta-decay”. In: *Physics Letters B* 263.1 (1991), pp. 33–38.
- [Fer34a] Enrico Fermi. “An attempt of a theory of beta radiation. 1.” In: *Z. Phys.* 88.UCRL-TRANS-726 (1934), pp. 161–177.
- [Fer34b] Enrico Fermi. “Versuch einer Theorie der  $\beta$ -Strahlen. I”. In: *Zeitschrift für Physik A Hadrons and Nuclei* 88.3 (1934), pp. 161–177.
- [FGM58] Richard P Feynman and Murray Gell-Mann. “Theory of the Fermi interaction”. In: *Physical Review* 109.1 (1958), p. 193.
- [GAC16] Martín González-Alonso and Jorge Martin Camalich. “Global effective-field-theory analysis of new-physics effects in (semi) leptonic kaon decays”. In: *Journal of High Energy Physics* 2016.12 (2016), p. 52.

- [GGS58] Maurice Goldhaber, L Grodzins, and AW Sunyar. “Helicity of neutrinos”. In: *Physical Review* 109.3 (1958), p. 1015.
- [GIM70] Sheldon L Glashow, Jean Iliopoulos, and Luciano Maiani. “Weak interactions with lepton-hadron symmetry”. In: *Physical review D* 2.7 (1970), p. 1285.
- [GK90] Klaus Grotz and Hans Volker Klapdor. *The weak interaction in nuclear, particle and astrophysics*. CRC Press, 1990.
- [GLW57] Richard L Garwin, Leon M Lederman, and Marcel Weinrich. “Observations of the failure of conservation of parity and charge conjugation in meson decays: the magnetic moment of the free muon”. In: *Physical Review* 105.4 (1957), p. 1415.
- [GM58] Murray Gell-Mann. “Test of the nature of the vector interaction in  $\beta$  decay”. In: *Physical Review* 111.1 (1958), p. 362.
- [GMB96] Walter Greiner, Berndt Müller, and David Allan Bromley. *Gauge theory of weak interactions*. Vol. 5. Springer, 1996.
- [Gri08] David Griffiths. *Introduction to elementary particles*. John Wiley & Sons, 2008.
- [GRL91] Robert Golub, David Richardson, and Steve K Lamoreaux. *Ultra-cold neutrons*. CRC Press, 1991.
- [GT36] George Gamow and Edward Teller. “Selection Rules for the  $\beta$ -Disintegration”. In: *Physical Review* 49.12 (1936), p. 895.
- [GZ01] Susan Gardner and Chi Zhang. “Sharpening low-energy, standard-model tests via correlation coefficients in neutron  $\beta$  decay”. In: *Physical review letters* 86.25 (2001), p. 5666.
- [Hic+17] KP Hickerson et al. “First direct constraints on Fierz interference in free-neutron  $\beta$  decay”. In: *Physical Review C* 96.4 (2017), p. 042501.
- [Hic13] Kevin Peter Hickerson. “The physics of ultracold neutrons and Fierz interference in beta decay”. PhD thesis. California Institute of Technology, 2013.
- [Hoe03] Seth A. Hoedl. “Novel Proton Detectors, Ultra-Cold Neutron Decay and Electron Backscatter”. PhD thesis. Princeton University, 2003.

- [Hol+12a] Adam T Holley et al. “A high-field adiabatic fast passage ultracold neutron spin flipper for the UCNA experiment”. In: *Review of Scientific Instruments* 83.7 (2012), p. 073505.
- [Hol+12b] Adam T Holley et al. “Ultracold Neutron Polarimetry in a Measurement of the beta Asymmetry.” PhD thesis. North Carolina State University, 2012.
- [Hol74] Barry R Holstein. “Recoil effects in allowed beta decay: the elementary particle approach”. In: *Reviews of Modern Physics* 46.4 (1974), p. 789.
- [Ito+07] TM Ito et al. “A multiwire proportional chamber for precision studies of neutron  $\beta$  decay angular correlations”. In: *Nuclear Instruments and Methods in Physics Research Section A: Accelerators, Spectrometers, Detectors and Associated Equipment* 571.3 (2007), pp. 676–686.
- [Ito+17] TM Ito et al. “Performance of the upgraded ultracold neutron source at Los Alamos National Laboratory and its implication for a possible neutron electric dipole moment experiment”. In: *arXiv preprint arXiv:1710.05182* (2017).
- [Jac99] John David Jackson. *Classical electrodynamics*. 1999.
- [JTW57] JD Jackson, SB Treiman, and HW Wyld. “Coulomb corrections in allowed beta transitions”. In: *Nuclear Physics* 4 (1957), pp. 206–212.
- [JTWJ57] JD Jackson, SB Treiman, and HW Wyld Jr. “Possible tests of time reversal invariance in beta decay”. In: *Physical Review* 106.3 (1957), p. 517.
- [KM73] Makoto Kobayashi and Toshihide Maskawa. “CP-violation in the renormalizable theory of weak interaction”. In: *Progress of Theoretical Physics* 49.2 (1973), pp. 652–657.
- [KRP36] Franz ND Kurie, JR Richardson, and HC Paxton. “The radiations emitted from artificially produced radioactive substances. i. the upper limits and shapes of the  $\beta$ -ray spectra from several elements”. In: *Physical Review* 49.5 (1936), p. 368.
- [Liaud+97] P Liaud et al. “The measurement of the beta asymmetry in the decay of polarized neutrons”. In: *Nuclear Physics A* 612.1 (1997), pp. 53–81.
- [LY56] Tsung-Dao Lee and Chen-Ning Yang. “Question of parity conservation in weak interactions”. In: *Physical Review* 104.1 (1956), p. 254.

- [LY57] Tsung D Lee and Chen-Ning Yang. “Parity nonconservation and a two-component theory of the neutrino”. In: *Physical Review* 105.5 (1957), p. 1671.
- [Mam+93] W Mampe et al. “Measuring neutron lifetime by storing ultracold neutrons and detecting inelastically scattered neutrons”. In: *JETP LETTERS C/C OF PIS’MA V ZHURNAL EKSPERIMENTAL’NOI TEO-RETICHESKOI FIZIKI* 57 (1993), pp. 82–82.
- [Mam10] Russell Rene Mammei. “Thin films for the transport of polarized ultracold neutrons for fundamental symmetry study”. PhD thesis. 2010.
- [Mat91] E Mathieson. “Induced charge distributions in proportional detectors”. In: *Brookhaven National Laboratory* (1991).
- [MBM76] Christopher L Morris, Wilfred J Braithwaite, and C Fred Moore. “A stable light pulser for gain stabilizing photomultiplier tubes”. In: *Nuclear Instruments and Methods* 136.1 (1976), pp. 197–198.
- [Men+13] MP Mendenhall et al. “Precision measurement of the neutron  $\beta$ -decay asymmetry”. In: *Physical Review C* 87.3 (2013), p. 032501.
- [Men14] Michael Praetorius Mendenhall. “Measurement of the neutron beta decay asymmetry using ultracold neutrons”. PhD thesis. California Institute of Technology, 2014.
- [Mor+02] CL Morris et al. “Measurements of ultracold-neutron lifetimes in solid deuterium”. In: *Physical review letters* 89.27 (2002), p. 272501.
- [Mor+09] CL Morris et al. “Multi-wire proportional chamber for ultra-cold neutron detection”. In: *Nuclear Instruments and Methods in Physics Research Section A: Accelerators, Spectrometers, Detectors and Associated Equipment* 599.2 (2009), pp. 248–250.
- [Mos+01] Yu A Mostovoi et al. “Experimental value of GA/GV from a measurement of both P-odd correlations in free-neutron decay”. In: *Physics of Atomic Nuclei* 64.11 (2001), pp. 1955–1960.
- [Mun+13] D Mund et al. “Determination of the Weak Axial Vector Coupling  $\lambda = g_A/g_V$  from a Measurement of the  $\beta$ -Asymmetry Parameter A in Neutron Beta Decay”. In: *Physical review letters* 110.17 (2013), p. 172502.
- [PG+16] C Patrignani, Particle Data Group, et al. “Review of particle physics”. In: *Chinese physics C* 40.10 (2016), p. 100001.

- [Pic+10] A Pichlmaier et al. “Neutron lifetime measurement with the UCN trap-in-trap MAMBO II”. In: *Physics Letters B* 693.3 (2010), pp. 221–226.
- [PJ+17] RW Pattie Jr et al. “Measurement of the neutron lifetime using an asymmetric magneto-gravitational trap and in situ detection”. In: *arXiv preprint arXiv:1707.01817* (2017).
- [Pla+08] B Plaster et al. “A solenoidal electron spectrometer for a precision measurement of the neutron  $\beta$ -asymmetry with ultracold neutrons”. In: *Nuclear Instruments and Methods in Physics Research Section A: Accelerators, Spectrometers, Detectors and Associated Equipment* 595.3 (2008), pp. 587–598.
- [Pla+12] Bg Plaster et al. “Measurement of the neutron  $\beta$ -asymmetry parameter A 0 with ultracold neutrons”. In: *Physical Review C* 86.5 (2012), p. 055501.
- [Ren90] Peter Renton. *Electroweak interactions: an introduction to the physics of quarks and leptons*. Cambridge University Press, 1990.
- [Rio+11] R Rios et al. “Sealed drift tube cosmic ray veto counters”. In: *Nuclear Instruments and Methods in Physics Research Section A: Accelerators, Spectrometers, Detectors and Associated Equipment* 637.1 (2011), pp. 105–108.
- [Sau+04] A Saunders et al. “Demonstration of a solid deuterium source of ultracold neutrons”. In: *Physics Letters B* 593.1 (2004), pp. 55–60.
- [Sau+13] A Saunders et al. “Performance of the Los Alamos National Laboratory spallation-driven solid-deuterium ultra-cold neutron source”. In: *Review of Scientific Instruments* 84.1 (2013), p. 013304.
- [Sch+08] Marc Schumann et al. “Measurement of the proton asymmetry parameter in neutron beta decay”. In: *Physical review letters* 100.15 (2008), p. 151801.
- [Ser+05] A Serebrov et al. “Measurement of the neutron lifetime using a gravitational trap and a low-temperature Fomblin coating”. In: *Physics Letters B* 605.1 (2005), pp. 72–78.
- [Sha71] RT Shann. “Electromagnetic effects in the decay of polarized neutrons”. In: *Il Nuovo Cimento A (1971-1996)* 5.4 (1971), pp. 591–596.

- [Sir67] A Sirlin. “General properties of the electromagnetic corrections to the beta decay of a physical nucleon”. In: *Physical Review* 164.5 (1967), p. 1767.
- [SM58] Eo CG Sudarshan and RE Marshak. “Chirality invariance and the universal Fermi interaction”. In: *Physical Review* 109.5 (1958), p. 1860.
- [Ste+12] Albert Steyerl et al. “Quasielastic scattering in the interaction of ultracold neutrons with a liquid wall and application in a reanalysis of the Mambo I neutron-lifetime experiment”. In: *Physical Review C* 85.6 (2012), p. 065503.
- [Wei58] Steven Weinberg. “Charge symmetry of weak interactions”. In: *Physical Review* 112.4 (1958), p. 1375.
- [Wil68] Fred L Wilson. “Fermi’s theory of beta decay”. In: *American Journal of Physics* 36.12 (1968), pp. 1150–1160.
- [Wil82] Denys H Wilkinson. “Analysis of neutron  $\beta$ -decay”. In: *Nuclear Physics A* 377.2-3 (1982), pp. 474–504.
- [Wu+57] Chien-Shiung Wu et al. “Experimental test of parity conservation in beta decay”. In: *Physical review* 105.4 (1957), p. 1413.
- [Yer+97] B Yerozolimsky et al. “Corrigendum: Corrected value of the beta-emission asymmetry in the decay of polarized neutrons measured in 1990”. In: *Physics Letters B* 412.3-4 (1997), pp. 240–241.
- [You17] A. R. Young. “Super-ratio with explicit spin-up and spin-down polarizations”. In: *Private Communication* (2017).
- [Yue+13] AT Yue et al. “Improved determination of the neutron lifetime”. In: *Physical review letters* 111.22 (2013), p. 222501.

# Vita

A brief vita goes here.